

OBSERVATIONAL INVESTIGATIONS OF  
THE PROGENITORS OF SUPERNOVAE

Joseph David Lyman

ASTROPHYSICS RESEARCH INSTITUTE

A thesis submitted in partial fulfilment of the requirements of

Liverpool John Moores University

for the degree of

Doctor of Philosophy.

March 20, 2014

The copyright of this thesis rests with the author. No quotation from it should be published without his prior written consent and information derived from it should be acknowledged © J. D. Lyman 2013.

# Declaration

The work presented in this thesis was carried out in the Astrophysics Research Institute, Liverpool John Moores University. Unless otherwise stated, it is the original work of the author.

Whilst registered as a candidate for the degree of Doctor of Philosophy, for which submission is now made, the author has not been registered as a candidate for any other award. This thesis has not been submitted in whole, or in part, for any other degree.

Joseph Lyman  
Astrophysics Research Institute  
Liverpool John Moores University  
Liverpool Science Park  
Brownlow Hill  
Liverpool  
L3 5RF  
UK

# OBSERVATIONAL INVESTIGATIONS OF THE PROGENITORS OF SUPERNOVAE

JOSEPH DAVID LYMAN

Submitted for the Degree of Doctor of Philosophy

ASTROPHYSICS RESEARCH INSTITUTE

October 2013

## **Abstract**

Supernovae (SNe) are the spectacular deaths of stars and have shaped the universe we see today. Their far-reaching influence affects the chemical and dynamical evolution of galaxies, star formation, neutron star and black hole formation, and they are largely responsible for most of the heavy elements that make up the universe, including around 90 per cent of the reader. They also provide laboratories of nuclear and particle physics far beyond what we can construct on Earth and act as probes of extreme density and energy. This thesis presents new research into understanding the nature of the progenitor systems of various types of SNe, as well as presenting results that will allow their study to be more productive in the future, through use of automated pipelines and methods to increase the science value of discovered SNe. An environmental study of two peculiar types of transients (‘Calcium-rich’ and ‘2002cx-like’), which may not be true SNe, reveals extremely different ages of the exploding systems that will constrain the current theoretical effort into discovering the progenitor systems. The GRB-SN 120422A/2012bz is investigated and found to be an extremely luminous and energetic SN, even amongst the infamously bright GRB-SNe. A method is presented that allows an accurate reconstruction of the bolometric light curve of a core-collapse SN, which relies on only two optical filter observations – this will hugely reduce the observational cost of constructing bolometric light curves, a tool of great importance when hoping to constrain the nature of a SN explosion and hence its progenitor. Finally, this method is utilised to construct the largest bolometric CCSN bolometric light curve sample to date, and these are

analytically modelled to reveal population statistics of the explosions, thus informing on the nature of the progenitors.

# Publications

In the course of completing this thesis work, the contents of a number of chapters have already been published by the author. These are:

- J. D. Lyman, P. A. James, H. B. Perets, J. P. Anderson, A. Gal-Yam, P. Mazzali, and S. M. Percival. Environment-derived constraints on the progenitors of low-luminosity Type I supernovae. *MNRAS*, 434:527–541, Sept. 2013
- J. D. Lyman, D. Bersier, and P. A. James. Bolometric corrections for optical light curves of core-collapse supernovae. *MNRAS*, 437:3848–3862, Feb. 2014
- Schulze et al. (inc. Lyman). GRB 120422A/SN 2012bz: A link between low- and high-luminosity GRBs? A&A accepted (arXiv:1401.3774), Jan. 2014

# Acknowledgements

I wish to begin by acknowledging the role played over the last three years of my supervisors, David Bersier and Phil James. Their guidance and insight, generally coupled with a heap of dry humour, have made my first years of research thoroughly enjoyable and productive. They have instilled in me a critical approach to research that has guided me towards becoming an independent researcher. Their attention to developing my career during these first years ensured I was always greeted with an open door to discuss and dissect the work of others as well as my own.

The atmosphere at the ARI has made it a pleasure to arrive each day, and I am especially grateful to the various organisers, and participants, of the pub outings and weekly football – both often needed sources of release after a week of performing stellar post-mortems.

In order to reach this point, I have relied upon the love and support provided by my family throughout my life. In particular, I would like to thank my parents for their unwavering support of my education and devotion to offer me every opportunity possible. For encouraging me to follow this passion wherever it leads, and for always insisting I reach for the stars.

Finally, I want to attempt to express my gratitude for the love provided to me by Naomi, without whom this thesis would not exist. You have been constant pillar of support throughout my university life and made these the best years of my life, and I will be eternally indebted to you for helping me reach where I am today. Love You.

# Contents

<b>Declaration</b>	<b>iii</b>
<b>Abstract</b>	<b>iv</b>
<b>Publications</b>	<b>vi</b>
<b>Acknowledgements</b>	<b>vii</b>
<b>Contents</b>	<b>viii</b>
List of Tables . . . . .	xiii
List of Figures . . . . .	xv
<b>1 Introduction</b>	<b>1</b>
1.1 Historical origins . . . . .	2
1.2 Modern SN Discoveries . . . . .	3
1.3 Classification of SNe . . . . .	3
1.4 Physics of the explosions and progenitor properties . . . . .	5
1.4.1 Thermonuclear SNe . . . . .	7
1.4.2 Core-collapse SNe . . . . .	9

1.5	Thesis introduction . . . . .	18
<b>2</b>	<b>Image subtraction and the CLASP pipeline</b>	<b>20</b>
2.1	Image subtraction . . . . .	20
2.2	CLASP . . . . .	25
2.2.1	SUBPIPE . . . . .	25
2.2.2	PHOTPIPE . . . . .	29
2.2.3	Examples of usage . . . . .	32
<b>3</b>	<b>The environments of low-luminosity type I supernovae</b>	<b>37</b>
3.1	Star-formation tracers in SN hosts as diagnostics for the progenitor systems	38
3.2	The environments of low-luminosity type I supernovae . . . . .	40
3.3	Introduction . . . . .	40
3.3.1	Ca-rich transients . . . . .	40
3.3.2	SN2002cx-like transients . . . . .	42
3.4	Methods . . . . .	44
3.5	Transient samples and observations . . . . .	49
3.6	Individual properties of the transients and their environments . . . . .	55
3.6.1	Ca-rich transients . . . . .	55
3.6.2	SN 2002cx-like transients . . . . .	63
3.7	Strength of association of transients with ongoing SF . . . . .	64
3.7.1	Host galaxy classifications . . . . .	64
3.7.2	Transient locations and ongoing SF . . . . .	66

3.8	<i>GALEX</i> NCR analysis . . . . .	70
3.9	Discussion . . . . .	72
3.10	Summary . . . . .	78
<b>4</b>	<b>Creating and modelling the bolometric light curve of SN 2012bz</b>	<b>79</b>
4.1	GRB-SNe and the case of GRB120422A/SN 2012bz . . . . .	80
4.2	The bolometric light curve of SN 2012bz . . . . .	81
4.3	Analytical modelling of SN 2012bz . . . . .	85
<b>5</b>	<b>Bolometric corrections to optical light curves of CCSNe</b>	<b>88</b>
5.1	Investigating the progenitors of CCSNe and the role of bolometric light curves	89
5.2	Data . . . . .	91
5.2.1	Photometry . . . . .	91
5.2.2	SN sample . . . . .	92
5.3	Method . . . . .	96
5.3.1	Interpolations of light curves . . . . .	96
5.3.2	SED construction . . . . .	97
5.4	Results . . . . .	100
5.4.1	Flux contributions with epoch . . . . .	100
5.4.2	Optical colours and bolometric corrections . . . . .	102
5.4.3	The radiatively-/recombination- powered phase . . . . .	104
5.4.4	The cooling phase . . . . .	108
5.4.5	Fits to other colours . . . . .	110

5.5	Discussion . . . . .	114
5.5.1	Treatment of the UV/IR . . . . .	115
5.5.2	Time-scales of validity . . . . .	118
5.5.3	Reddening . . . . .	120
5.5.4	Extracting Sloan magnitudes from Johnson–Cousins SEDs . . . . .	123
5.6	SNe 1987A and 2009jf and PTF 12dam – test cases . . . . .	126
5.6.1	SN 1987A . . . . .	126
5.6.2	SN 2009jf . . . . .	129
5.6.3	PTF 12dam . . . . .	130
5.7	Summary . . . . .	131
<b>6</b>	<b>Creating and modelling bolometric light curves of 36 literature SE SNe</b>	<b>133</b>
6.1	Data . . . . .	134
6.2	Method . . . . .	136
6.2.1	The analytical model . . . . .	137
6.3	Results . . . . .	143
6.3.1	Bolometric light curves . . . . .	143
6.3.2	Modelling . . . . .	144
6.4	Summary . . . . .	168
<b>7</b>	<b>Thesis summary and future research</b>	<b>170</b>
7.1	Thesis summary . . . . .	170
7.2	Future research . . . . .	171

<b>A</b>	<b>The Normalised Cumulative Rank method</b>	<b>174</b>
<b>B</b>	<b>The CLASP pipeline</b>	<b>181</b>
B.1	CLASP usage manual . . . . .	182
B.1.1	Quick Use . . . . .	182
B.1.2	Requirements . . . . .	183
B.1.3	The configuration files . . . . .	183
B.1.4	Command line . . . . .	184
B.1.5	GUI . . . . .	187
B.1.6	Output . . . . .	189
	<b>Bibliography</b>	<b>192</b>

# List of Tables

3.1	H $\alpha$ narrow-band filter properties. . . . .	48
3.2	Properties of Ca-rich transients and their host galaxies. . . . .	49
3.3	Properties of SN 2002cx-like transients and their host galaxies. . . . .	50
3.4	Observations of the host galaxies of Ca-rich transients. . . . .	51
3.5	Observations of the host galaxies of SN 2002cx-like transients. . . . .	52
3.6	Mean H $\alpha$ NCR values for the locations of different SN types. . . . .	70
3.7	<i>GALEX</i> NCR values for Ca-rich transients. . . . .	72
3.8	<i>GALEX</i> NCR values for SN2002cx-like transients. . . . .	73
5.1	Data for SNe in the sample. . . . .	94
5.2	Fit parameters for SE SNe. We indicate in bold the fits with the smallest dispersions (see text). . . . .	113
5.3	Fit parameters for SNe II. We indicate in bold the fits with the smallest dispersions (see text). . . . .	113
5.4	Fit parameters for the cooling phase, appropriate for both SNe types. We indicate in bold the fits with the smallest dispersions (see text). . . . .	114
6.1	Data for SNe used to create bolometric light curves. . . . .	134
6.2	Template bolometric light curve data for SNe IIb . . . . .	145

6.3	Template bolometric light curve data for SNe Ib . . . . .	145
6.4	Template bolometric light curve data for SNe Ic . . . . .	146
6.5	Template bolometric light curve data for SNe Ic-BL . . . . .	146
6.6	Photospheric velocity measurements for SE SNe . . . . .	153
6.7	Results of explosion parameter modelling for SE SNe . . . . .	162
6.8	Results of two-sample Kolmogorov-Smirnov test on explosion parameters between SE SNe types . . . . .	165

# List of Figures

1.1	Tycho's <i>nova stella</i> , past and present. . . . .	2
1.2	SN discoveries since 1900. . . . .	4
1.3	Supernova classification scheme . . . . .	6
1.4	Example light curves of SNe . . . . .	17
1.5	Example spectra of SNe . . . . .	18
2.1	Flow chart of SUBPIPE . . . . .	26
2.2	Flow chart of PHOTPIPE . . . . .	30
2.3	Examples of subtractions performed by CLASP . . . . .	34
2.4	Examples of subtractions performed by CLASP . . . . .	35
2.5	Examples of poor subtractions performed by CLASP . . . . .	36
3.1	Light curves and spectra of calcium rich transients . . . . .	43
3.2	Light curves and spectra of SN 2002cx-like transients . . . . .	45
3.3	R and H $\alpha$ band imaging of Ca-rich transient hosts . . . . .	56
3.4	R and H $\alpha$ band imaging of Ca-rich transient hosts ( <i>cont</i> ) . . . . .	57
3.5	R and H $\alpha$ band imaging of SN 2002cx-like transient hosts . . . . .	58
3.6	R and H $\alpha$ band imaging of SN 2002cx-like transient hosts ( <i>cont</i> ) . . . . .	59

3.7	Long slit spectra of the locations of SN 2000ds and SN 2003H . . . . .	60
3.8	The host galaxy types of Ca-rich and SN2002cx-like transients . . . . .	67
3.9	Cumulative distributions of NCR values for Ca-rich and SN2002cx-like transients compared to various SN types . . . . .	69
3.10	Cumulative distributions of NCR values for Ca-rich and SN2002cx-like transients from <i>GALEX</i> NUV and FUV imaging . . . . .	74
4.1	Light curves of SN 2012bz . . . . .	82
4.2	Spectral energy distributions of SN 2012bz . . . . .	83
4.3	Near infrared contributions to SN 2010bh . . . . .	84
4.4	Pseudo-bolometric light curve of SN 2012bz . . . . .	87
5.1	Fractional contributions of UV, optical and IR emission to bolometric light curves of CCNSe . . . . .	101
5.2	Overall bolometric correction fit to all CCSNe . . . . .	106
5.3	Overall pseudo-bolometric correction fit to all CCSNe . . . . .	107
5.4	Bolometric corrections fits to stripped-envelope and type II SNe . . . . .	109
5.5	Bolometric correction fit for all CCSNe during the post-shock breakout cooling phase . . . . .	111
5.6	Comparison of the UV for SN 2005cs between linear extrapolation and using <i>Swift</i> data . . . . .	117
5.7	Comparison of UV integrated luminosities of SEDS with <i>Swift</i> data . . . . .	118
5.8	Evolution of the bolometric correction with time for stripped-envelope CCSNe	121
5.9	Evolution of the bolometric correction with time for type II SNe . . . . .	122

5.10	Comparison of synthetic Sloan magnitudes and those found from SED interpolation . . . . .	127
5.11	The bolometric light curve of SN 1987A . . . . .	128
5.12	The bolometric light curve of SN 2009jf . . . . .	130
5.13	The bolometric light curve of PTF 12dam . . . . .	132
6.1	Photospheric phase model light curves of SE SNe . . . . .	147
6.2	Nebular phase model light curves of SE SNe . . . . .	148
6.3	Measuring the photospheric velocity from a SN spectrum . . . . .	149
6.4	Bolometric light curves of 36 literature SNe . . . . .	150
6.5	Evolution speed versus peak for SE SNe . . . . .	151
6.6	Template bolometric light curves for SE SNe . . . . .	152
6.7	Examples of fits to SE SN bolometric light curves . . . . .	157
6.8	Cumulative distributions of explosion parameters for SE SNe . . . . .	166
6.9	Correlations between explosion parameters for SE SNe . . . . .	167
6.10	Bolometric light curve of SN 2005bf and analytical fit . . . . .	168
A.1	Normalised cumulative sum/NCR values for a typical image . . . . .	176
A.2	Varying background removal via mesh interpolation . . . . .	177
A.3	Star-residual masking . . . . .	178
A.4	DS9 interface to NCR script . . . . .	179
A.5	Examples of NCR heat maps for SN hosts . . . . .	180
B.1	Screenshots of CLASP GUI window . . . . .	188

# Chapter 1

## Introduction

### Abstract

Supernovae (SNe) are hugely luminous events in the transient sky caused by the explosive death of a star. This death can be caused either by the collapse of a massive star (core-collapse SNe; CCSNe) or by a massive white dwarf (WD) undergoing a thermonuclear explosion, known as Type Ia SNe (SNe Ia). Despite originating from a stellar process, they can reach brightnesses comparable to entire galaxies for periods of a few weeks. As such, SNe act as beacons in the Universe, allowing them to be studied both nearby and at cosmological distances. Their study has intensified immensely in the past few decades as their link to massive stellar evolution and ability to probe the acceleration of the Universe's expansion have come to light. In the following sections, a discussion of SN discoveries, historical and modern, are presented as well as some highlights of SN research in recent years. The current state of knowledge about their progenitor systems is reviewed, before a brief introduction to the rest of this thesis.

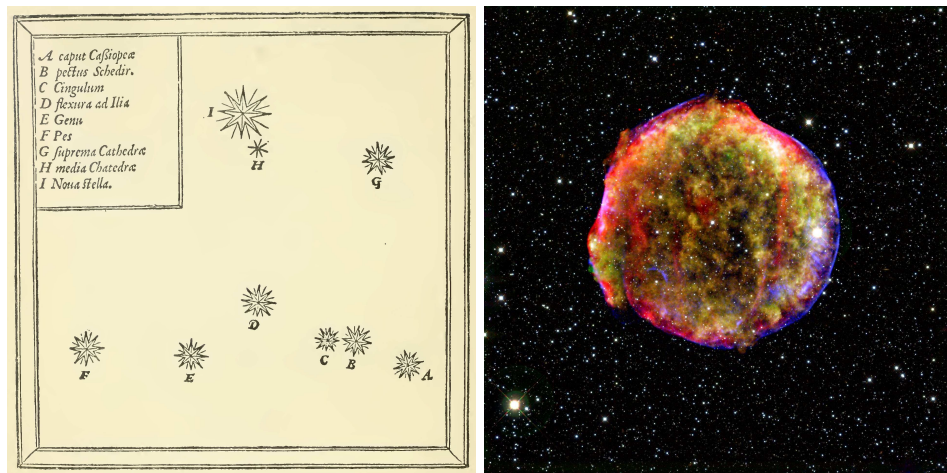


Figure 1.1: How SN 1572 looked to Tycho Brahe upon discovery (left, labelled as *Nova Stella*) and how it looks at present in high resolution imaging (right; image credit: NASA).

## 1.1 Historical origins

Before the arrival of modern astronomy (specifically, modern astronomical instrumentation), identification of SNe was reliant on the event being bright enough to be observed by the naked eye for an appreciable length of time<sup>1</sup>. This obviously meant the SN would need to be very nearby, within the Galaxy most likely, which naturally severely limits the volume in which an observable SN could explode, and so the rate. The earliest evidence for a potential SN was in 185AD, described in *Houhanshu*, although the cause of the ‘guest-star’ has been debated (Chin and Huang, 1994; Schaefer, 1995; Zhao et al., 2006). Since then a sparse and irregular stream of events have been documented. Two famous examples are SNe 1572 and 1604. SN 1572 was discovered by Tycho Brahe (Fig. 1.1) – such was his disbelief of this immensely bright intruder on the night sky, he asked servants to confirm his observations. The first recorded observation of SN 1604 is noted by Johannes Kepler, and it is still the most recent Galactic SN to have been observed during its initial, luminous explosion. Both SN 1572 and 1604 have been since classified as SNe Ia from observations of light echoes and analysis of the elemental abundances (e.g Krause et al., 2008).

<sup>1</sup>Also, a southern hemisphere event would be less likely to have surviving documentation from the civilisations of the time, if indeed it was documented.

## 1.2 Modern SN Discoveries

The rate of SN discoveries dramatically increased with the advent of astronomical instrumentation (which allowed extragalactic SNe to be observed), and regular night-sky observing, beginning around the middle of the 19th century. Interest in SNe also grew following the work of Fritz Zwicky and Walter Baade (e.g. [Baade and Zwicky, 1934](#); [Zwicky, 1942](#)), who linked them to exotic phenomena such as neutron stars, cosmic rays and dark matter. Throughout most of the 20th century supernovae were still discovered by professionals and amateurs manually observing repeated patches of the sky at regular intervals, looking for new objects that were not present in previous observations. Towards the end of the 20th century dedicated transient surveys began. With the efficiency of scheduled observations, and automated object detection in difference imaging (see [Chapter 2](#)), SN discoveries have increased from one a month to several every night in  $\sim 50$  years. The Supernova Legacy Survey ([Astier et al., 2006](#)) found around 1000 high redshift SNe from 2003-2008, and the Palomar Transient Factory ([Law et al., 2009](#); [Rau et al., 2009](#)) had discovered 2135 SNe as of 17/12/2013<sup>2</sup>, since its first detections in March 2009. These are just two examples of many recent surveys performing searches in this automated manner. The huge increase in discoveries is highlighted in [Fig. 1.2](#), which shows the discoveries of SN by year from the IAU SN list<sup>3</sup> – a noticeable rise in the SN discovery rate is evident post-1987, after the extremely close by SN 1987A was discovered, a landmark event in the study of SNe. Although a huge number of SNe are shown, this list does not include the majority of discoveries from the most recent dedicated, proprietary searches which would dramatically increase the number of discoveries for the years since 2000.

## 1.3 Classification of SNe

A large number of discoveries, as shown in [Fig. 1.2](#), has been coupled with intensive monitoring of a small sub-section of events. Such a strategy has led to great advances in the knowledge of SNe in a relatively short time-scale, and revealed the heterogeneity of SNe. A

---

<sup>2</sup><http://ptf.caltech.edu/iptf/>

<sup>3</sup><http://www.cbat.eps.harvard.edu/lists/Supernovae.html>

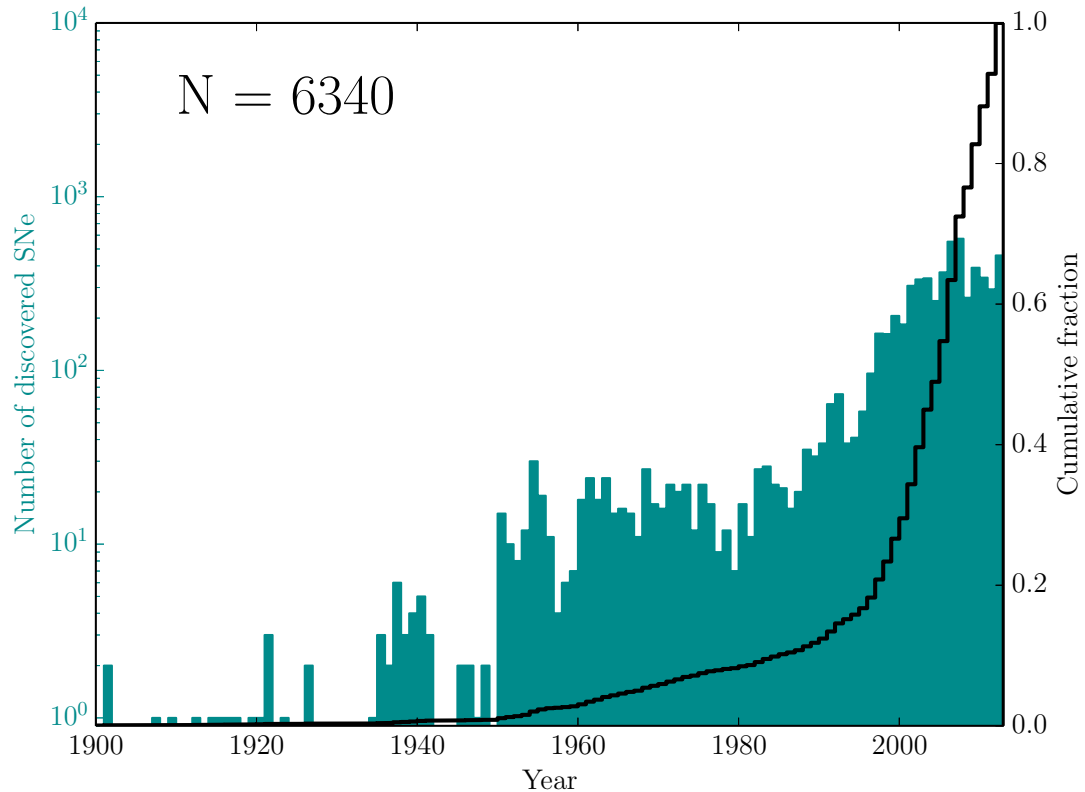


Figure 1.2: SN discoveries since 1900 from the IAU SN list as of 17/12/2013. Note this does not include the majority of recent (since 2000) SNe discovered by proprietary searches.

brief overview of the main SN classifications is given here, and the observational differences causing their classification. A graphical representation of the decision tree for the main SN classes is shown in Fig. 1.3.

After the initial distinction from Novae by Zwicky, ever increasing divisions have been made to the family of SNe, in order to group similar events. Beginning with Minkowski (1941), supernovae were grouped into Type I (SNe I), which displayed rather homogeneous characteristics, and Type II (SNe II) that appeared more diverse. The distinction being whether a SN displayed signatures of hydrogen in its spectra – classified as a SN I if there was no evidence for hydrogen, and a SN II if hydrogen features were observed (e.g. Oke and Searle, 1974).

Barbon et al. (1979) identified two subclasses to SNe II, IIP and IIL, through a study of 21 SNe II light curves. SNe IIP display a characteristic long lasting ( $\sim 100$ -120 days) *plateau*

after peak brightness, where the brightness of the supernova remains roughly constant. SNe IIL do not display this and *linearly* decline in brightness after peak.

SNe I now exist as three main subclasses, Ia, Ib and Ic. These are spectral classifications; SNe Ia display strong silicon absorption, SNe Ib and Ic show either weak or absent silicon features. The distinction between SNe Ib and Ic comes from the existence of helium features in the former that are absent in the latter. See Filippenko (1997) for a review of the spectral classification of SNe. SNe Ic also exist as *broad-line* variants (SNe Ic-BL). SNe Ic-BL exhibit unusually high explosion velocities (up to  $\sim 30000 \text{ km s}^{-1}$ , cf.  $\sim 10000 \text{ km s}^{-1}$  for normal SNe Ic) and are the only SNe type found to be associated with gamma-ray bursts (GRBs); a discussion of the SN-GRB connection can be found in Section 4.1.

Alongside these are other common designations for SNe that make up a smaller fraction of the observed explosions. One such is SNe I Ib, which initially appear as SNe II but the initially strong hydrogen features disappear on a time-scale of  $\sim$ a week to months, and they then evolve to resemble a SNe Ib. SN 1993J was the prototypical example of this class.

SNe IIn are SNe II that display unusual features in their hydrogen line emission. The classification of IIn is made when a *narrow* component, with a typical width of hundreds  $\text{km s}^{-1}$  (cf. normal SNe lines of many thousands  $\text{km s}^{-1}$ ), is observed overlaid on the existing, broader features of hydrogen in the SN's spectrum (Schlegel, 1990). These SNe can be exceptionally bright (although a very large range in peak absolute magnitude exists) and display wide-varying time-scales of evolution (e.g. Kiewe et al., 2012).

## 1.4 Physics of the explosions and progenitor properties

The empirically-driven classification system is naturally a consequence of the events that are observed. What may be considered a well defined class now, may have been considered 'peculiar' when first discovered, until a significant sample of similar events could be grouped by their common properties. Similarly 'peculiar' SNe now, will inevitably have a yet further designation once studies of their properties are complete. Such taxonomy is a relic of the initial attempt to categorise SNe without a knowledge of the underlying properties giving rise



curves displaying an intermediate plateau length of  $\sim 60$  days (Tominaga et al., 2013). At the other end of the brightness scale are super-luminous SNe (SLSNe; Gal-Yam, 2012), which appear to occur at large distances and are extremely bright, even by SN standards. Outshining even the brightest SNe Ia, they can reach peak magnitudes of  $M \lesssim -22$ . Already three distinct subclasses exist based on spectral and light curve features. The explosion mechanisms, and the energy sources of their light curves are areas of active study; pair-instability explosions (e.g. Woosley et al., 2007; Cooke et al., 2012), the synthesising of huge amounts of radioactive material (Young et al., 2010; Dessart et al., 2012, e.g.), CSM interaction (e.g. Chatzopoulos et al., 2013), and magnetar production in the core (Kasen and Bildsten, 2010; Nicholl et al., 2013, e.g.) have all been investigated as potential mechanisms to power such luminous events. The discussion in this introduction will be limited to thermonuclear and core-collapse, however.

### 1.4.1 Thermonuclear SNe

Thermonuclear SNe arise due to nuclear burning of degenerate material in a carbon-oxygen (CO) white dwarf (WD); this explosion mechanism is responsible for SNe Ia. Direct, very early time observations of SNe Ia constrain the exploding stars to be very compact objects, consistent with a WD origin. For example Nugent et al. (2011) concluded for SN 2011fe that the exploding star's radius was  $\leq 0.1 R_{\odot}$ , with Bloom et al. (2012) confirming the degenerate nature of the progenitor and favouring a WD. SN 2013dy was observed only a few hours after explosion and similarly had tight constraints on the progenitor radius of  $\lesssim 0.24 R_{\odot}$  (Zheng et al., 2013), indicative of a WD progenitor. The ability to standardise SNe Ia for use as cosmological distance indicators (Phillips, 1993) to probe the cosmic expansion of the universe (e.g. Perlmutter et al., 1998, 1999; Riess et al., 1998; Schmidt et al., 1998), has ensured ardent observational and theoretical study of them.

The details of how the WDs explode is an area of ongoing study and debate. The delayed-detonation model (Khokhlov, 1991), where an initially sub-sonic flame burns before the WD detonates, can produce explosions that match the characteristics of SNe Ia. Recent three-dimensional hydrodynamical simulations (e.g. Seitenzahl et al., 2013) are able to produce

the observed spreads in SN Ia properties (peak brightness, for example) and comparison to observed light curves and spectra reveals generally good agreement, although some discrepancies exist (Sim et al., 2013). Another explosion mechanism, the pure deflagration model (Nomoto et al., 1984), is generally thought to be applicable to sub-luminous type I SNe (see Chapter 3) due to the lower expansion velocities and peak brightnesses found from simulations utilising pure deflagration (e.g. Long et al., 2013). The lack of abundance stratification in the pure deflagration model is also at odds with what is seen in normal SNe Ia. Ignoring the nuances of the particular method of ignition, for an explosion, the CO WD must reach a point where carbon ignites. Since the WD is degenerate this means that the carbon burning increases the local temperature but does not decrease the density. Positive feedback from this reaction leads to a thermonuclear explosion that unbinds and explodes the WD.

How the WD reaches the conditions required for carbon burning is also a matter of great debate. Two competing models are the single degenerate (SD) and double degenerate (DD; Iben and Tutukov, 1984; Webbink, 1984) channels. In both cases the WD is in a proximate binary system. In the SD scenario, where the companion is a non-degenerate star, the gravitational pull of the WD causes the companion to fill its Roche lobe and material passes through the inner Lagrangian point to accrete on the WD (Roche lobe overflow; RLOF). Through this mechanism the WD grows in mass and thus the temperature can reach the carbon ignition temperature when it reaches the Chandrasekhar limit ( $\sim 1.4 M_{\odot}$ ). The nature of the companions in SD systems is not known; limits have been placed in Li et al. (2011a) for SN2011fe, where observations rule out red giants and most helium stars as possible companions. Observations of SN2011fe appear to favour a DD progenitor (Chomiuk et al., 2012), although the SD cannot be ruled out with current observations (Röpke et al., 2012). Observational support for the SD scenario came in the form of PTF11kx, where the circumstellar material (CSM) around the system is naturally explained by a red giant wind and multiple previous nova outbursts from the progenitor, prior to explosion as a SN Ia (Dilday et al., 2012). The effect of an evolved companion in the system can also produce SN IIn-like spectral features for a SN Ia (Hamuy et al., 2003, although also see Benetti et al. 2006), and indeed it is argued that a fraction of SNe classified as IIn are in fact Ia, masked beneath the dense CSM (Silverman et al., 2013). See Section 1.4.2 for a discussion of SNe IIn. In the

DD scenario the companion is another WD and it is the merger energy of these WDs that causes conditions sufficient for carbon ignition to occur in the merger remnant. A search for the surviving donor star companion of SN 1572 (Tycho's SN) found no plausible candidates (Kerzendorf et al., 2013), and as such a DD scenario is favoured for this SN. It is apparent that the SD and DD progenitor channels for SNe Ia both contribute to the observed population, and current studies are now focussing on the relative fractions of SNe Ia that are formed by each mechanism. A potential discriminating factor between the two channels could be the velocity of spectral features in SNe Ia, with higher (lower) velocities indicative of the SD (DD) scenario, which may also correlate with the host galaxy type, and thus age (see Maguire et al., 2012). A recent extensive review of the observational evidence for the various SN Ia progenitor systems is presented in Maoz et al. (2013).

The light curves of thermonuclear SNe are homogeneous in the main, with 'normal' SNe Ia obeying a width-luminosity relation (i.e. broader, more slowly evolving light curves are brighter; Phillips, 1993). Although some unusual sub-types contribute to a large spread in luminosities, the light curves are all powered by the radioactive decay of heavy elements, primarily  $^{56}\text{Ni}$  over the initial light curve peak. Two examples of SN Ia light curves can be seen in Fig. 1.4, including SN 1991T, the prototypical high-luminosity SN Ia. Spectra of SNe Ia are characterised by a lack of hydrogen or helium, with strong silicon absorption (see Fig. 1.5 Filippenko, 1997), often with high velocities.

## 1.4.2 Core-collapse SNe

The method of exploding via core-collapse is expected to occur only in massive stars. Theoretical (e.g. Iben and Renzini, 1983; Heger et al., 2003) and observational (e.g. Smartt, 2009) constraints place the lower limit for this to occur at  $\sim 8 \pm 1 M_{\odot}$ , with some dependence on metallicity (Ibeling and Heger, 2013). Upper limits are more uncertain as extremely massive stars may undergo a different explosion mechanism.

The life of a massive star, once the main sequence is reached, briefly comprises (see Woosley et al., 2002, for an in-depth review) the following stages.

- Steady burning of hydrogen to helium occurs in the core, primarily via the CNO cycle.
- Hydrogen burning continues via the CNO cycle in a shell around a massive, non-degenerate helium core, which is unable to support the outer layers of the star and contracts until the temperature increases to initiate helium burning ( $T \approx 10^8 \text{K}$ ).
- Helium burning produces a carbon-oxygen core surrounded by a helium-burning shell.
- Carbon burning occurs as the core contracts due to pressure from the outer layers. Pair annihilation becomes significant at the temperatures reached at this point and nuclear burning is now driven predominantly by replacing the lost energy from neutrinos by the star, rather than its radiated surface energy.
- After carbon, continued, rapid exhaustion of neon, oxygen and silicon follow in a similar manner, until nuclear statistical equilibrium occurs during the final stages of the silicon burning core – i.e. photodisintegration becomes important and reactions where nuclei gain particles are balanced by destructive inverse reactions.

At this point an iron core exists, with a shell of silicon burning occurring around it. While the silicon is burning the core will not contract as any attempt to do so will increase the burning rate, expanding the core and counteracting any contraction. This silicon shell will migrate out in mass until it passes the point where the mass interior to its extent, the iron core, is above that given by the Chandrasekhar limit. The degenerate iron core is now susceptible to collapse and does so on a thermal time-scale. The collapse is speeded up due to electron capture by iron-group nuclei, which removes electrons (responsible for much of the internal pressure) and also emits neutrinos that carry away energy. Photodisintegration of the nuclei also occurs, producing a large number of free  $\alpha$  particles. The resulting binding energy of the core is lowered and the energy gained by contraction is not enough to match that lost, resulting in an accelerating collapse that is complete in a few milli-seconds.

At the limit of its maximal density, dictated by neutron degeneracy pressure, the collapse abruptly stops. Outer core material falling in collides with this inner, incompressible material and the core rebounds. The supersonic interaction between this core rebound and the outer layers of the star that continue to fall inwards produces a strong shock wave. Al-

though the energy of this shock wave contains enough energy to unbind the outer layers, the shock wave loses a significant amount of energy by photodisintegrating the nuclei of these infalling layers that it encounters (losing around  $10^{52}$  erg/ $M_{\odot}$ ), and neutrino emission – as the shock wave propagates outwards, and thus encounters lower densities, neutrinos have a higher chance of escape beyond the shock front. As such, another mechanism is required to reinvigorate the shock wave, which is now believed to be neutrino energy deposition (first proposed by [Colgate and White, 1966](#)). The huge densities in the inner regions mean the neutrinos produced here will interact before escape (i.e.  $\nu$  mean free path  $\ll$  core radius), depositing the energy of the neutrinos into the dense inner material of the star before they can escape, thus providing a means to couple the energy injected by the core bounce to the outer layers of the star. This leads to an unbinding of the outer star and a CCSN.

Although it is thought this same principal explosion mechanism is responsible for inducing core-collapse, and the subsequent explosion of massive stars, CCSNe exhibit very heterogeneous properties; core-collapse is the responsible mechanism for SNe of types IIP, IIL, IIb, Ib, Ic and at least a fraction of IIn. The diversity in observed properties is due to the nature of the exploding star and the local medium into which it is expanding. Broad properties such as the mass, metallicity, rotation and binarity of the star, as well as intricacies such as the particulars of the star’s nuclear burning, internal magnetic fields and mixing of the ejecta during the propagation of the shock wave, will all affect the observed SN. Since the effects of many of these factors are not well understood, a broad overview of how the nature of the exploding star affects the observables of the SN will follow, neglecting many of the finer details which are subject to ongoing, intense theoretical work.

Whereas SNeIa follow a similar light curve evolution, CCSNe exhibit a wide spread in light curve properties and brightnesses. [Hamuy \(2003\)](#) found a 5-magnitude spread in the plateau luminosities of SNe IIP, similarly [Drout et al. \(2011\)](#) found a  $>5$  mag spread in peak brightnesses for a sample of SNe Ib/c. Despite this heterogeneity, efforts to make distance indicators of SNe IIP, following the method of [Kirshner and Kwan \(1974\)](#), and SNe IIn ([Potashov et al., 2013](#)), are being made since they can provide primary distance indicators, as oppose to SNe Ia that are reliant on local calibration. Examples of CCSN light curves can be seen in [Fig. 1.4](#).

The spectral difference between SNe II and SNe Ib/c is the presence or absence of hydrogen (see Fig. 1.5 for example spectra). In order for a massive star to exhibit signatures of massive amounts of hydrogen, as is seen in SNe II, the exterior envelope must be retained up to the point of core-collapse. The mass loss experienced by a star is thought to be highly dependent on its mass (O'Connor and Ott, 2011), alongside metallicity and rotation, to a lesser extent (e.g. Vink et al., 2001; Vink and de Koter, 2005). Thus SNe II are proposed to be massive stars at the lower end of the mass range for a CCSN progenitor in order to retain their external hydrogen envelopes, which is backed-up observationally through direct detection of progenitor systems that reveal them to be red and yellow supergiants, around  $8 - 15 M_{\odot}$  (e.g. Van Dyk et al., 2003; Smartt et al., 2004; Li et al., 2007; Van Dyk et al., 2012; Maund et al., 2011, see Smartt 2009 for a review). It follows then that we expect SNe Ib/c to arise from more massive stars (with SNe Ic being more massive than SNe Ib given they also lose their helium envelope before core-collapse). Such stars would be Wolf-Rayet (WR) stars, whose strong mass loss has stripped the outer layers throughout their evolution (Crowther, 2007); a tentative detection of a SN Ib, iPTF13bvn, which is consistent with a WR progenitor ( $M_{\text{ZAMS}} \simeq 30 - 40 M_{\odot}$ ) has been made (Cao et al., 2013; Groh et al., 2013a).<sup>4</sup> This scenario, however, encounters problems when one considers the stellar initial mass function (IMF). Due to the steep slope of the IMF, low mass star numbers dominate over high mass stars, and even moderately massive stars numbers (SNe II progenitors) will also dominate over very high mass stars (proposed SNe Ib/c progenitors). This simple argument is difficult to reconcile with the observed SN rates of the two classes. For example Arcavi et al. (2010), from an early analysis of PTF discovered SNe, find  $N(\text{Ib/c})/N(\text{II}) \simeq 0.23-0.25$  (depending on host mass), an earlier study by Bressan et al. (2002) found a similar fraction when considering all nearby SNe. The Lick Observatory Supernova Search (LOSS Li et al., 2011b) also found high proportions of SNe Ib/c – that they make up around 30 per cent of the core-collapse population. Taking a Salpeter IMF and mass limits at solar metallicity for various SN types from Heger et al. (2003), one would expect  $N(\text{Ib/c})/N(\text{II}) \simeq 0.10$ . This has driven interest in the role of close binaries in the progenitors of SNe Ib/c (e.g. Nomoto et al., 1995; Heger et al., 2003; Eldridge and Tout, 2004) as a potential solution to this problem. Binarity, specifically *close* binarity, will significantly alter the evolution of a star in the system

<sup>4</sup>Confirmation of the progenitor's disappearance in late time imaging being awaited at the time of writing.

from that of a single star (or, equivalently, one in a wide binary). The gravitational pull of the companion introduces the potential for RLOF to occur, hugely increasing the efficiency of envelope stripping and allowing even lower mass stars to explode with a spectrum that would warrant a Ib/c classification – therefore increasing the SN Ib/c/SN II ratio (Eldridge et al., 2008). This additional channel provides additional progenitor systems to SNe Ib/c, in order to support their relative prevalence cf. SNe II. Indeed, it is proposed that the majority of massive stars do not evolve alone, with more than half being in a binary system where the stars have some form of interaction (consequently a small fraction of massive stars being actually true single stars), as shown in Sana et al. (2012).

Nevertheless, it has been demonstrated through environmental studies that there exists a mass sequence of SN progenitors. This was statistically shown by Anderson et al. (2012), through correlations of SN location with  $H\alpha$  emission, who find a sequence, in order of increasing mass, of: SNe IIP  $\rightarrow$  SNe IIL  $\rightarrow$  SNe IIn  $\rightarrow$  SNe Ib  $\rightarrow$  SNe Ic. The discrepancy in progenitor life time (and thus mass) between various SN types has also been shown by Kelly et al. (2008); Kelly and Kirshner (2012); Crowther (2013), with the aforementioned sequence (or a broader classification version, but maintaining the order of increasing mass) being posited in each case. It is important to note that these are statistical studies of SN *populations*, and as such they can only distinguish between the average progenitor masses, i.e. it is possible to say that *on average* a SN Ib/c will be more massive than a SN II progenitor, but the distributions of the initial progenitor masses may indeed overlap (thus not ruling out a population of moderately massive SN Ib/c progenitors in binaries or the effects of metallicity in determining SN type).

Besides observing directly the progenitor system, or observing the environment of SN populations, observing the luminous transient itself can open a wealth of information on the progenitor. Light curve and spectral information act as a fingerprint for an explosion, identifying the structure of the progenitor and the nature of the explosion. The electromagnetic signature of a SN begins at shock breakout (SBO). This occurs when the shock wave that is propagating out of the star reaches an optical depth of  $\tau \sim 25$  (see Kistler et al., 2013, and references therein), at which point radiation from the shock front leaks from the star, emission peaking at  $\tau \sim 1$ . The signature of this SBO is an extremely bright burst of emis-

sion peaked in the UV/X-ray regime, whose duration is determined largely by the radius of the progenitor (e.g. [Tominaga et al., 2011](#)); the bolometric luminosity of the SBO can be  $\sim 10^{44}$  erg s<sup>-1</sup>, reached in seconds to hours. After this initial burst, the cooling phase occurs, during which the extremely hot, shocked material cools and expands causing the light curve to initially rise in the UV/optical for a short time while the peak of the black body emission from this shocked material is bluer than these wavelengths ([Piro and Nakar, 2013](#)), before fading as the peak of the thermal emission moves to longer wavelengths. The duration of this cooling phase is tied to the radius of the exploding star also – the very large red supergiant (RSG) progenitors of SNeIIP have been observed to show signatures of rising UV/optical emission for  $\sim 2$  days after explosion ([Gezari et al., 2010](#)), with the signature of emission from cooling of shocked material present in the fading UV/optical light curves observed for several days, and up to weeks ([Quimby et al., 2007](#)). For SE SNe the durations are much shorter (signatures of any emission related to the SBO disappear within a day of explosion, except for the most extended SN IIB progenitors), and there is consequently only a small number of SE SNe showing SBO cooling (e.g. SNe 1993J, [Richmond et al. 1994](#); 1999ex, [Stritzinger et al. 2002](#); 2008D, [Modjaz et al. 2009](#); 2011dh, [Arcavi et al. 2011](#)). The previously accepted notion that a larger pre-SN radius would result in a longer SBO (and associated cooling) duration has been questioned recently. This doubt has arisen from the detection of the progenitor of SN 2011dh, which was found to be a relatively large yellow supergiant (YSG; [Maund et al., 2011](#)), despite its modest and very short ( $\sim 1$  day) SBO signature. Observations were thought to be indicative of a compact progenitor ([Soderberg et al., 2012](#); although see [Bersten et al., 2012](#)), and it had been argued that the YSG observed at the location of SN 2011dh was the binary companion ([Van Dyk et al., 2011](#)). Late time imaging showed the YSG had disappeared, confirming it was the progenitor itself ([Van Dyk et al., 2013](#)).

SNe rebrighten after SBO cooling emission due to one of two sources. In SNe IIP the massive hydrogen envelope, which has been ionised by the shock wave passing through it, recombines and the photosphere recedes through this envelope as the outer ejecta cool and become transparent. This causes the plateau observed in SNe IIP, whereby the luminosity remains roughly constant for  $\sim 100$ – $120$  days. It is thought this plateau duration is very

short or non-existent in SNe IIL owing to a much less massive hydrogen envelope. This recombination energy source is also not available in other SE SNe (at least not at significant luminosity or duration), and it is the radiative heating from the decay of  $^{56}\text{Ni}$  that causes a rebrightening of the SN once it has diffused to the outer layers, typically peaking  $\sim 2$  weeks after explosion. The rise time of this peak is determined by the distribution of  $^{56}\text{Ni}$  in the star (Piro and Nakar, 2013), as well as the combination of mass and energy in the ejecta. The peak luminosity is determined by the amount of  $^{56}\text{Ni}$  synthesised in the SN (see Section 6.2.1 for a description of this in an analytical framework).

Over the evolution of a SN, deeper and deeper layers of the ejecta are probed as the photosphere recedes. Thus, the abundance and distribution of elements in the ejecta can be gleaned from good spectral coverage. Early spectra of cooling emission after SBO are generally quite featureless and display a strong blue continuum due to the high temperatures of the material at the photosphere (e.g. Quimby et al., 2007). In SNe II, the recombination of hydrogen then gives rise to strong hydrogen lines, whereas in SNe Ib/c it is helium and calcium that appear as prominent features initially. Given the large velocities involved in SN explosions, such features form P-Cygni like profiles, with blueshifted absorption and redshifted emission. From the minima of the blueshifted absorption, the velocity of the ejecta producing that spectral line can be determined (see Section 6.2.1). The explosions of SNe result in homologous expansion ( $v \propto R$ ) and it therefore follows that the velocities of these spectral features decrease with time, since it is the outermost ejecta that are probed initially, with the photosphere receding in ejecta velocity as time progresses. The recession of the photosphere in velocity and mass of the ejecta eventually leads to the *nebular* phase, ultimately revealing the composition of the entire ejecta (a few–several months past explosion). During the nebular phase the continuum becomes weak as the ejecta are optically thin, and forbidden lines begin to show. Nebular phase observations can reveal asymmetries of the explosion via double-peaked emission lines in spectra (Maeda et al., 2008), inform on amount of radioactive elements synthesised in the explosions, and give estimates of the progenitor’s initial mass through oxygen mass measurements, which are directly linked (Jerkstrand et al., 2012, 2013).

The expansion of the ejecta is very fast in CCSNe ( $\sim 10000\text{--}20000 \text{ km s}^{-1}$ ). These velocities

are much higher than typical velocities associated with stellar evolution. The ejecta therefore feel the influence of the progenitor's behaviour that occurred in the years to decades leading up to core-collapse as it catches-up previously ejected material. This interaction between the ejecta from the SN and the circumstellar material born of the progenitor system's prior evolution is responsible for SNe IIn. The aforementioned narrow lines exhibited in their spectra are a result of the collision of this ejecta with a dense CSM. Such high density (or highly-clumped) CSM is indicative of large, episodic mass-loss from the progenitor and massive star evolution theory would present luminous-blue variables (LBVs) as suitable progenitors. This has an observational grounding in [Gal-Yam et al. \(2007\)](#), where it was proposed the progenitor of the IIn SN2005gl was a very massive LBV star, which was later confirmed by post-explosion images ([Gal-Yam and Leonard, 2009](#)). Also, in [Smith et al. \(2011\)](#), a very massive ( $\geq 30 M_{\odot}$ ) progenitor for SN2010jl was found using pre-explosion images.

The cases for massive LBVs as SNe IIn progenitors, and the SN IIn class itself, are not clear cut however. Such massive progenitors retaining a significant hydrogen envelope up until explosion poses problems for stellar evolution models. Until recently models of massive star formation did not predict LBV stars to become SN, instead the star would evolve to a WR star, shedding its hydrogen envelope before reaching the conditions for core-collapse. [Groh et al. \(2013b\)](#) present recent models that can produce LBV progenitors for SNe, but suggest the resulting spectra are more representative of type IIb explosions, and in any case, these progenitors are  $20\text{--}25 M_{\odot}$ , much lower than the inferred progenitor detections thus far. When high mass-loss values are found that lead to favouring an LBV progenitor, the density profile for the CSM surrounding the SN is taken to be  $r^{-2}$ , which constitutes the case of steady mass loss. [Dwarkadas \(2011\)](#) argues this is an incorrect assumption, thus a high density medium (giving rise to the narrow emission lines in SN IIn spectra) is not reliant on high mass-loss rates from the progenitor. Clumpy media, or shells of high density produced from winds with different velocities colliding, are possible scenarios providing the requisite conditions for a IIn classification, for example. [Dwarkadas](#) suggests that SN IIn should not be designated as a separate class, but rather that they form a possible phase of evolution of any SN, regardless of class. It has also been found that a fraction of previously classified SNe IIn are in fact SNe Ia with a dense CSM, giving the appearance of IIn spectra

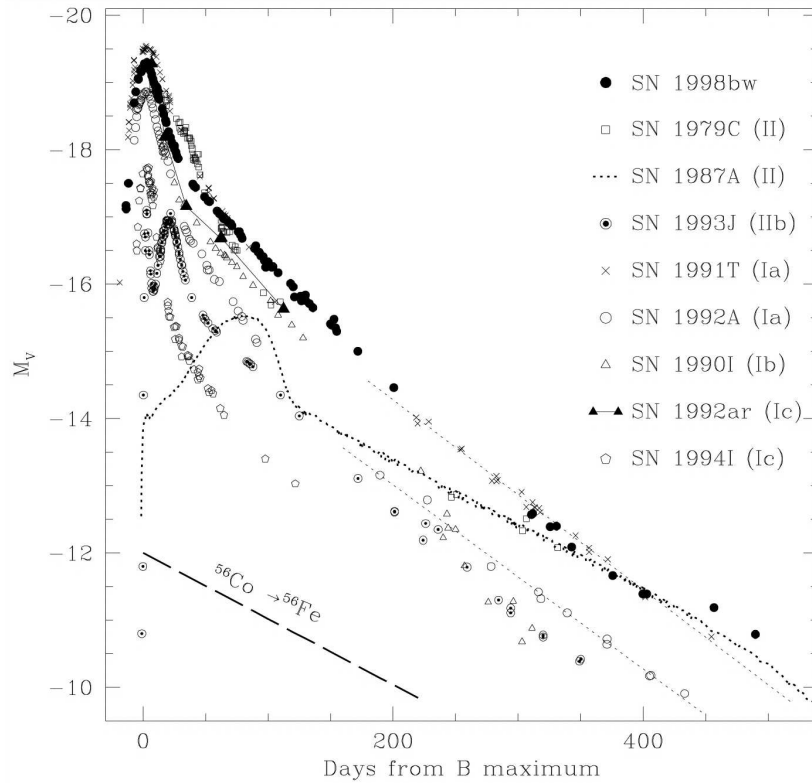


Figure 1.4: Example light curves of various types of SNe (taken from Patat et al. 2001).

(Silverman et al., 2013). This may account for some of the inconsistency environmental studies find between massive star locations and the locations of SNe II<sub>n</sub> (Anderson et al., 2012). The population of SNe II<sub>n</sub> are extremely heterogeneous and it is likely they arise from more than one progenitor system.

Although both photometric and spectroscopic observations have been fundamental to furthering knowledge regarding CCSN, perhaps the greatest success for the theory of CCSNe came from a non-electromagnetic source. Over a six second interval, eight neutrinos were detected by the Irvine-Michigan-Brookhaven detector in the USA, as reported by Bionta et al. (1987), with a simultaneous detection of 11 neutrinos in Japan by the Kamiokande-II detector (Hirata et al., 1987). The huge significance of these particular neutrinos is that they were shortly followed by the optical detection of SN 1987A in the Large Magellanic Cloud ( $D \sim 50$  kpc) – a resounding success for core-collapse theory that predicted very large neutrino luminosities for CCSNe.

Finally, it is proposed that mass ranges exist in which stars do not produce a luminous coun-

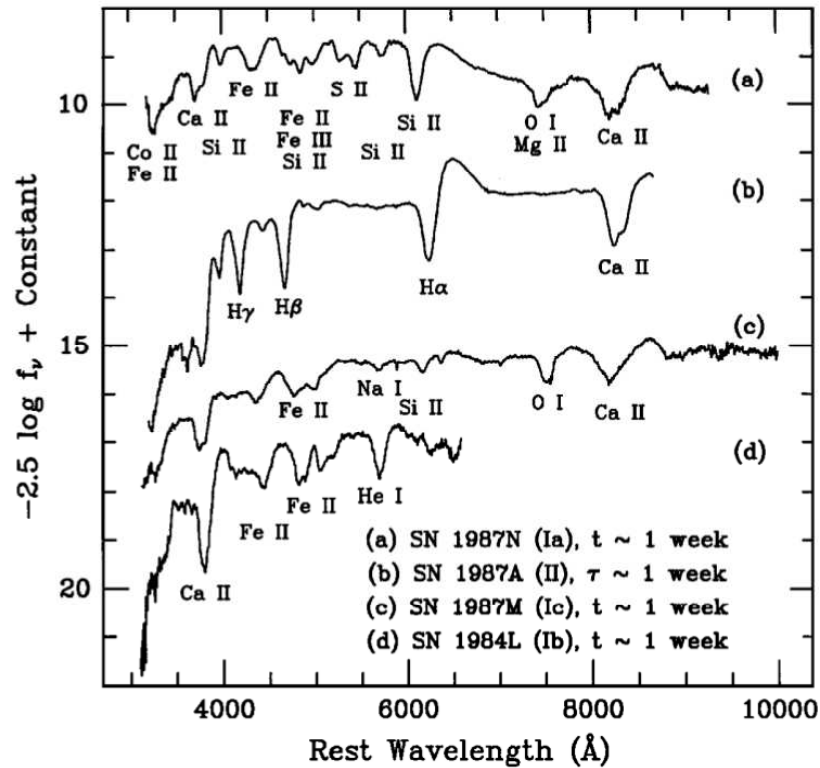


Figure 1.5: Example spectra of various types of SNe (taken from [Filippenko 1997](#)).

terpart to the collapse instead collapsing directly to a black hole. For example ([Kochanek, 2013](#)) suggest direct collapse of stars of initial mass  $\sim 16.5\text{--}25 M_{\odot}$ . This explains the lack of a detected SN IIP progenitor in this mass range, where one would expect RSGs to exist, and would also alleviate some of the inconsistency between the abundances of SNe II and SNe Ib/c when considering the stellar IMF.

## 1.5 Thesis introduction

SNe studies have advanced knowledge of massive star/WD evolution, and the ultimate fates of these stars. Each new advance in both theoretical and observational investigations, however, is coupled with new questions and, generally, even more bizarre explosions.

The next step for SNe research is to link directly between the progenitor star, and the nature of the explosion. To this end, this thesis investigates the host-galaxy environments of a two peculiar types of transients in Chapter 3. The terminal/non-terminal nature of the explosions

is not known so their description as a SN is even called into question. Constraints are placed on the ages of the progenitor systems of these peculiar transients and a discussion of the implications for theoretical models and explosion mechanisms is made. As is evident from Section 1.4.2, the light curves of SNe divulge important information on the explosion, and also the progenitor system. A particularly useful tool is the bolometric light curve of a SN, i.e. one that accounts for all the electromagnetic emission. A discussion of how these bolometric light curves can inform on the explosion parameters of a SN is given in Chapter 4, alongside an application of modelling to a GRB-SN. Despite their usefulness, bolometric light curves are observationally very expensive since a large wavelength range needs to be observed. To counteract this, bolometric corrections for CCSNe are presented in Chapter 5 which allow bolometric light curves to be made very inexpensively for CCSNe. These corrections are then utilised to construct and model the largest sample of bolometric light curves of CCSNe in Section 6.2.1, in order to investigate the explosion parameters of different types of CCSN and deducing differences or similarities between their progenitor systems.

# Chapter 2

## Image subtraction and the CLASP pipeline

### 2.1 Image subtraction

The night sky is largely unchanging on the time-scale of human lifetimes. In general, if one were to repeatedly observe a random patch of sky, there would be no difference between the images (aside from those differences arising from the effects of the Earth’s atmosphere, such as seeing and sky brightness); the same objects would remain, and at constant brightness. If a variable star, lensing event or transient happens to be in one of the observations however, they will be noticeable as a difference in brightness of an object (a variable star or a lensing event) or a new object (a transient).<sup>1</sup> Traditionally, photometry would need to be performed on all objects to detect any changes in brightness of objects in the field, or subsequent frames would be “blinked” to attempt to identify transients. This is clearly a labour intensive job given the scale of the problem, when one may be potentially searching for variables in an entire galaxy of sources, or searching many hundreds of frames a night to discover transients/lensing events. Image subtraction naturally provides a solution to both problems: each image is subtracted from a template. The template is simply another image

---

<sup>1</sup>For the purposes of this discussion, moving objects such as asteroids, minor planets or high proper motion stars, will be neglected. Although clearly these would also be noticeable on subsequent images of a field.

of the field that was taken previously, and is generally a deep stack of previous, good-seeing images.

Considering idealised data, a subtraction of the image from the template would result in an image containing only zero-valued pixels for the case of no detected variables or transients. A new transient or increase in brightness of a variable would be manifest as positively-valued pixels, as the pixels in the image at the location of the change would be larger than those in the template (similarly, a fading variable or transient would result in negatively-valued pixels). Study of such subtracted images then makes it trivial to identify interesting objects. Idealised data does not exist for observations however, and there are many factors associated with taking multiple observations that makes the process of image subtraction less straightforward. The following is a list of some important phenomena to consider when performing image subtraction with modern CCD detectors:

- i.* removal of cosmic rays, detector artefacts, and fringing patterns
- ii.* accurate alignment between the image and template
- iii.* sky-background level and variability across (and between) image and template
- iv.* brightness scale factor which will account for differing exposure times, filter transmissions<sup>2</sup>, observing conditions etc. between the image and template
- v.* saturation and non-linearity of detector response function
- vi.* point-spread function (PSF) variability within each observation and between image and template

Typical methods for dealing with these issues are:

*i.*

Correct reduction of the data beyond standard CCD reduction of bias/overscan removal and flat-field division can aid with obtaining a clean subtraction. Naturally cosmic rays will

---

<sup>2</sup>See Section 2.2.3 for a discussion of an application of image subtraction using different filters for the image and template.

appear in random locations on each frame and will result in ‘spikes’ or ‘holes’ over the subtraction. As well as this bad pixels in the detector will be present as it is likely that the frames will need some alignment (see *ii.*), and as such they will not be at the same pixel coordinates for the aligned image and template. The removal of cosmic rays and bad pixels is usually done by replacing the bad pixel values with values obtained from a simple interpolation of nearby good pixels over the shortest axis of the bad pixel region. A bad pixel mask is used to identify defects in the detector, whereas a detection algorithm must be run to identify cosmic rays, since these appear randomly for each image (see Section 2.2.1 for a description of the detection algorithm used by CLASP). Fringing patterns, although not varying in form by large amounts over reasonable timescales, do vary in strength on short timescales. Coupled with the small scale of variation (which cannot be easily removed by typical background fitting functions used in image subtraction, see *iii.*), fringe patterns must be removed from each of the image and template frames prior to subtraction to obtain a smooth, near-zero background over the image. Removal of a fringing pattern is done using a median-stacked image of dithered on-sky frames taken in the same filter as the observations. This fringe frame is then subtracted from the image and template, after scaling to match the pattern strength in each.

*ii.*

Alignment of frames, including rotation, scaling and flipping, can be performed using either a world coordinate system (WCS) transformation or object matching. WCS alignment is obviously reliant on an accurate WCS solution for each frame. Given two WCS solutions a transformation can be trivially produced by existing packages (such as WREGISTER in IRAF), however, this will *not* fail in the case of erroneous WCS solutions for one or both frames, in the sense that an alignment can always be found between two arbitrary coordinates on the sky as it is simply a geometrical transformation. This means that it is difficult in a programmatic sense to discover these erroneous alignments.<sup>3</sup> A more robust and fail-safe procedure is to find objects in the two frames and then compute the transformation based on creating matched coordinate pairs for objects in each image. By doing this, a

---

<sup>3</sup>There is also the possibility that an incorrect telescope pointing could produce an image or template with a nominally correct WCS solution, but of a different patch of sky. Again, in this case the WCS alignment routine will not fail, but the transformation will obviously be incorrect.

success alignment is dependant upon the two observations having common sources, and it will naturally fail in the case of no overlap between the frames. The alignment is sought by attempting to match triangles of objects in the frames, using the ratios of the triangle lengths to find corresponding triangles in each frame. This process is detailed further in Section 2.2.1.

*iii–vi.*

Even with cleaned and properly aligned images, there exist factors that must be accounted for in order to produce a useful subtraction. These differences arise from the varying conditions each observation will have been taken under; software packages have been developed that attempt to deal with these, such as ISIS (Alard, 2000) and HOTPANTS<sup>4</sup>, the methods of which follow. The atmospheric conditions and optical set up will produce background variation between the frames that varies as a function of position on the image. This is accounted for by firstly scaling each image based on the brightness of objects in each frame such that they match (typically an iterative sigma clipping of the object list which produces this scaling factor is performed so as to remove anomalous objects – i.e. variable or saturated objects). Then a two-dimensional function (low order polynomial or spline) is fit in order to match the form of the background in the image to that of the template. However, by far the biggest factor affecting the quality of the resulting subtraction is the difference in the PSF. Significant PSF variations can happen on timescales of minutes, and as such, even in the case of a template and image being taken sequentially on the same telescope and instrument, a treatment of the PSF variation must be included in the data manipulation before subtraction. This typically takes the form of a *kernel* (e.g. Alard and Lupton, 1998), with which one of the frames is convolved in order to match the PSF of the other. Since this convolution will always degrade the seeing of a frame, the convolution is applied to the better seeing. In the case where the image is worse seeing than the template the equation takes the form:

$$I(x, y) \otimes K(u, v) - T(x, y) = S(x, y), \quad (2.1)$$

where I is the image, K is the kernel, T is the template and S is the resulting subtraction. The

<sup>4</sup><http://www.astro.washington.edu/users/becker/v2.0/hotpants.html>

kernel is practically obtained by selecting a number of *stamps* within each image (regions of the frame centred on point sources), and modelling the functional form of the difference in the PSF between the frames at the locations of these stamps. The kernel model consists of a number of gaussians of varying order and full-width half-maximum (FWHM) superimposed<sup>5</sup>, and is typically allowed to vary in a low order polynomial fashion over the extent of the image to account for PSF variations (Alard, 2000). The FWHM of the gaussians should reflect the seeing of the frames otherwise they will not properly model the kernel, e.g. in the case of poor seeing (PSF is spread over a large number of pixels in each stamp) but narrow gaussians (small pixel widths), the full extent of the PSF will not be accounted for since the gaussians are not characteristic of the PSF's form. Again, the selection of stamps to use has an iterative sigma clipping applied in order to prevent artefacts or extended or saturated sources from inclusion in the final kernel creation. Naturally such bright stars, which have a deformed PSF from the rest of the image due to their pixel counts entering the regime of non-linearity for the detector, will not be cleanly subtracted. Most stars will leave some small imprint in the subtraction, but these bright stars may leave significant residuals, and so bright sources would be masked prior to detection algorithms being run on the subtraction.

Clearly, although image subtraction provides a natural solution to the task of finding variable and transient objects within subsequent observations of a field, there are still a large number of steps that must be performed, each with several parameters that affect the quality of the resulting subtraction. Typically large surveys will create or utilise real-time subtraction pipelines that perform some automated searching of the subtractions in order to flag potentially interesting sources. The advantages of this for a single survey are that they can produce source catalogues of variable stars to prevent repeated flagging of them, the data are of a consistent form and the details of the telescope and instrument setup are known. However, a large amount of image subtraction is still performed investigating individual objects, or on follow-up observations of transients detected by these large-scale surveys. The challenges here are not running detection routines on the subtractions (it is already known that a transient is in the frame), but an ease of usability by a wider audience and the accep-

---

<sup>5</sup>Although see Bramich (2008); Becker et al. (2012) for methods using delta functions to properly model the kernel at each pixel of the stamp, to remove the dependency on a functional form (e.g. a summation of gaussians).

tance of diverse imaging data from many different telescopes and instruments. This led to the development of CLASP.

## 2.2 CLASP

CLASP (Create Light curves with Alignment, Subtraction and Photometry) is a tool for performing small- to medium-scale image subtraction tasks, with a focus on usability and success for a wide variety of imaging data, regardless of the specific telescope/instrument setup. CLASP is reliant on some common FITS header values (such as an exposure time, date of observation, read noise and gain of detector). Appendix B describes the details of the requirements.

CLASP is written in PYTHON<sup>6</sup> (utilising IRAF<sup>7</sup> tasks through the PYRAF<sup>8</sup> package), calling on SExtractor<sup>9</sup> and HOTPANTS. It consists of a subtraction pipeline (SUBPIPE) to perform the image alignment and subtraction, a photometry pipeline (PHOTPIPE) to perform photometry on the subtracted image (producing it in the template's photometric system), and a GUI interface to both. A simplified outline of the actions of each pipeline is shown in the form of flow charts in Figs. 2.1 and 2.2, and a detailed description in plain English follows. See Appendix B.1 for practically how to use CLASP, including a fuller description of the optional arguments and details of the configuration files.

### 2.2.1 SUBPIPE

Designed to perform some data reduction (after basic flat-fielding and bias/overscan subtraction has been performed), image alignment and subtraction, SUBPIPE can be run on individual images or in batch mode on a directory of images. The three required elements are: one or more science images (*image*), a template image (*template*) to subtract from these, and a work directory (*workdir*) where all the output data are stored (along with logs and reports of

---

<sup>6</sup><http://www.python.org/>

<sup>7</sup><http://iraf.noao.edu/>

<sup>8</sup>[http://www.stsci.edu/institute/software\\_hardware/pyraf](http://www.stsci.edu/institute/software_hardware/pyraf)

<sup>9</sup><http://www.astromatic.net/software/sextractor>

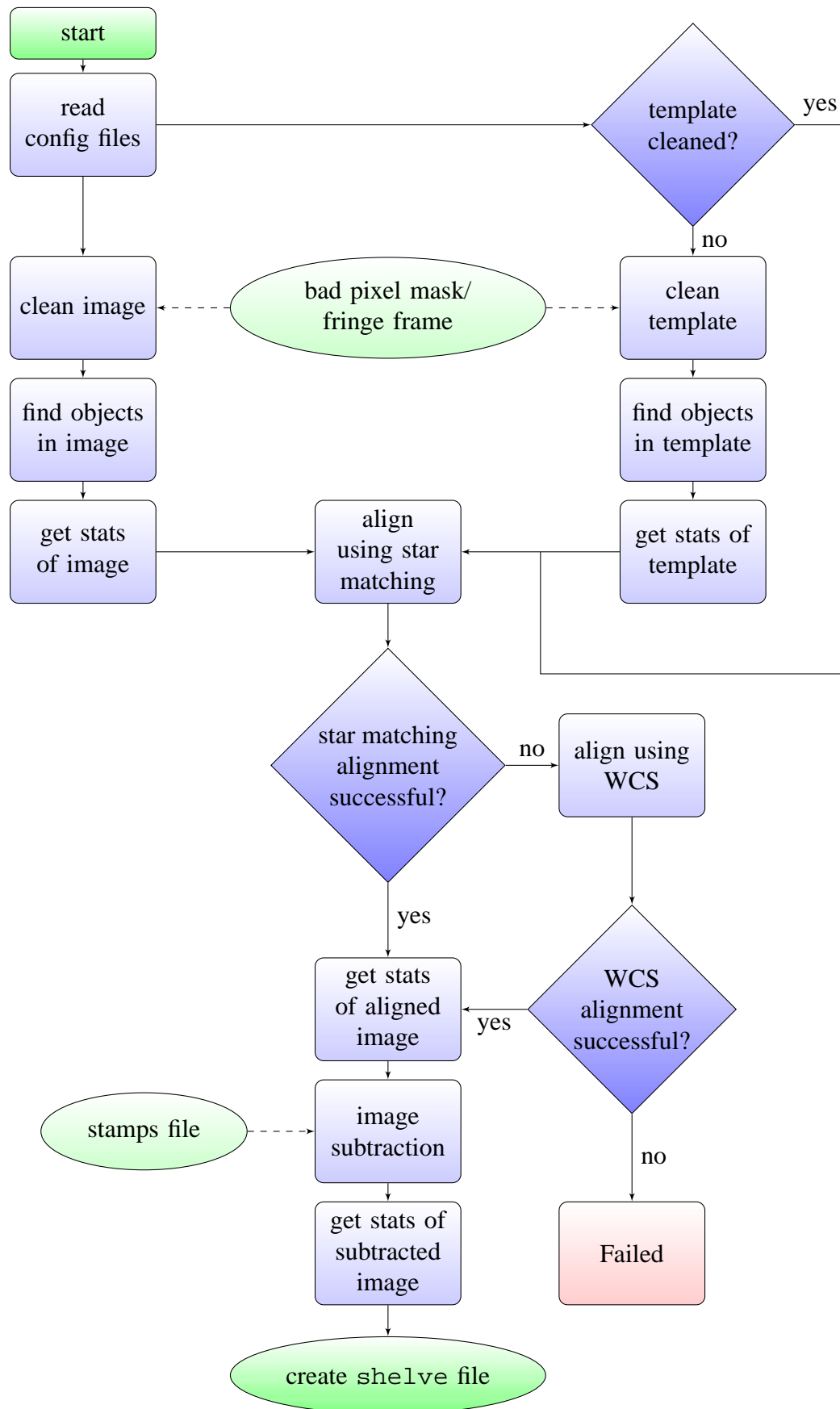


Figure 2.1: Flow chart showing the basic processes and decisions made by SUBPIPE

the pipe's progress). SUBPIPE then performs the following actions:

- A list of input images is created by searching the specified image directory based on file name selection criteria (e.g. "\*.fits"). If an image path is provided, a single image is sent forward for processing.
- *workdir* is created if it doesn't exist, or the user is prompted to clear its contents if it already exists. A log and a report are created to hold output information. A *shelve* file<sup>10</sup> is also created as a permanent store for the data that can be read by PHOTPIPE. The following are then copied into *workdir*:
  - *template*, into a sub-directory of *workdir* called 'template/
  - The configuration files `HOTPanTScfg.py` and `PIPEcfg.py`.
  - The first *image* in the list of science images.
- *image* is cleaned as required by the user and some information is stored about the image. (This is also performed for *template* on the first pass.)
  - image header is read as per the `PIPEcfg.py` file for date of observation, filter, read noise, gain and exposure time; the validity of the WCS is also checked.
  - Cosmic rays are removed using Laplacian edge detection as described in [van Dokkum \(2001\)](#), originally implemented in PYTHON by Malte Tewes<sup>11</sup>, and modified here for integration with SUBPIPE, as well as including bad-pixel masking.
  - A bad-pixel mask, if given, highlights pixels that will be interpolated over by the cosmic ray routine.
  - image is defringed if a fringe frame is offered using the RMFRINGE package of IRAF.
  - The median seeing is determined using SExtractor with clipping of non-point sources from the catalogue.

<sup>10</sup><http://docs.python.org/2/library/shelve.html>

<sup>11</sup>[http://obswww.unige.ch/~tewes/cosmics\\_dot\\_py/](http://obswww.unige.ch/~tewes/cosmics_dot_py/)

- SExtractor is run on *image* (and *template* if it is the first pass) iteratively until a satisfactory number of objects are detected (limits are read from `PIPECFG.PY`).
  - The threshold for detection is raised (lowered) a limited number of times to decrease (increase) the number of objects detected.
- Alignment of *image* and *template* is attempted if one or both of the alignment options are `True` in `PIPECFG.PY`. Pre-alignment is assumed if neither alignment option is `True`.
  - The object lists created by SExtractor are fed to XYXYMATCH in IRAF to attempt to align the images directly based on these object lists.
  - If XYXYMATCH fails, the coordinate lists are reduced to include only nearby objects in each frame (i.e. objects that exist in both *image* and *template* within a set number of pixels, to help if the two images are only slightly misaligned).
  - In the event that XYXYMATCH fails to align the images then WREGISTER is used, which is reliant only upon the solutions of the WCS in the respective headers. This is not used if the header of the image or template shows that the WCS solution was incorrect.
- The `HOTPANTSCFG.PY` configuration file is read to store the user's configuration of the subtraction to be performed.
- The SExtractor output catalogues of the aligned *image* and *template* are parsed to ensure objects are coincident in each frame (to sanity check the alignment). Direct comparison of the FWHM in each frame is made with an object-by-object comparison
  - the median seeing ratio is included in the report.
- The FWHM of the newly-aligned *image* and *template* are checked and the FWHM of the gaussians used to produce the kernel are increased in accordance with the seeing to achieve a better subtraction.
- HOTPANTS is called to subtract *template* from *image*, the direction of the convolution is by default to convolve the better-seeing frame but this may be overridden by the user.

- The subtracted image has its pixel statistics read (std. dev., mean etc.) as a measure of the goodness of subtraction and these are included in the report.
- PNG images of aligned *image* and the subtracted image are made for quick look analysis in *workdir*.
- A new line is added to the report with an overview of the previous subtraction (the seeing in each frame, alignment process used, which frame was convolved, pixel statistics of subtracted frame etc.)

The post-*workdir* creation process is repeated for each subsequent *image* in the list of input images (minus the steps specific to *template*, which only need to be performed once).

Potential failure points (barring simply poor data) are the inability to detect a good number of objects in *image* or *template* and the alignment process. Although, as mentioned in Section 2.1, the WCS alignment will not fail (provided both frames have a WCS fitted, correct or not), an additional check of the alignment is made by searching for sources in each frame and matching their positions to within a threshold of 2 pixels. If the number of matched objects is too low, the alignment is deemed to be incorrect. Success/failure of the subtraction is noted in the `shelve` file such that PHOTPIPE knows which to perform photometry on.

### 2.2.2 PHOTPIPE

PHOTPIPE will produce photometry of object(s) in the subtracted frames and transform these to the photometric system of *template*, meaning only the *template* needs to be calibrated and then the zeropoint of the *template* can easily be applied to the photometry output here. PHOTPIPE is reliant upon the presence of an unaltered SUBPIPE *workdir* that contains a valid `shelve` file. Alteration of names or deletion of directories/files between performing SUBPIPE and PHOTPIPE for a given *workdir* will result in unanticipated behaviour. Given a *workdir*, PHOTPIPE then performs the following:

- The coordinates of the object(s) on which to perform photometry are either read from the provided input or found through interactive selection:

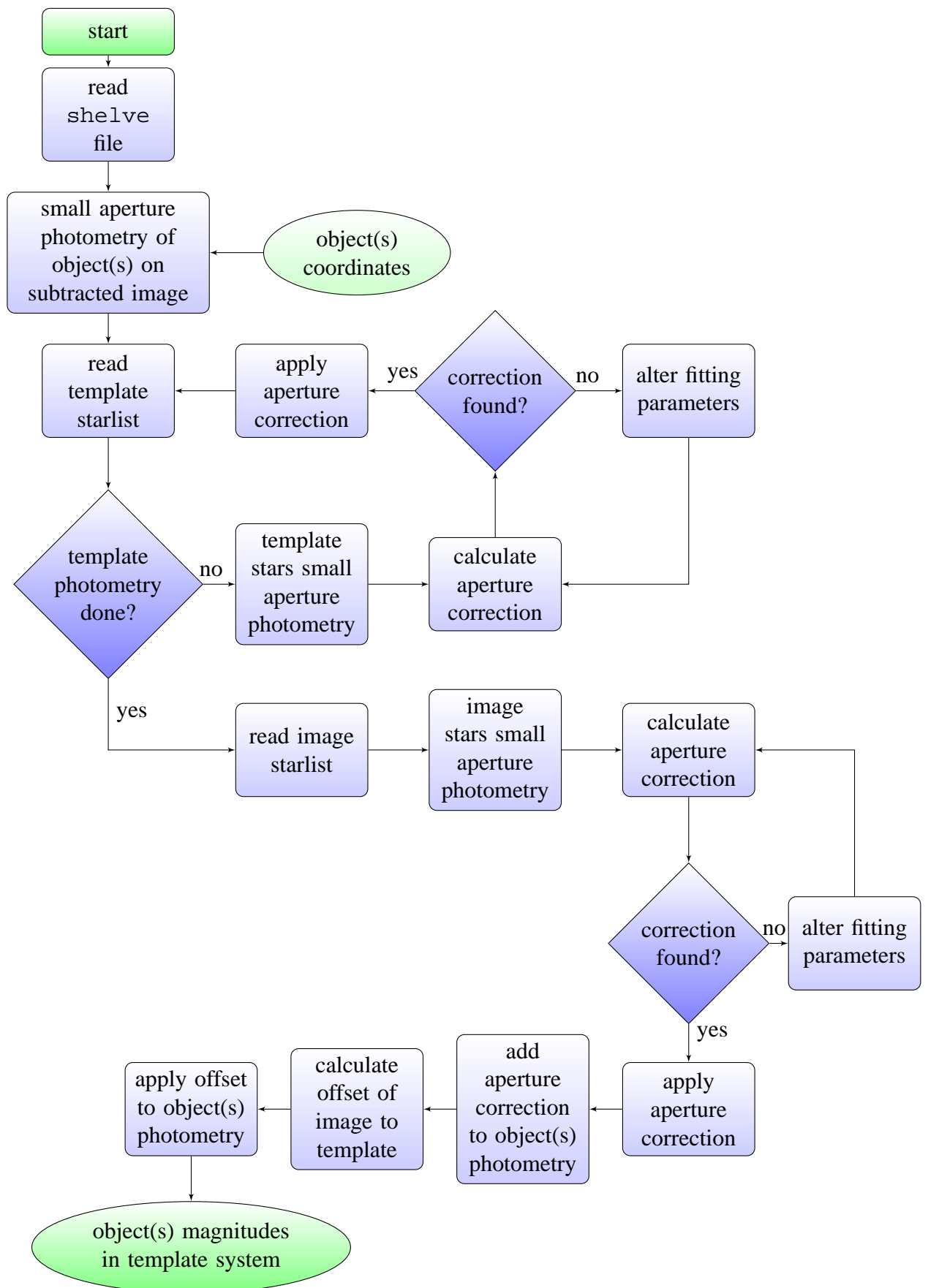


Figure 2.2: Flow chart showing the basic processes and decisions made by PHOTPIPE

- The astronomical image viewer DS9 is loaded and a subtracted image is shown.
- Via the IRAF package IMEXAM, the user can select one or more objects and their centres are passed to SUBPIPE.
- The a log and report file for PHOTPIPE are created in *workdir* alongside a `lightcurve.txt` file which will hold the final photometry.
- The `shelve` file is opened and the list of successful subtractions are stored.
- If a list of star coordinates is not supplied, *template* is shown to the user in DS9 and the user can select various stars by their annotated object number. These are the stars that will be used to calculate the aperture correction and the *image-template* offset.
- The IRAF aperture photometry routine, PHOT, is called to perform aperture photometry on the objects at the specified small aperture size.
- For *image* and *template* (for the first pass), PHOT is called to perform aperture photometry on the stars chosen in apertures of increasing radii up to the specified large aperture size (the aperture we wish to correct the objects photometry to).
- From this photometry a curve-of-growth (COG) model is formulated using MKAPFILE in IRAF for each image, and the object(s) small aperture photometry is corrected to the large aperture using the COG.
- A median offset between *image* and *template* is found by comparing the instrumental magnitudes of the large aperture photometry output by MKAPFILE on an object-by-object basis. A sigma-clip is applied to the list of offsets to remove contributions from anomalous objects.
- The offset value is applied to the large-aperture photometry of the object(s).
- A report line is added detailing the object photometry at each stage and the values and errors of the associated corrections.
- The corrected magnitudes and errors are output into a light curve file with a column for each object chosen, with a time column given by the date of observation which was gleaned from the header of *image* in SUBPIPE.

Again, in batch mode where the `shelve` file contains multiple subtractions, the process is repeated (from performing small aperture photometry on the objects) for each *image*, barring *template*-only steps, which only need to be performed once.

Potential failures include inability to determine the COG model and object photometry failing if the object has faded below the detection threshold in some images.

### 2.2.3 Examples of usage

Some examples of subtractions performed by CLASP are presented in Figs. 2.3 and 2.4. In Fig. 2.3, a trail left by a fast moving body is clear in the template of the second example, this is clearly visible in the subtraction but does not adversely affect it in a noticeable way as the background determination is largely robust from such small perturbations and the kernel determination is made from point sources only. Hugely saturated stars and associated diffraction spikes are also problematic for image subtraction, as shown in the penultimate example. The orientation of the diffraction spike is different as these images have been originally taken at different orientations and aligned by CLASP. The region around the saturated star clearly suffers from strong residuals, however note that the overall subtraction is clean and the background mean is indeed close to zero in regions away from the strong residual. This would make photometry of the SN located at the centre of the image possible.

The third row in Fig. 2.4 shows an image of SN2011fe in M51 taken with SkyCamZ – the very large large field-of-view (1 square degree) and strong misalignment between the image and template are dealt with by CLASP and the SN is well recovered in a clean subtraction (barring the asteroid/satellite trail near the top of the image).

CLASP, although designed to ease light curve creation for transient follow-up, was tested for a similar but initially unenvisaged subtraction task.  $H\alpha$  imaging must have the continuum level subtracted from it before being representative of just the  $H\alpha$  flux. This is typically done by observing in a narrow band filter centred on  $H\alpha$  and one centred just off it which should be subtracted, this could also be an R (or  $r$ ) band image which would need to be scaled before subtraction. Because the image subtraction routine incorporates a scaling fac-

tor which accounts for varying sky brightnesses, it turns out this can also absorb the varying transmission profile width of the narrow and R band images to scale them correctly before subtraction. The usefulness of CLASP to create continuum-subtracted  $H\alpha$  maps is shown in the bottom 3 rows of Fig. 2.4. The first of these suffers from anomalous background levels in the four quadrants of the frame, at different strengths in the image and template, due to varying amplifier noise – the subtraction shows no sign of this. Two sets of Isaac Newton Telescope (INT) observations (bottom 2 rows) produce excellent  $H\alpha$  maps with largely clean removal of foreground stars. This ability to produce  $H\alpha$  continuum maps allows CLASP to be used when considering the pixel statistics method of James and Anderson (2006). A study using CLASP and this method is given in Section 3.2.

When failures do occur (be they complete errors or just bad subtractions and thus bad photometry), the main reasons are:

**Inability to deduce the alignment.** This will not occur in the case of a correct WCS fitted to the image and template and with some overlap between the frames, but may occur when relying solely on star-matching.

**Large difference between each frame’s PSF.** Be it from elongation or just very poor seeing, these differences are difficult to reconcile to a common PSF in image subtraction, as as such the extended wings of the poor-seeing image may still be present around point sources in the subtraction.

**Not enough point sources to determined kernel.** This can be an intrinsic lack of point sources in the images, or only point sources in one region of the image, in which case the kernel function over the spatial dimensions of the image can vary wildly away from these point source tie points.

**Wrong convolution direction.** Although HOTPANTS makes some attempt to deduce the best convolution direction, this can sometimes be incorrect, resulting in a poor subtraction – forcing HOTPANTS to convolve in the other direction solves this problem (see Appendix B).

Two examples of poor subtractions are given in Fig. 2.5

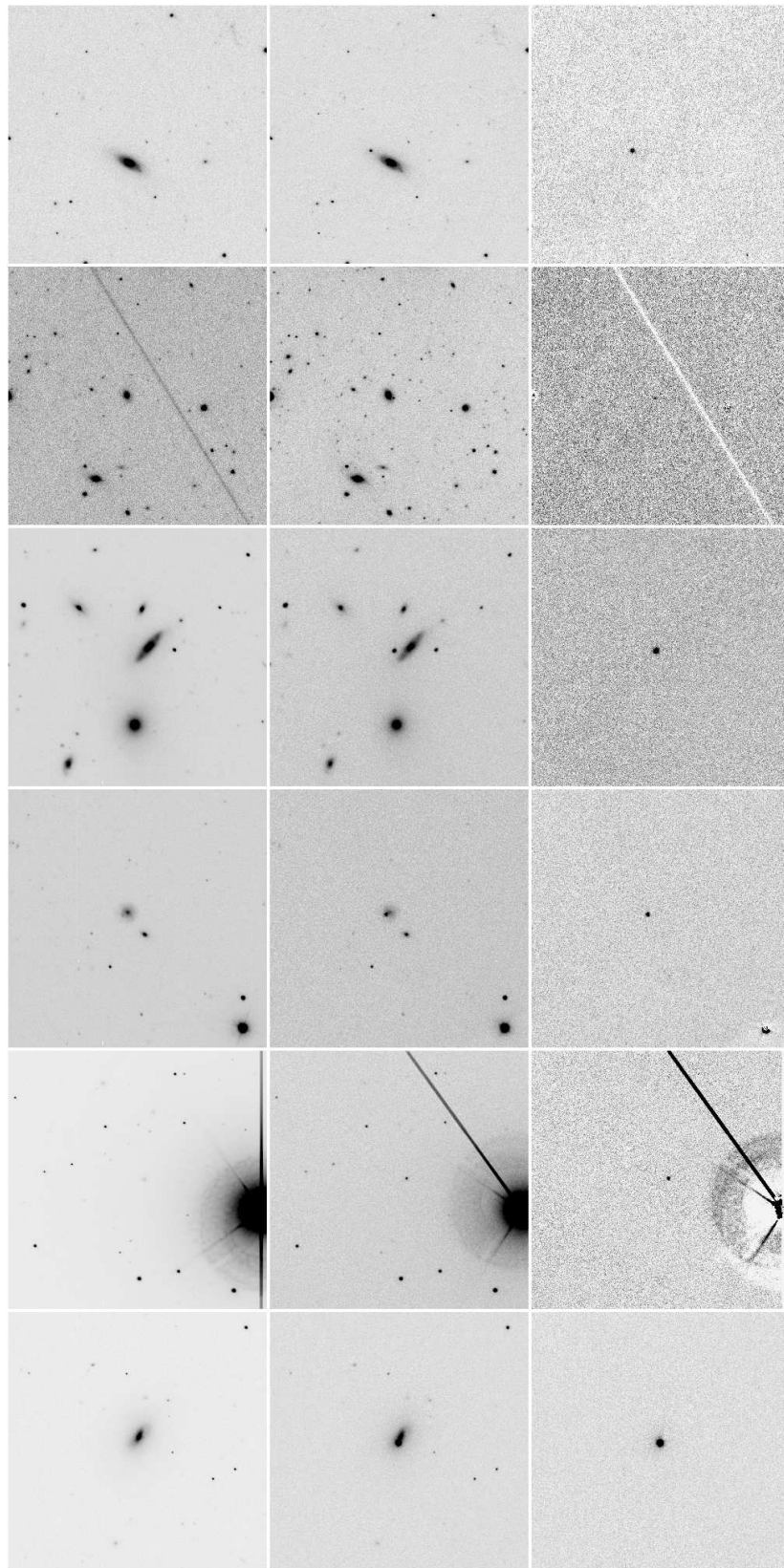


Figure 2.3: Examples of subtractions performed by CLASP on Liverpool Telescope images (RATCam and IO:O) of various SNe. *Left:* the templates, *Centre:* the science images, *Right:* the subtractions.

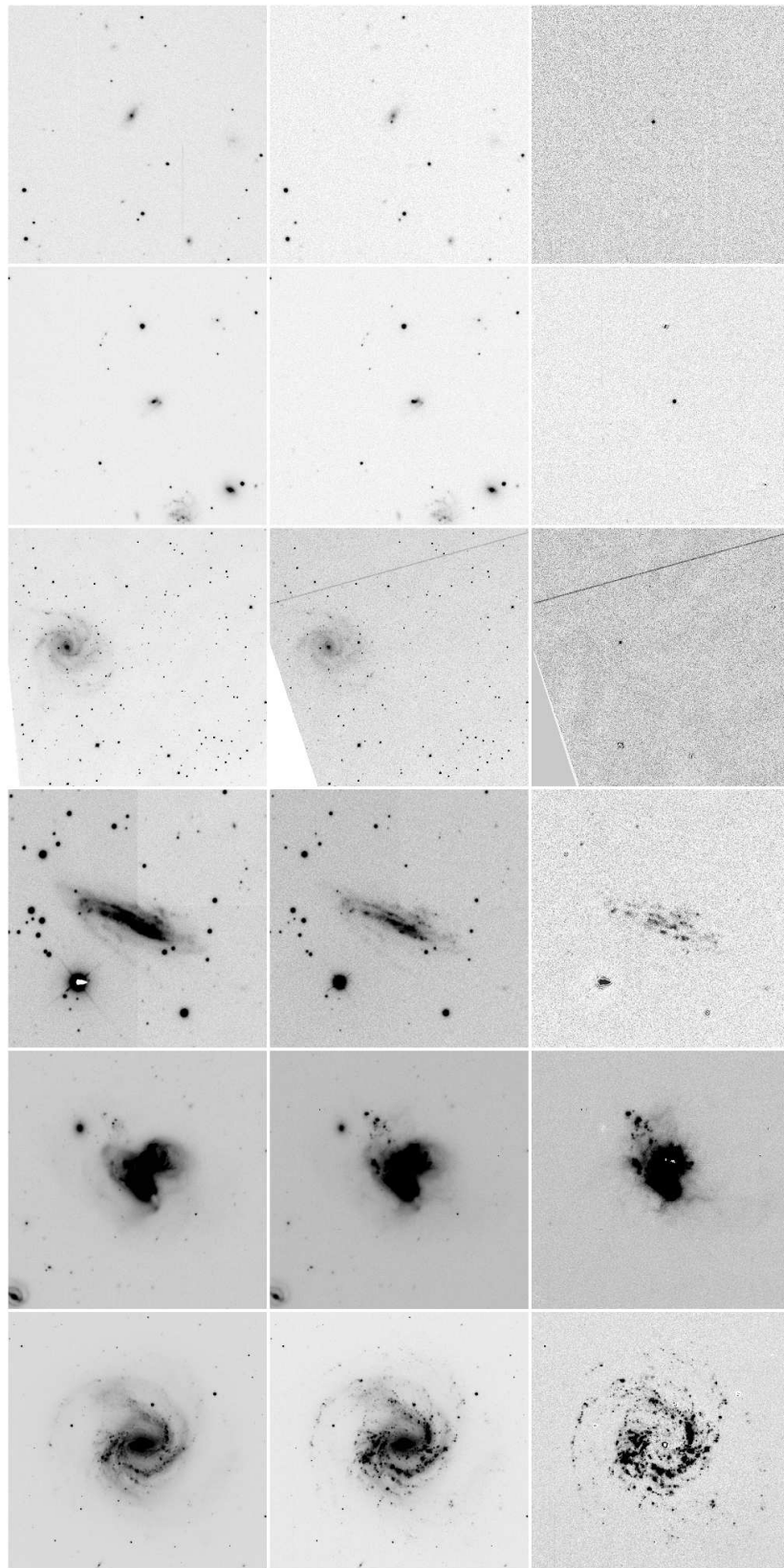


Figure 2.4: Examples of subtractions performed by CLASP on Liverpool Telescope (RAT-Cam, SkyCamZ and LT IO:O) and INT+WFC. Columns are the same as Fig. 2.3. The last three columns are R-band,  $H\alpha$  and continuum-subtracted  $H\alpha$  images of star forming galaxies. The excess seen in these galaxies is not residuals, but genuine  $H\alpha$  flux above the continuum level.

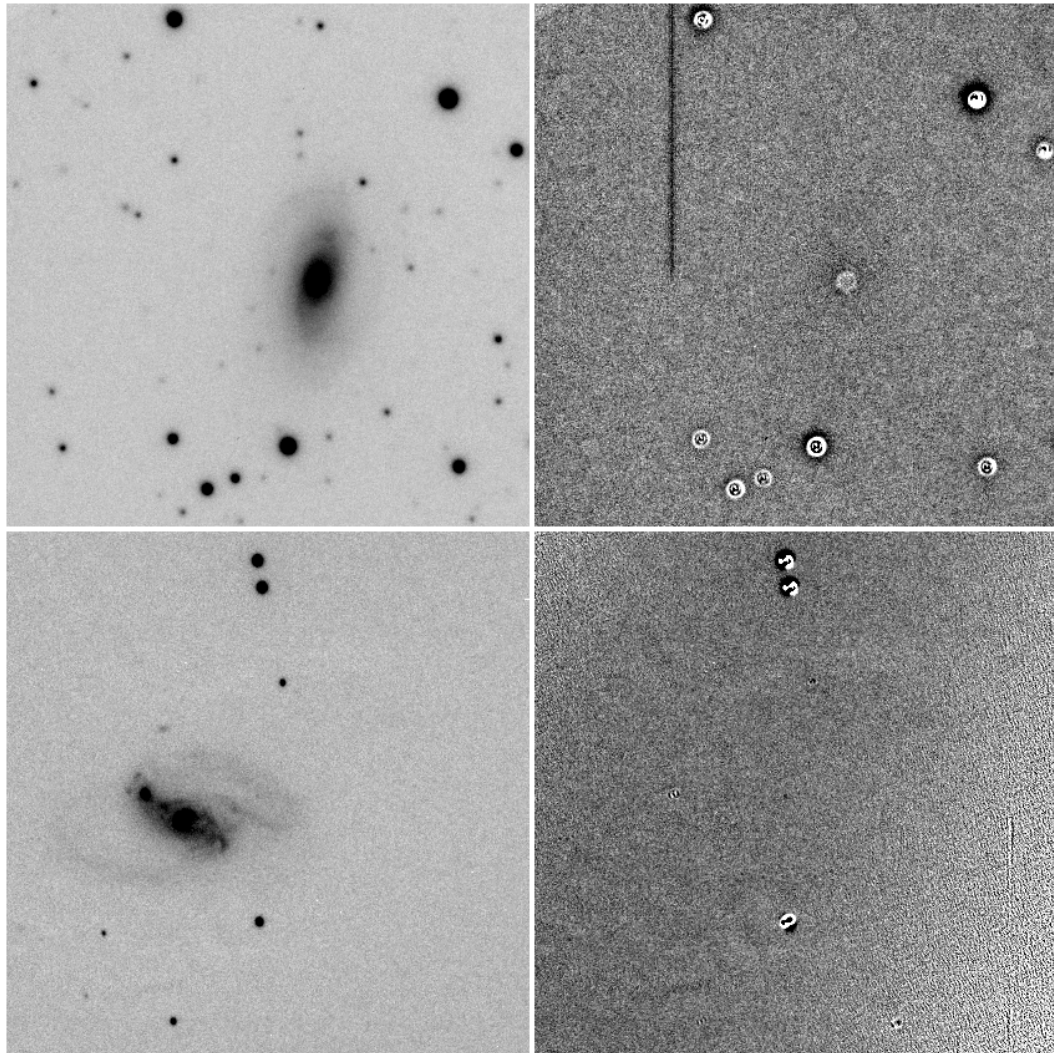


Figure 2.5: Examples of poor subtractions performed by CLASP on Liverpool Telescope images (RATCam) of various SNe. The top row shows an example of very poor seeing in the science image, hence the wings of the PSF are visible on the subtracted image since the kernel is too small to cover this large area. The bottom row has only a few point sources, all concentrated down the centre of the image, from which to construct the kernel. In this case the polynomial function of the kernel varies greatly when no tie points are present, i.e. the top left and bottom right of the image – using a lower order (or non-varying) kernel may alleviate this. *Left*: the science images, *Right*: the subtractions.

## Chapter 3

# The environments of low-luminosity type I supernovae

### Abstract

This chapter describes a study using CLASP to investigate the properties of the locations of supernovae within their host galaxies. Utilising star formation tracers, constraints can be placed on the ages of progenitors by investigating the spatial coincidence of SNe with these tracers. This method is used to investigate the properties two types of unusual transients, both being sub-luminous compared with the major classes of supernovae. Those of one type exhibit unusually strong calcium features, and have been termed ‘Ca-rich’. Those of the second type, with SN 2002cx as the prototype, have some properties in common with the first, but show typically lower ejecta velocities, and different early spectra. Important differences in the environments of the two types are confirmed, with Ca-rich transients preferentially occurring in galaxies dominated by old stellar populations. Quantitatively, the lack of association of the Ca-rich transients with regions of ongoing star formation is well matched to that of the overall Type Ia supernovae population. The SN 2002cx-like transients are very different, with none of the present sample occurring in an early-type host, and a statistical association with very recent star-formation similar to that of Type IIP supernovae, meaning a similar delay time of  $\sim 30\text{--}50$  Myr. Further constraints from ultraviolet imaging confirm the progenitor lifetimes of SN 2002cx-like events to be  $< 100$  Myr.

### 3.1 Star-formation tracers in SN hosts as diagnostics for the progenitor systems

Stars are luminous at a range of wavelengths throughout their lives from the onset of nucleosynthesis, to their ultimate fate. Thus photometric observations of a stellar population in an arbitrary wavelength range (filter) will include contributions from stars of a wide range of ages and masses. In order to specifically observe certain types of stars, observations can be made in specific wavelength ranges where the emission is primarily comprised of light from those stars. Discussion here will concentrate on *star-formation* (SF) tracers, i.e. those wavelengths of emission that are present only for a relatively short time after stellar birth, and hence act as a diagnostic for recent star formation, for the case of unresolved stellar populations.<sup>1</sup>

SF tracers are generally the result of the emission directly from young, massive stars, or from its effect on the immediate surroundings. Massive (short-lived) OB stars are extremely hot (blue) and luminous. A large fraction of their emission is in the UV regime, hence observations revealing UV-bright stellar populations are a diagnostic for recent star formation over the life time of these stars (a few–30 Myr). This large amount of UV emission also affects the dust local to the recent SF. Given the increased likelihood of interaction with dust grains for UV compared with optical or near-infrared emission, and the fact these higher energy photons will heat the dust to higher temperatures, the influence is different to that from older stellar populations (Helou, 1986). Characterisation of the temperature of dust through mid- to far-IR observations (as derived from the peak of the SED in this regime given the black body nature of the emission) can thus also point to the presence of young, massive stars – recent SF. The need to characterise the SED over a range of wavelengths, and the uncertain contributions from the underlying, older stellar populations makes the IR a less straightforward tracer of SF. The radiation from these hot, young stars also contains a significant number of hydrogen-ionising photons, that is, photons of wavelength  $<912 \text{ \AA}$ , which ionise the local medium. Cascading electrons recaptured by ionised hydrogen

---

<sup>1</sup>The particulars of deriving absolute SF rates from such tracers, and the assumptions inherent to this of constant versus instantaneous SF, will be neglected in favour of detailing simply the observations that would be indicative of a young stellar component.

produce very strong hydrogen emission lines, including the optical Balmer series, meaning observations of  $H\alpha$  or  $H\beta$ , for example, are tracers of SF. The amount of ionising flux is strongly dependent on the mass of the star, i.e. the most massive stars will dominate the ionising flux of a SF region. Given this, the  $H\alpha$  flux from a new stellar population also rapidly evolves since the extremely massive stars, which are contributing significantly to the flux, will explode as SNe in a very short time. As such  $H\alpha$  and similar emission tracers are probes of very recent SF, with measurable fluxes diminishing several Myr after the cessation of the SF episode.

By comparing the locations of SNe in external galaxies to the presence of such SF tracers, it is possible to determine if there has been any recent SF at the location of the SN within the time-scale probed by the tracer being used. This allows estimates to be placed on the age of the SN, e.g. if a SN is coincident with a  $H\alpha$  emitting HII region, it is probable that the SN progenitor lived less than the time-scale probed by  $H\alpha$  emission ( $\sim 10$ - $20$  Myr), whereas an absence of such emission would be indicative of a progenitor outliving this time-scale. Naturally for a given SN in a given host, such a method is subject to uncertainties and indeed the presence or absence of a tracer may be unrelated to the SN's parent population. For example, line-of-sight effects, where the SN is along the line-of-sight to a burst of recent SF but not coincident, may give an anomalous result, and extinction, particularly important for UV tracers where the wavelengths probed are highly diminished by such extinction, may veil the appearance of emission at the SN's location. However, by looking at a *statistical* association between the locations of many SNe in many galaxies, the contamination by such effects should be minimised. Furthermore, when looking at *relative* differences between the associations of different SN types, these contaminations should be roughly equivalent for each type and thus any differences are due to the differences in the ages of the progenitor systems. This analysis is employed in the following section (Section 3.2) as a follow up study to the larger scale studies of [James and Anderson \(2006\)](#); [Anderson and James \(2008\)](#); [Anderson et al. \(2012\)](#).

## 3.2 The environments of low-luminosity type I supernovae

### 3.3 Introduction

With the advent of dedicated SN searches that are discovering many SNe in a single night, coupled with in-depth follow-up that is now possible, inevitably events will be discovered that challenge the current understanding of SNe. Indeed, we are moving away from the observationally based classification system as increasing numbers of events are discovered that do not fit this system. It is not even known if many of these luminous events are in fact SNe in the sense of the death of a star or stellar remnant, and this introduces other possibilities for progenitor systems and explosion mechanisms. Two examples of such transient types are ‘Ca-rich’ and ‘SN2002cx-like’. Given the uncertain nature of these events, ‘transients’ rather than ‘SNe’ will be used to describe them. An overview of each type is now presented.

#### 3.3.1 Ca-rich transients

Named ‘Ca-rich’ on the basis of the relative strength of calcium lines in spectra observed during the nebular phase these transients are also known as ‘SN 2005E-like’ after the prototypical event (Perets et al., 2010), example light curves and spectra are shown in Fig. 3.1. In their overall spectral properties, the Ca-rich transients quite closely resemble CCSNe of Type Ib (i.e. lacking hydrogen, but showing strong helium features). Their very low ejected masses ( $\sim$  a few tenths of  $M_{\odot}$ ) have calcium to total-ejecta mass ratios many tens or hundreds times that of other SNe types – for example, Perets et al. (2010) found almost half of the total ejecta of SN 2005E was calcium and showed that these transients actually produce more calcium in absolute terms than ordinary SN per explosion, despite CCSN releasing up to several solar masses of ejecta. Their contribution to the total calcium production budget of the intracluster medium could be very significant (Mulchaey et al., 2014), although rates remain uncertain currently. The spectral similarity to SNe Ib led to the claim by Kawabata et al. (2010) that one of the members of the class, SN 2005cz, could indeed be a core-collapse object with a  $10 M_{\odot}$  zero-age progenitor. This would be a surprising discovery, given that

the host galaxy of SN 2005cz, NGC 4589, is an elliptical galaxy with a ‘classical E2 morphology’ (Sandage and Bedke, 1994), and a corresponding expectation of a predominantly old stellar population. Simultaneously, the even more extreme environment of SN 2005E, the prototypical member of the Ca-rich class that occurred far from the disc plane of an early type S0/a galaxy, NGC 1032, led Perets et al. (2010) to conclude that these explosions are likely to arise from the accretion of helium on to an old, low-mass progenitor, probably a WD. Modelling was used to show that such a progenitor can reproduce the observed properties, with ejecta that has high velocities but low masses, and a composition that is dominated by the products of helium burning, without the iron-group elements indicative of explosive nucleosynthesis found in SNe Ia. Perets et al. (2011) extended this analysis to SN 2005cz in NGC 4589, again preferring a low-mass, long-lived progenitor, in contradiction to Kawabata et al. (2010).

The spectroscopic and environmental properties of the general class of these Ca-rich transients have been investigated by Perets et al. (2010) and Kasliwal et al. (2012). The former identified eight SNe in this group (SN 2000ds, SN 2001co, SN 2003H, SN 2003dg, SN 2003dr, SN 2005cz, SN 2005E and SN 2007ke) and the latter identified three additional objects in this class from the Palomar Transient Factory survey (Law et al., 2009; Rau et al., 2009, henceforth PTF). Kasliwal et al. (2012) combined these three new objects (PTF 09dav, PTF 10iuv (SN 2010et) and PTF 11bij) with two of the better observed earlier events (SN 2005E and SN 2007ke) which share common properties of low peak luminosities, fast photometric evolution, high ejecta velocities, strong Ca emission lines and locations in the extreme outskirts of their host galaxies. They follow Perets et al. (2010, 2011) in preferring long-lived, low-mass progenitors, pointing out that the core-collapse objects with the lowest generally-accepted progenitor masses, Type IIP SNe (SNe IIP), are almost never found at the extreme outlying locations that characterise these five Ca-rich events.

Valenti et al. (2014) have reported on another possible member of the Ca-rich class, SN 2012hn, that was discovered by the Catalina Real-Time Transient Survey. This was initially classified as a peculiar Type Ic SN (Benitez-Herrera et al., 2012), but Valenti et al. (2014) conclude from analysis of later spectroscopic and light-curve data that SN 2012hn much more closely resembles members of the Ca-rich class, with a low peak luminosity and rapid evolution.

This is supported by its location in the outskirts of an early type (E/S0) galaxy (discussed further in this chapter). However, it should be noted that [Valenti et al. \(2014\)](#) find some detailed spectral differences between SN 2012hn and other members of the Ca-rich class.

A study by [Yuan et al. \(2013\)](#) has investigated the progenitors of the Ca-rich class by comparing their host galaxy locations to results from cosmological simulations. By comparison to the simulated metallicity distribution in hosts, they find the progenitors are likely to be of low metallicity and, tied with their remote locations compared to the bulk of the host stellar mass, consequently of old age ( $\sim 10$  Gyr). They conclude that a massive star origin for such events is disfavoured.

### 3.3.2 SN2002cx-like transients

Some similarities exist between the Ca-rich events and the unusual transient SN 2008ha ([Valenti et al., 2009](#); [Foley et al., 2009, 2010a](#)), in particular the extremely low luminosity and the inferred low ejecta-mass, and some similarities in the late spectra. SN 2008ha, however, does not show evidence for helium – it is classified as a SN Type Ia (SNe Ia) event – and has extremely low photospheric velocity ( $\sim 2000$  km s<sup>-1</sup> cf. 6000-11000 km s<sup>-1</sup> for the Ca-rich transients). [Foley et al. \(2013\)](#) have recently linked SN 2008ha and similar objects, including the prototypical example SN 2002cx ([Li et al., 2003](#)), to a proposed new class of stellar explosion, that they term ‘Iax’. These differ from normal SNe Ia in having lower maximum-light ejecta velocities (2000-8000 km s<sup>-1</sup>) and lower peak luminosities for a given light-curve shape. SN 2008ha then appears as probably the most extreme object in this class identified to date, with the lowest peak luminosity, and ejecta velocities at the bottom end of the range for this class. [Foley et al. \(2013\)](#) infer high rates, with  $\sim 30$  for every 100 SNe Ia in the local Universe. Example light curves and spectra of SN 2002cx-like transients are shown in Fig. 3.2.

Various models were suggested for the origin of these transients including complete thermonuclear deflagration of a WD ([Li et al., 2003](#); [Branch et al., 2004](#)), failed detonation of a C/O WD ([Jordan et al., 2012](#)) or possibly a peculiar type of CCSN event ([Valenti et al., 2009](#)). [Foley et al. \(2013\)](#) suggested the progenitors to be C/O WDs that accrete material from a He-

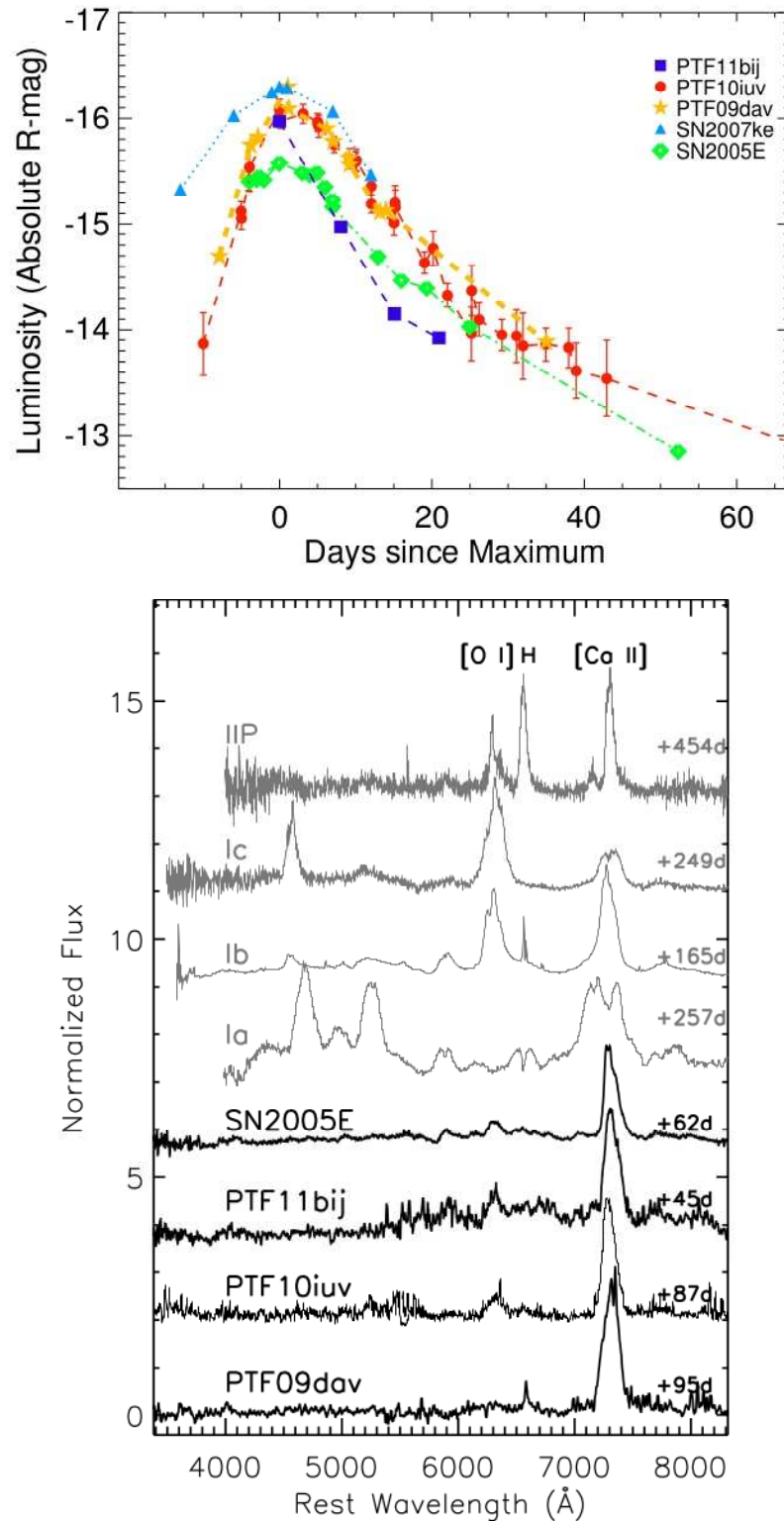


Figure 3.1: Example light curves (top panel) and nebular spectra (bottom panel) of Ca-rich transients. The low velocity, fast evolution and strong calcium/oxygen ratio compared to other CCSNe are evident. Taken from Kasliwal et al. (2012).

star, and therefore consider some possible connections between SN 2002cx-like and Ca-rich transients, where both type of events arise from a He-shell detonation scenario. However, one of the major differences between the two types is their environment, as first noted by [Perets et al. \(2010\)](#). The Ca-rich events occur in all galaxy types (with a large fraction in early-type galaxies), and/or far from the centres of host galaxies ([Kasliwal et al., 2012](#)), whereas SN 2002cx-like transients preferentially occur in late-type, star-forming galaxies, indicating a possibility for having younger progenitor systems. [Foley et al. \(2013\)](#) suggest that the difference might originate from a different origin of the accreted He in the two cases, i.e. SN 2002cx-like events arise from accretion from a He-rich non-degenerate donor star, whereas the Ca-rich events originate from accretion from a degenerate He-WD.

[Valenti et al. \(2009\)](#) discuss the class of SN 2002cx-like events in general, and SN 2008ha specifically, and conclude that these may be low-luminosity CCSNe, with progenitors that are either high-mass (25-30  $M_{\odot}$ ) Wolf-Rayet stars, or stars from the low-mass limit of CC-SNe (7-9  $M_{\odot}$ ). However, [Eldridge et al. \(2013\)](#) have recently discussed SN 2008ha in the context of a study of the rates of CCSNe, and on the balance of evidence decide in favour of a thermonuclear interpretation. They thus exclude it from their study, although they warn that the evidence is far from conclusive, and that further study of SN 2008ha and other SN 2002cx-like transients is clearly required.

### **3.4 Methods**

It is clear from the above discussion that the association with different types of stellar environment is of key importance in distinguishing between these different types of luminous transients, and in constraining the possible progenitor systems. However, much of the environmental information, e.g. the association of the Ca-rich transients with old populations and SN 2002cx-like transients with young, lacks quantification and in many cases is little more than anecdotal. Host galaxy classifications give some useful information, but they are notoriously subjective and, even if free from actual errors, they do not give precise information on the stellar population at the location of the transient event. For example, even a late-type spiral may have a bulge, or extreme outer disc, that is entirely composed of old stars. In this

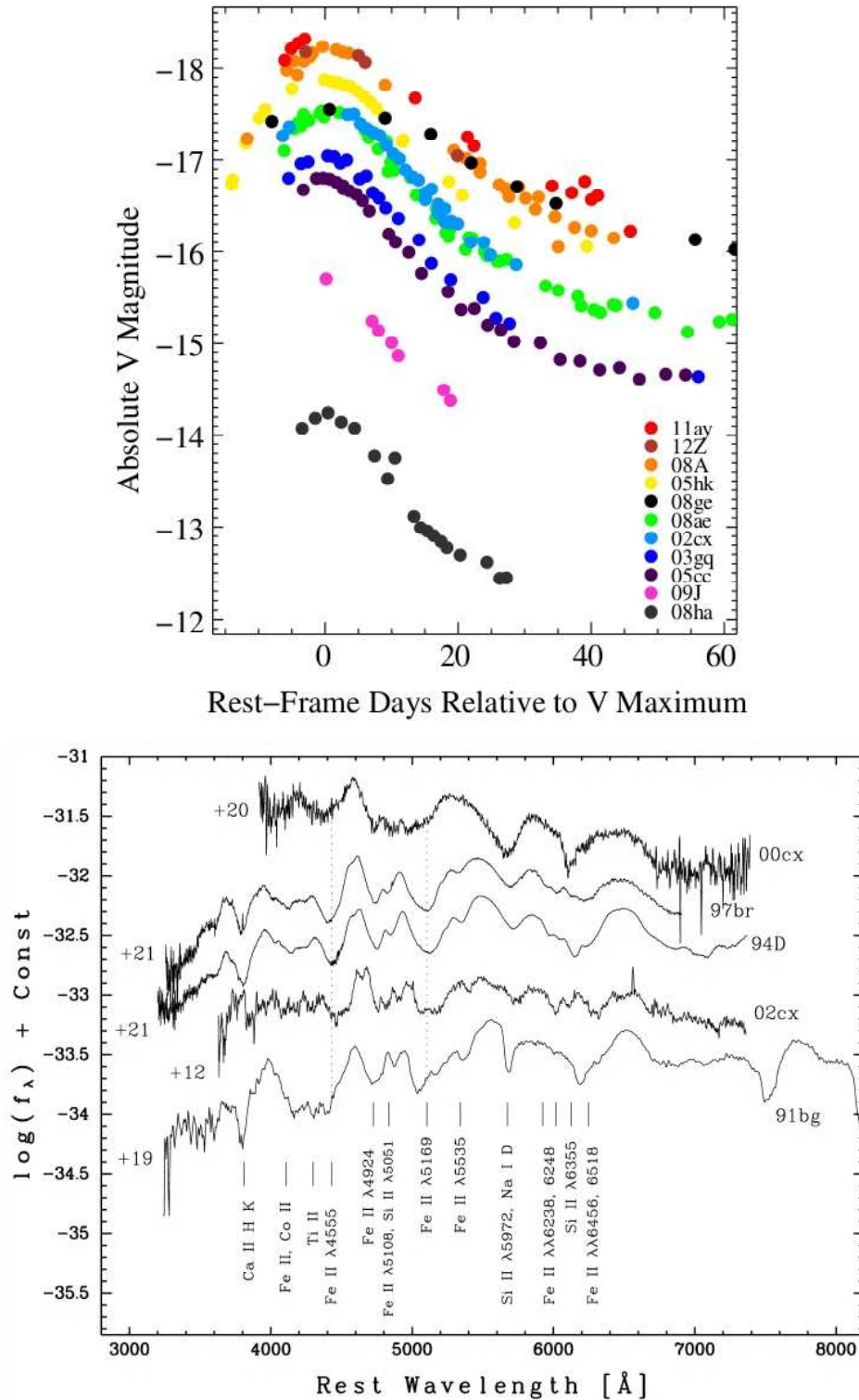


Figure 3.2: Example light curves (top panel) of SN 2002cx-like transients. A spectrum of SN 2002cx at  $\sim 12$  days past peak (bottom panel) shows the lower velocity features compared to other SNe Ia, including the sub-luminous SN 1991bg. Taken from Foley et al. (2013) and Li et al. (2003).

section, both host galaxy types and quantified measures of SF activity, local to the sites of events within their host galaxies, will be applied specifically to the known samples of Carich and SN 2002cx-like transients, to determine whether they appear to rise from the same progenitor populations, and to compare these populations with the same measures for other types of SN (including ‘normal’ SNe Ia, and core collapse types SNe Ib, Ic and IIP).

The idea of obtaining a statistical association between SN types and recent SF, as introduced in Section 3.1, is implemented here as a quantified analysis of these transients’ environments. This analysis takes the form of the Normalised Cumulative Rank (NCR) method. The NCR method is explained in the specific context of the manner in which it is applied here in [James and Anderson \(2006\)](#). It is also discussed at length in more general terms, focussing on the mathematical and data reduction steps, in Appendix A. The NCR method has been previously applied to large samples of supernovae in [Anderson and James \(2008\)](#); [Anderson et al. \(2012\)](#), and the latter provides the main comparison sample for the current work.

Briefly, each transient is assigned an NCR, based on pixel statistics of a continuum-subtracted  $H\alpha$  image of the host (taken either prior to, or long after the transient), as a measure of the degree of association of the transient with recent SF within its host. The continuum subtracted  $H\alpha$  images are trimmed to contain the host and transient location and then binned  $3 \times 3$  such that the pixel location of the transient given by the WCS forms the centre of a  $3 \times 3$  ‘super-pixel’. A pixel in the binned images represents  $\sim 0.9$  arcsec across the various instruments used, or  $\sim 260$  pc at the mean galaxy distance. Star residuals and artefacts arising from saturation in the subtracted images are masked using a local median. Pixel values in this binned image are sorted, cumulatively summed and then normalised by the total sum of pixel values. In this way each pixel now has an associated NCR value between 0 and 1 (any negative values are set to 0). Any pixel with  $NCR = 0$  is considered a background pixel, i.e. there is no  $H\alpha$  flux at that position. Positively valued pixels are then ranked within the NCR method such that low values have an association with weak emission, and high values are coincident with the brightest  $H\alpha$  emitting regions of the host. Specifically, the NCR value is the fraction of host galaxy flux that is below the level of flux at the location of the transient, i.e.  $NCR = 1$  means the transient location is at the site of the most intense SF activity within its host galaxy.

Using these methods, [Anderson et al. \(2012\)](#) find a clear separation of the CCSN subtypes, with types IIP, Ib and Ic forming a clear sequence of increasing strength of association with current sites of SF, and high mean NCR values. This is most simply interpreted in terms of a sequence of increasing mean progenitor mass, and hence decreasing progenitor lifetime.

[Crowther \(2013\)](#) has looked at the progenitor constraints that can be drawn from association of SNe with ongoing SF, using a smaller sample than [Anderson et al. \(2012\)](#) with higher spatial resolution, and employing rather different statistical methods based on distance to the nearest region of  $H\alpha$  emission. [Crowther \(2013\)](#) finds very similar results to [Anderson and James \(2008\)](#) and [Anderson et al. \(2012\)](#) in terms of the difference of strength association between SNe II and SNe Ibc, which he interprets in terms of a large fraction of SNe II outliving their natal SF regions. [Crowther \(2013\)](#) argues that the complications involving lack of resolution of individual SF regions should obscure any differences between the correlation strengths for shorter-lived, higher-mass progenitors than those of the SNe II, but this argument seems hard to reconcile with the clear statistical differences found for the populations of SNe Ib and Ic investigated by [Anderson et al. \(2012\)](#).

$H\alpha$  was chosen as a SF tracer since there already exists large samples of NCR values for the more common SN types which can be compared to. The typical duration of  $H\alpha$  emission from HII regions is comparable to that of the ages of the middle-to-lower mass end of CC-SNe. [Kuncarayakti et al. \(2013\)](#) show the evolution of the  $H\alpha$  equivalent width for a single burst in Starburst99, which weakens strongly after 5 Myr, falling to very low values after  $\sim 15$  Myr (roughly the lifetime of a  $14 M_{\odot}$  star). Although this is very much a lower limit in terms of the time-scale of SF, since a typical SF region will not form stars in a delta-function manner, it must be stressed that the loss of gas is not taken into account (i.e. the earliest SNe will disperse the gas), which will strongly diminish the emitted flux of a region after several Myr.  $H\alpha$  imaging allows, through the NCR method, to distinguish between transients whose progenitor ages fall entirely within, or overlap with, this limit. Since each transient's NCR value is normalised to its own host, the analysis is not sensitive to absolute calibration issues of  $H\alpha$  as a SF rate tracer ([Lee et al., 2009](#); [Botticella et al., 2012](#)).

The NCR method is particularly reliant on the  $H\alpha$  filter used for observations. Its transmission profile must allow for detection of  $H\alpha$  over a reasonable velocity range so as to detect

Table 3.1: H $\alpha$  narrow-band filter properties.

Filter name	Telescope	Wavelength limits $\text{\AA}$	$V_{rec}$ limits km/s
‘Halpha’	INT	6522–6614	–1865–2357
‘Ha 6657’ <sup>a</sup>	INT	6618–6697	2400–6100
‘H-alpha-100’	LT:RATCam	6517–6617	–2093–2478
‘Ha_6566’	LT:IO	6522–6610	–1865–2164
‘Ha_6634’	LT:IO	6608–6662	2080–4520
‘Ha_6705’	LT:IO	6680–6733	5349–7764
‘Ha_6755’	LT:IO	6729–6783	7595–10047
‘Ha_6822’	LT:IO	6798–6849	10747–13097
‘665/12’	MPI-2.2	6598–6713	1616–6857

<sup>a</sup> No scanned transmission profile is available for this filter so the limits are based on manufactured specification.

all host galaxy emission, whilst being narrow enough to allow for accurate subtraction of the underlying continuum light. Clearly, if a filter fails to transmit H $\alpha$  emission from some regions of the host, this will affect the NCR value of the transient. As such, transients that are potentially well separated from their hosts in recession velocity ( $V_{rec}$ ) provide a problem of filter choice, especially when  $V_{rec}$  cannot be determined for the transient itself. In the present study, for all cases except PTF 09dav, the filter with a central wavelength best matching the host-H $\alpha$  wavelength was chosen; for PTF 09dav, the redshift of the transient was used to find the best matched filter as its host is anonymous. Given the widths of the filters (typically  $\sim 2000\text{--}3000\text{ km s}^{-1}$ ), this meant H $\alpha$  over a broad range of host velocities would be detected, giving confidence that the observations are not missing some regions of H $\alpha$  emission in the host or, importantly, at the location of the transient.

Alongside H $\alpha$  NCR analysis, UV NCR values are obtained using *GALEX* archive imaging following the same method as detailed above. *GALEX* is a space-based UV telescope with imaging in two filters, the near- and far-ultraviolet (NUV;  $\lambda_{eff} = 2267\text{\AA}$ , FUV;  $\lambda_{eff} = 1516\text{\AA}$ ). The large field of view of (1.2 degrees diameter) makes it ideal for observing the large, nearby hosts of these transients. The data reduction specific to these observations and the results of this analysis are given in Section 3.8.

### 3.5 Transient samples and observations

Table 3.2: Properties of Ca-rich transients and their host galaxies.

SN name	Host galaxy	Host type	$V_{rec}$ (km s <sup>-1</sup> )	Discovery Abs. mag (unfiltered mag)	IAU classn.
2000ds	NGC 2768	E6	1373	-13.59	Ib/c
2001co	NGC 5559	SBb	5166	-15.69	Ib/c
2003H	NGC 2207	SABbc	2741	-14.16	Ib/c
2003dg	UGC 6934	Scd (edge-on)	5501	-15.31	Ib/c
2003dr	NGC 5714	Scd (edge-on)	2237	-15.06	Ib/c
2005E	NGC 1032	S0/a (edge-on)	2694	-15.86	Ib/c
2005cz	NGC 4589	E2	1980	-16.36	Ib
2007ke	NGC 1129	E	5194	-15.71	Ib
PTF 09dav	Anon	Sb <sup>a</sup>	11123	-14.7	-
2010et	Uncertain	-	-	-13.8	-
PTF 11bij	IC 3956	E	10406	-15.9 <sup>b</sup>	-
2012hn	NGC 2272	SAB0	2130	-16.0 <sup>c</sup>	I-p

<sup>a</sup> Classified by P.A. James based on the imaging presented here

<sup>b</sup>  $M_R$  at discovery taken from [Kasliwal et al. \(2012\)](#)

<sup>c</sup>  $M_R$  at peak taken from [Valenti et al. \(2014\)](#)

The samples of transients analysed here are inevitably somewhat eclectic and subject to selection biases, and thus cannot be considered in any sense to represent a statistically complete sample of objects of either type. This is unavoidable for classes of transient objects that are both relatively rare (although the global rates are highly uncertain) and substantially fainter than the main SN types. Thus, in order to compile the samples of Ca-rich and SN 2002cx-like transients presented here, a variety of sources were used. Most of the Ca-rich transients are listed in [Perets et al. \(2010\)](#) and [Kasliwal et al. \(2012\)](#), alongside SN 2012hn ([Valenti et al., 2014](#)). For a complete recent compilation of the SN 2002cx-like transients, see [Foley et al. \(2013\)](#).

It should be stressed here that although this is an investigation of two classes of transients, their unknown nature, and the lack of detailed observations for some, means that there is potential contamination in each sample by transients of different origin and the potential for diversity within the each sample. Discussion of progenitor constraints for each sample will be presented as a whole due the small numbers in each sample, however it may be true that some specific events differ from these conclusions due to their erroneous classification.

Table 3.3: Properties of SN 2002cx-like transients and their host galaxies.

SN name	Host galaxy	Host type	$V_{rec}$ (km s <sup>-1</sup> )	Discovery Abs. mag (unfiltered mag)	IAU classn.
1991bj	IC 344	SBcd <sup>a</sup>	5440	-15.46	Ia
2004gw	CGCG 283-003	Sab <sup>a</sup>	5102	-16.33	Ia
2005P	NGC 5468	SABcd	2842	-15.14	?
2005cc	NGC 5383	SBb pec	2270	-15.18	?
2005hk	UGC 272	SABd	3895	-17.05 <sup>b</sup>	Ia-p
2006hn	UGC 6154	SBa	5156	-18.69	Ia
2007J	UGC 1778	Sdm	5034	-15.92	Ia
2008A	NGC 634	Sa (edge-on)	4925	-16.57	Iap
2008ha	UGC 12682	Im	1393	-12.7 <sup>c</sup>	Ia?
2009J	IC 2160	SBc pec	4739	-16.17	Ia-p
2012Z	NGC 1309	SAbc	2136	-14.62	Ia-p

<sup>a</sup> Classified by P.A. James based on the imaging presented here

<sup>b</sup>  $M_R$  at discovery taken from Phillips et al. (2007)

<sup>c</sup> Puckett et al. (2008)

New imaging observations presented here were made using the Isaac Newton Telescope (INT) and Liverpool Telescope (LT) at La Palma and the MPI2.2 at ESO. For each transient, exposures were taken in the R band, to characterise the continuum light, and a narrowband H $\alpha$  filter. Details of the H $\alpha$  filters used are given in Table 3.1, where wavelength and corresponding  $V_{rec}$  limits are defined as the 50 per cent transmission limits of the filter. Exposure times were 300 seconds for R band and 900 seconds for H $\alpha$ , which corresponds to a limiting H $\alpha$  flux of  $\sim 3.8 \times 10^{-16}$  erg s<sup>-1</sup> cm<sup>-2</sup> (see Anderson et al. 2012 for a discussion of SF limits using this method). Images taken with the LT were reduced using the automated pipeline; standard bias and overscan subtraction and flat fielding was performed for other data. Typical seeing was 1–2 arcsec. Subtraction of the R band images from the H $\alpha$  images was performed using a version of SUBPIPE, an image subtraction pipeline that is detailed in Section 2.2 (note this earlier version used the ISIS code of Alard 2000, cf. HOTPANTS, which is used currently).

Data for the Ca-rich and SN 2002cx-like transients in the present study are given in Tables 3.2 and 3.3, respectively. These list the International Astronomical Union (IAU) supernova name for all transients except PTF 09dav and PTF 11bij, which are not on the IAU list; the host galaxy name, classification and recession velocity from the NASA Extragalac-

Table 3.4: Observations of the host galaxies of Ca-rich transients.

SN name	Host galaxy	$V_{rec}$ ( $\text{km s}^{-1}$ )	Telescope	Obs. date	Seeing (arcsec)	Filter name	$\text{H}\alpha$ range ( $\text{km s}^{-1}$ )	NCR index	SF detected in host?
2000ds	NGC 2768	1373	INT	Jan 2012	1.6	‘Halpha’	−1865–2357	0.000	No
2001co	NGC 5559	5166	INT	Mar 2007	1.6	‘Ha 6657’	2400–6100	0.357	Yes
2003H	NGC 2207	2741	LT:IO	Sep 2012	1.8	‘Ha_6634’	2080–4520	0.312	Yes
2003dg	UGC 6934	5501	INT	Jan 2012	1.3	‘Ha 6657’	2400–6100	0.626	Yes
2003dr	NGC 5714	2237	INT	Jan 2012	1.6	‘Halpha’	−1865–2357	0.000	Yes
2005E	NGC 1032	2694	LT:IO	Jan 2013	1.3	‘Ha_6634’	2080–4520	0.000	No
2005cz	NGC 4589	1980	INT	Jan 2012	1.2	‘Halpha’	−1865–2357	0.000	No
2007ke	NGC 1129	5194	INT	Jan 2012	1.7	‘Ha 6657’	2400–6100	0.000	No
PTF 09dav	Anon	11123	LT:IO	Dec 2012	1.6	‘Ha_6822’	10747–13097	0.000	Yes
2010et	Uncertain	–	LT:IO	Mar 2013	2.9	‘Ha_6705’	4900–7640	0.000	–
PTF 11bij	IC 3956	10406	LT:IO	Jan 2013	3.0	‘Ha_6822’	10747–13097	0.000	No
2012hn	NGC 2272	2130	LT:IO	Feb 2013	2.4	‘Ha_6566’	−1865–2164	0.000	No

Table 3.5: Observations of the host galaxies of SN 2002cx-like transients.

SN name	Host galaxy	$V_{rec}$ ( $\text{km s}^{-1}$ )	Telescope	Obs. date	Seeing (arcsec)	Filter name	$H\alpha$ range ( $\text{km s}^{-1}$ )	NCR index	SF detected in host?
1991bj	IC 344	5440	INT	Jan 2012	1.9	‘Ha 6657’	2400–6100	0.163	Yes
2004gw	CGCG 283-003	5102	INT	Jan 2012	1.7	‘Ha 6657’	2400–6100	0.000	Yes
2005P	NGC 5468	2842	INT	Feb 2008	1.4	‘Ha 6657’	2400–6100	0.055	Yes
2005cc	NGC 5383	2270	LT:RATCam	Dec 2005	1.8	‘H-alpha-100’	–2093–2478	0.621	Yes
2005hk	UGC 272	3895	LT:IO	Oct 2012	1.1	‘Ha 6634’	2080–4520	0.000	Yes
2006hn	UGC 6154	5156	INT	Jan 2012	1.3	‘Ha 6657’	2400–6100	0.289	Yes
2007J	UGC 1778	5034	INT	Jan 2012	1.1	‘Ha 6657’	2400–6100	0.904	Yes
2008A	NGC 634	4925	INT	Jan 2012	0.9	‘Ha 6657’	2400–6100	0.000	Yes
2008ha	UGC 12682	1393	LT:IO	Oct 2012	1.9	‘Ha 6566’	–1865–2164	0.407	Yes
2009J	IC 2160	4739	MPI2.2	Feb 2010	1.9	‘665/12’	1616–6857	0.000	Yes
2012Z	NGC 1309	2136	LT:RATCam	Aug 2009	1.5	‘H-alpha-100’	–2093–2478	0.000	Yes

tic Database (NED)<sup>2</sup>, the absolute discovery magnitude (taken from the Asiago Supernova Catalog<sup>3</sup>, using distance modulus values for the host taken from NED); and the classification of the supernovae from the IAU database.

Details of the observations and NCR values are given in Tables 3.4 and 3.5 for the Ca-rich and SN 2002cx-like transients respectively. Velocity limits from Table 3.1 are shown for the H $\alpha$  filter used — the bulk of the detected light in the continuum-subtracted images will come from emission within these velocity limits (although the filters also have non-negligible transmission for a few hundred km s<sup>-1</sup> outside these limits). Whether any recent SF (i.e. H $\alpha$  emission) is detected in the host in the observations is also noted.

Images of the of the twelve Ca-rich hosts are shown in Fig. 3.3, showing the R band and continuum-subtracted H $\alpha$  exposures with the location of the transient marked. Of these, six (NGC 2768, NGC 1032, NGC 4589, NGC 1129, IC 3956 and NGC 2272) are early-type galaxies, and hence should have no recent SF. Indeed, no SF as traced by H $\alpha$  is found at the location of the transients in these early hosts or anywhere else in the hosts. The only apparent emission in the subtracted images arises from the very centre of these galaxies; due to the difficulties in obtaining a clean subtraction on such extremely bright regions, this is most likely to be artefacts arising from the image subtraction process and saturation effects rather than real H $\alpha$  flux, although neither can be ruled out conclusively. It is not clear which galaxy hosted the very isolated transient SN 2010et, as discussed below. The remaining five hosts all display varying levels of SF.

Fig. 3.5 shows the corresponding images for the SN 2002cx-like sample. All these hosts are late type, and all display strong ongoing SF with prominent HII regions.

Further discussion of the hosts of the two samples is given in Section 3.7.1.

As a check on the presence and nature of emission lines at the locations of these events, long-slit optical spectroscopy was obtained (with a slit width of 1.5'') of two of the host galaxies in the samples (Fig. 3.7). The observations were taken on the INT in January 2013 using the IDS spectrograph with the R632V grating. The slit was positioned to include both

<sup>2</sup><http://ned.ipac.caltech.edu/>

<sup>3</sup><http://heasarc.gsfc.nasa.gov/W3Browse/all/asiagosn.html>

the galaxy nucleus, as a positional reference, and the location of the transient. The spectral range covered included the location of any potential  $H\alpha$  emission. NGC 2768 (SN 2000ds) was observed at an airmass of 1.3 in seeing of  $1.8''$ , the corresponding values for NGC 2207 (SN 2003H) were 1.57 and  $0.8''$ .

## 3.6 Individual properties of the transients and their environments

### 3.6.1 Ca-rich transients

**SN 2000ds in NGC 2768.** NGC 2768 is classified as an E6 galaxy in NED, and in the Third Reference Catalog (de Vaucouleurs et al., 1991). This classification is discussed by Hakobyan et al. (2008), who ultimately prefer a classification of S0. As expected, no  $H\alpha$  is found in the observations (apart from the region affected by subtraction artefacts at the very centre) indicating a lack of recent SF at the transient location, or indeed anywhere within this host galaxy. The INT+IDS long-slit spectrum crossing the nucleus of NGC 2768 and the location of SN 2000ds is shown in Fig. 3.7, confirming the lack of any line emission close to the location of the SN. There is weak, diffuse line emission in  $H\alpha$  and [NII] in the central regions of the galaxy, far from the SN location, that is probably related to the known LINER nucleus of this galaxy.

**SN 2001co in NGC 5559.** An inclined spiral galaxy, NGC 5559 displays prominent SF throughout the disc. SN 2001co is located near the edge of the disc and is coincident with some diffuse SF.

**SN 2003H in NGC 2207.** NGC 2207 is a close interaction with Sc galaxy IC 2163 at  $2765 \text{ km s}^{-1}$ ; SN 2003H lies immediately between the bulges of the two galaxies on an area of intermediate-level  $H\alpha$ . For the purposes of the NCR analysis, the pixels used included those from both galaxies since they cannot be cleanly distinguished as separate systems. As such, SN 2003H's NCR value is relative to the interacting system as a whole. A long-slit spectrum crossing the nucleus of NGC 2207 and the location of SN 2003H is shown in Fig. 3.7, showing that there is clearly detectable SF at the location of SN 2003H, although it appears to lie in the outer regions of a SF complex. The interacting system of NGC 2207 and IC 2163 has also hosted SNe 1975A (Ia), 1999ec (Ib) and 2010jp (IIn).

**SN 2003dg in UGC 6934.** The host displays strong HII regions along its highly inclined disc. SN 2003dg appears to be somewhere in the plane of the disc, but due to line of sight

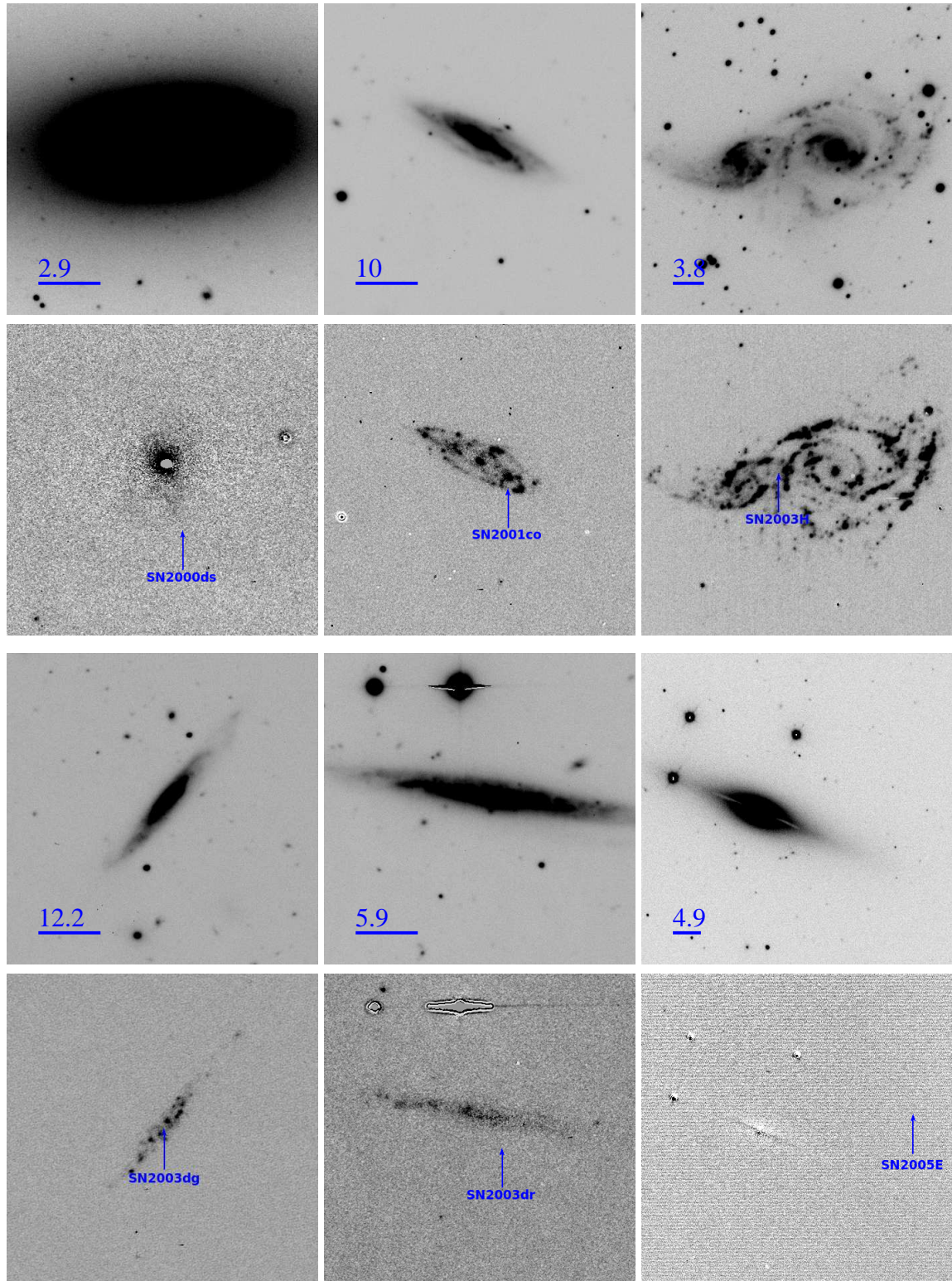


Figure 3.3: R band (top) and continuum-subtracted  $H\alpha$  (bottom) images of Ca-rich transients. The location of the transient is marked in each case on the continuum-subtracted  $H\alpha$  image. The bars in each R band image indicate 30 arcsec and are labelled with the linear size at the distance of the host in kpc. For all images North is up, East is left.

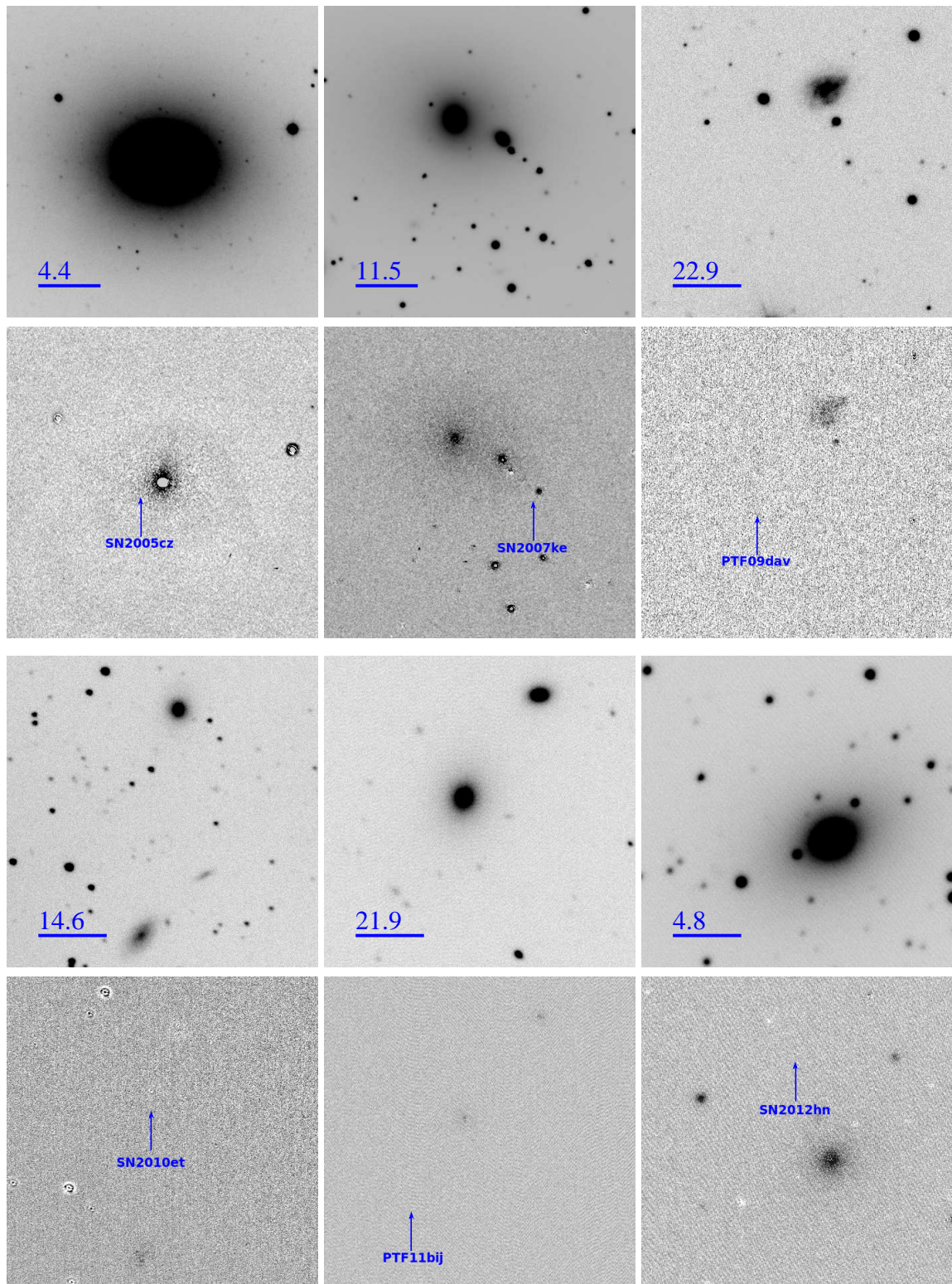


Figure 3.4: Same as Fig. 3.3, for the rest of the Ca-rich sample.

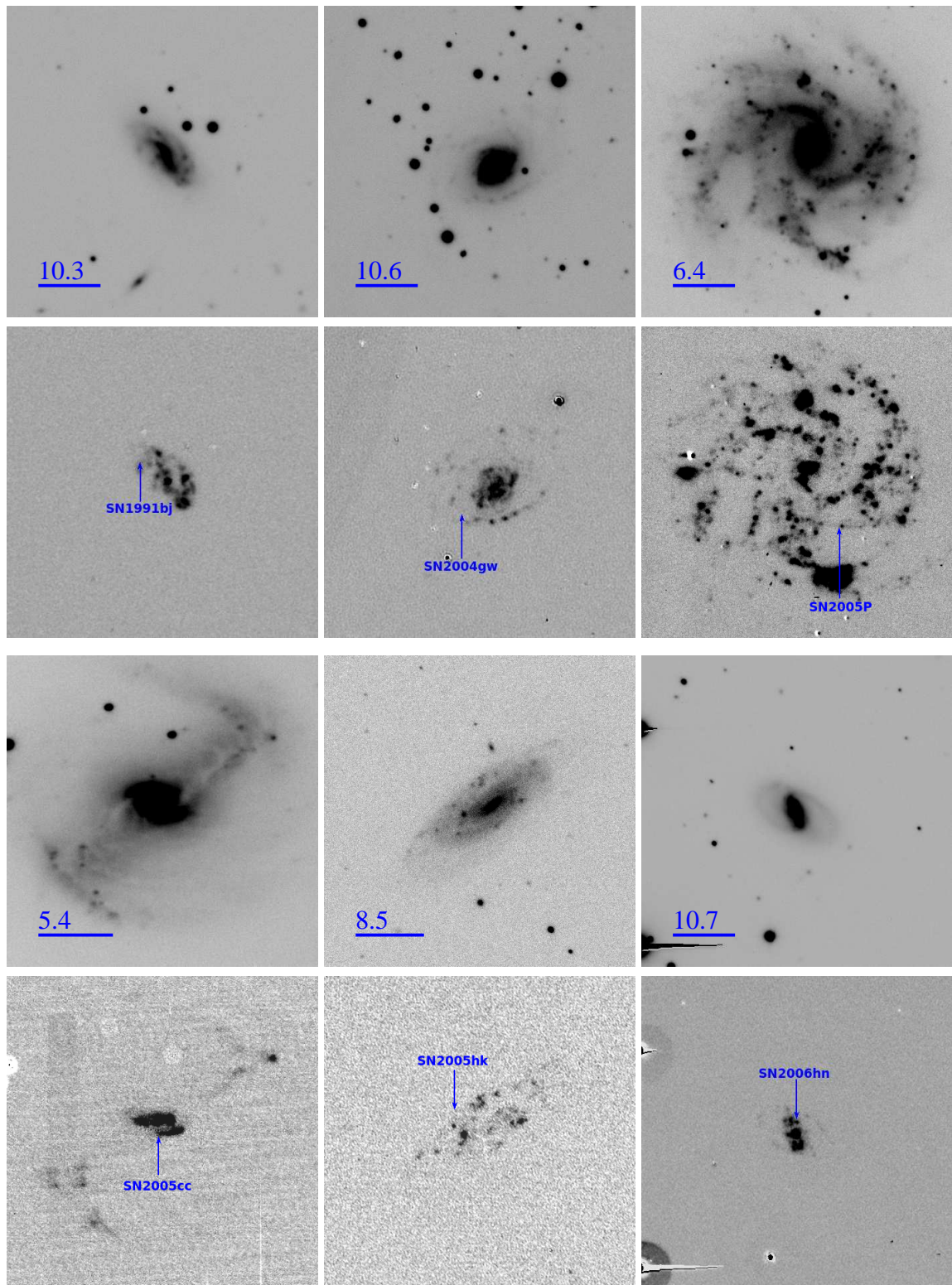


Figure 3.5: Same as Fig. 3.3 but for the SN 2002cx-like transients.

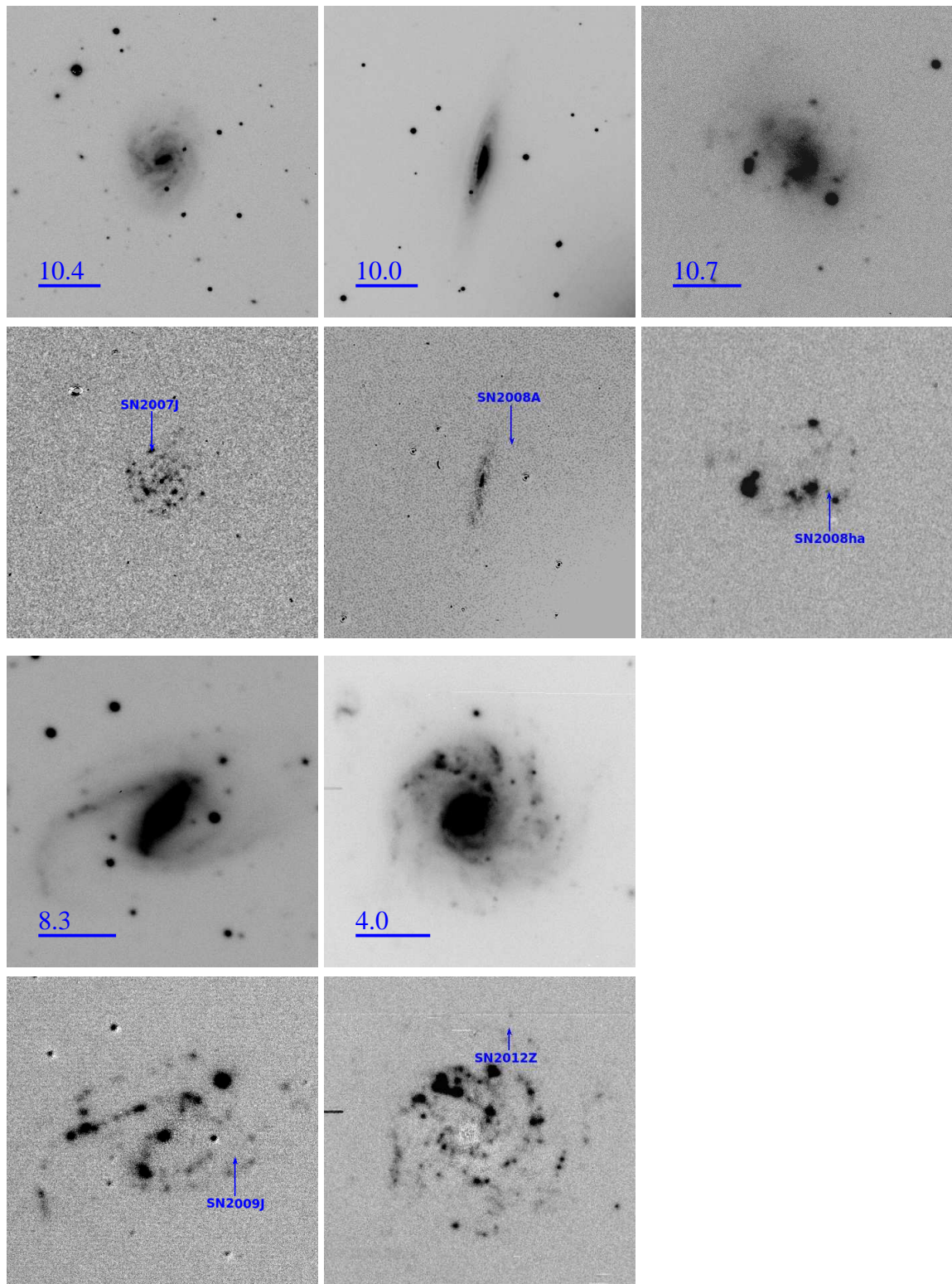


Figure 3.6: As for Fig. 3.3, for the rest of the SN2002cx-like sample.

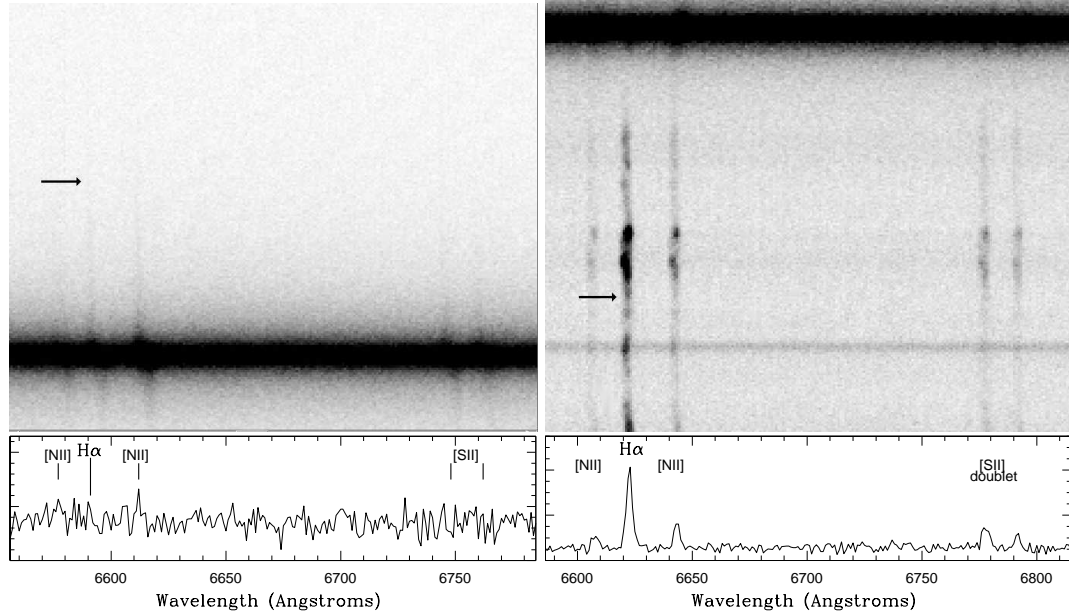


Figure 3.7: Spectra showing the  $H\alpha$  region of the long slit spectra of SN 2000ds in NGC 2768 (left) and SN 2003H in NGC 2207 (right). The arrows indicate positions corresponding to  $H\alpha$  emission from the location where each transient occurred. A 1D spectrum is extracted for each at the position of the transient and shown below in relative flux. SN 2000ds and SN 2003H are located 33.4 arcsec and 51.4 arcsec away from their respective hosts' nuclei.

effects it cannot be determined where in the disc it lies. This means the NCR value may not be accurate (see Section 3.7.2). From the projected view, SN 2003dg is coincident with some fairly bright  $H\alpha$  emission.

**SN 2003dr in NGC 5714.** SN 2003dr occurred in another galaxy that is viewed almost exactly edge-on, but in this case the transient location lies well outside the plane of the disc. Thus it is safer to say it is indeed in a region of no recent SF. The only apparent SF in NGC 5714 is diffuse and concentrated along the plane.

**SN 2005E in NGC 1032.** NGC 1032 is an S0/a galaxy, and no  $H\alpha$  is found along the plane of the disc lending weight to the argument this is a lenticular galaxy. The host is edge-on and the transient well separated from the disc plane with no  $H\alpha$  evident at its location.

**SN 2005cz in NGC 4589.** NGC 4589 is classified as an E2 elliptical galaxy in NED, and in the Third Reference Catalog (de Vaucouleurs et al., 1991). Moellenhoff and Bender (1989) find unusual central kinematics, and a minor axis dust lane, which they interpret as the re-

sult of merging activity. However, they conclude from the regular shape, and a smooth light profile that follows the classic  $R^{\frac{1}{4}}$  profile characteristic of elliptical galaxies (de Vaucouleurs, 1948), that ‘the merging already is in an advanced state’. As with NGC 2768, in the very bright central region a saturated core is observed, with associated subtraction residuals, which accounts for the apparent  $H\alpha$  emission seen in the continuum-subtracted image. No other detected SF is seen from the host, as is expected if its E2 morphology is accepted. The transient is located fairly close to the centre of the galaxy, although it is still outside the region of subtraction residuals.

**SN 2007ke in NGC 1129.** The central excess in the continuum-subtracted frame may again be due to saturation effects, although it is less clear in this case. However, SN 2007ke is very distant from the centre of this halo on a location of no detected  $H\alpha$ . (Note that the bright spot nearest SN 2007ke in the subtracted frame is a foreground star residual and was masked prior to NCR analysis.) Although NGC 1129 is the proposed host, clearly seen between this galaxy and the transient is another galaxy, MCG+07-07-003, at  $V_{rec} = 4967 \text{ km s}^{-1}$ . Due to the similarity of the velocities of the two galaxies, the chosen narrowband filter would have detected any  $H\alpha$  from both these galaxies, so there is confidence that the observations are not missing potential SF from MCG+07-07-003 (the location of MCG+07-07-003 was included in the NCR analysis since it lies between the putative host and the transient). MCG+07-07-003 appears to be an elliptical galaxy, possibly of the compact cE type, and so it is immaterial whether this galaxy or NGC 1129 is adopted as the host for the discussion of the statistics of host types in Section 3.7.2.

**PTF 09dav.** The most distant transient in the sample, this could prove a problem for the NCR method when trying to compare consistently with the other, much nearer examples where the resolving distance at the host will be much smaller. However the extreme separation of the transient from the host negates this problem and no  $H\alpha$  is detected anywhere near the transient, though there is clear SF in the disc of the putative host galaxy  $\sim 40 \text{ kpc}$  away. Kasliwal et al. (2012) present a limiting magnitude of  $M_R \sim -10$  for any underlying dwarf host at the location of the transient.

**SN 2010et.** SN 2010et = PTF 10iuv was discovered by PTF in a very isolated location, with no obvious host galaxy. The images, shown in Fig. 3.4, contain three galaxies which prob-

ably constitute a small galaxy group, since they have similar recession velocities. These are  $6997 \text{ km s}^{-1}$  for the elliptical galaxy toward the right-hand edge of the images,  $7132 \text{ km s}^{-1}$  for the faint edge-on spiral galaxy, and  $7407 \text{ km s}^{-1}$  for the brighter spiral toward the left-hand edge of the images. The brighter spiral is the only galaxy in the frame to show evidence for  $\text{H}\alpha$  emission, and hence for ongoing SF, but this galaxy is very remote from the location of SN 2010et. The elliptical galaxy is marginally the most likely host, given its luminosity and somewhat lower (but still substantial) projected distance. However, it would be very misleading to claim any strong preference for a host galaxy in this case, and so SN 2010et is omitted from the analysis of host galaxy types presented later in this chapter. The NCR index for the location of SN 2010et is unsurprisingly 0.000, i.e. consistent with an empty ‘sky’ location. The limiting magnitude for an underlying dwarf galaxy is estimated as  $M_R \sim -12$  by Kasliwal et al. (2012).

**PTF 11bij in IC 3956.** Another relatively distant example, the transient is located 33 kpc from IC 3956, an elliptical galaxy that displays no definite  $\text{H}\alpha$  emission in the continuum-subtracted image. The recession velocity, unfortunately for this study, lies in the overlap region of the transmission curves of two  $\text{H}\alpha$  filters, where both have transmissions of about half of their peak values. The filter with the slightly better transmission at the  $V_{rec}$  of IC 3956 was chosen, however a strong caveat must be attached to the analysis of this transient as there is a possibility that the observations miss potential  $\text{H}\alpha$  emission. Regardless of this problem, the remote location around an early type galaxy would indicate an unlikely place for significant SF and hence  $\text{H}\alpha$  emission. Kasliwal et al. (2012) present a limiting magnitude of  $M_R \sim -12.5$  for any underlying dwarf host.

**SN 2012hn in NGC 2272.** The host galaxy is an early type (SAB0 in NED, E/S0 in HyperLeda<sup>4</sup>) with no detected SF in the imaging shown here, although it should be noted that the recession velocity of the host galaxy would put any  $\text{H}\alpha$  emission only just within the half-peak transmission limit of the filter used. The transient location lies well away from the nucleus, and no emission is seen close to its location in either the broad or narrow-band imaging.

---

<sup>4</sup><http://leda.univ-lyon1.fr/>

### 3.6.2 SN 2002cx-like transients

**SN 1991bj in IC 344.** IC 344 is a spiral galaxy showing clumpy SF in strong HII regions. SN 1991bj lies on a region of weak H $\alpha$  emission within the disc.

**SN 2004gw in CGCG 283-003.** Weak SF is displayed throughout the disc, apart from the southerly arm, which displays several bright areas of H $\alpha$  emission. The bulk of the SF is centrally located. The transient location is close to regions of very diffuse H $\alpha$  emission, but is not coincident with any.

**SN 2005P in NGC 5468.** Clumpy H $\alpha$  structure with some regions of extremely intense SF are seen in this face-on spiral. SN 2005P is located on the edge of a fairly bright HII region, although the low NCR value of 0.055 is warranted by the other, intensely bright regions in the host. NGC 5468 also hosted SN 1999cp (Ia), SN 2002cr (Ia) and SN 2002ed (IIP).

**SN 2005cc in NGC 5383.** A strongly barred galaxy, NGC 5383 displays strong H $\alpha$  emission in the centre of the bar including an intense star burst region. Lower-level, diffuse emission occurs near the ends of the bar and the base of the spiral arms. SN 2005cc is located on a bright region on the southern edge of the bulge.

**SN 2005hk in UGC 272.** The transient is located towards the outer edge of the host's disc, which displays several regions of strong H $\alpha$  emission. SN 2005hk is located close to some very faint emission but is coincident with an area devoid of any detected flux and thus has  $NCR = 0$ .

**SN 2006hn in UGC 6154.** Star formation is concentrated around the bar region in this spiral with little elsewhere in the disc. The transient is located on the cusp of a moderately bright HII region.

**SN 2007J in UGC 1778.** Star formation is clumpy, spread evenly across nearly all of the disc. SN 2007J lies towards the outer edge of the disc coincident with one of the brightest HII regions.

**SN 2008A in NGC 634.** NGC 634 is a highly inclined spiral galaxy that shows reasonably strong H $\alpha$  emission in the central region with weaker emission coming from the disc plane.

Line-of-sight effects mean the NCR can potentially be erroneously high, but for SN 2008A,  $NCR = 0$ , meaning it is likely to indeed be in a region of no SF. NGC 634 also hosted SN 2006Q (type given in the IAU list as ‘II?’).

**SN 2008ha in UGC 12682.** An irregular galaxy, UGC 12682 displays several regions of strong SF. SN 2008ha is located directly on top of a region of moderate  $H\alpha$  emission.

**SN 2009J in IC 2160.** A strongly barred spiral showing some clumpy SF. The transient, SN 2009J is near very low level SF but coincident with a region of no detected  $H\alpha$  emission. IC 2160 also hosted SN 2009iw (Ia).

**SN 2012Z in NGC 1309.** Intense regions of  $H\alpha$  emission are observed in the arms of the face-on spiral galaxy NGC 1309. The transient is located far out in the disc of the host, on a region devoid of  $H\alpha$  emission.

## 3.7 Strength of association of transients with ongoing SF

### 3.7.1 Host galaxy classifications

The first indications of the association of these transients with ongoing SF come from the Hubble types of the host galaxies. For the Ca-rich transients, the most important observation is that six of the eleven which have host types arise from early type galaxies (four ellipticals and two lenticulars) which, as expected, are shown by the observations to have no detectable SF as revealed by  $H\alpha$  emission. The other five Ca-rich transient hosts are all nominally spiral galaxies; these are bright, star-forming galaxies with types in the range Sb–Scd, which are the types that dominate the overall SF rate in the local Universe (James et al., 2008). One of these five is PTF 09dav, which lies at a projected distance of 40.6 kpc from a bright, disturbed star-forming galaxy that was identified as the probable host by Sullivan et al. (2011), and which has been classified as being of type Sb from the imaging presented here. However, the identification of this galaxy as the host is far from certain, given the very substantial projected offset.

The host galaxies of the eleven SN 2002cx-like transients are all clearly of star-forming types, ten being spiral galaxies and one a Magellanic-type irregular. Two are classified as Sa, one as Sab, one as Sb, one as Sbc, one as Sc, two as Scd, one as Sd, one as Sdm and one as Im.

These distributions of host galaxy types can be compared with the expectations for the typical host environments of low- and high-mass stars, picked at random from across the ensemble of all galaxy types, with the important caveat that both sets of transients are likely to be subject to substantial selection biases. For low-mass stars, a reasonable comparison is with the distribution of total stellar mass across the population of galaxies in the local Universe, which has been estimated by [Driver et al. \(2007a,b\)](#). [Driver et al. \(2007a\)](#) gives the following fractions of stellar mass in different galaxy components: discs  $58\pm 6$  per cent; elliptical galaxies  $13\pm 4$  per cent; bulges  $26\pm 4$  per cent; 3 per cent other. While the significance is far from compelling, this indicates that the Ca-rich transients are if anything more strongly weighted towards elliptical galaxies than would be expected if they accurately traced the low-mass stellar population. The expectation might be for one to lie in an elliptical host, whereas four are actually found. For the SN 2002cx-like transients, the reverse is true; none of the hosts is an elliptical galaxy. From an inspection of [Fig. 3.5](#), all occurred within the star-forming disc components of their host galaxies, with the debatable exception of SN 2008A, which would be a surprising finding if they follow the distribution of old stellar mass.

To determine the expectations for high-mass stars picked at random from local galaxies, estimates of the contributions made by galaxies of different types to the SF density of the local Universe are used, presented in [James et al. \(2008\)](#). This comparison is made in [Fig. 3.8](#), where the filled circles in both frames represent the contributions made to the local SF rate density by galaxies of the different types. Thus, Sc galaxies (T-type=5) make the largest single contribution, and host about 25 per cent of the current SF in the local Universe. The differences between the distribution of Ca-rich host types and those contributing to the SF rate density are striking. The lower frame of [Fig. 3.8](#), where all the quantities are plotted as cumulative, normalized distributions, confirms this discrepancy for the Ca-rich transients (solid line), which show a large excess of early-type hosts. However, this cumulative distribution comparison shows that the SN 2002cx-like transients (dashed line) much more closely

match the expectations for a population that traces SF and hence high-mass progenitors.

The numbers of transients involved in this study are small, and the sample is potentially subject to significant selection effects. Noting these important caveats, it is still interesting to test the statistical significance of the difference between the distributions shown in Fig. 3.8. A one-sample Kolmogorov–Smirnov (KS) test gives a critical  $D$  value of 0.468 for a sample of eleven objects and a probability  $P$  of 0.01; the observed maximum  $D$  between the Ca-rich hosts and the SF density distribution summed over types is larger than the critical value, at 0.523. Thus the Ca-rich hosts are significantly different from the expectations for a population that traces cosmic SF. A two-sample KS test shows that Ca-rich and SN 2002cx-like host galaxies differ significantly, with a maximum  $D$  value of 0.55 and a probability of only 0.047 that the two sets of host galaxies could be drawn from the same parent distribution.

It is useful, in the interests of increasing sample size, to look at the host types of other SN 2002cx-like events, even those for which no suitable  $H\alpha$  imaging exists. Some events prohibit a confident host classification to be made due to the distance to and/or a lack of high resolution imaging of the host. Additional transients included are SN 2002bp (UGC 6332, SBa), SN 2003gq (NGC 7407, Sbc), SN 2004cs (UGC 11001, Sdm), SN 2008ge (NGC 1527, SAB0), SN 2010ae (ESO 162-17, Sb), SN 2010el (NGC 1566, SABbc), SN 2011ay (NGC 2315, S0/a) and SN 2011ce (NGC 6708 Sb); see [Foley et al. \(2013\)](#) for a discussion of each event. As can be seen in Fig. 3.8, this enlarged sample of 19 transients broadly follows the host distribution of the  $H\alpha$ -imaged SN 2002cx-like sample, as expected, although one transient has an early-type host classification — SN 2008ge in NGC 1527. This may argue against a young age for the progenitor; indeed, [Foley et al. \(2010b\)](#) find an absence of evidence for recent SF at the transient’s location and conclude that the progenitor is likely to be a WD, however see Section 3.8. SN 2008ge is further discussed in Section 3.9

### 3.7.2 Transient locations and ongoing SF

To further quantify the apparent association of the two transient populations with current sites of SF, the NCR statistic is used, applied to a pixel-by-pixel analysis of the continuum-subtracted  $H\alpha$  images, which was introduced in Section 3.4.

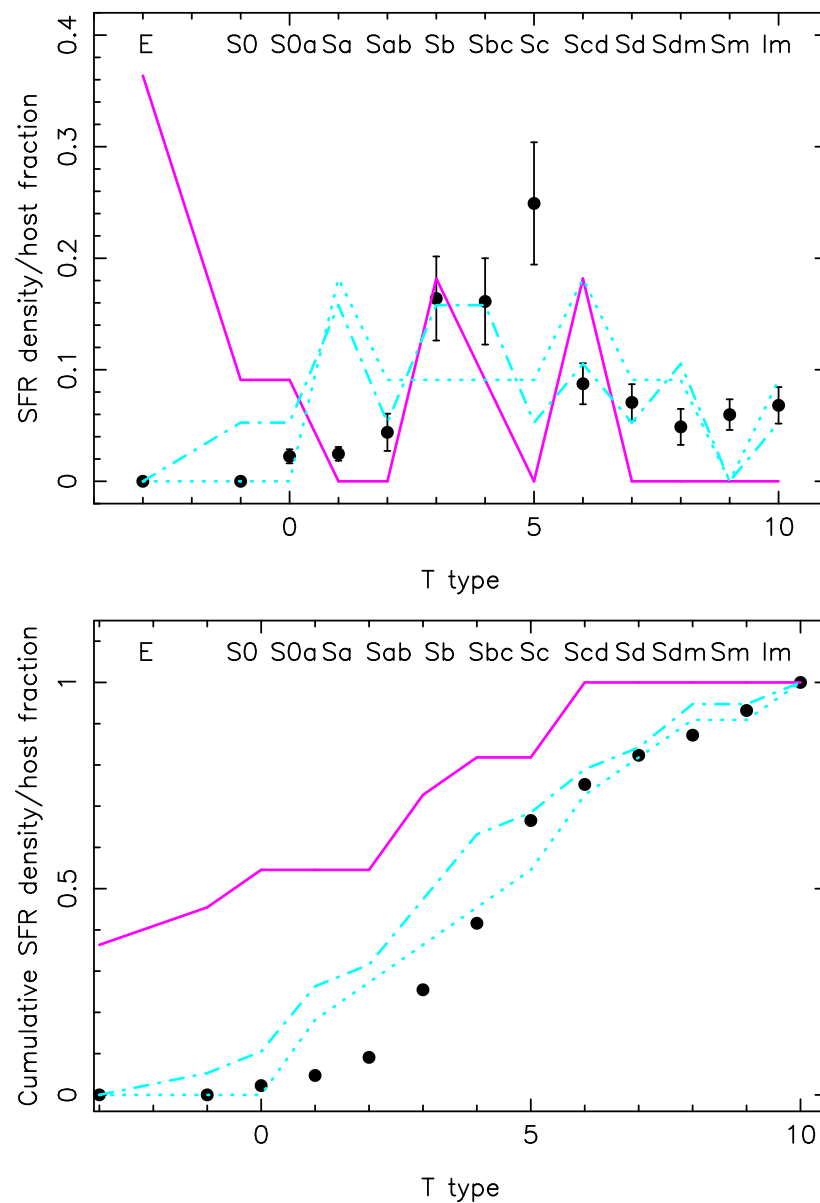


Figure 3.8: The SF density of the local Universe as a function of galaxy T-type (solid circles), compared with the distribution of types of the host galaxies of Ca-rich (solid lines) and SN 2002cx-like (dotted lines) transients. Also shown are the host types of the full sample SN 2002cx-like events for which a good host classification can be made (see text; dot-dashed lines). Both frames show the same data, but quantities plotted in the lower frame are cumulative values along the sequence from early- to late-type galaxies.

For the five Ca-rich transients in galaxies with detectable SF, the mean NCR value is 0.259 (standard error on mean 0.119), range 0.000-0.626. Including the seven for which the H $\alpha$  imaging reveals no SF anywhere in the galaxy (including SN 2010et which has no obvious host), and which all thus have NCR values of 0.000, this value falls to 0.108 (0.060).

The Ca-rich transient with the strongest apparent association with an HII region is SN 2003dg. This occurred in the disc plane of UGC 6934, an edge-on Scd spiral galaxy. This galaxy orientation makes the interpretation of the NCR index highly ambiguous, with a greatly increased probability of line-of-sight projection effects resulting in spurious apparent correlations, and large, poorly-constrained extinction effects. Thus, edge-on galaxies were excluded from the NCR analysis in previous papers ([James and Anderson, 2006](#); [Anderson and James, 2008](#); [Anderson et al., 2012](#)), with a limiting criterion of a major- to minor-axis ratio of 4.0. For UGC 6934, this ratio is 7.7, so it would have been excluded from earlier studies. Removing SN 2003dg from the sample, the mean NCR value falls to 0.061 (0.041).

Two more of the Ca-rich transients, SN 2003dr and SN 2005E, occurred in disc galaxies that are very close to being exactly edge-on. In these cases, the transient occurred far from the disc plane, so the line-of-sight projection argument does not apply. However, for the sake of consistency the average NCR value is recalculated with all three edge-on hosts removed, giving an average for the remaining nine of 0.074 (0.049).

For the eleven SN 2002cx-like transients, the mean NCR value is 0.222 (0.092), range 0.000 - 0.904. Removing SN 2008A, which occurred in the edge-on Sa galaxy NGC 634, this mean is 0.244 (0.099).

Figure 3.9 shows the distributions of NCR values for the two samples presented here, and of other SN classes. The values for Ia, IIP, Ib and Ic types are taken from [Anderson et al. \(2012\)](#). The study of [Anderson et al. \(2012\)](#) was of only star-forming galaxies however, whereas this sample has six early type hosts in the Ca-rich transient class that display no detected SF. In order to compensate for this fact, the rate of SNe Ia going off in early type galaxies from LOSS ([Li et al., 2011b](#)),  $\sim 27$  per cent, is used. With no SF, any location in the host will have  $\text{NCR} = 0$ , so by adding 27 per cent to the SNe Ia sample as  $\text{NCR} = 0$  events, this will give an expected SNe Ia distribution across all galaxy types. The number of CCSNe that

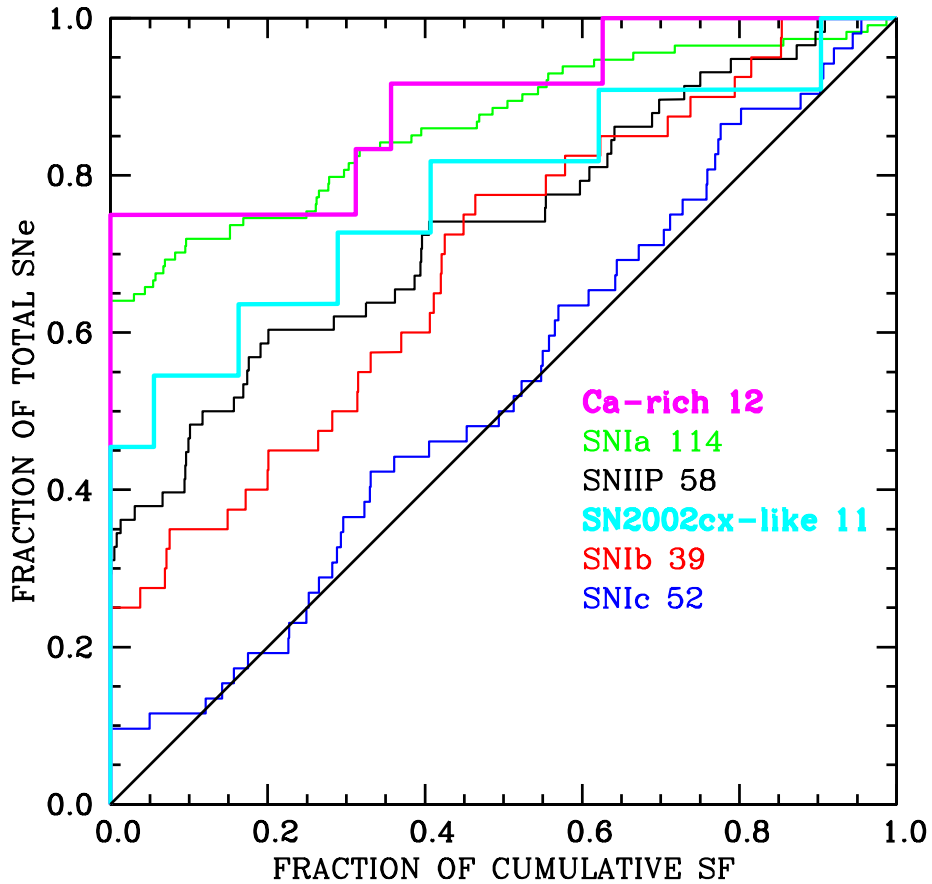


Figure 3.9: Cumulative distribution of the Ca-rich and SN 2002cx-like samples as compared to other SN types. Data for other SNe are based on [Anderson et al. \(2012\)](#), with a correction factor applied to the SN Ia sample to account for the fact that only star-forming galaxies were included in that study (see text).

have been observed in non-star-forming early type hosts is  $\sim 0$ , and as a result no correction was applied to the SN II, Ib or Ic distributions.

The KS test was applied to the distributions of NCR values shown in Fig. 3.9. These confirm the extreme nature of the environments of the Ca-rich transients; even with a small sample (12 objects), the test conclusively shows that the values are not consistent with a distribution that perfectly traces the SF activity in the host galaxies (the black diagonal line in Fig. 3.9), with a probability of these distributions being consistent of  $< 0.1$  per cent. More importantly, the Ca-rich transient NCR values are inconsistent with the distributions for SNe of Type II (including all subtypes and unclassified Type II; see [Anderson et al., 2012](#)) and Ib, with probabilities less than 2.5 per cent of being drawn from the distributions of either type; the

Table 3.6: Mean  $H\alpha$  NCR values for the locations of different SN types.

SN Type	No.	Mean	Std. err.
Ca-rich	9	0.074 <sup>a</sup>	0.049
Ca-rich	12	0.108	0.060
Ia	98	0.114 <sup>b</sup>	0.019
SN 2002cx-like	11	0.222	0.092
SN 2002cx-like	10	0.244 <sup>c</sup>	0.099
IIP	58	0.264	0.039
Ib	39	0.318	0.045
Ic	52	0.469	0.040

<sup>a</sup> All edge-on hosts excluded

<sup>b</sup> Corrected for an assumed early-type fraction of 27 per cent; mean in star-forming hosts is 0.157

<sup>c</sup> Edge-on host excluded

consistency with the SNe IIP sample shown in Fig. 3.9 is  $\sim 5$  per cent. Notwithstanding the small sample size, a clear distinction exists between Ca-rich transients and SNe II/Ib.

The Ca-rich transient distribution is completely consistent with that of SNe Ia, and by eye the two distributions overlay very closely, given the constraints of small number statistics. For the SN 2002cx-like transients, the situation is less clear; formally the NCR values of these eleven transients could have been drawn from any of the other distributions shown in Fig. 3.9. However, the distribution most closely approximates that of SNe IIP, and indeed, again considering the small number statistics, reproduces it well. The distribution of SN 2002cx-like transients shows a stronger association to SF than that of SNe Ia, with the mean NCR being larger even in the case of considering only star-forming hosts of SNe Ia (see Table 3.6).

### 3.8 GALEX NCR analysis

Investigations thus far have concentrated on the use of  $H\alpha$  imaging to build NCR distributions as there exist comparative samples of these distributions for ‘normal’ SN types. However, the duration of appreciable  $H\alpha$  emission post SF, although ideal to probe the lifetimes of very massive stars, is not conducive to investigating the longer time-scales these transients appear to exhibit. For this reason the excellent coverage of the ultraviolet (UV) sky afforded

by the *GALEX* observatory is exploited. The FUV and NUV bands act as tracers of SF on longer time-scales, up to  $\sim 100$  Myr for the NUV, with FUV being a slightly longer time-scale than  $H\alpha$  (Stewart et al., 2000; Gogarten et al., 2009). The same method as described in Section 3.4 is employed but here using the *GALEX* UV imaging instead of continuum-subtracted  $H\alpha$  imaging. The *GALEX* archive<sup>5</sup> was queried on the locations of all Ca-rich in Table 3.2 and all SN2002cx-like events listed in Foley et al. (2013). 21 (20) out of 25 SN2002cx-like events have suitable NUV (FUV) imaging, with 8 of the Ca rich appearing in the archive. For each host the ‘Sky background image’ was subtracted from the ‘Intensity map’ to obtain a zero-mean background. The normal NCR method was then applied to this subtracted image.<sup>6</sup> The results of the NCR analysis are given in Tables 3.7 and 3.8, the cumulative distributions of NCR values are shown in Fig. 3.10.

Fig. 3.10 shows that SN2002cx-like transients appear to almost perfectly trace the NUV emission with only 10 per cent having  $NCR = 0$ . The FUV distribution, however, deviates significantly from tracing the underlying emission with 40 per cent occurring on regions of no FUV emission. This is not unexpected as the FUV probes a similar time-scale to  $H\alpha$ , but is a good sanity check for ruling out very short-lived progenitors. This allows constraints on the progenitor ages of  $< 100$  Myr, i.e. shorter-lived than the time-scales of NUV emission, with a probable age of a few tens of Myr, given that they outlive FUV emission and appear quantitatively similar to SNe IIP in terms of  $H\alpha$  association<sup>7</sup>. One interesting note is regarding SN 2008ge where, notwithstanding the SAB0 classification for its host, *GALEX* imaging reveals extended emission in both NUV and FUV. The NCR values are 0.917 and 0.000 for NUV and FUV, respectively. This would indicate there has been fairly recent SF in the host, and specifically SF at the location of SN 2008ge, potentially meaning this was a young system (cf. Foley et al., 2010b).

For the Ca-rich transients, the association to FUV is not beyond that which might be reasonably expected from random coincidence ( $> 60$  per cent have  $NCR = 0$ ), as expected from the

<sup>5</sup><http://galex.stsci.edu/GR6/?page=mastform>

<sup>6</sup>The pixel scale of *GALEX* is 1.5 arcsec, and the WCS solutions will be more robust than ground based imaging, we therefore do not apply a binning factor to the images prior to NCR analysis, as was done in the case of  $H\alpha$  imaging.

<sup>7</sup>The similarity between SN2002cx-like transients and SNe IIP is also strikingly evident when comparing Fig. 3.10 with figure 4 of Anderson et al. (2012).

Table 3.7: *GALEX* NCR values for Ca-rich transients.

SN name	NUV NCR	FUV NCR
2000ds	0.583	0.000
2001co	0.332	0.233
2003H	0.342	0.000
2003dg	0.782	0.431
2003dr	0.000	0.353
2005E	0.000	—
2005cz	0.674	0.000
2007ke	0.000	0.000
PTF09dav	0.000	0.000
2012hn	0.000	0.000

$H\alpha$  distribution in Fig. 3.9. We also see that even the longer time-scale of the NUV emission also does not encompass the progenitor lifetimes of these transients, with  $> 40$  per cent outliving the NUV emission. This gives confidence that these Ca-rich transients have indeed very old progenitors.

One potential issue with *GALEX* data is the relatively coarse spatial resolution at  $\sim 4\text{--}5$  arcseconds. This may result in an observed coincidence of the transients location with NUV/FUV that is, in reality, spatially distinct and could erroneously shift a distribution towards a closer association to the emission. Even with this effect, the Ca-rich display little if any association and this reinforces a long-lived progenitor nature for these transients. Some confidence that this effect is not completely distorting the distribution of the SN2002cx-like transients comes from the comparison of their  $H\alpha$  distribution (Fig. 3.9) with their FUV distribution (Fig. 3.10) – since these tracers probe similar time-scales of SF it is expected they would display similar distributions for each, as is seen. 6

### 3.9 Discussion

Though the total rate of Ca-rich and SN 2002cx-like transients might be significant compared to SNe Ia, the actual number of observed events is still small, mostly due to their low luminosity, which limits their detection at large distances. For this reason the sample sizes in this study are limited. Nevertheless, a clear picture emerges from these results, pointing

Table 3.8: *GALEX* NCR values for SN2002cx-like transients.

SN name	NUV NCR	FUV NCR
1999ax	0.481	0.000
2002cx	0.392	0.872
2003gq	0.453	0.000
2004cs	0.974	0.170
2004gw	0.000	0.000
2005P	0.304	0.248
2005cc	0.796	0.000
2005hk	0.125	0.154
2006hn	0.498	0.491
2007J	0.091	—
2007ie	0.781	0.618
2007qd	0.148	0.168
2008A	0.000	0.000
2008ae	0.376	0.000
2008ge	0.919	0.000
2008ha	0.373	0.037
2009ku	0.818	1.000
2010ae	0.849	0.814
2010el	0.500	0.452
2011ay	0.560	0.000
2012Z	0.132	0.214

to significant differences between the host environments of these two transient types, which, in turn, implies different types of progenitor systems. The clear distinction between the two classes is strengthened by the possible contamination from misclassified transients in each sample. Such contamination would serve to dilute any distinct behaviour between the two samples.

The first indications for such difference come from the host galaxy populations analysis. All SN 2002cx-like transients have host galaxies that display strong, recent SF activity. The progenitor systems are therefore likely associated with a young stellar population, quite similar to that of CCSNe. Conversely, six of the eleven Ca-rich hosts (disregarding SN 2010et, where the host is not certain) are early-type galaxies with no detected SF, and therefore point to an old stellar population lacking any young, massive stars.

The host galaxy distributions provide strong support to the suggestion of [Perets et al. \(2010\)](#) of an old progenitor system for Ca-rich transients. Their original analysis of a smaller sample

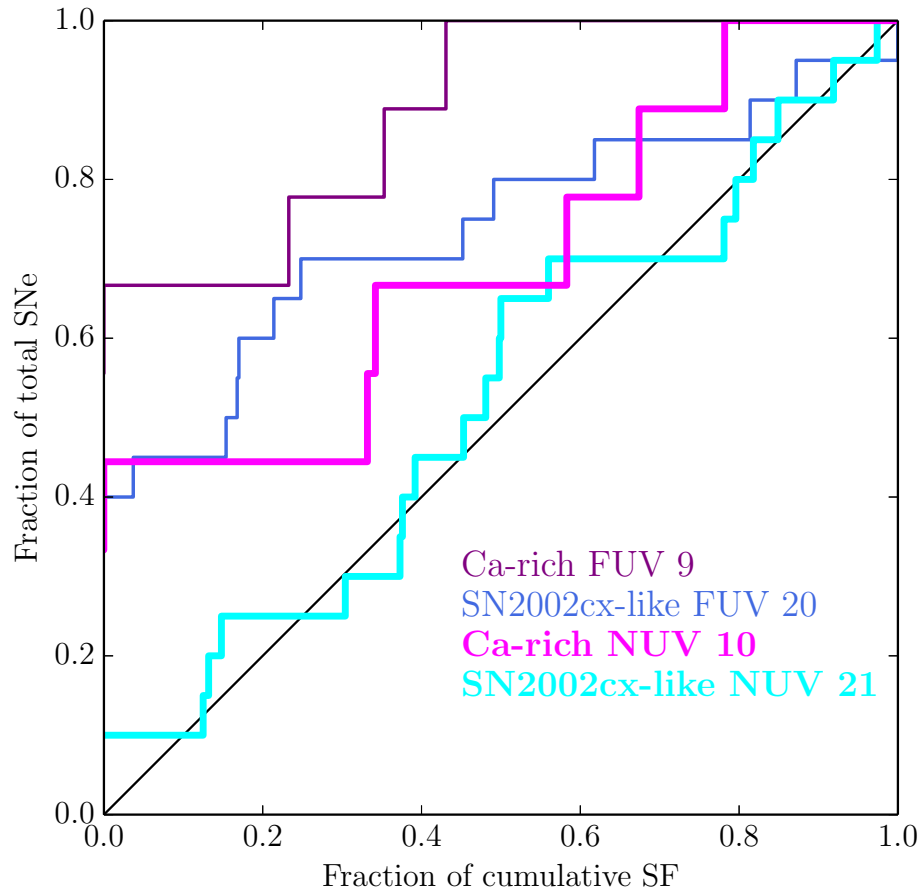


Figure 3.10: Cumulative distributions of NCR values for Ca-rich and SN2002cx-like transients from *GALEX* NUV and FUV imaging. The black line indicates a distribution that perfectly traces the SF.

of events, showed the host galaxy distribution of various SN types compared with the Ca-rich events. The distribution of Ca-rich transient hosts displays similarities with that of regular SNe Ia, a trend strengthened by the addition of similar events identified since then and presented here.

Furthermore, the NCR analysis allows the locations of the transients *within* their respective hosts to be investigated. More than simply saying the SN 2002cx-like transients are found in hosts that display ongoing SF, a quantitatively good match between SN 2002cx-like events and SNe IIP with respect to association with very recent SF ( $H\alpha$ ) in their host galaxy is found. Such a match would indicate a similar progenitor age for SN 2002cx-like transients and SNe IIP (i.e. a typical delay time of 30 – 50 Myrs). This suggestion is reinforced by the association of SN2002cx-like transients to NUV emission, and through their almost perfect

tracing of NUV emission it can be concluded that their lifetimes are  $< 100$  Myr. From the NCR analysis it is confirmed that Ca-rich transients do not appear to follow very recent SF in their hosts and closely resemble the distribution of ‘normal’ SNe Ia, whose progenitors are expected to have significant life times ( $\sim$  Gyrs). The longer time-scale of NUV emission is not traced by these transients either, lending support to the argument of very long lived progenitors.

The samples are, as mentioned previously, inherently eclectic and suffer many biases relative a volume-limited sample. Their fainter magnitudes compared to SNe in general would suggest that they will be difficult to detect on bright galaxy regions. Note, however, that SN 2003dg (Ca-rich) and SN 2005cc (SN 2002cx-like), both typical of the mean brightness of their sample, were discovered on the brightest central regions of their respective hosts. The preference for discovery in fainter host locations would strengthen the argument for SN 2002cx-like events’ association with SF, given it is plausible to miss some of these events if they are coincident with the brightest HII regions. The discovery magnitudes quoted in Tables 3.2 and 3.3 show there is no statistically significant difference between the distributions of brightnesses in the two samples, suggesting any bias from magnitude-limited searches will affect each sample similarly (although their faintness will possibly affect the comparison to ‘normal’ SN types).

For the Ca-rich transients at large host offsets, nothing underlying is detected in these data at their locations. It should be noted the limits of these data will not rule out the majority of underlying potential systems, such as low surface brightness dwarf galaxies or globular clusters. Literature limits provide more useful restrictions on underlying dwarf galaxies and find nothing to  $M_R \sim -12$  for a small subset of the sample. When looking at very deep imaging, Lyman et al. (in prep) find nothing at the locations of SNe 2005E and 2012hn, with limits deep enough to probe down the globular cluster luminosity function, ruling out a globular cluster origin at high confidence. Limits on surviving massive binary companions (or other massive stars at the locations) are also placed, with nothing detected to stringent limits.

This analysis provides new clues regarding the origin of these peculiar transient events, and can help constrain the suggested theoretical models. In the following a discussion of these

constraints, in view of the suggested theoretical models for these transients, is provided.

*Ca-rich transients:* Several models were suggested for the origin of the Ca-rich events. The model of He-shell detonation on a CO WD, following He accretion from a He-WD, was suggested by [Perets et al. \(2010\)](#), with support from the theoretical analysis by [Shen and Bildsten \(2009\)](#) and [Waldman et al. \(2011\)](#). Such a model points to a double degenerate origin for these types of transient. In particular [Waldman et al. \(2011\)](#) suggested a low mass CO WD progenitor, which requires a long lived stellar origin, and possibly a low metallicity environment. An alternative model of a CC origin as suggested by [Kawabata et al. \(2010\)](#) (see also discussion by [Kasliwal et al. 2012](#)) would require a young, star-forming environment. This  $H\alpha$ -based analysis of the hosts of the Ca-rich transients makes clear that the majority of these are occurring a very long way from any detectable SF. This also strengthens the arguments of [Perets et al. \(2010\)](#) and [Kasliwal et al. \(2012\)](#) that even extremely high-velocity, high-mass runaway stars are implausible candidates as progenitors of the Ca-rich transients. It can be concluded therefore that this analysis consistently points towards old progenitor systems, and a likely thermonuclear origin, for the Ca-rich transients (see additional support through the analysis of [Yuan et al. 2013](#)).

*SN 2002cx-like transients:* Several models were also suggested for the origin of SN 2002cx-like events. [Li et al. \(2003\)](#) and [Branch et al. \(2004\)](#) suggested they originate from the deflagration of a Chandrasekhar mass C/O WD. This model encounters difficulties explaining the diversity of such events and in particular the extremely low-mass and sub-luminous SN 2008ha event. A more recent and detailed model by [Jordan et al. \(2012\)](#); see also [Calder et al., 2004](#); [Livne et al., 2005](#); [Kromer et al., 2013](#)) discusses a failed detonation model, in which a deflagration scenario fails to explode the WD, and only burns and ejects a fraction of the WD, leaving behind an intact (but now lower mass and polluted) WD remnant. This scenario can similarly explain the low velocities observed for SN 2002cx-like events due to deflagration, but in addition provides a robust explanation for the diversity of the SN 2002cx-like events and the possible production of extremely low-mass and low luminosity events. Both of these models begin with a Chandrasekhar mass WD, similar to the single-degenerate model suggested for SNe Ia. WDs initially formed at high masses (which in turn form from higher mass stellar progenitors with shorter lifetimes) and require less ad-

ditional accretion in order to achieve the Chandrasekhar mass. This would generally point to their association with younger environments, where more massive stars and binaries evolve and transfer mass. However, the evolution towards the Chandrasekhar mass is still expected to be generally longer, and sometimes much longer, than the typical lifetimes of CCSN stellar progenitors ( $>8 M_{\odot}$  stars). Although some SN 2002cx-like transients have been found in supposedly old environments (Foley et al., 2013), these findings suggest a very young environment for the progenitors of these transients, comparable with that of SNe IIP. The environmental constraints found here therefore do not exclude, but are less favourable for a Chandrasekhar mass C/O WD explosion.

Fernández and Metzger (2013) suggest neutron star-WD mergers as a possible origin for SN 2002cx-like events. Some of the properties of SN 2002cx-like transients are qualitatively reproduced by the model, but more detailed studies are needed. This model would suggest a mixed distribution of old and young environments, due to the distribution of the gravitational wave inspiral time leading to the merger, in contrast with the strong bias to very young environment found here. In addition, the total rate of neutron star-WD mergers is about 3 per cent of that of SNe Ia – even if all such mergers resulted in an SN 2002cx-like event, the expected rates would be an order of magnitude lower than those observed (Foley et al., 2013).

Valenti et al. (2009) suggested that SN 2002cx-like transients arise from a variant of CC-SNe with low ejecta velocity, although currently no detailed theoretical modelling of such events has been done. The findings of similar environments for both these transients and those of CCSNe, are therefore consistent with the CC origin of SN 2002cx-like transients. In particular, the detailed NCR statistics indicate that SN 2002cx-like events share similar environments to those of SNe IIP, i.e. while they are evidently associated with SF, a substantial fraction appear to outlive their natal HII regions, resulting in lower values of the NCR index than would be expected for the highest mass progenitors. In the context of this scenario, this analysis would therefore point to the lower-mass,  $7\text{--}9 M_{\odot}$  (with typical lifetimes of  $30\text{--}50$  Myrs) progenitors discussed by Valenti et al. (2009), rather than the alternative high-mass Wolf-Rayet stars also discussed by them. The inclusion of SN 2008ge as a young progenitor is still debatable as Foley et al. (2010b) conclude a lack of any recent SF at the

transient's location, however, our NUV NCR analysis would indicate the host, and the location of SN 2008ge has undergone moderately recent SF.

Two of the SN 2002cx-like transients show spectral evidence for helium. Taken together with the young environment found for these events, [Foley et al. \(2013\)](#) suggest this as possible evidence for their origin from a helium star accretion on to a WD. However, a helium layer may also form following hydrogen accretion and burning into helium on a WD ([Cassisi et al., 1998](#); and references therein). It is therefore concluded that although the existence of helium in even a small fraction of these events is a potentially important clue for their origin, its interpretation is still inconclusive.

### 3.10 Summary

The investigations presented here of the environments and host types of Ca-rich transients show a lack of association with recent SF (similar to that of SNe Ia), and thus point to old progenitor systems, consistent with helium-shell detonation on low mass C/O WDs, and inconsistent with a CCSN origin. Conversely, SN 2002cx-like transients are well matched by young progenitors ( $< 100$  Myr lifetime and likely to be 30–50 Myr) through a close association to NUV emission and an association to very recent SF that is similar to that displayed by SNe IIP. Such young progenitors are less favourable to failed detonations of Chandrasekhar mass C/O WDs, and more consistent with either the core-collapse of a 7–9  $M_{\odot}$  star, or a WD explosion following the accretion of helium star. While the failed detonation model for these events appears to be consistent with the observable parameters of SN 2002cx-like events themselves, the latter two models currently lack an actual detailed study. Therefore, they can not yet be adequately compared with observations, beyond the generally consistent aspects of their expected environments as studied here.

# Chapter 4

## Creating and modelling the bolometric light curve of SN 2012bz

### Abstract

The bolometric light curve of a SN is a powerful tool to investigate the nature of the explosion since it contains the entire kinetic energy output of the SN (modulo non-electromagnetic sources, e.g. neutrinos, which can account for 99 per cent of the energy). As such bolometric light curves often form a tight constraint for any modelling of SNe.

In this chapter the gamma-ray-burst-SNe (GRB-SNe) phenomenon will be introduced and specifically the recent case of GRB120422A/SN 2012bz. The bolometric light curve of SN 2012bz is created through the integration of spectral energy distributions based on broadband photometry with a correction for the missing near-infrared regime based on another GRB-SN, SN 2010bh. An analytical model for bolometric light curves of stripped-envelope SNe is briefly introduced and used to model SN 2012bz. Despite being an unremarkable GRB in cosmological terms, SN 2012bz was very luminous by SN standards (excluding SLSNe), brighter than SN 1998bw and an inferred  $M_{\text{Ni}}$  amongst the largest for SNe ( $\sim 0.6 M_{\odot}$ ). A comparison of the results of this modelling is made against those found with more involved spectral analysis performed by others, with generally good agreement found.

## 4.1 GRB-SNe and the case of GRB120422A/SN 2012bz

The link between long GRBs (LGRBs; i.e. those bursts with gamma ray emission  $>2$  seconds) and CCSNe is well established both theoretically and observationally. Proposed under the ‘collapsar’ model of Woosley (1993), the collapse of a massive star can create a stellar mass black hole with an accretion disc. The accretion onto the black hole (the central engine) powers a relativistic jet which penetrates the outer layers of the star, producing narrow, beamed emission of gamma rays, most likely due to colliding shells of differing Lorentz factor within the relativistic jet (the exact emission mechanism for the gamma rays is an area of ongoing study, for a recent review see Mészáros, 2013). The duration of this emission is intrinsically linked to the time-scale of the central engine and this is thought to depend somewhat on the size of the collapsing star, where a larger sized collapsing body will fuel the central engine for a longer duration.

Observational support arrived in the error box of the very low redshift GRB980425, where an emerging SN was seen to be brightening temporally coincident with this burst (Galama et al., 1998). The SN, SN 1998bw, was very luminous and classified as a SN Ic-BL, due to the very high photospheric velocity it exhibited (resulting in *broad-line* features in its spectra). The observational association has been cemented, with Hjorth and Bloom (2012) counting 11 objects with good light curve, and at least some spectroscopic, evidence for a SN in the light curve of a GRB afterglow (not including the very recent examples SN 2012bz, Melandri et al. 2012; Schulze et al. 2014; SN 2013cq Xu et al. 2013 and SN 2013dx Cenko et al., in prep). In each case that a classification is possible, the identified SN has been of type Ic-BL. Previous studies comparing GRBs that have an observed SN to ‘cosmological’ GRBs (i.e. those at high redshift, or where no SN was detected) appeared to show a bias towards lower luminosity for GRBs that show a SN (Guetta and Della Valle, 2007), with the notable exception of GRB030329/SN 2003dh (Stanek et al., 2003).

However, Xu et al. (2013) present GRB 130427A/SN 2013cq – with the GRB being extremely luminous even for cosmological GRBs, despite its moderate redshift of  $z = 0.3399$ . Coupled with GRB030329, this would suggest there is in fact a common progenitor system for GRB-SN to those GRB at high redshift, and high explosion energy events are capable of

producing a SN. Further to this, GRB 030329 and 130427A were very long duration bursts (in terms of the time-scale of gamma-ray emission). This poses a contradiction between the putative compact Wolf-Rayet progenitors (given they displayed SNe Ic) and consequently short fall back time, and the long time-scale of the central engine, suggesting progenitor size and central engine duration may not be so simply linked (Zhang et al., 2013).

GRB120422A was nearby in GRB terms at  $z = 0.283$ . Monitoring of the event revealed the accompanying SN, SN 2012bz which peaked around a fortnight after the GRB. True to previous GRB-SNe, it was classified as a SN Ic-BL. Interestingly the GRB is intermediate between the typically lower luminosities of GRB-SNe and high redshift cosmological GRBs and is likely a transition event in this parameter space (Hjorth, 2013; Schulze et al., 2014).

## 4.2 The bolometric light curve of SN 2012bz

Construction of bolometric light curves can be observationally expensive even for very nearby objects. In principle all wavelengths should be observed, but this is infeasible and as such bolometric light curves often rely on theoretically motivated prescriptions for very long and very short wavelengths, with observations concentrated in the near ultraviolet (NUV) to near infrared (NIR) regime. Presented here is an example construction of a pseudo-bolometric light curve that covers the NUV to NIR.

GRB120422A was subject to intensive observational follow up. The accompanying SN, SN 2012bz also contained well sampled coverage in the *griz* bands. The light curves in each filter were fitted with spline interpolations starting at 2 days past the GRB trigger (to avoid including points dominated by the GRB afterglow in the fits), such that an estimated magnitude for all four bands was available at each epoch of observation. The fitted splines are shown in Fig. 4.1. Magnitudes were converted into monochromatic fluxes at the effective (rest-frame) wavelengths of the filters using:

$$F_{\lambda_{eff}} = \frac{c}{\lambda_{eff}^2} \times 10^{-\frac{m_{AB}+48.6}{2.5}} \text{ erg s}^{-1} \text{ cm}^{-2} \quad (4.1)$$

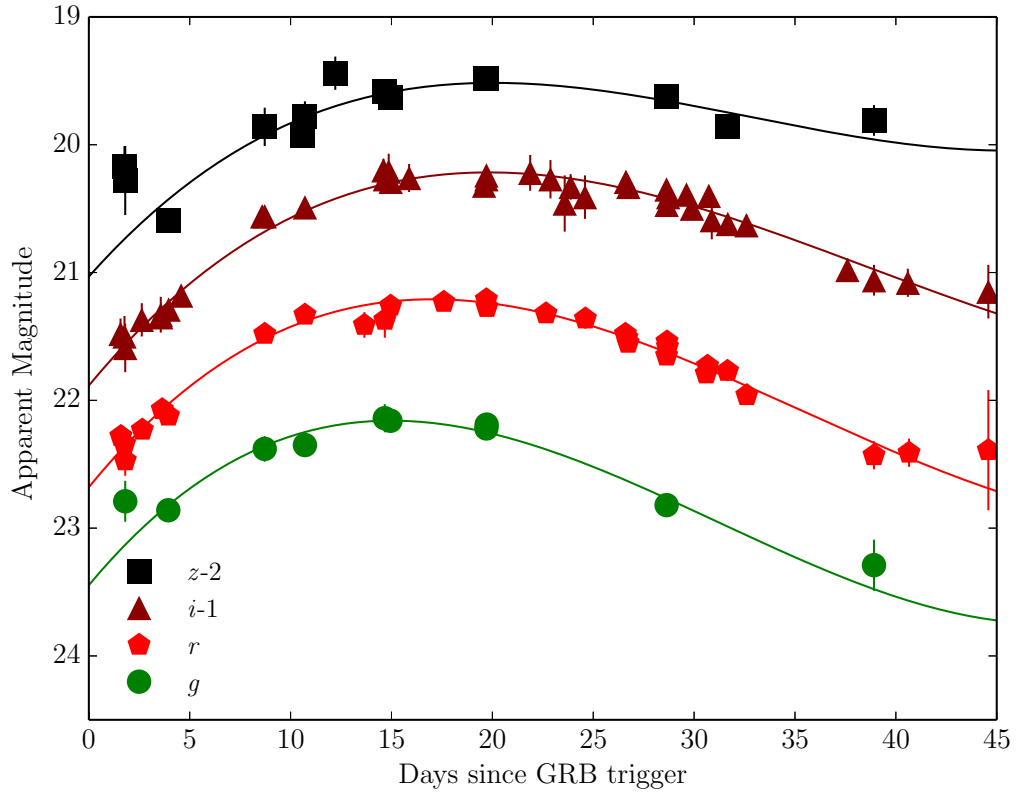


Figure 4.1: Light curves of SN 2012bz taken from [Schulze et al. \(2014\)](#), data have been corrected for Galactic extinction ( $E(B - V) = 0.04$  mag). Very early data where the GRB afterglow dominates have been removed ( $\lesssim 2$  day). The cubic splines used to interpolate the light curves are shown (solid lines).

where  $c$  is the speed of light,  $m_{\text{AB}}$  is the AB magnitude, and  $\lambda_{\text{eff}}$  is the effective wavelength of the filter. This was done for each filter at every epoch to produce an SED.<sup>1</sup>

Each SED was then interpolated linearly in flux and integrated over the limits of the filter wavelength range, assuming zero flux at the rest-frame blue edge of  $g$  and red edge of  $z$  ( $\sim 3000$  and  $8000 \text{ \AA}$  respectively). Some example SEDs are shown in Fig. 4.2. The differential peaking of the light curves (i.e. peaking later in redder bands; Fig. 4.1) is evident in the form of these SEDs. The integrated fluxes were converted to luminosities using a distance modulus of  $\mu = 40.79$ .<sup>2</sup>

<sup>1</sup>Since the SED is being evaluated for every observation, nearby epochs (within  $< 0.2$  days of each other) were first calculated individually and then averaged when producing the final bolometric light curve for clarity.

<sup>2</sup>Based on  $z = 0.283$  and a  $\Lambda$ CDM cosmology of  $H_0 = 71 \text{ km s}^{-1} \text{ Mpc}^{-1}$ ,  $\Omega_m = 0.27$ , and  $\Omega_\Lambda = 0.73$  ([Larson et al., 2011](#)).

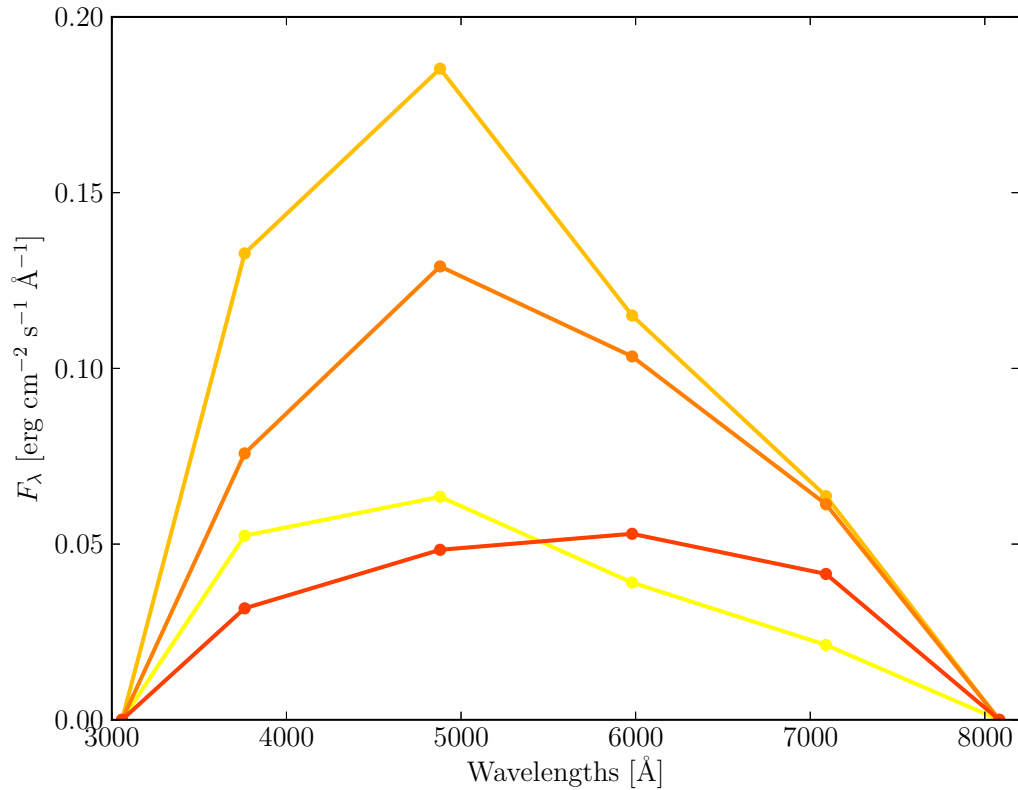


Figure 4.2: Sample SEDs of SN 2012bz constructed from *griz* photometry (the sequence yellow to red represents increasing time past the GRB trigger). The SEDs are artificially tied to zero flux at the blue edge of the *g* band and red edge of the *z* band.

Contributions to the flux (and hence luminosity) outside this regime, however, are not insignificant. This is particularly true in the NIR, wherein the fraction of the total luminosity emitted increases with time, reaching a comparable contribution to the optical within 30 days (e.g. Valenti et al., 2008). By using the fractional NIR flux of a similar transient, an estimate of the missing flux can be applied to SN 2012bz. A photometric study by Olivares et al. (2012) of the low redshift ( $z = 0.059$ ) XRF100316D/SN 2010bh contains well sampled light curves in  $zJH$  bands, extending upon the rest-frame wavelength limits. The contribution of wavelengths  $> 8000 \text{ \AA}$  to the flux was determined by first integrating SN 2010bh’s dereddened SED over wavelengths  $\leq 8000 \text{ \AA}$  and then wavelengths  $> 8000 \text{ \AA}$ . Thus, for each epoch of SN 2010bh observation, the NIR contribution as a fraction of the  $\sim$ ‘optical’ flux ( $\sim 4000\text{--}8000 \text{ \AA}$ ) is obtained. This fractional flux is then applied to SN 2012bz after similarly obtaining integrated fluxes for the optical regime. The phases of these fractional contribu-

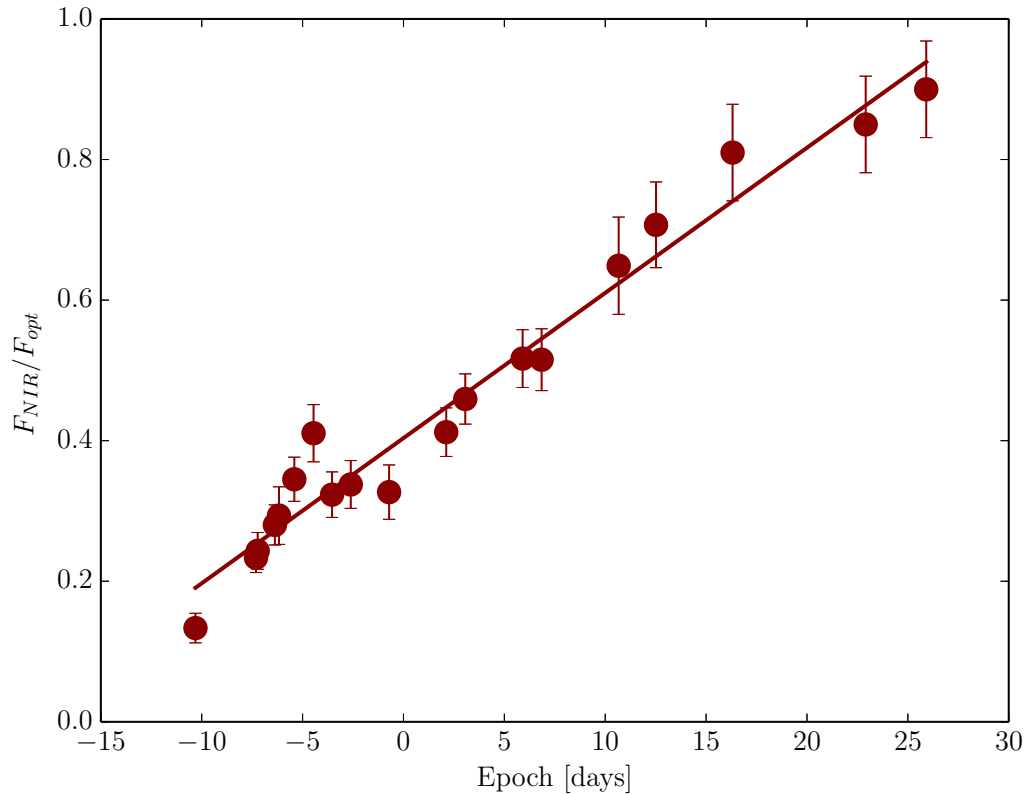


Figure 4.3: NIR contributions to SN 2010bh as a fraction of the ‘optical’ flux ( $\sim 4000\text{--}8000\text{ \AA}$ ). The fitted polynomial is shown. Epochs are normalised and stretched to match those of SN 2012bz (see text).

tions were normalised so  $t=0$  was the optical peak of the respective SNe, and stretched by a factor  $\Delta m_{15,optical}$  (à la Phillips, 1993) to match the light curve shape of the two SNe (0.78 for SN 2012bz, 1.00 for SN 2010bh). The peak and  $\Delta m_{15,optical}$  values were found by fitting polynomials to the data around peak. The fractional NIR values of SN 2010bh were fitted with a polynomial (Fig. 4.3) in order to sample it at the epochs of SN 2012bz observations, and the appropriate amount was added to the optical flux of SN 2012bz. The result is a NIR-corrected light curve covering  $3000\text{--}17000\text{ \AA}$  for SN 2012bz. No attempt was made to account for flux missed below  $3000\text{ \AA}$ , due to the paucity of data constraining the UV in such objects.

The resulting pseudo-bolometric light curves are shown in Fig. 4.4 along with modelling fits (see Section 4.3).

### 4.3 Analytical modelling of SN 2012bz

The bolometric light curve of a stripped-envelope SNe (SE SNe) can be modelled using the simplified analytical prescription of Arnett (1982), updated by Valenti et al. (2008), to obtain physical parameters of the explosion, the mass of  $^{56}\text{Ni}$ , the mass ejected and the kinetic explosion energy ( $M_{\text{Ni}}$ ,  $M_{\text{ej}}$  and  $E_K$  respectively). The model is briefly introduced here with results of the modelling of SN 2012bz. The model is further detailed in Chapter 6, along with a discussion of the relevant equations and assumptions, where it is applied to a large sample of SE SNe.

Although the model formally describes a bolometric light curve of a SE SN, the pseudo-bolometric light curve (plus NIR correction) created in Section 4.2 is used as an approximation since observations of wavelengths outside these wavelengths do not exist. The data cover the photospheric phase of SN evolution, when the ejecta are considered optically thick. The opacity is chosen to be  $\kappa = 0.07 \text{ cm}^2 \text{ g}^{-1}$  (see Cano et al., 2011). To constrain the degeneracy in the  $E_K/M_{\text{ej}}$  ratio, a *scale velocity* is required (see equation 54 in Arnett, 1982), and this is taken to be the photospheric velocity ( $v_{\text{ph}}$ ) at peak. FeII lines are a good tracer of  $v_{\text{ph}}$  (Valenti et al., 2011), and the peak of the pseudo-bolometric light curve occurs at  $\sim 13.9$  days (from fitting low-order polynomials around peak). Using data from Schulze et al. (2014),  $20500 \text{ km s}^{-1}$  is used for  $v_{\text{ph}}$  by linearly interpolating between the measurements taken from spectra at epochs 11.380 days and 14.575 days.

Fitting to the optical bolometric light curve reveals the following parameters:  $M_{\text{Ni}} \simeq 0.4 M_{\odot}$ ,  $M_{\text{ej}} \simeq 4.7 M_{\odot}$  and  $E_K \simeq 3.3 \times 10^{52} \text{ erg}$ , when including the NIR contribution from SN 2010bh, the fit results obtained are  $M_{\text{Ni}} \simeq 0.6 M_{\odot}$ ,  $M_{\text{ej}} \simeq 5.9 M_{\odot}$  and  $E_K \simeq 4.1 \times 10^{52} \text{ erg}$ . The first 8 days were ignored in the fit as contributions from other sources (GRB afterglow, SN shock-breakout cooling) would compromise the assumptions of the SN model. SN 2012bz shows one of the highest nickel masses ever seen in a GRB-SNe (Bufano et al., 2012).

Systematic errors arise from both the simplifying assumptions in the model (spherical symmetry, centrally concentrated  $^{56}\text{Ni}$  mass etc.) and the choice of parameters for the fit, which typically dominate statistical errors. For example, taking an uncertainty in  $v_{\text{ph}}$  of

2000 km s<sup>-1</sup> translates to an error in  $M_{ej}$  and  $E_K$  of  $\sim 10\%$  and  $\sim 25\%$  respectively. The  $M_{Ni}$  value derived is more secure given the GRB signal gives an extremely precise time to set as the time of explosion in the model. The rise time is therefore very well constrained, however any uncertainty in the peak luminosity directly affects the  $M_{Ni}$  value derived. The redshift of the host has a well determined redshift of 0.283 (Schulze et al., 2012); a 10% error in  $M_{Ni}$  is therefore estimated, arising from the inherent photometric errors (which affects SED construction) and also uncertainties on the NIR contribution. The two-component model for hypernovae by Maeda et al. (2003) would suggest these data are only representative of the outer, lower density region of the ejecta that is visible during the photospheric phase ( $\lesssim 30$  days), and a fraction is hidden in a denser, inner component during this time, this means the quoted values will have a more uncertain upper limit – studies show this inner component can be  $\sim 10\%$  of the total flux but can reach up to 15 – 30% in some cases (Valenti et al., 2008). A fuller detail of the errors inherent to the modelling scheme employed here is provided in Chapter 6, including a discussion of the assumptions that are used and their effect on the resulting parameters.

Although the afterglow component of GRB120422A is shown not to contribute significantly around the SN peak, potential contamination by underlying host galaxy light is included in this bolometric light curve, although the potential impact on the resulting parameters would be small compared to other systematics detailed.

Melandri et al. (2012) modelled SN 2012bz using a scaled spectral model for SN 2003dh to obtain estimates of the physical parameters. They obtained values of  $M_{Ni} \approx 0.35 M_{\odot}$ ,  $M_{ej} \approx 7 M_{\odot}$  and  $E_K \approx 3.5 \times 10^{52}$  erg using a bolometric light curve covering 3300-7400 Å. Comparing these to the values for the 3000-8000 Å bolometric light curve, the  $M_{Ni}$  values are in good agreement, given the slightly extended wavelength range here (and hence higher derived luminosity),  $E_K$  values are consistent, however the ejected mass found is lower compared to their value. Differences could be caused by choices of  $v_{ph}$  and  $\kappa$ , or asymmetries, which spectral modelling can account for.

One thing to note is the importance of the NIR contribution to the extracted parameters from such modelling. A  $\sim 45\%$  increase in the nickel mass obtained is found, and a  $\sim 25\%$  increase in  $M_{ej}$  and  $E_K$  when including this correction. Although SN 2010bh was clearly

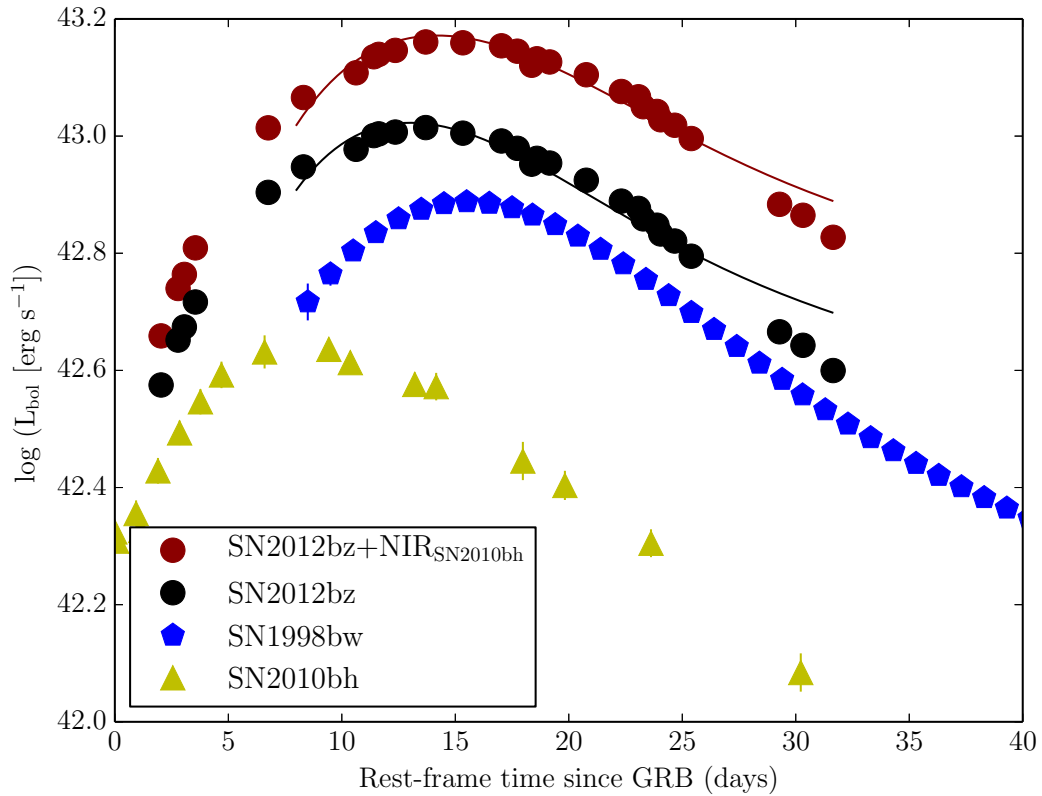


Figure 4.4: Pseudo-bolometric light curves of SN 2012bz from direct integration of the SED over *griz* filters, and including a NIR contribution as found for SN 2010bh. For comparison the *UBVRI* light curve of SN 1998bw (Clocchiatti et al., 2011) and the *grizJH* light curve of SN 2010bh are shown (Olivares et al., 2012). The models for SN 2012bz are shown as solid lines. Early time data are not fit as the analytical model does not account for other non-negligible sources of luminosity at these times (see text). Only photometric and calibration uncertainties are included in the error bars.

different from SN 2012bz, the NIR contribution as a fraction of the optical is not expected to differ hugely across SN of the same type (see Fig. 5.1). The contribution of the NIR is clear when comparing the analytical models to the data in Fig. 4.4; much better agreement is found at late times when including a NIR correction, when the fractional flux contained at these longer wavelengths is substantial.

# Chapter 5

## Bolometric corrections to optical light curves of CCSNe

### Abstract

With the usefulness of bolometric light curves of CCSNe as probes of the progenitors systems, it is beneficial to expedite their creation in terms of observational cost, given the huge mismatch between the resources of telescope time and the rate of SN discoveries. Characterisation of the bolometric light curve of a SN requires well-sampled observations over the NUV to NIR regime, since these wavelengths exhibit the largest diversity and will contain the vast majority of the total flux over nearly all epochs of a SN's evolution. To perform this for even a very small fraction of discovered SNe is infeasible. In this chapter we collect literature SN photometry over a wide range of wavelengths, and make simple but robust approximations for the flux emitted in less well observed wavelengths to construct bolometric light curves for a large sample of SNe. These bolometric light curves are correlated with easily-obtained optical colours and a tight relation is found for several optical colours. The method presented here shows that the bolometric output of a CCSN can be reliably determined from just two-filter observations in the optical window, vastly reducing the telescope time required to construct bolometric light curves. Such a method has implications for large-scale supernovae surveys by making it possible to construct bolometric light curves for a large fraction of their discovered supernovae using only their own optical monitoring.

## 5.1 Investigating the progenitors of CCSNe and the role of bolometric light curves

Core-collapse supernovae (CCSNe) are spectacular highlights throughout the transient universe. As the extremely luminous end-point of the evolution of massive stars ( $\geq 8 M_{\odot}$ ; [Smartt, 2009](#)), CCSNe are valuable tools to many areas of astrophysical research. Their ability to probe the environments they inhabit and our understanding of the diverse range of explosions that occur, however, is limited by our knowledge of the progenitor system for each event, and the surrounding medium.

If the event occurs in a local galaxy, searches in high resolution archival imaging can allow direct observations of the progenitor system to be made; such analysis has proved successful in a growing number of cases (e.g. [Van Dyk et al., 2003](#); [Smartt et al., 2004](#); [Li et al., 2007](#); [Gal-Yam and Leonard, 2009](#); [Van Dyk et al., 2012](#); [Maund et al., 2011](#); see [Smartt 2009](#) for a review). This technique is clearly reliant on the proximity of the SN, to be able to resolve individual progenitor systems from star clusters, and also the existence of archival high-resolution imaging to a sufficient depth for direct detection or stringent upper limits to be made (preferably in several bands). For the vast majority of discovered SNe, direct studies cannot be performed; post-explosion observations and modelling of the luminous event must be used to infer the properties of the progenitor star and the explosion. Dedicated SN searches are finding SNe of all types with such regularity that in-depth observational follow up, required for accurate modelling, is not feasible for most SNe discovered.

Modelling of CCSNe, from simple analytical descriptions of the light curve evolution ([Arnett, 1982](#); [Valenti et al., 2008](#)) to spectral synthesis codes (e.g. [Mazzali and Lucy, 1993](#)) and hydrodynamical modelling (e.g. [Nakamura et al., 2001](#); [Utrobin, 2007](#); [Tanaka et al., 2009](#)) can provide good estimates of the physical parameters of the explosion; typically the mass of nickel synthesised and the mass and kinetic energy of the ejecta. Such modelling typically requires at the very least one spectroscopic observation near peak (for analytical methods), with good spectroscopic coverage into the nebular phase desired to obtain the most accurate results from spectral/hydrodynamical modelling. However, to obtain accurate explosion pa-

rameters, models must typically be scaled to a bolometric light curve, this is particularly true for hydrodynamical modelling.

A NUV–NIR light curve contains the vast majority of the light from a SN, but obtaining well-sampled data over this wavelength range is expensive, especially for significant samples of objects. Data are often limited to much shorter wavelength ranges, meaning estimates of bolometric magnitudes can be vastly underestimating the emitted flux. *(U)BVRI* integrated light curves have been used as a proxy for a bolometric light curve, although a comparable amount of flux is emitted in the near-infrared (NIR) alone. Either no attempt is made to correct for flux outside this regime (e.g. [Young et al., 2010](#); [Sahu et al., 2011](#)), since no reliable methods exist, or a zero order assumption, that the fraction of flux outside the observed window is constant with time, is made ([Elmhamdi et al., 2011](#)), despite this demonstrably not being the case (e.g. [Valenti et al., 2008](#); [Modjaz et al., 2009](#); Section 5.4.1). An improved method is to find a similar object and assume the same proportional flux to be emitted outside the observed window ([Valenti et al., 2008](#); [Mazzali et al., 2013](#); Schulze et al. in prep). Bolometric light curves are therefore created using a variety of methods and this introduces uncertainties on how to compare the results of modelling consistently across events.

[Bersten and Hamuy \(2009\)](#) have investigated bolometric corrections (BC) to three well-observed type II-P SNe (SNe II-P) and two sets of atmosphere models. The progenitor stars of SNe II-P are expected to be at the lower end of the mass range for CCSNe ([Smartt, 2009](#)) and to have kept their outer layers throughout their evolution. These hydrogen-rich envelopes make their evolution well approximated by spherical explosions whose evolution is blackbody-like and continuum-dominated (until the end of the plateau phase). [Bersten and Hamuy \(2009\)](#) indeed find very tight correlations between the BC and optical colour of the SNe/models in their sample, providing a parameterised way of obtaining bolometric magnitudes from *BVI* photometry. Including another well-observed SN II-P, [Maguire et al. \(2010\)](#) looked at BCs versus time, and found relatively similar evolution of the BC to *R*-band magnitudes between the four SNe, although the *V*-band BC appears rather more diverse.

[Pritchard et al. \(2013\)](#), utilising *Swift* data, have considered all CCSNe types to produce bolometric and ultraviolet corrections (UVC). The *Swift* data set is uniquely able to constrain the behaviour of SNe in the  $\sim 1800\text{--}3000$  Å wavelength regime. By correlating directly with

optical colours and UV integrated fluxes, both taken with the UVOT instrument, they find a linear behaviour of the UVC, which appears to have no strong dependence on CCSN type. These correlations, however, are subject to substantial spread, which highlights the diversity of UV evolution in CCSNe. An attempt was also made to create a BC for CCSNe, however since the reddest filter available on UVOT is  $V$ , the BC is reliant upon modelling and the blackbody (BB) approximation for wavelength regimes that contain the majority of the bolometric flux at all but the very earliest epochs. As the authors noted, ground-based observations will provide a more robust estimate for the contribution of these longer wavelengths to CCSN bolometric light curves, particularly when including NIR observations.

Clearly a consistent manner in which to obtain an approximation for the bolometric output, particularly for stripped-envelope CCSNe (SE SNe, i.e. types Ib, Ic and IIb), is lacking. Such a method would allow results from modelling to be compared more consistently, as well as providing further tests for current and future models and simulations of SNe.

In this chapter literature data for well observed CCSNe is utilised to investigate flux contributions of different wavelength regimes, and to construct BCs based on optical colours. Although these literature SNe are predominantly observed in the Johnson–Cousins systems, fits in Sloan optical bands are also presented, given their prevalence in current and future SN surveys. The data and SN sample are presented in Section 5.2, Section 5.3 describes the steps involved in creating spectral energy distributions (SEDs) for the SN sample. Results and fit equations are presented in Section 5.4 and discussed in Section 5.5.

## 5.2 Data

### 5.2.1 Photometry

SEDs, from which to calculate integrated light curves, would ideally be constructed from spectra. However the expense of such spectral coverage, and consequent dearth of available observations, means that the SEDs analysed here have been constructed exclusively from broad-band photometric data. The phase ranges covered by this analysis (typically  $< 70$

days past peak for SE SNe, and the duration of the plateau for type II SNe; SNe II) are regions where continuum emission dominates the brightness of a SN, with line emission only dominating in the later, nebular phases. As such, photometric and spectroscopic integrated luminosities will typically agree well in the phase ranges explored here.

All photometric data used here are taken from the literature where a CCSN has photometric coverage over the  $U$ -to- $K$  wavelength range. All types of CCSNe are included except those exhibiting strong interaction with their surrounding medium (typically with an ‘n’ designation in their type). Strong CSM interaction introduces a range of photometric and spectroscopic evolution, as well as the possibility of early dust formation (e.g. SN2006jc; Nozawa et al., 2008; Smith et al., 2008), making SED evolution between these events diverse.<sup>1</sup> See Moriya et al. (2013) for an analytical treatment of SNe II in bolometric light curves.

### 5.2.2 SN sample

Naturally, a sample of well-observed SNe taken from the literature will be extremely heterogeneous since it is often the events that display unusual or peculiar characteristics (and/or are very nearby) that find the most attention. As such this sample is by no means a representative sample of discovered CCSNe, or CCSNe as a whole. This makes it more difficult to break down the sample by type as some are unique events. The unusual characteristics across this sample are evident from the uncertain and peculiar flags on their initial IAU typing.<sup>2</sup> In Table 5.1 we present SN type, as taken from more detailed literature studies of the objects, host galaxy name and redshift from the NASA Extragalactic Database (NED)<sup>3</sup>,  $E(B - V)$  values for Galactic and total reddening, the filters used to construct the SED, an epoch range over which the full filter set can be reliably used in constructing the SED (see Section 5.3.1), and a  $\Delta m_{15,V}$  value (see Section 5.4.1) for each SN in the sample.

The sample includes a GRB-SN (SN1998bw), XRF-SNe (SN2006aj, SN2008D) and the unusual SN2005bf that displayed two peaks and a transition from type Ic to Ib, discussed

<sup>1</sup>Furthermore, recent evidence suggest some fraction of SN II in could be type Ia, thermonuclear, explosions that are expanding into a dense hydrogen-rich medium (Silverman et al., 2013).

<sup>2</sup><http://www.cbat.eps.harvard.edu/lists/Supernovae.html>

<sup>3</sup><http://ned.ipac.caltech.edu/>

variously as a magnetar (Maeda et al., 2007) and an asymmetric Wolf-Rayet explosion (e.g. Folatelli et al., 2006). See the references in Table 5.1 for a detailed discussion of individual events and further unusual characteristics.

Given the limited sample and the previously mentioned eclectic and peculiar nature of many of them, we limit our sub-typing to SE SNe (i.e. those of type Ib, Ic and IIb) and SNe II (i.e. those of any type II except IIb). Practically, we consider SN1987A, SN1999em, SN2003hn, SN2004et, SN2005cs and SN2012A as the SNe II sample ( $N = 6$ ), with all others being SE SNe ( $N = 15$ ).

Table 5.1: Data for SNe in the sample.

SN name	Type	Host	Redshift	$E(B - V)_{\text{MW}}$ (mag)	$E(B - V)_{\text{tot}}$ (mag)	Filter coverage	Full SED coverage <sup>a</sup> ( $\Delta t_{\text{peak},V}$ )	$\Delta m_{15,V}$ <sup>b</sup> (mag)	Refs.
1987A	II-pec	LMC	0.0009	0.08	0.17	<i>UBVRIJHK</i>	2–134 <sup>c</sup>	–	1–4
1993J	I Ib	M81	-0.0001	0.081	0.194	<i>UBVRIJHK</i>	–18 to –10, 14–27	0.935	5–7
1998bw	Ic-BL	ESO 184-G82	0.0087	0.065	0.065	<i>UBVRIJHK</i>	6, 31, 49	0.816	8,9
1999dn	Ib	NGC 7714	0.0093	0.052	0.10	<i>UBVRIJHK</i>	24, 38, 123	0.500	10
1999em	II-P	NGC 1637	0.0024	0.043	0.10	<i>UBVRIJHK</i>	11–117 <sup>c</sup>	–	11,12
2002ap	Ic-BL	M74	0.0022	0.072	0.09	<i>UBVRIJHK</i>	–8 to 25	0.881	13–20
2003hn	II-P	NGC 1448	0.0039	0.014	0.187	<i>UBVRIYJHK</i>	20–140	–	12
2004aw	Ic	NGC 3997	0.0159	0.021	0.37	<i>UBVRIJHK</i>	4–27	0.558	21
2004et	II-P	NGC 6946	0.0001	0.314	0.41	<i>UBVRIJHK</i>	8–112 <sup>c</sup>	–	22,23
2005bf	Ib/c	MCG +00-27-5	0.0189	0.045	0.045	<i>UBVriJHK</i>	–17 to 20 <sup>d</sup>	0.462	24
2005cs	II-P	M51	0.0015	0.035	0.050	<i>UBVRIJHK</i>	3–80 <sup>c</sup>	–	25
2006aj	Ib/c	Anon.	0.0335	0.142	0.142	<i>UBVRIJHK</i>	–7 to 6	1.076	26,27
2007Y	Ib	NGC 1187	0.0046	0.022	0.112	<i>uBgVriYJHK</i>	–13 to 29	1.049	28
2007gr	Ic	NGC 1058	0.0017	0.062	0.092	<i>UBVRIJHK</i>	–3 to 141	0.861	29
2007uy	Ib	NGC 2770	0.0065	0.022	0.63	<i>UBVRIJHK</i>	–4 to 5,33–35	0.815	30
2008D	Ib	NGC 2770	0.0065	0.023	0.6	<i>UBVRIJHK</i>	–16 to 18	0.697	31
2008ax	I Ib	NGC 4490	0.0019	0.022	0.4	<i>uBVrRIJHK</i>	–10 to 25	0.909	32,33

2009jf	Ib	NGC 7479	0.0079	0.112	0.117	<i>UBVRIJHK</i>	−17 to 54	0.592	34,35
2011bm	Ic	IC 3918	0.0015	0.032	0.064	<i>UBVRIJHK</i>	8–56	0.251	36
2011dh	Iib	M51	0.0015	0.031	0.07	<i>UBVRIJHK</i>	−18 to 70	0.968	37
2012A	II-P	NGC 3239	0.0025	0.028	0.037	<i>UBVRIJHK</i>	9–90 <sup>c</sup>	–	38

<sup>a</sup> The phase(s) over which there exists a full complement of filter observations (or well constrained interpolations) from which to construct an SED in days relative to the *V*-band peak

<sup>b</sup> Difference in magnitudes of the *V*-band light curve at peak and 15 days later

13–20

<sup>c</sup> Phase is quoted with respect to estimated explosion date

<sup>d</sup> The second *V*-band peak is used as  $t_{peak}$ , SN 2005bf is the famous ‘double-humped’ SN.

References: (1) [Menzies et al. \(1987\)](#); (2) [Catchpole et al. \(1987\)](#); (3) [Gochermann et al. \(1989\)](#); (4) [Walker and Suntzeff \(1990\)](#); (5) [Richmond et al. \(1994\)](#); (6) [Matthews et al. \(2002\)](#); and IAU circulars within); (7) [Matheson et al. \(2000\)](#); (8) [Clocchiatti et al. \(2011\)](#); (9) [Patat et al. \(2001\)](#); (10) [Benetti et al. \(2011\)](#); (11) [Elmhamdi et al. \(2003\)](#); (12) [Krisciunas et al. \(2009\)](#); (13) [Mattila et al. \(2002\)](#); (14) [Hasubick and Hornoch \(2002\)](#); (15) [Riffeser et al. \(2002\)](#); (16) [Motohara et al. \(2002\)](#); (17) [Gal-Yam et al. \(2002\)](#); (18) [Takada-Hidai et al. \(2002\)](#); (19) [Yoshii et al. \(2003\)](#); (20) [Foley et al. \(2003\)](#); (21) [Taubenberger et al. \(2006\)](#); (22) [Zwitter et al. \(2004\)](#); (23) [Maguire et al. \(2010\)](#); (24) [Tominaga et al. \(2005\)](#); (25) [Pastorello et al. \(2009\)](#); (26) [Mirabal et al. \(2006\)](#); (27) [Kocevski et al. \(2007\)](#); (28) [Stritzinger et al. \(2009\)](#); (29) [Hunter et al. \(2009\)](#); (30) [Roy et al. \(2013\)](#); (31) [Modjaz et al. \(2009\)](#); (32) [Taubenberger et al. \(2011\)](#); (33) [Pastorello et al. \(2008\)](#); (34) [Valenti et al. \(2011\)](#); (35) [Sahu et al. \(2011\)](#); (36) [Valenti et al. \(2012\)](#); (37) [Ergon et al. \(2013\)](#); (38) [Tomasella et al. \(2013\)](#).

## 5.3 Method

Flux evolution and BCs are found through integrations of various wavelength regimes of SEDs for our SN sample. A description of how these SEDs are constructed from the photometric data, and the treatment of unconstrained wavelengths follows.

### 5.3.1 Interpolations of light curves

Photometric data will not have equal sampling across all filters. For example optical data may be taken on a different telescope to the NIR, or poor weather prevent the observations in one or more bands on a given night. Since we are interested in obtaining a full SED over the  $U$ -to- $K$  filter range, we must rely on interpolations in order to provide good estimates for these missing data.

Such interpolations were fitted to each filter light curve as a whole and chosen as the best estimate of the missing evolution of the light curve. Typically interpolation functions were either linear, spline or a composite fit (consisting of an exponential rise, a Gaussian peak, and magnitude-linear decay; see [Vacca and Leibundgut, 1996](#)). The choice of function was linked to the sampling; where the light curve had densely sampled evolution ( $\sim$  daily), linear interpolation was sufficient, whereas splines and the composite model were used when the light curve had substantial gaps ( $\gtrsim$  several days) where the light curve was not constrained.

Interpolated values were used to fill in missing values from literature photometry such that at every epoch of observation a full complement of magnitudes in each filter of the  $U$ -to- $K$  range existed from a mixture of observed and interpolated data points. Epochs over which the interpolations were valid were noted and interpolated values were only trusted within a few days of observations; for regions of simple behaviour, where we could be confident the interpolation accurately represented the missing part of the light curve (e.g. epochs on the plateau for SNe II), this limit was increased. Any epoch where the evolution of the SN light curve in one or more filters was not well constrained was rejected from further analysis. Extrapolations were typically not relied upon, although some cases warranted extrapolated magnitudes to be used in one or two filters – these were only used  $\lesssim 2$  days beyond the data,

and where the function was well-behaved. See Table 5.1 for ranges where full  $U$ -to- $K$  fluxes could be used in SED construction for each SN.

### 5.3.2 SED construction

SED construction is performed using a different method for three different wavelength regimes: the optical–NIR (3659–21900 Å; the wavelength range covered by the  $U$ -to- $K$  photometry), the BB tail (>21900 Å) and the UV (<3569 Å). A discussion of the construction of the SED in each regime follows.

#### The optical-NIR regime

In this wavelength range we are constrained by photometric observations from the interpolated light curves, which form tie points of the SED. Prior to SED construction, the photometry is corrected for extinction assuming a Fitzpatrick (1999)<sup>4</sup>  $R_V = 3.1$  Galactic extinction curve for both Milky Way and host galaxy extinction.  $E(B - V)_{\text{tot}}$  ( $= E(B - V)_{\text{MW}} + E(B - V)_{\text{host}}$ ) values are given in Table 5.1.

Extinction-corrected magnitudes are then converted to fluxes ( $F_\lambda$ ). An optical-NIR SED is created for every epoch of observation using the  $F_\lambda$  and effective wavelength ( $\lambda_{\text{eff}}$ ) values of each filter. Filter zeropoints, to convert to  $F_\lambda$ , and  $\lambda_{\text{eff}}$  values are taken from Fukugita et al. (1996), Bessell et al. (1998) and Hewett et al. (2006). Note that  $K$ -corrections were neglected in this analysis due to the very low redshift of the sample (see Table 5.1).  $K$ -corrections were investigated using available spectra of the SN sample at similar epochs to SED construction in WISeREP (Yaron and Gal-Yam, 2012), with over 90 per cent of measurements across all filters having  $|K| < 0.03$  mag.

---

<sup>4</sup>The choice of extinction law has minimal impact on the final results.

### The BB tail

Although longer wavelengths than the  $K$ -band are not expected to contribute significantly to the bolometric flux, a treatment of these wavelengths in the SEDs must be made to avoid systematically underestimating the bolometric flux. During the photospheric epochs mainly investigated here, we assume the flux evolution of the long wavelength regime to be well described by a BB tail – see Section 5.5.1 for a discussion of this approximation.

A BB was fitted using the  $R$  (or  $r$ ),  $I$  (or  $i$ ),  $J$ ,  $H$  and  $K$ -band fluxes ( $R$ -to- $K$ ), since optical fluxes, particularly for SE SNe, fall below the expectation from a BB once strong line development of Fe-group elements begins (see Filippenko, 1997; and references therein). Epochs where bluer bands are expected to be well characterised by a BB fit ( $\lesssim 20$  days for SE SNe and prior to the end of the plateau for SNe II), were also separately fitted, here including the  $B$ - and  $V$ -bands, to ascertain the difference to the  $R$ -to- $K$  fits. Including these extra bands had very little impact on the fits and resulting integrated luminosities. As such we favour using the  $R$ -to- $K$  bands for our BB fits, since this is appropriate for each SNe at all epochs investigated here and we reduce the danger of erroneously fitting to wavelengths that are not described by a BB.

CURVE\_FIT in the SCIPY<sup>5</sup> package was used on each pair of parameters in an initial grid of reasonable SN temperatures and radii to find the global  $\chi^2$  minimised BB function. The resulting function was appended to the optical–NIR SED at the red cut-off of the  $K$ -band filter (defined as 10 per cent transmission limit, 24400 Å) and extended to infinity. The  $K$ -band and beginning of the BB tail were linearly joined in the SED.

### The UV

The UV represents a wavelength regime with complex and extremely heterogeneous evolution for CCSNe (Brown, 2009). Coupled with a dearth of observations, correcting for flux in the UV is uncertain. Early epochs in the evolution of a SN can be dominated by the cooling of shocked material which emerges after the short-lived shock breakout (SBO)

---

<sup>5</sup><http://www.scipy.org/>

emission. This cooling phase is observed as a declining bolometric light curve that is very blue in colour. After this the radioactively powered component of the light curve begins to dominate and the light curve then rises to the radioactive peak (in SE SNe; for SNe II-P the recombination-powered light curve will become dominant and the light curve will settle to the plateau phase). The time over which the cooling phase dominates is highly dependent on the nature of the progenitor star, primarily driven by its size. The extended progenitors of SNe II, which have retained their massive envelopes, can display the signature of this cooling phase for many days, whereas in compact SE SNe progenitors it is shorter and often  $\lesssim 1$  day. Indeed for SE SNe it has only been seen in a handful of cases (e.g. SNe 1993J, [Richmond et al. 1994](#); 1999ex, [Stritzinger et al. 2002](#); 2008D, [Modjaz et al. 2009](#); 2011dh, [Arcavi et al. 2011](#)), generally thanks to extremely early detections. The evolution in the UV regime also quickly falls below the expectations of a BB approximation, as mentioned in Section 5.3.2, and as such a BB fit to these wavelength ranges over most of the evolution of a SN would be inconsistent with one drawn from longer wavelengths. During the cooling phase however, a BB fit across all wavelengths is appropriate as the SN is dominated by the hot, continuum flux.

Given the changing behaviour of the UV we utilise two treatments for the differing cases. For epochs over the cooling phase, the UV flux is taken to be the integrated flux of a BB function, from zero  $\text{\AA}$  to the blue edge of the  $U$ -band (following e.g. [Bersten and Hamuy, 2009](#)); the BB is fitted and joined to the SED in the same manner as Section 5.3.2. (Note that for these epochs we opted to include the  $B$  and  $V$  filters as further constraints for the BB.) Signatures of this cooling phase were taken to be early declines in the  $U$ - and  $B$ -bands in the light curves of SNe. All SNe II and SNe 1993J, 2008D and 2011dh had epochs during the cooling phase which contained full  $U$ -to- $K$  photometry, i.e. where we could construct SEDs for them. The extent of the cooling phase was determined by observing a drop in the  $U$ -band flux in the SED, relative to that predicted by the BB fit.

To account for UV flux at later epochs, when the BB approximation is not appropriate, each SED was tied to zero flux at  $2000 \text{\AA}$  by linearly extrapolating from the  $U$ -band flux. This was found to be a good estimate of the UV flux when compared to UV observations, as discussed in Section 5.5.1.

## 5.4 Results

Using the constructed SEDs, investigations into the contributions of different wavelength regimes can be made over various epochs of SN evolution and across different types.

### 5.4.1 Flux contributions with epoch

Initially, SEDs were integrated over three wavelength regimes: an optical regime (defined here as covering the *gri* bands; 3924–8583 Å), the IR (including the BB tail; 9035 Å–infinity) and the UV (0–3924 Å). For the SE SNe each SED was assigned an epoch relative to the peak of the *V*-band light curve, where the peak was found by fitting a polynomial to the data near maximum. A  $\Delta m_{15,V}$  value for each SN was also found, following the method of Phillips (1993), using the *V*-band.  $\Delta m_{15,V}$  values are presented in Table 5.1. Each SN was normalised to the evolution of the average  $\Delta m_{15,V}$  (0.758) in order to correct for varying light curve evolution time-scales. This was done by applying a linear stretch factor,  $S$  to the epoch for each SN, where  $S = \Delta m_{15,V}/0.758$ . For SNe II each SED epoch was made relative to the time of explosion (see references in Table 5.1).

The behaviour of the flux contained in the UV, optical, and IR are plotted as a function of the total bolometric flux in Fig. 5.1. Clearly the individual components, as fractions of the total emitted flux, evolve strongly with respect to time, as has been indicated previously for individual or small samples of events (e.g. Valenti et al., 2008; Modjaz et al., 2009; Stritzinger et al., 2009). This behaviour appears to be qualitatively similar for all SE SNe (after normalising to a common light curve evolution time-scale). IR fractions typically reach a minimum on or slightly before *V* peak and then rise until  $\sim 20/S$  days after peak, reaching a comparable fraction of the bolometric flux to that of the optical. The UV is weak at most epochs, falling from  $\sim 10$ –20 per cent prior to peak to just a few per cent a week past peak for most SE SNe. However, in the case of an observed SBO cooling phase, as is the case particularly for SN1993J and, to a lesser extent, SNe 2008D and 2011dh, the UV contributes a significant fraction of the bolometric flux for a short time after explosion. Due to the putative compact nature of the progenitors of these SNe however, the fraction of the

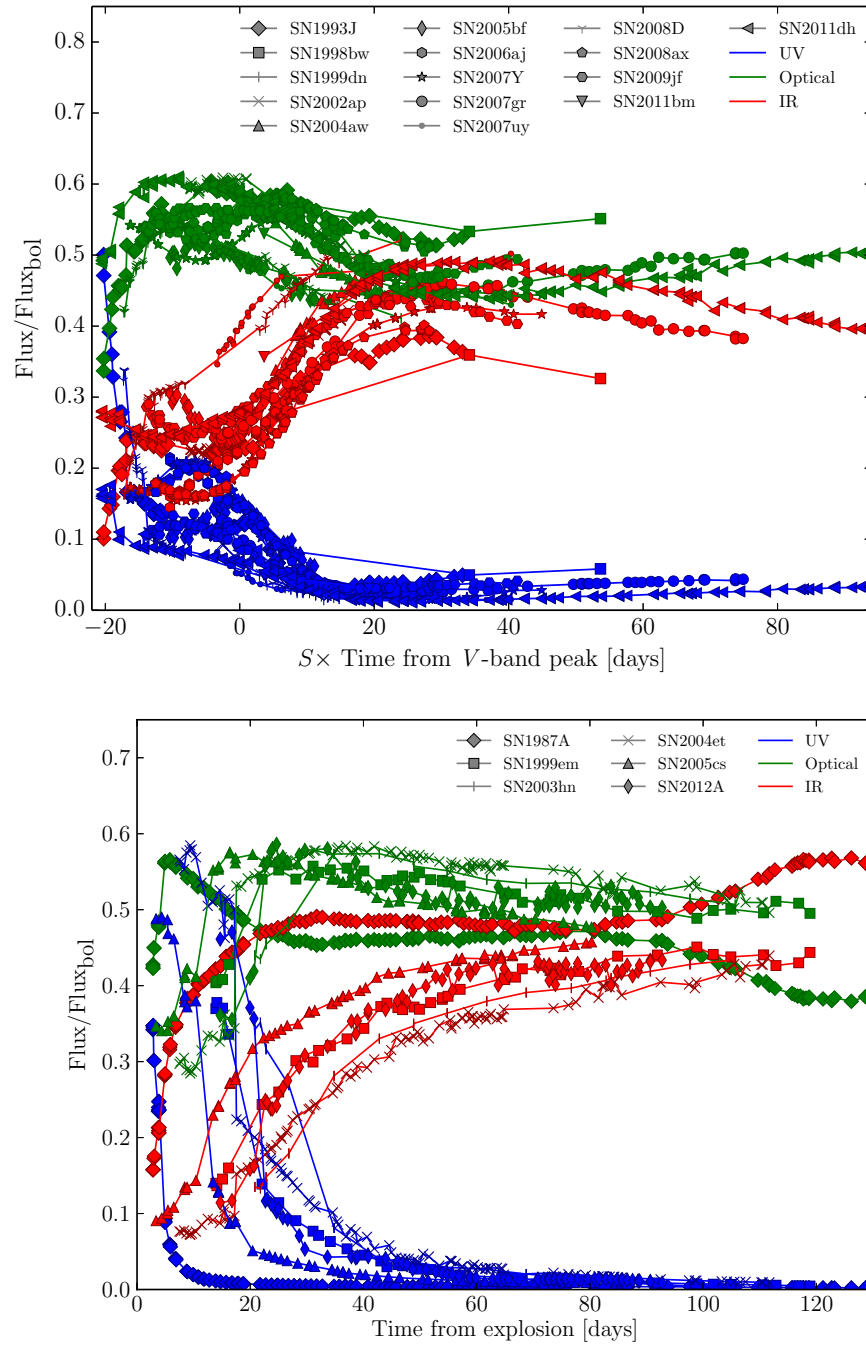


Figure 5.1: The evolution with time of the UV (blue), optical (green), and IR (red) fluxes as a fraction of the bolometric flux for SE SNe (top) and SNe II (bottom). Light curve evolution has been stretched for each SE SNe to a common  $\Delta m_{15,V}$  of 0.758 (see text).

light emitted in the UV falls rapidly.

For SNe II we see largely coherent behaviour amongst the sample in the three regimes, albeit very different from that of SE SNe. The IR rises almost monotonically from explosion until the end of the plateau, where it contributes  $\sim 40$  per cent to the bolometric flux. The optical remains roughly constant with time indicating the BC to optical filters should be roughly constant (e.g. Maguire et al., 2010). The UV contributes a larger fraction than in SE SNe and for a longer time, owing largely to the generally much more extended cooling phase that SNe II exhibit, for example SN2003hn shows significant UV contributions to its bolometric flux ( $\sim 30$  per cent) more than 20 days past explosion. SN1987A, however, is very unusual compared to the other events. Being UV deficient (Danziger et al., 1987), any significant contribution from the cooling phase rapidly falls, with the UV making up only a few percent of the bolometric flux within a week of explosion. The IR of SN1987A also increases much more rapidly than other SNe II, maintaining a similar fraction as that of the optical from 20 days, and overtaking the optical as the dominant regime after  $\sim 80$  days.

## 5.4.2 Optical colours and bolometric corrections

CCSNe evolve strongly in colour during the rise and fall of their brightness. Previous work looking at the optical colours of SE SNe and SNe II (e.g. Maguire et al., 2010; Drout et al., 2011) shows that the colour evolution changes strongly as a function of time. The driving force of these large colour changes during the photospheric evolution of a SN is the change in temperature of the photosphere, with some smaller contribution from development of heavy element features in the spectra. It is expected that the BC should be linked to the colour of the SN (a diagnostic for the temperature) at that epoch. Given the relative ease of obtaining colours for SNe as oppose to characterising entire flux regimes as is given in Section 5.4.1, it is prudent to quantify BCs as functions of the colours sensitive to the SN's temperature (i.e. those in the optical regime).

For filters used in the construction of the SEDs, obtaining the colour at each epoch is trivial. However, when one or both filters are not observed and thus do not form tie points of the flux in the SEDs, we must rely on interpolations. The linear SED interpolations used in order

to integrate over wavelength were used to sample the SEDs at the  $\lambda_{eff}$  of the desired filter, and fluxes in  $F_\lambda$  were then converted to apparent magnitudes. The continuum-dominated SEDs largely do not contain significant fluctuations on the scale of broad-band filter widths between neighbouring broad-band filters and one would not expect large deviations from a linear interpolation between neighbouring filters. In the interest of presenting results that will be useful for future surveys, corrections to Sloan magnitudes were investigated. An analysis of using these linear interpolations to derive Sloan magnitudes is made in Section 5.5.4 by comparing to the expected magnitudes directly from contemporaneous spectra. We find that  $g$  and  $r$  magnitudes are very well estimated by the linear interpolation method; however, there is some systematic offset in  $i$ .

Given the highly uncertain nature of the UV correction, two types of BC were investigated. These are a ‘true’ BC including the UV, and what will be termed a *pseudo*-BC (*pBC*) which will neglect contributions from the UV (i.e. the BB integration to zero Å or linear extrapolation to 2000 Å, see Section 5.3.2) and instead cut-off at the blue edge of the  $U$ -band. This makes the *pBC* independent of the treatment of the UV presented here and makes no attempt to account for these shorter wavelengths, useful in the case where UV observations exist, where indications of unusual UV behaviour are present, or where a complementary treatment of the UV exists that may be added to the *pBC*.

The SEDs were integrated over each of the wavelength ranges to obtain (pseudo-)bolometric fluxes. These were then converted to luminosities, and finally to bolometric (or pseudo-bolometric) magnitudes using:

$$M_{bol} = M_{\odot, bol} - 2.5 \log_{10} \left( \frac{L_{bol}}{L_{\odot, bol}} \right), \quad (5.1)$$

where  $M_{bol}$  and  $L_{bol}$  can be replaced by their pseudo-bolometric counterparts. A BC (or *pBC*) to filter  $x$  can then be defined as:

$$BC_x = M_{bol} - M_x, \quad (5.2)$$

where  $M_x$  is the absolute magnitude of SN in filter  $x$  that has been corrected for extinction (see Section 5.3.2). This definition can also be expressed in observed magnitudes

( $BC_x = m_{bol} - m_x$ ) using the distance modulus for each SN host.<sup>6</sup>

All colours and ( $p$ )BCs in the  $BVRI$  and  $gri$  ranges were computed. For both the  $p$ BC and BC, the tightest correlation for the Johnson–Cousins filters was  $BC_B$  against  $B - I$  colour. For the Sloan filters this was the  $BC_g$  against  $g - i$  colour; however, as detailed in Section 5.5.4, the  $i$ -band derived magnitudes are susceptible to a systematic offset, and as such we present  $g - r$  as the representative fit.

We will limit our discussion here to mainly the BC to  $B - I$ , alongside plotting the BC to  $g - r$  relation for a visual comparison; the parameters for all reasonable  $p$ BC and BC fits, which may be useful in the case where good coverage is not available in either of these filter pairs, are presented in Section 5.4.5.

Furthermore, distinct behaviour was observed for those epochs during the cooling phase (see Section 5.3.2) and subsequent epochs, mainly due to the differing behaviour of the UV and subsequent differing treatment in our method. We thus present the two phases separately and offer distinct fits to each.

### 5.4.3 The radiatively-/recombination- powered phase

Those epochs post cooling from SBO are analysed here. The  $B - I$  and  $g - r$  data for these epochs are plotted in Fig. 5.2 for the BC and Fig. 5.3 for the  $p$ BC.<sup>7</sup> As is evident, even across all SNe types, we find a tight correlation between the ( $p$ )BC, and the respective colour. Such a universal trend of behaviour allows us to construct fits to describe the bolometric evolution of CCSNe for each filter set. The BC has some parabolic evolution evident at blue and very red epochs, and as such a second order polynomial is fitted for the BC in each case.

Equations (5.3) and (5.4) describe the BC fits to the entire sample, which allow a good estimate of a SN’s bolometric magnitude to be made based on the colour in each equation,

$$BC_B = -0.057 - 0.219 \times (B - I) - 0.169 \times (B - I)^2 \quad (5.3)$$

<sup>6</sup>Although the BC is accounting for missing flux, its value can be positive in magnitudes, given the difference in the zeropoints for the filter magnitudes and  $M_{bol}$ .

<sup>7</sup>All plots of BC against a given colour have equal plotted ranges. for ease of comparison.

$$\text{BC}_g = 0.055 - 0.219 \times (g - r) - 0.629 \times (g - r)^2, \quad (5.4)$$

The BC in each case is a tight correlation, with deviations of just  $\sim 0.1$  mag from the best fitting function for even the most extreme objects in each case. The rms scatter and colour range for the  $B - I$  fit are 0.053 mag and  $-0.4$  to 2.8. For the  $g - r$  fit the rms and colour range are 0.070 mag and  $-0.3$  to 1.2.

Despite the generally universal behaviour of the SNe in the sample, there is certainly a difference in scatter and colour range between the two types, with SNe II populating very red regions of the plots, and, although there is no indication for a strong divergence of the SE SNe from the extended behaviour of the SNe II, each SN type should only be trusted over the observed colour range. For these reasons, it is useful to define individual fits for SE SNe and SNe II separately. These are plotted in Fig. 5.4 for each filter set, colour-coded by type and with the individual fits to SE SNe and SNe II shown. As is clear from these fits, there is good agreement between the two samples over the range of colours for which the samples overlap.

The equations describing the SE SN-sample fits shown in Fig. 5.4 are:

$$\text{BC}_B = -0.055 - 0.240 \times (B - I) - 0.154 \times (B - I)^2 \quad (5.5)$$

$$\text{BC}_g = 0.054 - 0.195 \times (g - r) - 0.719 \times (g - r)^2, \quad (5.6)$$

and for the SNe II sample, the fits are:

$$\text{BC}_B = 0.004 - 0.297 \times (B - I) - 0.149 \times (B - I)^2 \quad (5.7)$$

$$\text{BC}_g = 0.053 - 0.089 \times (g - r) - 0.736 \times (g - r)^2 \quad (5.8)$$

As might be expected given their more homogeneous evolution, SNe II appear to evolve extremely similarly (including SN1987A, which displayed a very unusual light curve) until the end of the plateau, the time range over which this analysis is made. This confirms the coherent behaviour of SNe II-P shown by [Bersten and Hamuy \(2009\)](#) and indicates that colour is a very good indicator of the BC for SNe II. We present the bolometric light curve

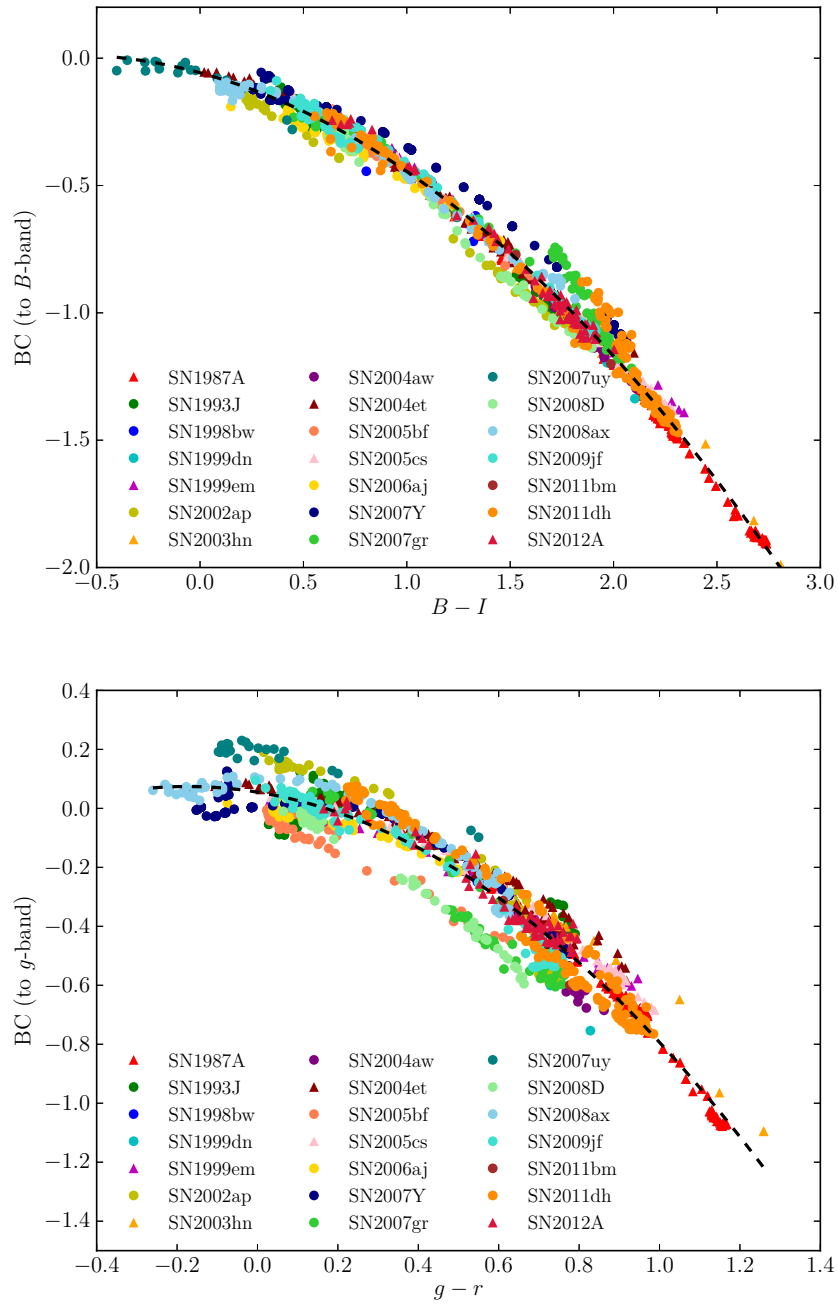


Figure 5.2: BC for all SNe in the sample presented for a relation in the Johnson–Cousins (top) and Sloan (bottom) filters. Epochs shown *do not* include those exhibiting signatures of strong cooling after SBO. SNe II are denoted by triangles. A best-fitted second order polynomial is shown for each (see text).

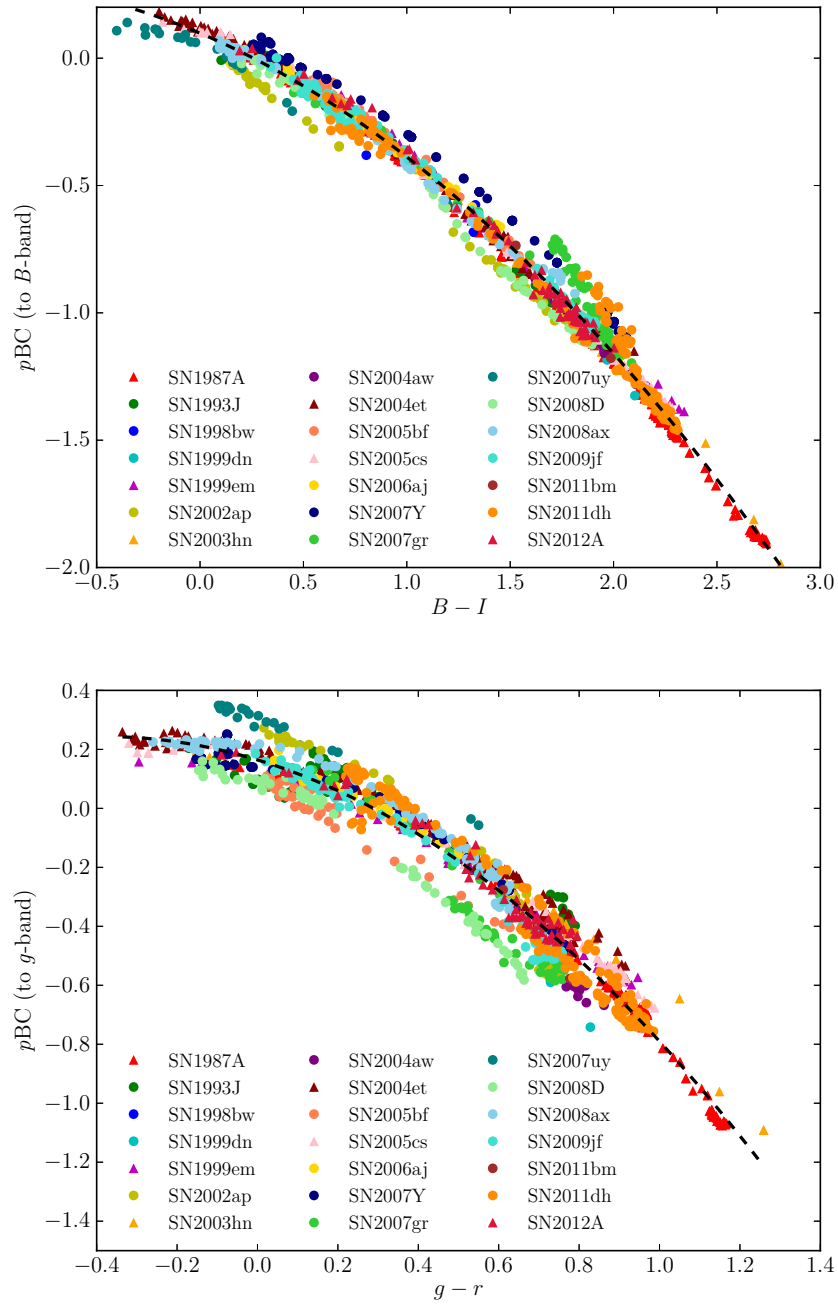


Figure 5.3:  $pBC$  for all SNe in the sample presented for a relation in the Johnson–Cousins (top) and Sloan (bottom) filters. Epochs shown include those exhibiting signatures of strong cooling after SBO, since the UV is not accounted for in the  $pBC$ . SNe II are denoted by triangles. A best-fitted second order polynomial is shown for each (see text).

of SN1987A constructed using the fits of [Bersten and Hamuy \(2009\)](#) and those presented here in [Section 5.6](#). We find a simple second-order polynomial sufficient to define the BC from our colours with a larger sample (up until the end of the plateau), which means the bolometric light curve of a SN II can be robustly estimated from just two-filter observations with minimal scatter in the relation. An increase in sample size is obviously desired to improve and confirm this relation across the family of SNe II.

SE SNe are an inherently diverse range of explosions given their various expected progenitor channels; notwithstanding this, we still see evolution remarkably well described by a second-order polynomial in each colour. Rather the opposite of investigating a “typical” SE SNe sample, we here show many unique and unusual outbursts, which suggests that the spread observed here is plausibly close to the worst-case scenario of uncertainties on computing a bolometric magnitude for a given SE SN that is constrained only in the optical. SN2007uy appears as somewhat of an outlier from the SE SNe fit and this SN is discussed further in [Section 5.5.1](#).

For the fits to  $B - I$  the rms values are 0.061 and 0.026 mag for SE SNe and SNe II, respectively. The SE SN (SN II) fit is valid over the  $B - I$  colour range  $-0.4$  to  $2.3$  ( $0.0$ – $2.8$ ).

For the fits to  $g - r$  the rms values are 0.076 and 0.036 mag for SE SNe and SNe II, respectively. The SE SN (SN II) fit is valid over the  $g - r$  colour range  $-0.3$  to  $1.0$  ( $-0.2$  to  $1.3$ )

#### 5.4.4 The cooling phase

Due to the different treatment of the UV during the cooling phase of SNe evolution from that at later phases, where the BB approximation is more valid than a linear interpolation, we find these epochs require a separate treatment as they are not well described by the parabolas given in [Section 5.4.3](#). This is clearly displayed [Fig. 5.5](#), where the epochs over the cooling phase are plotted alongside the data from the radiative and recombination epochs. The fact this cooling phase forms a ‘branch’ in this plot rather than an extension in colour

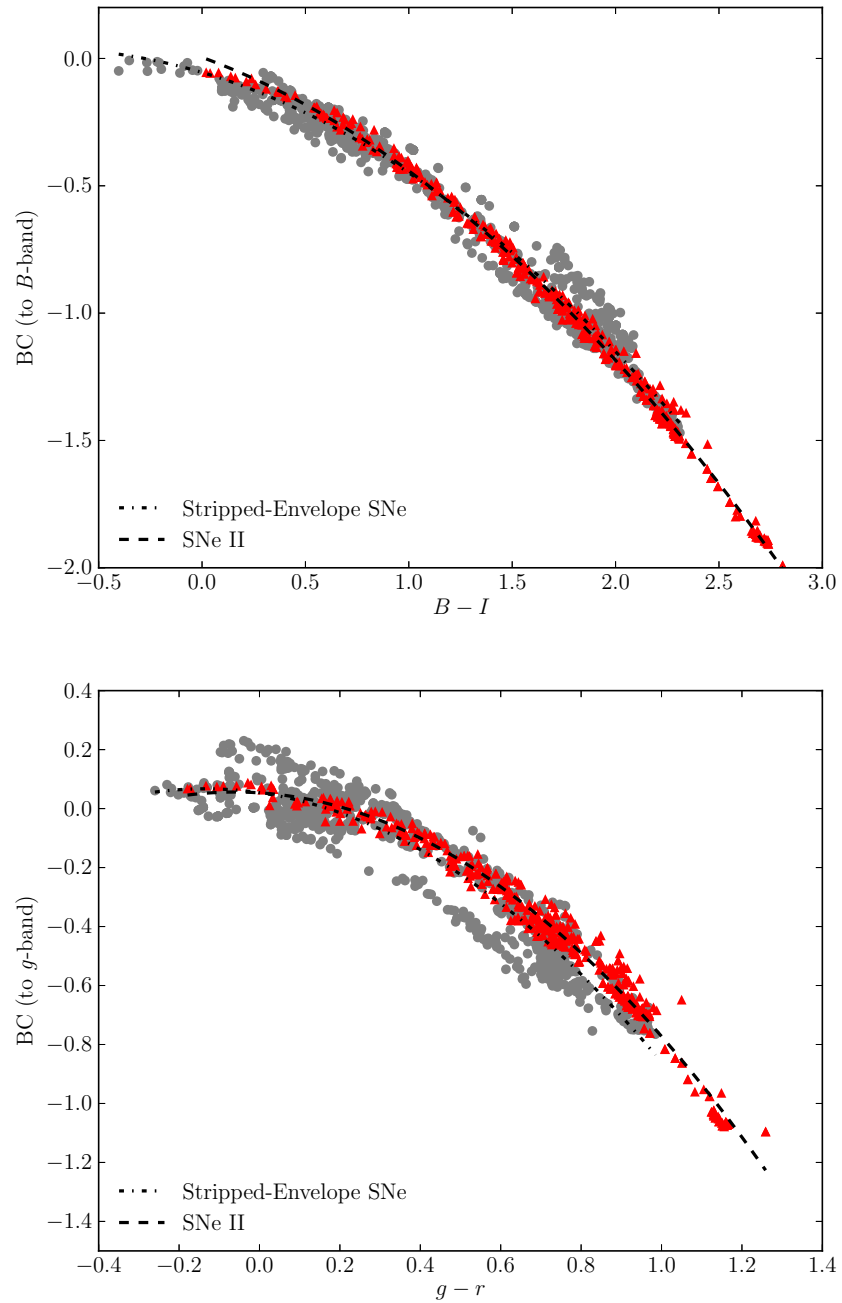


Figure 5.4: As for Fig. 5.2 but SNe are split between SNe II (red triangles) and SE SNe (Ib/c, IIb; grey circles) with a best-fitting second-order polynomial constructed for each SN type. Epochs shown *do not* include those exhibiting signatures of strong cooling after SBO.

also prompts a separate fit, since the cooling phase occurs over the same optical colours as the later evolution for some SNe. We follow the same procedure as in Section 5.4.3 and fit parabolas to the cooling phase data for each colour. Separate fits for SE SNe and SNe II were not done due to the low number of points. The fitted functions are:

$$\text{BC}_{B,\text{cool}} = -0.473 + 0.830 \times (B - I) - 1.064 \times (B - I)^2 \quad (5.9)$$

$$\text{BC}_{g,\text{cool}} = -0.146 + 0.479 \times (g - r) - 2.257 \times (g - r)^2 \quad (5.10)$$

The rms value for  $B - I$  ( $g - r$ ) is 0.072 (0.078) and the colour range is  $-0.2$  to  $0.8$  ( $-0.3$  to  $0.3$ ). The cooling branch, as expected, is only observed over the bluer colours of SNe evolution, and shows a larger scatter than the later epochs for each colour, which is reflected in the generally larger rms values of the fits given in Section 5.4.5. The reader's attention is drawn to Section 5.5.1 for a discussion of the UV treatment in this regime.

### 5.4.5 Fits to other colours

Following [Bersten and Hamuy \(2009\)](#), we present all calculated fits for our BC and  $p\text{BC}$  as tables of coefficients to the polynomials:

$$\text{BC}_x = \sum_{i=0}^2 c_i (x - y)^i \quad (5.11)$$

$$p\text{BC}_x = \sum_{i=0}^2 c_i (x - y)^i \quad (5.12)$$

where  $\text{BC}_x$  and  $p\text{BC}_x$  are the bolometric and  $p\text{BC}$  to filter  $x$ , based on colour  $x - y$ . The coefficients are presented in Tables 5.2 and 5.3 for SE SNe and SNe II respectively. The parameters for the BC appropriate during the cooling phase are provided in Table 5.4, note these are appropriate for both SE SNe and SNe II, as we neglect to divide the sample by type during this phase due to the small numbers involved. Also given are the colour ranges over which the fitted data extend and rms values of the fits in magnitudes.

Note that the data used to produce the  $g - r$  fits were corrected for the systematic offset found

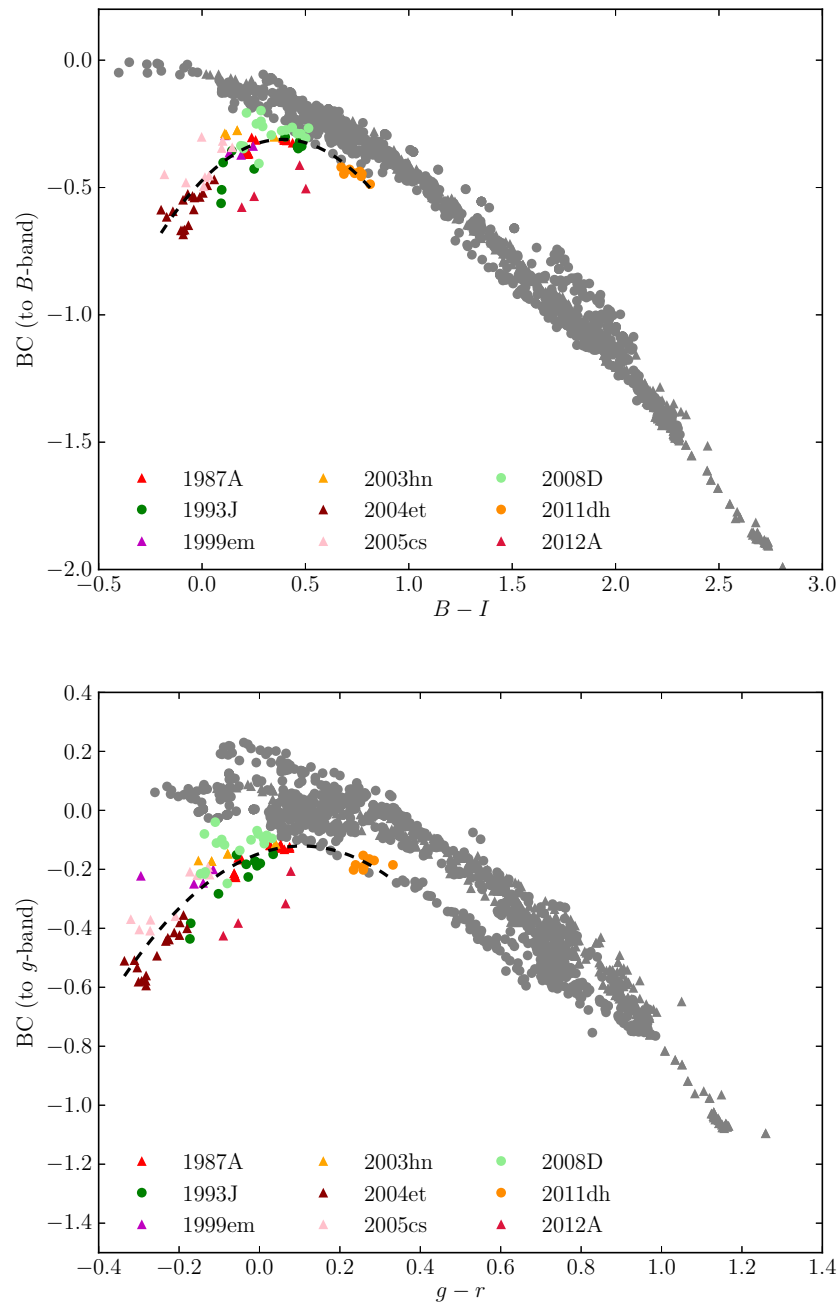


Figure 5.5: As for Fig. 5.2 (grey markers), overlaid with those epochs which exhibit the signature of strong cooling after SBO emission. As is clear these epochs do not occur at unique colours, and as such a separate fit must account for this phase of evolution. A best-fitted second-order polynomial is shown for each, fitted to all SNe types (see text).

when estimating  $i$ -band fluxes from a linear interpolation of the SED, see Section 5.5.4 for more details. However, it was found that the  $g - i$  relation has the smallest intrinsic scatter of any colours investigated here, and a fit to this colour should be reassessed once a data set of SNe observed in Sloan filters with good UV/NIR coverage exists.

Fits to  $R - I$  and  $r - i$  were calculated, but the scatter about these fits was rather larger than the fits presented here, and as such are not included in Tables 5.2 to 5.4. The larger scatter is probably due to both of these pairs of filters failing to characterise the peak of the SED at any epoch. As such, a given value for either of these colours has a large uncertainty on the strength of the peak of the SED, where the majority of the flux is emitted, and thus a large uncertainty on the BC (or  $p$ BC).

Table 5.2: Fit parameters for SE SNe. We indicate in bold the fits with the smallest dispersions (see text).

$x$	$y$	$x - y$ range	<b>BC</b>				<b><math>p</math>BC</b>			
			$c_0$	$c_1$	$c_2$	rms	$c_0$	$c_1$	$c_2$	rms
$B$	$V$	0.0–1.3	-0.083	-0.139	-0.691	0.109	+0.076	-0.347	-0.620	0.112
$B$	$R$	0.1–2.0	-0.029	-0.302	-0.224	0.069	+0.136	-0.464	-0.181	0.067
$B$	$I$	-0.4 to 2.3	-0.055	-0.240	-0.154	<b>0.061</b>	+0.097	-0.354	-0.131	<b>0.064</b>
$V$	$R$	-0.2 to 0.7	+0.197	-0.183	-0.419	0.101	+0.299	-0.372	-0.358	0.087
$V$	$I$	-0.7 to 1.1	+0.213	-0.203	-0.079	0.090	+0.306	-0.283	-0.084	0.072
$g$	$i$	-0.8 to 1.1	-0.029	-0.404	-0.230	<b>0.060</b>	+0.051	-0.511	-0.195	<b>0.055</b>
$g$	$r$	-0.3 to 1.0	+0.054	-0.195	-0.719	0.076	+0.168	-0.407	-0.608	0.074

Table 5.3: Fit parameters for SNe II. We indicate in bold the fits with the smallest dispersions (see text).

$x$	$y$	$x - y$ range	<b>BC</b>				<b><math>p</math>BC</b>			
			$c_0$	$c_1$	$c_2$	rms	$c_0$	$c_1$	$c_2$	rms
$B$	$V$	0.0–1.6	-0.138	-0.013	-0.649	0.094	+0.058	-0.331	-0.520	0.092
$B$	$R$	0.1–2.5	+0.004	-0.303	-0.213	0.037	+0.124	-0.406	-0.191	0.038
$B$	$I$	0.0–2.8	+0.004	-0.297	-0.149	<b>0.026</b>	+0.121	-0.387	-0.131	<b>0.028</b>
$V$	$R$	0.0–0.9	+0.073	+0.902	-1.796	0.050	+0.059	+1.039	-1.958	0.060
$V$	$I$	0.0–1.2	+0.057	+0.708	-0.912	0.043	+0.065	+0.744	-0.953	0.053
$g$	$i$	-0.5 to 1.4	-0.007	-0.359	-0.336	<b>0.022</b>	+0.063	-0.497	-0.268	<b>0.024</b>
$g$	$r$	-0.2 to 1.3	+0.053	-0.089	-0.736	0.036	+0.165	-0.332	-0.612	0.037

Table 5.4: Fit parameters for the cooling phase, appropriate for both SNe types. We indicate in bold the fits with the smallest dispersions (see text).

			<b>BC</b>			
$x$	$y$	$x - y$ range	$c_0$	$c_1$	$c_2$	rms
$B$	$V$	-0.2 to 0.5	-0.393	+0.786	-2.124	0.089
$B$	$R$	-0.2 to 0.8	-0.463	+0.790	-1.034	0.078
$B$	$I$	-0.2 to 0.8	-0.473	+0.830	-1.064	<b>0.072</b>
$V$	$R$	0.0–0.4	-0.719	+4.093	-6.419	0.125
$V$	$I$	0.0–0.4	-0.610	+2.244	-2.107	0.146
$g$	$i$	-0.7 to 0.1	-0.158	-0.459	-1.599	<b>0.069</b>
$g$	$r$	-0.3 to 0.3	-0.146	+0.479	-2.257	0.078

## 5.5 Discussion

Our results show that it is possible to obtain the full bolometric flux of a CCSN from two-filter observations through a simple second-order polynomial correction. Here we will discuss aspects of the results in terms of the BC, although they also largely apply to the  $p$ BC relation as well (excluding discussion of UV treatment).

We observe differing scatter for the two samples. As mentioned, SNe II are expected to be a more homogeneous type of explosion, with the large hydrogen-rich envelopes of the progenitors upon explosion meaning continuum-dominated emission occurs throughout the plateau. The expected sphericity (and likely single-star nature) of the events also means viewing angle will introduce little if any scatter in the relations. We see extremely similar evolution across our SN II sample, even the peculiar SN1987A. The SE SNe are subject to other factors that could explain the increased scatter we observe in their relations. First, several progenitor channels are proposed and it is likely that a combination produce the SNe we observe. Binarity and rotation of the progenitor and the intrinsic asphericity of the explosions (e.g. [Maeda et al., 2002](#)) are all likely to contribute to scatter in the BC across the sample. High-energy components (e.g. gamma-ray burst afterglow components) could be expected also to affect the colours of the SNe. For example we see that SN2008D lies somewhat below the general trend in the  $g - r$  fit, and to a lesser extent in  $B - I$  fit, as shown in Fig. 5.2, although other SNe with high-energy components are well described by

the fit (e.g. SNe 1998bw and 2006aj). The stripped nature also introduces a range of possible evolution time-scales as more highly stripped progenitors will reveal their heavier elements earlier than those retaining more of their envelopes, making their spectra potentially diverge from homogeneous evolution due to the different chemical composition and pre-mixing of the progenitors.

A factor that could affect the evolution of any SN is the CSM into which it is expanding. Although we have ruled out SNe that show strong interaction with their surrounding medium, in reality, all SNe will have some level of interaction that is dictated by density and composition of the CSM; this being linked to the mass-loss of the progenitor system in the final stages of its evolution. Again, this may affect the SE SN sample more markedly than SNe II, which are expected to have retained the vast majority of their envelopes until explosion.

### 5.5.1 Treatment of the UV/IR

Some extremely well-observed SNe have observations that show that the bulk of the light is emitted in the near-ultraviolet (NUV) to NIR regime. The observed wavelength range investigated here stops at 24400 Å due to a paucity of data in wavelengths redder than this for CCSNe. Ergon et al. (2013) show that the MIR regime contributes at most few per cent to their UV-MIR light curve of SN2011dh and the contribution diminishes to negligible values beyond these wavelengths ( $\sim 1$  per cent). There are no mechanisms producing significant sources of flux at long wavelengths in CCSNe over the epochs investigated here (e.g. Soderberg et al., 2010) and as such the treatment of wavelengths longer than the NIR as a Rayleigh-Jeans law is appropriate.

Wavelengths shorter than the  $U$ -band constitute a significant fraction of the bolometric flux at certain epochs<sup>8</sup> and this fraction is difficult to quantify for a large sample of SNe due to the inherently diverse behaviour, the prospect of strong, very blue emission occurring after the SBO in certain SNe, and the fact it is not a very well observed wavelength range in CCSNe. The validity of the treatment of the UV used here (a BB extrapolation to zero Å

---

<sup>8</sup>We neglect a treatment of very high energy emission since this is insignificant in terms of bolometric luminosity on the time-scales of SN detections.

during the cooling phase and a linear extrapolation to zero flux at  $2000 \text{ \AA}$  for epochs of no strong cooling) was tested using UV observations. Eight SNe of the sample presented (two SNe II and six SE SNe) have sufficient existing *Swift* data, as presented in Pritchard et al. (2013), to test our method. For each SN with UV data, SEDs were constructed using both the method described in Section 5.3.2 and the following: instead of extrapolating the UV flux (using the UV approximation appropriate to each epoch), *Swift* UV observations are added to our SEDs, having corrected their magnitudes for reddening using the same method as for the optical and NIR filters. The large red leak of the *uvw2* filter (as demonstrated in relation to SN2011dh by Ergon et al., 2013) was evident from a strong excess in some SEDs for this filter. For this reason the *uvw2* filter was only used for SNe 2007uy, 2008ax and 2012A in epochs  $< 2$  weeks from detection, when the blue continuum will minimise contamination in *uvw2* from the red leak. Each SED constructed with *Swift* data was tied to  $1615 \text{ \AA}$  (the blue cut-off of *uvw2*) in all cases. The UV luminosities at each epoch were computed in each case via an integration of the wavelengths from  $1615 \text{ \AA}$  ( $2030 \text{ \AA}$  in the linear extrapolation case) to the *U*-band. By comparing the UV luminosity results of each method of SED construction, the accuracy of the UV treatments used here was tested. For a visual representation of the treatment of the UV cf. *Swift* data for SN 2005cs, see Fig. 5.6.

The results of this test are shown in Fig. 5.7 for the  $B - I$  colour. There is generally good agreement between our simple treatments of the UV and when including *Swift* data for the majority of the epochs, with differences in most cases being of the order of a few per cent of the bolometric luminosity. SN2007uy, the SN which shows the largest deviation barring epochs with strong post-SBO cooling (although still  $< 10$  per cent), has extremely large and uncertain reddening (Roy et al., 2013). The larger discrepancy between the linear interpolation and the *Swift* data seen for this SN could be indicative of an incorrect reddening value, or reddening law, but it cannot be ruled out that it is intrinsic to the SN. Contributions from wavelengths shorter than  $1615 \text{ \AA}$  will not contribute much to the bolometric flux except during the cooling phase, when SNe are UV bright. Thus the *Swift* data and, given the good agreement seen, our linear extrapolation method, accounts for the vast majority of the UV flux in a SN.

The cooling branch in this plot, however, displays fairly large discrepancies, even though we

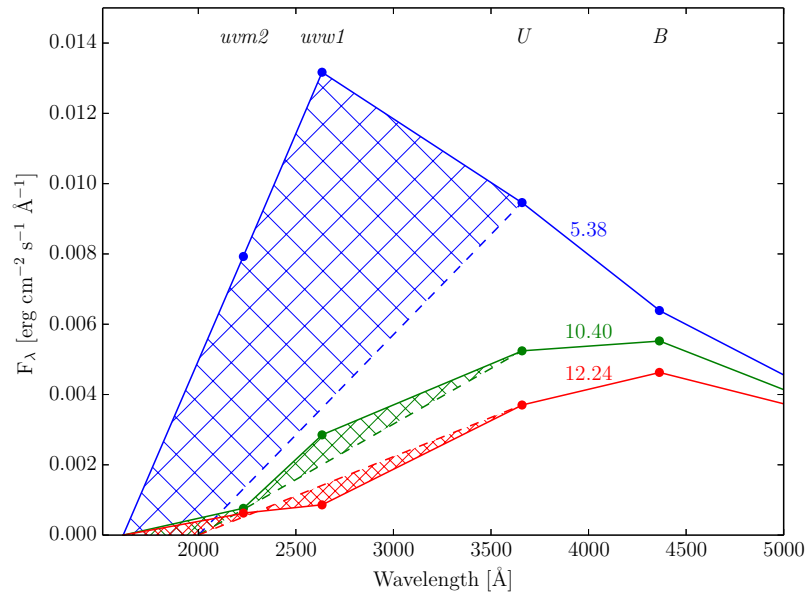


Figure 5.6: The SED of SN 2005cs shown at three early epochs, with the time after explosion given in days above each SED. SEDs including *Swift* data (solid lines) are shown compared to linearly extrapolating the UV from *U*-band to zero flux at 2000Å (dashed lines). The difference between the two methods is highlighted as the hatched region in each case. Clearly, the very early SED of 5.38 days shows the linear method significantly underestimates the true flux – the BB approximation of the UV flux is used in such cases as a better approximation. At 10 days after explosion the linear extrapolation becomes a better approximation, with the two methods of SED construction agreeing well at 12.24 days post explosion and subsequent epochs, when the UV bright cooling emission diminishes in favour of an optically/IR dominated SED (Fig. 5.1).

are unfortunately limited to three SNe (2005cs, 2011dh and 2012A) that have contemporaneous UV–optical–NIR data over the cooling phase. As may be expected from its relatively modest cooling phase, SN2011dh exhibits the best agreement, with even the earliest epochs ( $\lesssim 2$  day after explosion) discrepant by less than 5 per cent at all epochs. The BB treatment of 2005cs and 2012A, both of type II-P, appears to overestimate the UV luminosity at early epochs by 10–20 per cent. An explanation that may account for some of this discrepancy is that the *Swift* SED is tied to zero flux at 1615Å (the limit of the UV integration), whereas the BB will obviously be at some positive flux value. This ‘cutting-off’ of the *Swift* SED is an under estimation of the flux, especially in these extremely blue phases, but a lack of data at shorter wavelengths necessitates this treatment. Two very early epochs of the evolution of SN 2005cs are well matched by the BB treatment however, and it may be that the later

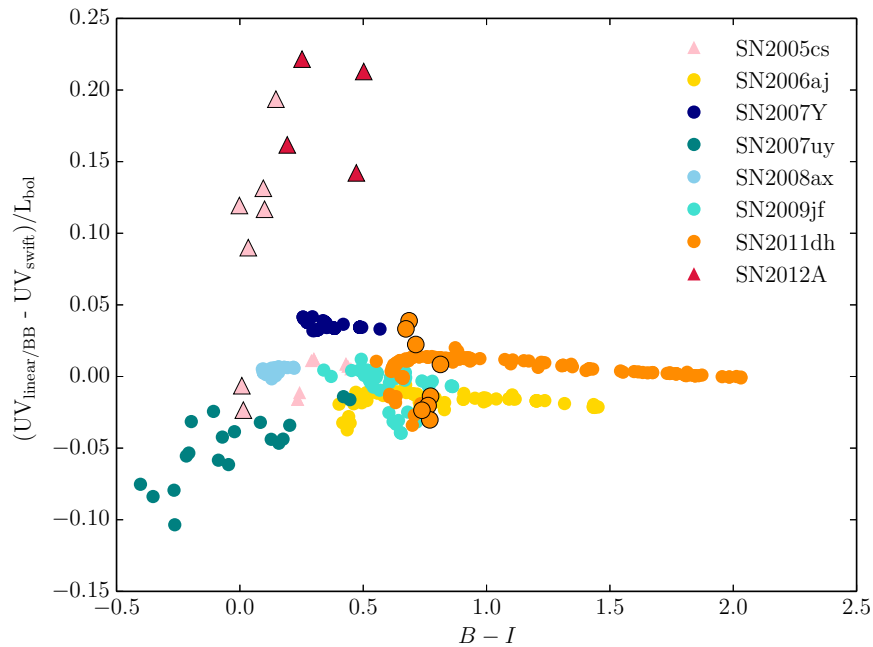


Figure 5.7: The difference between the UV integrated luminosities (as a fraction of the bolometric luminosity) between using *Swift* data in SED construction and the UV treatments presented here. Larger, black-edged points represent the epochs where the BB extrapolation method was used for the UV, whereas smaller points represent a linear extrapolation to  $2000\text{\AA}$  (see Section 5.3.2). The methods are consistent within a few per cent except for the case of strong SBO cooling emission for SNe 2005cs and 2012A.

cooling phase epochs are falling from the BB approximation quicker than expected. The intrinsically heterogeneous nature of this cooling phase is evident in the large scatter observed during these epochs (Fig. 5.5) and we must also add the caveat that our simple UV treatment may be discrepant at the 10–20 per cent level. This discrepancy, however, appears only evident in SNe II-P and at the very early epochs. An increase in sample size is desired to further quantify this and thus improve upon the UV treatment at these epochs. Given this, for events where UV data exist which is indicative of post-SBO cooling emission, it is advisable to use the *pBC* and add the UV contribution directly from observations.

### 5.5.2 Time-scales of validity

It is important to determine over what epoch range these relations are valid for each sample. Fig. 5.8 shows the evolution in time of the SE SNe in the BC plot. The intrinsic scatter

about the fits does not change dramatically with epoch and a largely coherent evolution from top-left to bottom-right in each plot is observed, with very late-time data beginning to move top-left again. The duration of validity after the peak is tied to the time-scale of evolution of the SNe. We have normalised our SE SN evolution by making use of the  $\Delta m_{15,V}$  value for each SN (Section 5.4.1). When evolution is normalised by this factor, the two SNe with the data furthest past peak are SN2011dh ( $\sim 93$  days) and SN2007gr ( $\sim 75$  days). The data representing these late epochs are clearly visible in Fig. 5.8, with the evolution of SN2011dh explicitly shown offset from the data – both show a trend towards moving above (below) the  $B - I (g - r)$  fit at late epochs. Data covering  $U$ -to- $K$  for SN2007gr actually extend to roughly 120 days after optical peak. These data are not included as they diverge from the correlation, as appears to be happening for SN2011dh. SN2011dh and SN2007gr are at the higher end of the  $\Delta m_{15,V}$  range (0.968 and 0.861, respectively) and may be considered to give a good limit for the range of validity of this fit. The data presented show the corrections for SE SNe to be valid from shortly after explosion (earliest data are  $\sim 2$  days post-explosion) to  $\sim 50$  days past peak, and potentially further, although we are limited to analysing only two SNe.

Figure 5.9 shows the evolution of the BC for the SN II sample, where the colour indicates days from explosion date. For the SN II sample we see that even very early data (e.g. beginning at  $\sim 5$  days past explosion for SN1987A) have a small dispersion. Evolution in this plot appears to be simpler than the SE SNe with a smooth transition from top-left to bottom-right. However, SN1987A undergoes a phase of little evolution in colour (and BC) from days  $\sim 40$ – $80$ , with other SNe II displaying a similar period of inactivity in the plot during the plateau phase. Despite the fact that SN1987A also appears to evolve much more rapidly and evolves to much redder colours, as can be seen in Fig. 5.1, its evolution is still remarkably consistent with the other objects in the BC plots, and its additional, redder, evolution follows the parabolic fit. The phase range investigated here is broadly over the plateau of SNe II, after which the deeper layers of the ejecta act to destroy any homogeneous evolution. For example, Inserra et al. (2012) show optical colours for several SNe II-P to late times, with diverse behaviour observed after  $\sim 120$  days (the end of the plateau). This can also be seen in the BCs presented by Bersten and Hamuy (2009), where the BC scatter increases dramatically

after the end of the plateau. We therefore limit the use of these fits from explosion until the time of transition from plateau to radioactive tail.

It must be stressed however that the use of these fits will primarily be for SNe detected only in the optical regime. As such, there is no knowledge of any UV bright SBO cooling emission, given that the optical colour ranges overlap for the cases of strong and no cooling emission (as shown for the fits in Fig. 5.5). Relying only on optical follow up, although vastly increasing the number of SNe with the requisite data, means there is uncertainty in the early light curve. Hence, although the above described fits *are* valid at early epochs, they are valid only for the case of no strong SBO cooling emission. In the case where unobserved SBO emission is present, the fits will under predict the actual bolometric luminosity. In such cases, use of the cooling phase fits will provide an alternate, plausible, bolometric luminosity in these early epochs by assuming the case of strong SBO cooling emission. This uncertainty can be coupled with previous knowledge of the durations of SBO cooling emission and the type of SN. For example, a SN Ib/c would not be expected to have SBO cooling emission beyond 1–2 days and the cooling fit would over estimate the luminosity at further epochs. Complementary data indicative of SBO cooling emission would warrant the sole use of the cooling phase fit for those epochs, or the use of the *p*BC and a separate treatment of the UV emission from the available data. The cooling phase fits include data from early after explosion ( $\sim 2$  days) to the end of the SBO cooling being dominant.

### 5.5.3 Reddening

An uncertainty when constructing the SEDs is the reddening towards each SN. Although Galactic reddening may be well known,  $E(B - V)_{host}$  values are generally less certain. Additional to this, the reddening law for each host is assumed to match that of the Galaxy, an assumption made in the absence of detailed knowledge of the gas and dust properties of the hosts. An increase in assumed  $E(B - V)$  will cause a decrease in  $B - I$  and  $g - r$  (i.e. make the SN intrinsically bluer); this will also affect the BC, however. The BC becomes more positive with increasing  $E(B - V)$  as the  $g$  (or  $B$ )-band value increases more rapidly than the bolometric magnitude for a given change in  $E(B - V)$ . Combining these effects

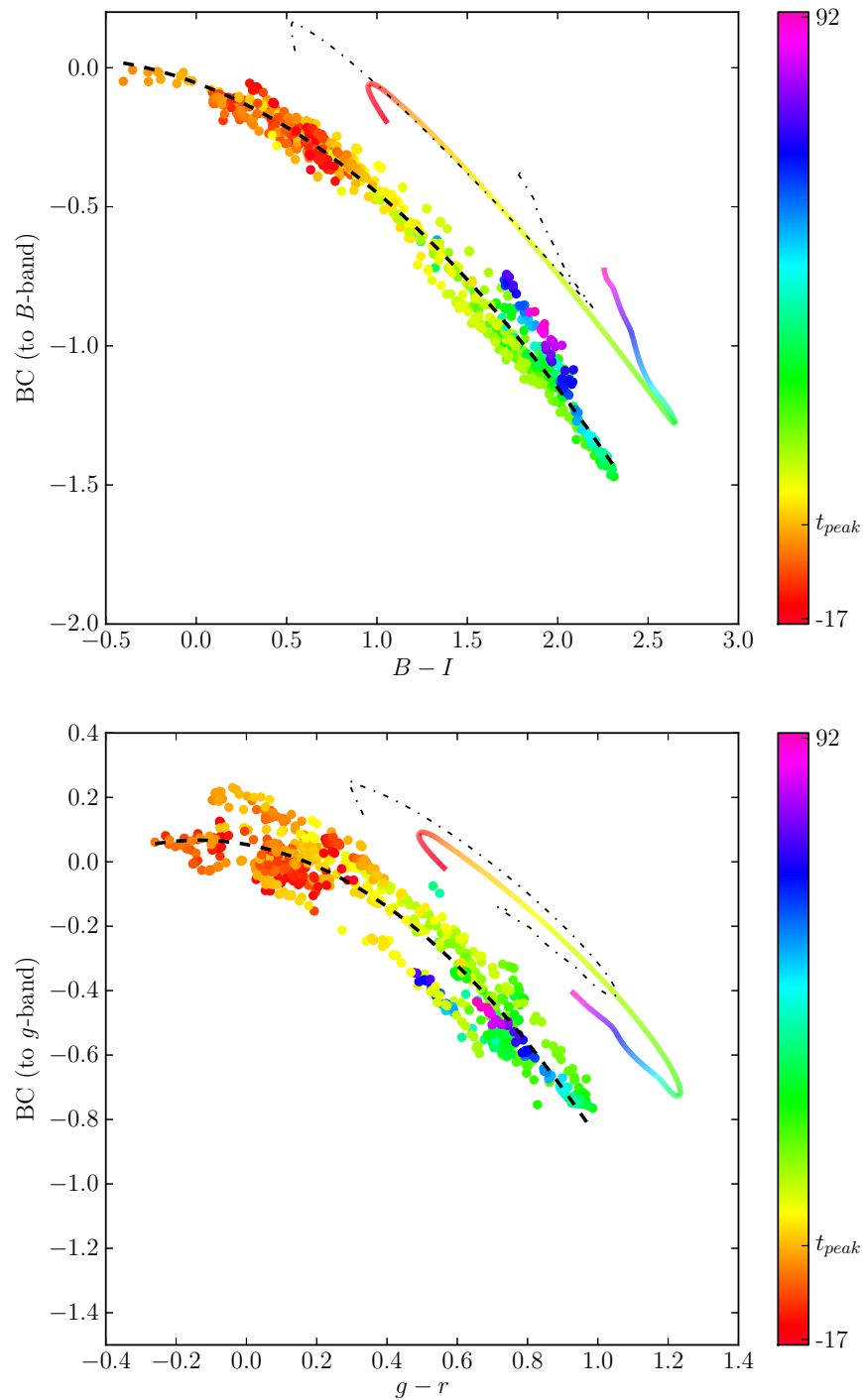


Figure 5.8: The BC for SE SNe, colour-coded to show evolution with time. The colour bar indicates the phase with respect to the  $V$ -band peak ( $t_{peak}$ ), where the SN evolution has been stretched such that  $\Delta m_{15,V} = 0.758$  (see Section 5.4.1). Epochs shown *do not* include those exhibiting signatures of strong cooling after SBO. To illustrate the typical movement of a SN in this plot, the polynomial-smoothed evolution of SN2011dh is plotted offset from the data. The effect of reddening is shown by re-analysing SN2011dh with an increase in  $E(B - V)$  of 0.2 (black dot-dashed line). Eq. 5.6 (top) and Eq. 5.5 (bottom) are also plotted for each filter set (thick black dashed line).

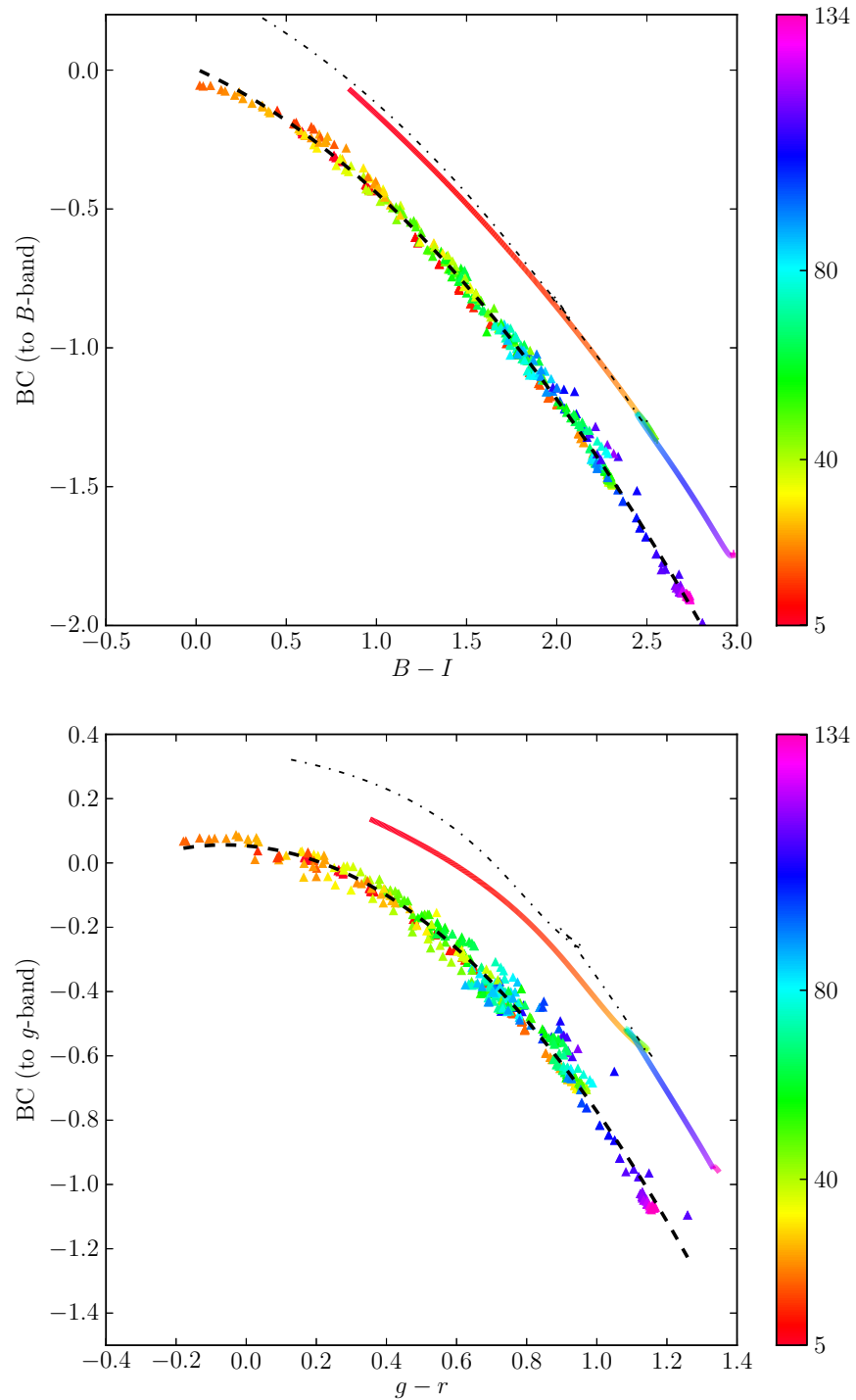


Figure 5.9: The BC for SNe II, colour-coded to show evolution with time. The colour bar indicates the phase with respect to the explosion date. Epochs shown *do not* include those exhibiting signatures of strong cooling after SBO. To illustrate the typical movement of a SN in this plot, the polynomial-smoothed evolution of SN1987A is plotted offset from the data. The effect of reddening is shown by re-analysing SN1987A with an increase in  $E(B - V)$  of 0.2 (black dot-dashed line). Eq. 5.8 (top) and Eq. 5.7 (bottom) are also plotted for each filter set (thick black dashed line).

means that the SNe actually move somewhat along the fits when reddening is varied. This effect is plotted in Figs. 5.8 and 5.9 via an artificial increase of 0.2 in  $E(B - V)$  for the offset SN in each plot. Moderate reddening uncertainties do not affect the actual value of the fits drastically, although clearly an accurate reddening value is desired when using the fits, to ensure the SN's true colour for a given epoch is measured (and consequently the correct value for the BC is used).

The effect of uncertain reddening is largest on the BCs to optical colours with a large  $\lambda_{eff}$  difference between the filters (e.g.  $B - I$ ), since a given change in reddening will affect these colours the most. Taking  $B - I$ , an uncertainty of  $\Delta E(B - V) = 0.2$  mag results in an uncertainty of  $\Delta B - I \simeq 0.5$ . During the early phase of evolution this corresponds to an uncertainty on the BC of  $\sim 0.5$  mag and at later times  $\sim 0.8$  mag (Figs. 5.8 and 5.9). The usefulness of an almost 1 mag error in the decline phase of a CCSN (before including distance uncertainties etc.) is very limited, however a  $\sim 0.5$  mag error in the peak could still be useful for inclusion when studying the behaviour of populations of SNe, but would limit the accuracy of any modelling specific to that explosion. Some reasonable knowledge of the reddening is therefore required to effectively use these BCs, although the colour information shown here may be used to gauge the presence of a large amount of reddening. The behaviour in optical colours of a large sample of CCSNe is shown; should an object display colours not characteristic of this sample at similar phases of evolution (e.g. at peak), or show optical colours outside the ranges shown here, it may be indicative of a mistreatment of the reddening – however the possibility of an intrinsically unusual explosion could not be ruled out. Drout et al. (2011) show a method to obtain a reasonable estimate of the reddening for a SE SN using the  $V - R$  colour 10 days after  $V$ -band peak, extending this to other optical colours would be useful for the BCs presented here.

#### 5.5.4 Extracting Sloan magnitudes from Johnson–Cousins SEDs

It is desirable, particularly given the impending prevalence of their use for large-scale surveys, to present BCs using Sloan filters. The SN sample here, however, is literature-based, and as such is predominantly observed in Johnson–Cousins filters. Sloan magnitudes were

derived for these SNe by extracting fluxes from the SEDs constructed with Johnson–Cousins measurements at the corresponding  $\lambda_{eff}$  of the filters. Large deviations from a linear interpolation between neighbouring filters are not expected since the widths of the filters ( $\sim 2000 \text{ \AA}$ ) are much larger than individual spectral features and there is a large amount of overlap between Sloan filters and their neighbouring Johnson–Cousins counterparts. However, it may be that some systematic error could be introduced by this method, particularly when one considers the effect of the extremely strong  $H\alpha$  emission line in SNe II, or that the strong Ca II NIR triplet absorption borders on the  $I$ -band. These deviations could make the linear interpolation a poor estimate of the true flux in some specific SN types or at specific epochs.

To test the linear interpolation method we have collated all spectra in WISEREP of our SNe sample that cover a sufficient wavelength range (i.e. completely cover the transmission profile of at least one of the  $gri$  filters and the appropriate neighbouring Johnson–Cousins filters) and are at similar epochs to those when the photometric SEDs are constructed (see Table 5.1). Synthetic photometry was performed on the de-reddened spectra (using the  $R = 3.1$  curve of Fitzpatrick 1999) via:

$$F_x = \frac{\int T_x(\lambda) f(\lambda) \lambda d\lambda}{\int T_x(\lambda) \lambda d\lambda} \quad (5.13)$$

to obtain the flux in filter  $x$ , based on spectral flux of the SN,  $f(\lambda)$ , and the transmission profile of filter  $x$ ,  $T_x(\lambda)$ . This was done for each of the  $griBVRI$  filters where spectral coverage allowed. After accounting for the filter zeropoints, a directly measured value of the magnitude in each the filters was obtained. Neighbouring Johnson–Cousins filters were interpolated linearly in flux between their  $\lambda_{eff}$  values such that a flux (subsequently converted to a magnitude) for the appropriate Sloan filter could be made at its  $\lambda_{eff}$  (e.g. flux values for  $B$  and  $V$  were interpolated to obtain an estimate for the  $g$ -band).

The comparison of the Sloan magnitudes found via direct synthetic photometry ( $m_{synth}$ ) and using the linear interpolation method ( $m_{linear}$ ) is presented in Fig. 5.10. Firstly, it was found that there was no dependency on SN type or epoch for the values of  $m_{synth} - m_{linear}$ . Given this, the  $g$  and  $r$  mean offsets fall extremely close to zero, with values of  $-0.019$  (rms  $0.034$ ) and  $0.0004$  ( $0.044$ ) mag respectively. We can therefore say our method is not introducing any systematic offset for quantities reliant on these filters and as such consider the BC and

$p$ BC fits to  $g$  against  $g - r$  colour to be valid.

However, it is true we see some systematic offset in the measurements of the  $i$ -band, with the mean being 0.111 (0.032) mag, despite the Sloan  $i$  and Cousins  $I$ -band transmission curves overlapping heavily. This overestimation of  $i$ -band flux from the linear interpolation method suggests that the  $g - i$  colours derived from SED interpolations are likely to be redder than the intrinsic  $g - i$ . For this reason we increase the magnitude values obtained for  $i$  in our linear interpolation method by the mean offset (0.111 mag), to give estimates that will be free from this systematic offset. These corrected  $i$  values were used when computing fits to  $g - i$  that are presented in Tables 5.2 to 5.4.

The difference in the BC (and  $p$ BC) due to this change in  $i$  values for a given  $g - i$ , when compared to calculating the fits without accounting for the offset, is 0.103 mag for the reddest SE SNe colour (i.e.  $g - i = 1.1$ ), with differences reaching 0.198 mag for the reddest SNe II colours ( $g - i = 1.4$ ). The differences are less for typical SN colours and approaching zero for bluer colours ( $g - i < -0.5$ ). Similarly for the cooling phase fit, differences for the bluest colours ( $g - i < -0.5$ ) reach 0.182 mag, with the average difference being 0.078 mag.

An investigation into this systematic offset in  $i$  showed the choice of  $\lambda_{eff}$  to be mainly responsible. There is no knowledge of the spectral features of a SN based on photometric data, above that which can be discerned from colours. As such we are limited, as has been done in similar previous work, to using a single  $\lambda_{eff}$  for each filter (taken from the literature, or based on the transmission profile), when in reality this should change according to the shape of the underlying spectrum being observed, as in:

$$\lambda_{\text{eff}} = \frac{\int T_x(\lambda) f(\lambda) \lambda^2 d\lambda}{\int T_x(\lambda) f(\lambda) \lambda d\lambda} \quad (5.14)$$

for photon-counting devices (e.g. [Bessell and Murphy, 2012](#)).

It was found that the  $\lambda_{eff}$  for the  $I$ -band when using this equation was particularly susceptible to large deviations compared to the value we used when constructing SEDs, whereas filters  $BVR$  were more stable. This is most likely due to the  $I$ -band being consistently on the ‘tail’ of the flux distribution, coupled with strong absorption due to the calcium triplet

bordering on the red edge of the transmission curve. These effects weight the  $\lambda_{eff}$  to lower values, although no significant dependence on epoch was found either in the change of  $\lambda_{eff}$  or the value of the offset in  $m_{synth} - m_{linear}$  for  $i$ . This change in  $\lambda_{eff}$  obviously impacts on the gradient of the linear interpolation between  $R$  and  $I$ , and hence on the estimate of  $i$ . When accounting for the changing  $\lambda_{eff}$ , the mean systematic offset in  $i$  was more than halved, whilst  $g$  and  $r$  remained very close to zero. However, we take no account of changing  $\lambda_{eff}$  in our SED construction since we have no a priori information on spectral shape from photometry. Hence we opt not to include it here in our test of the method, but present these findings to highlight the potential uncertainties in the choice of  $\lambda_{eff}$  when constructing SEDs from photometric data for SNe.

We therefore conclude that the determination of Sloan magnitudes derived from our method of linearly interpolating the SEDs constructed with Johnson–Cousins filters is robust *for the cases of  $g$ - and  $r$ -bands*, however *there is a systematic offset in the  $i$ -band magnitude determination* from the two methods. We neglect to correct our derived  $g$ - and  $r$ -band magnitudes, given the mean difference is very close to zero in both cases, but do correct our  $i$ -band measurements by the mean offset before calculating fits based on this filter. It is obviously desirable to reassess the fits to these filters once an appreciable data set of SNe observed directly in Sloan filters with good NIR (and ideally UV) coverage exists.

## 5.6 SNe 1987A and 2009jf and PTF 12dam – test cases

In order to practically test the reliability of the fits, we recover the bolometric light curves of one SN in each sample as well as a recently observed super-luminous SN (SLSN).

### 5.6.1 SN 1987A

Being the best observed SN to date, SN 1987A represents a good test of the method. Here we reconstruct the bolometric light curve of SN 1987A using the optical photometry of [Menzies et al. \(1987\)](#). Extinction was corrected for using  $E(B - V) = 0.17$  and the procedure

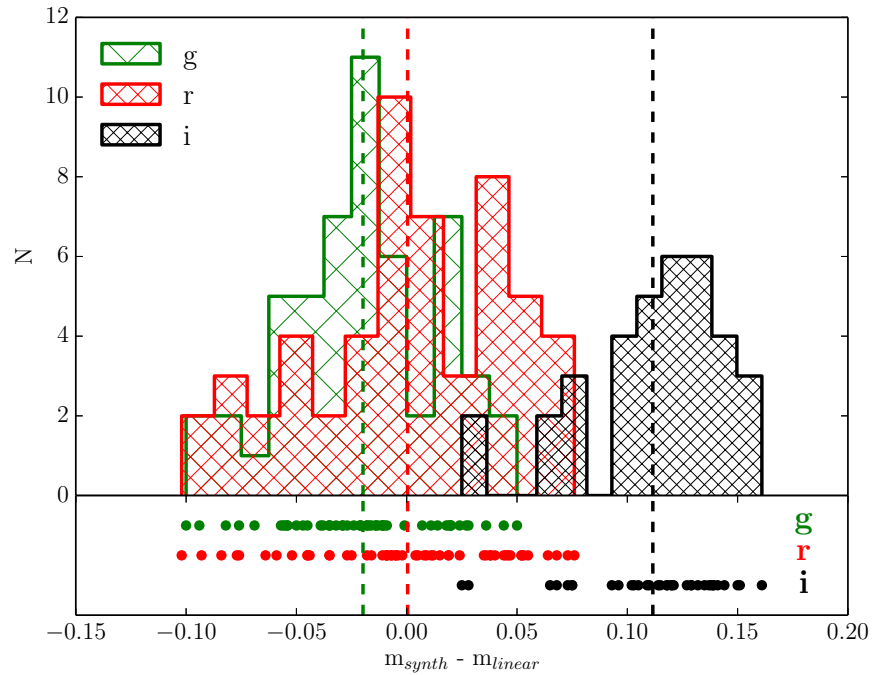


Figure 5.10: Residuals found between obtaining Sloan synthetic magnitudes from spectra ( $m_{\text{synth}}$ ) and those using a linear interpolation from neighbouring Johnson–Cousins filters ( $m_{\text{linear}}$ ) for all spectra of the SN sample during the epochs where SEDs have been constructed in the main investigation. The mean values for the three distributions are marked as the vertical dashed lines.

described in Section 5.3.2. Two fits with differing rms values were used:  $B - V$  and  $B - I$ . Eq. 5.11 was used with the appropriate fit parameters (the first 2.1 days were calculated with the cooling phase fits given in Table 5.4, subsequent epochs used the appropriate BC in Table 5.3) to turn each of these colours into a bolometric magnitude using Eq. 5.2. Using a distance modulus of  $\mu = 18.46$ , this was converted to an absolute magnitude and then to a bolometric luminosity via Eq. 5.1. Alongside this we also make use of the BC presented in Bersten and Hamuy (2009) to reproduce their bolometric light curve for SN 1987A. Finally we also use the data of Suntzeff and Bouchet (1990) for the UV-optical-IR observed bolometric light curve of SN 1987A for comparison.

The four bolometric light curves of SN 1987A are shown in Fig. 5.11. First to note is the good agreement between all four methods, and particularly the agreement between the BC methods and the observed bolometric light curve. The extremely early data  $<1$  day are slightly underestimated, and we again stress here the caveat that emission from cooling post-

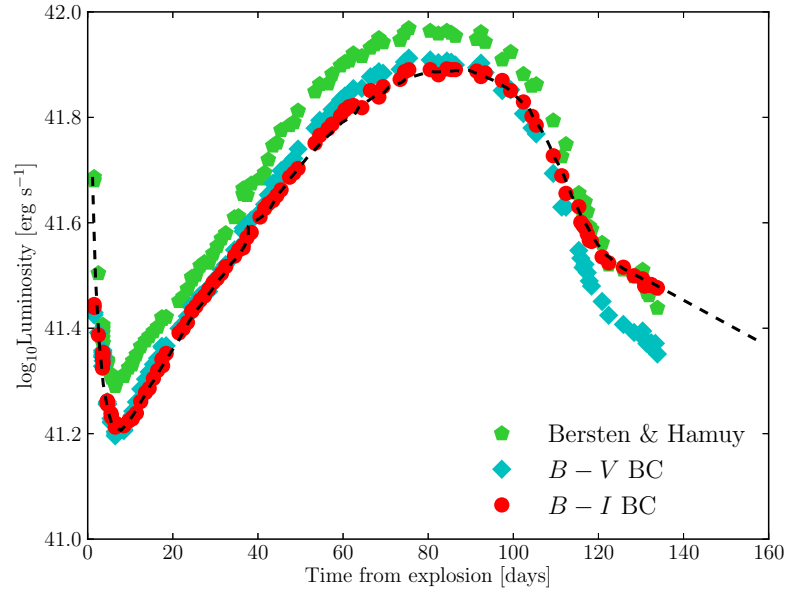


Figure 5.11: The bolometric light curve of SN 1987A constructed from optical colours using the  $B - I$  and  $B - V$  corrections presented here, and the fit of [Bersten and Hamuy \(2009\)](#). Also plotted is the observed bolometric light curve of [Suntzeff and Bouchet \(1990\)](#) (black dashed line).

SBO is subject to larger uncertainties when using these fits. After this, including the tail of the cooling phase, we observe excellent agreement over the rest of the evolution. Although our IR extends nominally to infinity, the observed data stop in the MIR. The excellent agreement between our  $B - I$ -derived bolometric luminosity and the observed bolometric light curve thus suggests that these very long wavelengths make little difference to the bolometric flux, and certainly not at a level to affect derived parameters from modelling.

Happily enough, we also note that when using a fit with larger scatter (i.e.  $B - V$ ), we recover a bolometric light curve consistent to that produced by the  $B - I$  fit and, importantly, the observed light curve. Some deviation is observed  $>110$  days and this is most likely a result of the two relatively blue filters used in this colour not tracing the evolution of the IR particularly well.

### 5.6.2 SN 2009jf

SN 2009jf has good coverage over rise, peak and decline in *UBVRIJHK* filters (used to construct the SED in Section 5.3.2). However, alongside these data there exists a set of well-calibrated Sloan observations (Valenti et al., 2011), including good *g*- and *r*-band coverage from which to test the Sloan fit – both in terms of the actual fits as well as using the SED interpolations to extract Sloan magnitudes. The *g* and *r* data were used to construct the pseudo- and full bolometric light curve of SN 2009jf.

Initially the *g* and *r* data of Valenti et al. (2011) were corrected for reddening, which was done in the manner of Section 5.3.2 with  $E(B - V)_{\text{tot}} = 0.117$  mag. For epochs of simultaneous *g*- and *r*-band observations, *g* – *r* values (corrected for reddening) were fed into Eqs. (5.11) and (5.12) using the parameters in Table 5.2 to obtain values of the BC and *p*BC, these were converted into apparent bolometric and pseudo-bolometric magnitudes via Eq. 5.2 using the *g* magnitudes. The distance modulus ( $\mu = 32.65$ ) converted these to an absolute magnitudes, and finally Eq. 5.1 was used to convert this to a luminosity.

The SED (constructed as in Section 5.3.2) was integrated from 2000 Å to infinity and the *U*-band to infinity to obtain the observed bolometric and pseudo-bolometric light curves from *U*-to-*K* photometric data.

A comparison of the two methods’ results of producing the pseudo-bolometric light curve is shown in Fig. 5.12. As is clear, with only *g* and *r* filter observations and the method presented here, an excellent estimation of the pseudo-bolometric luminosity can be obtained, even including uncertainties of extracting Sloan magnitudes from linear interpolation of a Johnson–Cousins SED (Section 5.5.4). Plotting the bolometric and pseudo-bolometric light curves highlights the contribution of the UV shown in Fig. 5.1, with an appreciable contribution diminishing to negligible values soon after peak – where the pseudo- and bolometric points overlap.

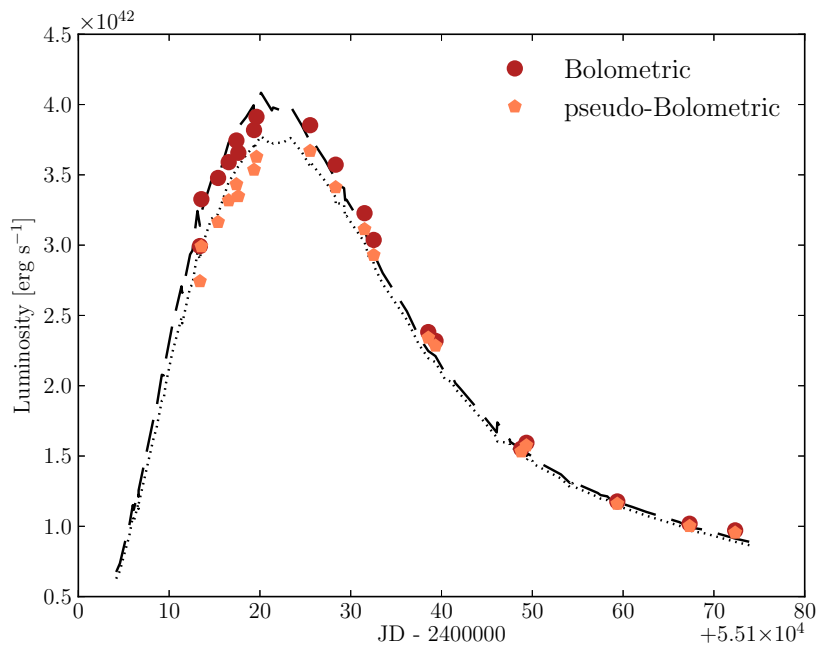


Figure 5.12: Comparison of the observed bolometric and pseudo-bolometric light curves found by SED integration (dashed and dotted lines respectively) with the bolometric and pseudo-bolometric light curves constructed using the BC and  $p$ BC fits to  $g - r$  (circles and pentagons respectively) for SN 2009jf.

### 5.6.3 PTF 12dam

SLSNe are defined as such by having  $M \leq -21$  and have been divided into 3 main subtypes (see Gal-Yam, 2012). PTF 12dam occurred in a host galaxy at  $z = 0.107$  and peaked at  $M \sim -21.3$ , securing its status as a SLSN. The slowly fading nature of the light curve suggests a common explosion mechanism to SN 2007bi, i.e. pair-instability SN (PISN Gal-Yam et al., 2009), but Nicholl et al. (2013) find the rapidly rising light curve to be incompatible with PISN models and favour a magnetar powered SN. Notwithstanding the unknown and potentially exotic nature of the explosion, the excellent data coverage of PTF 12dam presented in Nicholl et al. (2013) is used to compare the method to the observed bolometric light curve of this SLSN. The observed bolometric is constructed from UV to NIR wavelengths, with the bolometric light curve construction process detailed in Nicholl et al. (2013) (although broadly the same method as presented here is used). The comparatively large redshift means the UV, as observed by *Swift*, is probed to very short wavelengths. This cosmological distance also means that  $K$ -corrections must be applied to the optical photometry

before using the colours in the BC equations and the values found in Nicholl et al. (2013) are used. PTF 12dam was observed in the Sloan filters and as such we make use of the  $g - r$  and  $g - i$  fits presented here. The fits used were those applicable for SE SNe since PTF 12dam showed no hydrogen or helium in its spectra – making it spectrally similar to a SN Ic. The results are presented in Fig. 5.13. The fits generally reproduce the observed light curve well over the majority of the SN’s evolution. It must be emphasised here that the errors quoted on the values obtained from the fits only take into account the error on the colour (from the photometry) and thus the uncertainty on the value of the BC derived from the fit. Late time data appears to deviate and may be an indication of a transformation into the nebular phase, where the fits would not be expected to work. Early data is not well fit but is also subject to large uncertainties. This disagreement could be surmised from a comparison between Fig. 5.1 and figure 7 of Inserra et al. (2013), who plot the UV/optical/IR contributions to SLSNe. Early epochs for SLSNe, prior to peak, appear much more UV bright, at the expense of the IR, when compared to the SE SNe investigated here. The cooling branch fit of  $g - r$  is plotted for interest, which gives an accurate, if not precise, representation of the early data. The huge uncertainties in the early epoch data make it difficult to place any confidence or significance on this agreement beyond happenstance (although it would favour the SLSN SED being well described by a BB in the UV at these epochs). Nevertheless, the good agreement found around peak light means these fits can also be used to construct bolometric light curves of at least one type of SLSN (PTF 12dam is the only SLSN observed over an appreciable wavelength range as to make a observed bolometric light curve to compare to). This is of particular importance during this data-starved era for SLSN studies.

## 5.7 Summary

We have presented simple fits making it possible to easily obtain accurate estimates of the bolometric light curves of any CCSN given only two filter observations. We have presented both Johnson–Cousins and Sloan colour corrections and shown our method for determining Sloan magnitudes is robust for  $g$  and  $r$ , and accounted for the systematic offset present in  $i$ -band determinations. Fits to  $B - I$  and  $g - r$  are presented as the best fits to each filter

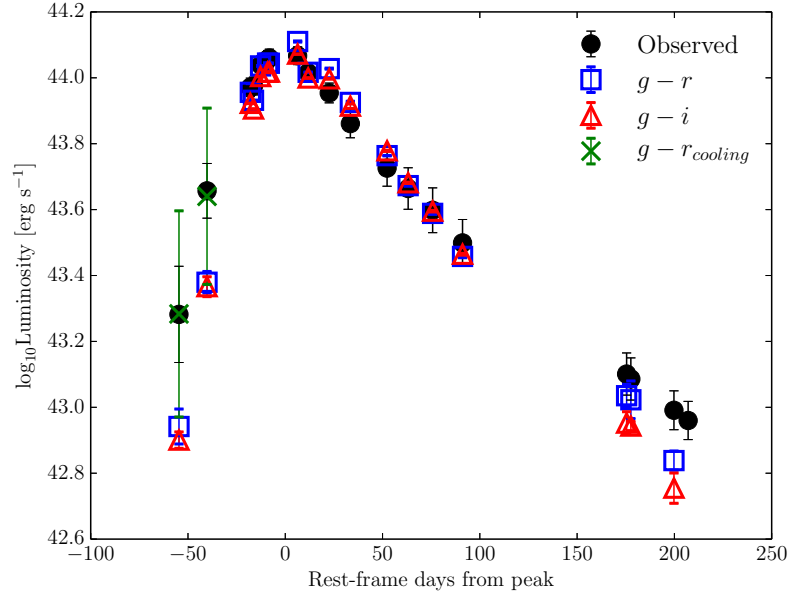


Figure 5.13: Comparison of the observed bolometric light curve (black circles) with the bolometric light curve recovered using the  $g-r$  and  $g-i$  fits (blue squares and red triangles respectively). Good agreement between each fit and the observed data is found. Very late time data  $>150$  days past peak is not well fit, as may be expected if the limits of SE SN agreement were applied to this SN (see Section 5.5.2). Very early data is not well fit, albeit there are large errors on the SED construction. The cooling phase fit for  $g-r$  is shown for the two earliest epochs (see text).

set. The SE SNe corrections (Eqs. (5.5) and (5.6)) are constrained in the colour ranges  $-0.4 < B-I < 2.3$  (rms 0.061 mag) and  $-0.3 < g-r < 1.0$  (0.076 mag). The SNe II corrections (Eqs. (5.7) and (5.8)) hold for  $0.0 < B-I < 2.8$  (0.026 mag) and  $-0.2 < g-r < 1.3$  (0.036 mag). Corrections for other optical colours are presented; these corrections are valid over the radiatively/recombination powered, photospheric epochs of CCSN evolution. Evolution during epochs that show cooling following SBO emission are fitted separately (Eqs. (5.9) and (5.10)) and are subject to larger uncertainties. Given the diversity and uncertainty of UV evolution, separate pseudo-bolometric fits are given where no treatment of the UV regime is made.

The BCs presented here will allow current and future SNe surveys, where the sheer number of detected events prevents intense monitoring of the large majority of SNe, to accurately and easily use their optical detections to obtain estimates of the bolometric light curves of CCSNe of all types, essential for modelling of such events.

## Chapter 6

# Creating and modelling bolometric light curves of 36 literature SE SNe

### Abstract

An extensive literature search is carried out to collate the data for all SE SNe that have good light curve coverage in more than one optical band. Through the use of the BCs presented in Chapter 5, bolometric light curves are created and templates for sub types provided. The peak light distributions and decay rates are investigated; no correlation between peak and light curve width is observed, and SNe subtypes are not cleanly distinguished in this parameter space, although some grouping of types does occur. The bolometric light curves are modelled with a simple analytical prescription and results are found to agree with those of more detailed studies on individual SNe (modulo the fact truly bolometric light curves are being modelled here). The distributions of the explosion parameters shows the extreme nature of SNe Ic-BL in terms of their  $^{56}\text{Ni}$  mass and the energy of the explosions, however ejected masses are similar to those of other subtypes. The ability of SNe Ib and Ic to reach similar  $^{56}\text{Ni}$  masses to the most luminous SNe Ic-BL, alongside the similarity in ejected masses, indicates that these parameters in the exploding core do not dictate the emergence (or not) of a SNe Ic-BL and something else must be driving the huge energies of these explosions.

## 6.1 Data

Since a method of creating bolometric light curves from just optical colours has been formulated (Chapter 5), the creation of bolometric light curves is now not limited to those SNe with extended photometric coverage, but rather is possible for any SN with coverage in just two optical bands. Additional to this, distance and reddening determinations are needed in order to convert to luminosity and correct for the effects of dust.

The sample consists of all SE SNe presented in Chapter 5, as well as many other literature SE SNe that have good light curve coverage in at least two bands from which to construct a colour, which is in turn used to derive the BC. Here there requirement of ‘good’ coverage refers to capturing at least the peak of the light curve (and preferably epochs prior to this) and a large number of epochs within the next  $\sim 60$  days, extending at least 15 days past peak. We restrict our SNe to low redshift (comparable to the redshifts of those in Table 5.1) in order to neglect the requirement of  $K$ -corrections. The sample consists of 7 IIb, 13 Ib, 8 Ic and 8 Ic-BL. The SN IAU names, types, colours used, reddening values and distance moduli (to host) are presented in Table 6.1.

Table 6.1: Data for SNe used to create bolometric light curves.

SN name	Type	$E(B - V)_{\text{tot}}$ (mag)	Distance modulus (mag)	Colour used	Refs.
1993J	IIb	0.194	27.81	$B - I$	1–3
1994I	Ic	0.3	29.6	$B - I$	4
1996cb	IIb	0.03	31.0 <sup>a</sup>	$B - R$	5
1998bw	Ic-BL	0.065	32.89	$B - I$	6
1999dn	Ib	0.10	32.95	$B - I$	7
1999ex	Ib	0.3	33.42	$B - I$	8
2002ap	Ic-BL	0.09	29.5	$B - I$	9–16
2003bg	IIb	0.02	31.68	$B - I$	17
2003jd	Ic-BL	0.144	34.46	$B - I$	18
2004aw	Ic	0.37	34.17	$B - I$	19
2004dk	Ib	0.337	31.81	$V - R$	20

2004dn	Ic	0.568	33.54	$V - R$	20
2004fe	Ic	0.315	34.29	$V - R$	20
2004ff	Ic	0.302	34.82	$V - R$	20
2004gq	Ib	0.253	32.07	$V - R$	20
2005az	Ib	0.441	32.96	$V - R$	20
2005bf	Ib-pec	0.045	34.5	$B - V$	21
2005hg	Ib	0.685	34.67	$g - i$	22
2005kz	Ic-BL	0.514	35.3	$V - R$	20
2005mf	Ic	0.398	35.27	$g - i$	22
2006T	IIb	0.075 <sup>b</sup>	32.58	$g - i$	22
2006aj	Ic-BL	0.142	35.81	$B - I$	23
2006el	IIb	0.303	34.23	$V - R$	20
2006ep	Ib	0.035 <sup>b</sup>	33.84	$B - I$	22
2007C	Ib	0.682	31.99	$V - R$	20
2007Y	Ib	0.112	31.36	$g - i$	24
2007gr	Ic	0.092	29.84	$B - I$	25
2007ru	Ic-BL	0.27	34.15	$B - I$	26
2007uy	Ib	0.63	32.4	$B - V, B - I^c$	27
2008D	Ib	0.6	32.46	$B - I$	28
2008ax	IIb	0.4	29.92	$B - I$	29,30,31
2009bb	Ic-BL	0.58	33.01	$B - I$	32
2009jf	Ib	0.117	32.65	$B - I$	33
2010bh	Ic-BL	0.507	36.90	$g - i$	34
2011bm	Ic	0.064	34.90	$B - I$	35
2011dh	IIb	0.07	29.48	$B - I$	36

<sup>a</sup> Taken from NED.

<sup>b</sup> Galactic extinction only.

<sup>c</sup> The  $B - V$  correction was used for early *Swift* data, with  $B - I$  used for subsequent data.

References: (1) Richmond et al. (1994); (2) Matthews et al. (2002; and IAU circulars within); (3) Matheson et al. (2000); (4) Richmond et al. (1996); (5) Qiu et al. (1999); (6) Clocchiatti et al. (2011); (7) Benetti et al. (2011); (8) Stritzinger et al. (2002); (9) Mattila et al. (2002); (10) Hasubick and Hornoch (2002); (11) Riffeser et al. (2002); (12) Motohara et al. (2002); (13) Gal-Yam et al. (2002); (14) Takada-Hidai et al. (2002); (15) Yoshii et al. (2003); (16) Foley et al. (2003); (17) Hamuy et al. (2009); (18) Valenti et al. (2008); (19) Taubenberger et al. (2006); (20) Drout et al. (2011); (21) Tominaga et al. (2005); (22) Modjaz (2007); (23) Mirabal et al. (2006); (24) Stritzinger et al. (2009); (25) Hunter et al. (2009); (26) Sahu et al. (2009); (27) Roy et al. (2013); (28) Modjaz et al. (2009); (29) Taubenberger et al. (2011); (30) Pastorello et al. (2008); (31) Tsvetkov et al. (2009); (32) Pignata et al. (2011); (33) Valenti et al. (2011); (34) Olivares et al. (2012); (35) Valenti et al. (2012); (36) Ergon et al. (2013);

## 6.2 Method

Firstly, photometric data extracted from the literature for each SN were dereddened assuming a Fitzpatrick (1999)  $R_V = 3.1$  Galactic extinction curve for both Milky Way and host galaxy extinction (as is done in Section 5.3.2). The same methods of light curve interpolation are employed as in Section 5.3.1, in order to obtain values of simultaneous observations in the chosen filters, which give the colour. Extrapolations were not used for this analysis.

The reddening-corrected values of the chosen colour (see Table 6.1) were then fed into the polynomials fits of the BC found in Table 5.2. The resulting BC was then applied to the appropriate SN light curve (e.g. for colour  $B-I$ , the BC is applied to the  $B$ -band light curve). Using the distance modulus we can convert  $m_{\text{bol}}$  to  $M_{\text{bol}}$  and finally to  $L_{\text{bol}}$ . For clarity in plotting, nearly contemporaneous data have been combined by averaging any epochs within 0.2 days of each other.

The results then provide the largest sample of bolometric light curves for SE SNe on which a simple analytical model can be applied, in order to extract estimates for the explosion parameters.

### 6.2.1 The analytical model

The analytical model presented is appropriate for SE SNe, where the light curve is powered predominantly by the decay of  $^{56}\text{Ni}$ , and describes the evolution of a SN over the early photospheric phase (the first 1-2 months, depending on the speed of the SN) and the nebular phase. The bolometric output is described by the model, and as such the model should be fit to a bolometric light curve, with an additional constraint required in the form of a characteristic velocity of the ejecta (Section 6.2.1). From this simple analytical fitting, estimates of the mass of nickel synthesised ( $M_{\text{Ni}}$ ) and the mass and kinetic energy of the ejecta ( $M_{\text{ej}}$ ,  $E_{\text{K}}$  respectively) can be found and readily compared to those obtained from more detailed modelling of the same SNe.

Naturally an analytical approximation requires some simplifying assumptions. These are listed in Arnett (1982); Valenti et al. (2008) and also presented here:

**$R_{t=0} \rightarrow 0$**  The radius of the star at the onset of explosion is very small. This is relevant for the analysis of SE SNe which have shed their extended outer layers and are comparatively compact upon explosion.

**Homologous expansion with spherical symmetry** Expansion of the ejecta follows  $V \propto R$ . Spherical symmetry is a simplification required for an analytical solution, although SE SNe do show evidence for some degree of asphericity of the ejecta, as gleaned from double-peaked nebular emission features (Maeda et al., 2008). Such an assumption is valid for moderately energetic SNe, given Maeda et al. (2008) find an only moderately aspherical model to best describe the SE SNe in their sample, however extreme examples, such as GRB-SNe are likely to have higher asphericity.

**Constant optical opacity** A single choice of opacity ( $\kappa_{\text{opt}}$ ) is made over the early optically-thick regime. However, the opacity will change even over this early evolution and additionally, its absolute value is dependant on the composition of the ejecta. The effect of varying the choice of  $\kappa_{\text{opt}}$  is analysed as part of the error budget in Section 6.3.2, however this treatment is a strong caveat that must be acknowledged when interpreting results.

**Centrally concentrated  $^{56}\text{Ni}$**  The amount of mixing will affect the rise time of the SNe since radiation from high-velocity (i.e. further out in radius, given homologous expansion)  $^{56}\text{Ni}$  will have a shorter diffusion time and thus make the SN rise faster than a centrally concentrated approximation. 3D modelling has shown that a small fraction of high-velocity  $^{56}\text{Ni}$  is not uncommon in SE SNe, although the bulk is generally located close to the centre (Hammer et al., 2010). Modest differences in the  $^{56}\text{Ni}$  distribution will have a noticeable impact only on the early rising light curve and will not be a significant source of uncertainty given other assumptions and observational uncertainties.

**$^{56}\text{Ni}$  and  $^{56}\text{Co}$  power the light curve** These radioactive isotopes represent the main source of energy to a CCSNe, dominating the luminosity evolution for many months. Other isotopes are much less abundant and have longer decay time-scales, and consequently affect only very late time light curve evolution. As such, this is a valid assumption when very early data are excluded from the fit (since other processes may be contributing to the luminosity, e.g. SBO cooling).

During the *photospheric* phase of evolution, optically thick ejecta is assumed. Taking this together with the above assumptions, Valenti et al. (2008), following from Arnett (1982), showed that the luminosity is described by the following equation:

$$L_{\text{phot}}(t) = M_{\text{Ni}} e^{-x^2} \times \left[ (\epsilon_{\text{Ni}} - \epsilon_{\text{Co}}) \int_0^x 2z e^{-2zy+z^2} dz + \epsilon_{\text{Co}} \int_0^x 2z e^{-2zy+2zs+z^2} dz \right] \quad (6.1)$$

where  $x \equiv t/\tau_m$ ,  $y \equiv \tau_m/2\tau_{\text{Ni}}$  and  $s \equiv [\tau_m(\tau_{\text{Co}} - \tau_{\text{Ni}})/2\tau_{\text{Co}}\tau_{\text{Ni}}]$ .  $\epsilon_{\text{Ni}}$  ( $= 3.90 \times 10^{10} \text{ erg s}^{-1} \text{ g}^{-1}$ ) and  $\epsilon_{\text{Co}}$  ( $= 6.78 \times 10^9 \text{ erg s}^{-1} \text{ g}^{-1}$ ) are the energy production rate of nickel and cobalt respectively.

The time-scale of the light curve, dictated by the effective diffusion time,  $\tau_m$ , is given by:

$$\tau_m = \left( \frac{\kappa_{\text{opt}}}{\beta c} \right)^{0.5} \left( \Lambda \frac{M_{\text{ej}}^3}{E_k} \right)^{0.25} \quad (6.2)$$

In the current work, as is done in Valenti et al. (2008),  $\Lambda = 10/3$ ; see Cano (2013) and

references therein for a discussion of the choice of this value and its impact on the derived parameters. Opacity,  $\kappa_{\text{opt}}$ , is chosen to be  $0.06 \text{ cm}^2 \text{ g}^{-1}$  (e.g. [Maeda et al., 2003](#); [Valenti et al., 2011](#)), although the impact of the uncertainty in this value is analysed later (Section 6.3.2).  $\beta \simeq 13.8$  is a constant of integration.

Model photospheric light curves are shown in Fig. 6.1. The top panel shows that the peak luminosity of a SN is directly linked to the amount of  $^{56}\text{Ni}$  synthesised in the explosion at a fixed rise time. When keeping  $M_{\text{Ni}}$  constant, varying  $\tau_m$  alters the rise and decline time-scales of the light curve and can also affect the peak luminosity. Since restrictions on the light curve width come from the declining phase of a SN, the value of  $\tau_m$  can still be estimated in lieu of early, rising data, this alleviates to some level the potential degeneracy between increasing  $M_{\text{Ni}}$  or lowering  $\tau_m$ , which both act to brighten the peak luminosity.

As the optical depth of the ejecta becomes lower, the SN enters the *nebular* phase of evolution and the energy input comes from that deposited by gamma rays emitted in the decay of  $^{56}\text{Ni}$  and  $^{56}\text{Co}$ , where a fraction of the energy released in  $^{56}\text{Co}$  is in the form of positrons. During the nebular phase, the luminosity is given by

$$L_{\text{neb}}(t) = M_{\text{Ni}}\epsilon_{\text{Ni}}e^{-t/\tau_{\text{Ni}}} + 0.81\xi \left(1 - e^{-(F/t)^2}\right) + 0.164\xi \left(1 - e^{-(F/t)^2}\right) \left(1 - e^{-(G/t)^2}\right) + 0.036\xi \left(1 - e^{-(G/t)^2}\right) \quad (6.3)$$

([Valenti et al., 2008](#); and references therein), where the first term describes the energy deposited by nickel decay and the subsequent three terms describe the energy released by cobalt decay (the gamma-rays emitted in  $^{56}\text{Co}$  decay, the gamma-rays emitted from positron annihilation and the kinetic energy of the positrons, respectively).

$$\xi = M_{\text{Ni}}\epsilon_{\text{Co}} \left(e^{-t/\tau_{\text{Co}}} - e^{-t/\tau_{\text{Ni}}}\right) \quad (6.4)$$

describes the energy production rate of  $^{56}\text{Co}$ .  $\tau_{\text{Ni}}$  (= 8.8 days) and  $\tau_{\text{Co}}$  (= 113.7 days) are the time-scales of nickel and cobalt decay respectively. Functions  $F$  and  $G$  can be approximated (after sensible choices of opacities are assumed) to be  $F \simeq 32M_{\text{ej}}/\sqrt{E_{51}}$  and  $G \simeq 515M_{\text{ej}}/\sqrt{E_{51}}$  ([Clocchiatti and Wheeler, 1997](#)), where  $E_{51}$  is the kinetic energy in units of  $10^{51}$  ergs. The exponential terms involving these parameters describe the evolution

of the trapping of gamma-rays, which powers the light curve.

Maeda et al. (2003), however, noted a discrepancy between the parameters derived from their modelling of the two phases of evolution (photospheric and nebular) for some SE SNe. They interpret this as a difference in the optical depth of the ejecta that is contributing in each regime and use a model where the SN is made up of two distinct regions. During the early, photospheric phase, the outer layer contributes to the luminosity of the SN. Additional to this is a much denser inner component whose contribution to the luminosity only emerges once the outer layer becomes optically thin – during the nebular phase. Using this two-component model Maeda et al. (2003) find much better fits to the observed light curves of a sample of SNe Ic-BL. Incorporating this two-component model into the above modelling scheme manifests itself as two free parameters:  $f_M$  and  $f_E$ , the fractions of mass and energy respectively within the inner dense component.<sup>1</sup> The initial fit to the photospheric phase constrains the masses and kinetic energy in the outer layer, which are then fixed for the nebular phase fit, and the additional contribution from the inner component is fitted for using  $f_M$  and  $f_E$ .

The form of the nebular phase model is shown in Fig. 6.2. The early, bright light curve is due to this model making no account for diffusion (cf. photospheric model), and shows the overall instantaneous deposition of energy in the ejecta with time (“instant diffusion”; see Arnett 1982). The case of  $f_M = f_E = 0$  (solid black line) passes through the peak of the photospheric fit since this case assumes *all* the  $^{56}\text{Ni}$  is located in the outer layer, which is therefore the same as that accounted for by the photospheric fit. When increasing  $f_M$ , the effect is to brighten the light curve above that of the photospheric peak, as the model is now accounting for additional heating from inner  $^{56}\text{Ni}$  that is not considered in the photospheric model. Varying  $f_E$  affects the late time slope of the light curve, the gradient of colour in the late time curve shows that only a modest amount of energy in this inner component causes a large change in the slope, with much larger values quickly saturating to a near-similar outcome. An increase in  $f_E$  at constant  $f_M$  raises the value of  $F$  and  $G$  (both  $\propto M_{\text{ej}}/E_K$ ). The fractions of gamma-rays and kinetic energy from radioactive decay that are thermalised

<sup>1</sup>The assumption of a homogeneous distribution of nickel is made, such that  $f_M$  describes both the fraction of nickel and of the total ejecta contained in the inner component.

in the ejecta evolve with time with factors  $(1 - e^{-(F/t)^2})$  and  $(1 - e^{-(G/t)^2})$ , respectively. Thus, as  $F$  and  $G$  increase, this factor is lower for given  $t$ , and consequently the luminosity is lower.

When data exist regarding the time of explosion (e.g. from the SBO signature or accompanying GRB), this is also used as a constraint to the model. Otherwise this was left as a free parameter. Note, however, that very early data are not included in the fit regardless, since the assumptions in the model are not appropriate (i.e. exclusively  $^{56}\text{Ni}$  powered emission and the approximation of centrally concentrated  $^{56}\text{Ni}$ ).

The fitting of these equations to the bolometric light curve data was done via the `CURVE_FIT` function in `SCIPY`. In order to prevent the least-squares fitting from finding a local minimum, a custom ‘global fit’ function was used as a method of locating the global minimum. Each fitting step was performed over a grid of values for all parameters, over wide value ranges since computation time was not an issue (e.g.  $M_{\text{Ni}}$  initial guesses ran from 0.01 to 1  $M_{\odot}$ ). `CURVE_FIT` was performed for each set of parameters specified by the grid – this would locate the solution from that set of initial guesses. Comparison of  $\chi^2$  values of each of the solutions meant the globally best-fitting parameters were found.

### Scale velocity of SNe

As is clear from Eq. 6.2, a degeneracy exists between  $M_{\text{ej}}$  and  $E_{\text{K}}$ , as derived from this model. This is resolved by including a *scale velocity* for the SN, which observationally is set as the photospheric velocity near maximum-light ( $v_{\text{ph}}$ ). The relationship between the photospheric (scale) velocity and the parameters  $M_{\text{ej}}$  and  $E_{\text{K}}$  takes the form:

$$v_{\text{sc}} \equiv v_{\text{phot}} = \sqrt{\frac{6E_{\text{K}}}{5M_{\text{ej}}}}. \quad (6.5)$$

SNe exhibit strong P-Cygni line profiles in their spectra due to the fast moving ejecta. This causes absorption that is blue-shifted by the velocity of the ion relative the rest wavelength of the spectral line. Due to the stratification of the ejecta and the homologous expansion, elements near towards the outer layers of the ejecta (e.g. helium and calcium) can exhibit

large velocities compared to heavier, more centrally concentrated elements. Two elements that appropriately trace the photospheric velocity are silicon and iron, with Si II  $\lambda 6355$  and the Fe II set of lines clustered around 4500-5200 Å generally used (e.g. Pastorello et al., 2008; Valenti et al., 2011; Corsi et al., 2011).

Practically the measurements consist of a simple Gaussian fitting procedure to the absorption features on a wavelength- and flux-calibrated spectrum of the SN taken on or near peak (generally obtained from WISEREP), performed in the IRAF package SPLIT. This was initially attempted for Fe II lines, before averaging to obtain a value of  $v_{\text{ph}}$ . In the case where Fe II lines could not be accurately measured (e.g. strong line blending or no spectral coverage at those wavelengths), the Si II  $\lambda 6355$  feature was measured. When data were not available, literature values had to be relied upon. These were typically found using a similar Gaussian fitting technique or through spectral fitting. Measurements from this simple Gaussian-fitting method were found to agree well with those of from detailed spectral fitting codes in the cases where a comparison was possible. Both methods have uncertainties of several hundred to a thousand  $\text{km s}^{-1}$  (S. Valenti, private communication). Such errors arise from the data quality as well as the broad-featured characteristic of SNe spectra at maximum light – velocities of at least several thousands of  $\text{km s}^{-1}$ , as is seen for CCSNe, make line blending an issue and it is often the case that one cannot attribute a single absorption feature to one specific transition. Similarly, nearby emission from other transitions will also impact on the shape of the absorption feature, affecting the Gaussian fit and, ultimately, the photospheric velocity derived. A visual representation of the Gaussian fitting method is shown in Fig. 6.3. Finally, in the absence of appropriate data or literature value for a SN,  $v_{\text{ph}}$  was taken to be the median  $v_{\text{ph}}$  for the SN's type from a collation of literature values, as presented in Cano (2013). These are 7700, 8150 and 14000  $\text{km s}^{-1}$  for SNe types Ib, Ic and Ic-BL, respectively (additionally the SN Ib median  $v_{\text{ph}}$  was used for SNe Iib). Branch et al. (2002) provide a power law fit to their estimates of  $v_{\text{ph}}$  values for SNe Ib (as determined from Fe II lines), with the value at peak being slightly higher than the median used here,  $\sim 9000 \text{km s}^{-1}$ . The values of  $M_{\text{ej}}$  and  $E_{\text{K}}$  derived from SNe modelled using these averages are clearly susceptible to larger systematic uncertainties, but  $^{56}\text{Ni}$  masses are largely unaffected.

## 6.3 Results

### 6.3.1 Bolometric light curves

The bolometric light curves are presented in Fig. 6.4. The time and value of the peak of each light curve ( $t_{\text{peak}}$  and  $M_{\text{peak}}$ , respectively) were found with a low-order polynomial, fitted to data around peak. The diversity of SE SNe becomes apparent from these plots and some interesting observations can be made. A spread of  $\sim 3$  magnitudes is observed in  $M_{\text{peak}}$ ; interestingly, two SNe Ib encompass the extremes of the spread, ranging from SN 2007Y at  $M_{\text{peak}} \sim -16.3$  to SN 2005hg at  $M_{\text{peak}} \sim -19.2$ .<sup>2</sup> This spread in  $M_{\text{peak}}$  is similar to that found by Drout et al. (2011) in their  $V$ - and  $R$ -band imaging when considering the overlapping sample. The decline rates of the sample vary greatly, to parametrise the speed of the evolution, a  $\Delta m_{15,\text{bol}}$  value is used, i.e. the number of magnitudes from peak the bolometric light curve has declined by 15 days after peak (values were found from polynomial fits to the light curves). SN 1994I, despite being often cited as a ‘prototypical’ SN Ic, has unusually fast evolution, as has been previously noted, with  $\Delta m_{15,\text{bol}} = 1.37$  calculated here. SN 2011bm displays the slowest evolution, with  $\Delta m_{15,\text{bol}} = 0.20$ . The evolution speeds appears to form a continuum, as is evident from the bottom panel of Fig. 6.4, although SNe 1994I and 2011bm are noticeably displaced from the extremities of the distribution. Perhaps unexpectedly, a GRB-SN, SN 2010bh, is exceeded only by SN 1994I in terms of speed of evolution. This extremely fast evolution was noticed by Olivares et al. (2012), but is highlighted here when compared to many other SE SNe. Such fast evolution is at odds with the perception of GRB-SN progenitors/explosions being massive/energetic when considering the analytical form of SE SN light curves (Eq. 6.2).

To investigate any possible correlation between light curve peak and width in these bolometric light curves, we plot  $\Delta m_{15,\text{bol}}$  against  $M_{\text{peak}}$  for the sample in Fig. 6.5. There appears to be some trend towards having a narrower light curve (faster evolution) at high luminosity, with the fainter SNe evolving slower, the Spearman’s rank coefficient is not significant enough to reject the case of no correlation however. There appears to be no reason why

<sup>2</sup>The classification of SN 2005hg was originally made as a SN Ic (Modjaz et al., 2005a), before the detection of He lines in Modjaz et al. (2005b).

bright, slowly evolving SNe would be missed compared to quicker evolving events at similar luminosities, and it may indeed indicate that events such as SNe 2005kz and 2011bm are intrinsically rare. Conversely, fainter, quickly evolving SNe are most likely to have been missed from detection (particularly prior to peak, which is one of the criteria imposed on this sample). As this is a literature based sample, the selection effects cannot be analysed beyond these qualitative statements. However, the literature-based nature of the sample would also mean that any peculiar SNe that may inhabit these unusual regions of parameter space would be likely to be included since unusual events tend to be the best observed. By colour coding the SN by type it is clear the various types do not inhabit exclusive regions of this parameter space, although some clustering of SNe I Ib and SNe Ic-BL (with two exceptions) occurs. All SNe I Ib in the sample occur within a small region of roughly average evolution speed and modest peak magnitudes when compared to the entire sample. SNe Ic-BL are all luminous when compared to the rest of the sample with the exception of SN 2002ap, and all have fast evolution with the exceptions of SNe 2002ap and 2005kz. This analysis indicates that bolometric light curves alone cannot be used to reliably distinguish between SE SN types.

Template bolometric light curves for SE SNe are presented in Fig. 6.6, showing the median value and the standard deviation. The data for these templates are presented in Tables 6.2 to 6.5 with the phases being relative to the peak of  $L_{\text{bol}}$ . These were found by sampling interpolations of the bolometric light curves and calculating the median and standard deviation of those SNe who had a light curve covering that particular phase.

### 6.3.2 Modelling

The  $v_{\text{ph}}$  values are presented in Table 6.6. These values were used to break the degeneracy in  $E_{\text{K}}$  and  $M_{\text{ej}}$ , arising from Eq. 6.2, by using Eq. 6.5. Velocity determinations were found to agree well with literature values that were determined from both the Gaussian-fitting technique and also spectral modelling. Furthermore, no significant correlation of  $v_{\text{ph}}$  was found with either peak luminosity or light curve width. The previously noted fast evolution of the SN-Ic-BL 2010bh still allows for a large  $E_{\text{K}}$  value when reconciled with its huge  $v_{\text{ph}}$  ( $\sim 30000 \text{ km s}^{-1}$ ) and Eq. 6.5.

Table 6.2: Template bolometric light curve data for SNe Ib

Phase (days)	$\log_{10} L_{\text{bol}}$ erg s <sup>-1</sup>	std. dev.	Phase (days)	$\log_{10} L_{\text{bol}}$ erg s <sup>-1</sup>	std. dev.	Phase (days)	$\log_{10} L_{\text{bol}}$ erg s <sup>-1</sup>	std. dev.
-18	42.172	0.547	12	42.092	0.076	42	41.702	0.092
-17	42.129	0.422	13	42.070	0.074	43	41.694	0.091
-16	41.785	0.370	14	42.071	0.113	44	41.686	0.090
-15	41.859	0.290	15	42.052	0.113	45	41.677	0.089
-14	41.930	0.226	16	42.035	0.113	46	41.669	0.087
-13	41.933	0.167	17	42.020	0.114	47	41.662	0.086
-12	41.936	0.138	18	42.005	0.114	48	41.654	0.085
-11	42.023	0.116	19	41.992	0.114	49	41.647	0.084
-10	42.116	0.103	20	41.979	0.115	50	41.640	0.083
-9	42.200	0.096	21	41.967	0.115	51	41.633	0.082
-8	42.245	0.093	22	41.956	0.115	52	41.627	0.082
-7	42.294	0.092	23	41.944	0.115	53	41.620	0.082
-6	42.341	0.094	24	41.933	0.116	54	41.614	0.081
-5	42.385	0.097	25	41.947	0.120	55	41.646	0.116
-4	42.357	0.105	26	41.935	0.116	56	41.602	0.082
-3	42.308	0.106	27	41.901	0.116	57	41.596	0.082
-2	42.316	0.111	28	41.891	0.116	58	41.590	0.083
-1	42.320	0.115	29	41.882	0.117	59	41.583	0.084
0	42.317	0.117	30	41.874	0.117	60	41.577	0.084
1	42.311	0.117	31	41.866	0.117	61	41.569	0.085
2	42.300	0.115	32	41.859	0.117	62	41.561	0.085
3	42.286	0.113	33	41.852	0.118	63	41.580	0.069
4	42.269	0.109	34	41.845	0.119	64	41.569	0.070
5	42.250	0.105	35	41.838	0.119	65	41.557	0.072
6	42.229	0.100	36	41.830	0.121	66	41.545	0.073
7	42.207	0.095	37	41.797	0.088	67	41.533	0.075
8	42.184	0.091	38	41.788	0.087	68	41.522	0.076
9	42.160	0.086	39	41.728	0.093	69	41.496	0.015
10	42.137	0.082	40	41.720	0.093	70	41.488	0.015
11	42.114	0.079	41	41.711	0.093	71	41.481	0.017

Table 6.3: Template bolometric light curve data for SNe Ib

Phase (days)	$\log_{10} L_{\text{bol}}$ erg s <sup>-1</sup>	std. dev.	Phase (days)	$\log_{10} L_{\text{bol}}$ erg s <sup>-1</sup>	std. dev.	Phase (days)	$\log_{10} L_{\text{bol}}$ erg s <sup>-1</sup>	std. dev.
-20	41.649	0.417	8	42.498	0.306	36	42.082	0.252
-19	41.799	0.337	9	42.472	0.307	37	42.071	0.250
-18	41.920	0.270	10	42.445	0.308	38	42.061	0.249
-17	41.895	0.394	11	42.418	0.309	39	42.052	0.248
-16	41.934	0.362	12	42.392	0.310	40	42.051	0.257
-15	42.047	0.318	13	42.367	0.312	41	42.156	0.192
-14	42.146	0.276	14	42.421	0.304	42	42.147	0.192
-13	42.049	0.335	15	42.401	0.302	43	42.139	0.192
-12	42.143	0.325	16	42.380	0.300	44	42.131	0.192
-11	42.239	0.318	17	42.360	0.317	45	42.125	0.191
-10	42.421	0.348	18	42.340	0.298	46	42.120	0.191
-9	42.458	0.324	19	42.321	0.297	47	42.116	0.189
-8	42.418	0.329	20	42.302	0.297	48	42.112	0.188
-7	42.452	0.326	21	42.285	0.296	49	42.109	0.186
-6	42.545	0.315	22	42.267	0.293	50	42.106	0.183
-5	42.574	0.301	23	42.251	0.297	51	42.103	0.180
-4	42.595	0.297	24	42.235	0.296	52	42.198	0.164
-3	42.603	0.294	25	42.220	0.296	53	42.192	0.169
-2	42.613	0.292	26	42.205	0.295	54	42.186	0.171
-1	42.618	0.290	27	42.191	0.295	55	42.181	0.170
0	42.619	0.289	28	42.175	0.309	56	42.068	0.108
1	42.617	0.299	29	42.163	0.308	57	42.067	0.105
2	42.613	0.299	30	42.151	0.307	58	42.062	0.107
3	42.604	0.300	31	42.051	0.320	59	42.062	0.105
4	42.594	0.302	32	42.035	0.319	60	42.060	0.105
5	42.569	0.302	33	42.021	0.319	61	42.058	0.107
6	42.547	0.303	34	42.099	0.254			
7	42.524	0.305	35	42.092	0.254			

Table 6.4: Template bolometric light curve data for SNe Ic

Phase (days)	$\log_{10} L_{bol}$ erg s <sup>-1</sup>	std. dev.	Phase (days)	$\log_{10} L_{bol}$ erg s <sup>-1</sup>	std. dev.	Phase (days)	$\log_{10} L_{bol}$ erg s <sup>-1</sup>	std. dev.
-9	42.583	0.239	22	42.264	0.316	53	41.878	0.422
-8	42.498	0.188	23	42.232	0.339	54	41.869	0.421
-7	42.506	0.277	24	42.208	0.342	55	41.697	0.468
-6	42.553	0.263	25	42.185	0.345	56	41.694	0.468
-5	42.507	0.279	26	42.164	0.348	57	41.690	0.468
-4	42.529	0.254	27	42.144	0.351	58	41.687	0.469
-3	42.571	0.204	28	42.127	0.353	59	41.682	0.470
-2	42.588	0.197	29	42.111	0.355	60	41.679	0.472
-1	42.599	0.193	30	42.096	0.356	61	41.675	0.476
0	42.652	0.183	31	42.084	0.357	62	41.849	0.390
1	42.650	0.183	32	42.072	0.358	63	41.846	0.389
2	42.644	0.185	33	42.062	0.359	64	41.844	0.389
3	42.633	0.188	34	42.053	0.360	65	41.842	0.388
4	42.618	0.192	35	42.020	0.389	66	41.841	0.388
5	42.602	0.197	36	42.012	0.390	67	41.840	0.387
6	42.584	0.204	37	42.004	0.391	68	41.839	0.387
7	42.566	0.211	38	41.997	0.392	69	41.839	0.387
8	42.547	0.219	39	41.989	0.393	70	41.836	0.387
9	42.529	0.228	40	41.982	0.394	71	41.833	0.387
10	42.511	0.237	41	41.974	0.394	72	41.832	0.387
11	42.495	0.245	42	41.966	0.394	73	41.830	0.387
12	42.479	0.254	43	41.958	0.395	74	41.829	0.387
13	42.457	0.263	44	41.950	0.394	75	41.825	0.387
14	42.431	0.271	45	41.942	0.394	76	41.824	0.387
15	42.406	0.278	46	41.935	0.394	77	41.822	0.387
16	42.388	0.285	47	41.928	0.393	78	41.819	0.387
17	42.371	0.292	48	41.921	0.393	79	41.816	0.387
18	42.347	0.298	49	41.915	0.393	80	41.814	0.387
19	42.325	0.304	50	41.910	0.393	81	41.812	0.387
20	42.303	0.309	51	41.895	0.424	82	41.810	0.387
21	42.283	0.313	52	41.887	0.423			

Table 6.5: Template bolometric light curve data for SNe Ic-BL

Phase (days)	$\log_{10} L_{bol}$ erg s <sup>-1</sup>	std. dev.	Phase (days)	$\log_{10} L_{bol}$ erg s <sup>-1</sup>	std. dev.	Phase (days)	$\log_{10} L_{bol}$ erg s <sup>-1</sup>	std. dev.
-6	42.731	0.146	20	42.548	0.270	46	42.168	0.138
-5	42.743	0.340	21	42.525	0.273	47	42.160	0.099
-4	42.818	0.287	22	42.393	0.270	48	42.150	0.104
-3	42.859	0.282	23	42.371	0.273	49	42.139	0.108
-2	42.912	0.256	24	42.350	0.277	50	42.129	0.114
-1	42.924	0.256	25	42.440	0.277	51	42.118	0.116
0	42.928	0.256	26	42.422	0.278	52	42.108	0.118
1	42.925	0.255	27	42.427	0.137	53	42.097	0.120
2	42.916	0.255	28	42.407	0.137	54	42.086	0.121
3	42.903	0.254	29	42.389	0.137	55	42.075	0.121
4	42.886	0.253	30	42.372	0.137	56	42.065	0.122
5	42.868	0.253	31	42.372	0.177	57	42.054	0.123
6	42.849	0.252	32	42.341	0.139	58	42.043	0.124
7	42.829	0.251	33	42.327	0.139	59	42.033	0.126
8	42.809	0.251	34	42.314	0.140	60	42.022	0.125
9	42.789	0.250	35	42.301	0.142	61	42.135	0.123
10	42.770	0.250	36	42.290	0.143	62	42.126	0.124
11	42.746	0.250	37	42.278	0.144	63	42.117	0.125
12	42.718	0.250	38	42.267	0.146	64	42.108	0.126
13	42.688	0.249	39	42.256	0.147	65	42.099	0.127
14	42.707	0.266	40	42.245	0.148	66	42.091	0.128
15	42.679	0.266	41	42.233	0.149	67	42.082	0.129
16	42.651	0.266	42	42.222	0.149	68	42.074	0.130
17	42.624	0.267	43	42.209	0.148	69	42.066	0.131
18	42.598	0.268	44	42.196	0.146	70	42.059	0.132
19	42.573	0.269	45	42.183	0.142	71	42.051	0.133

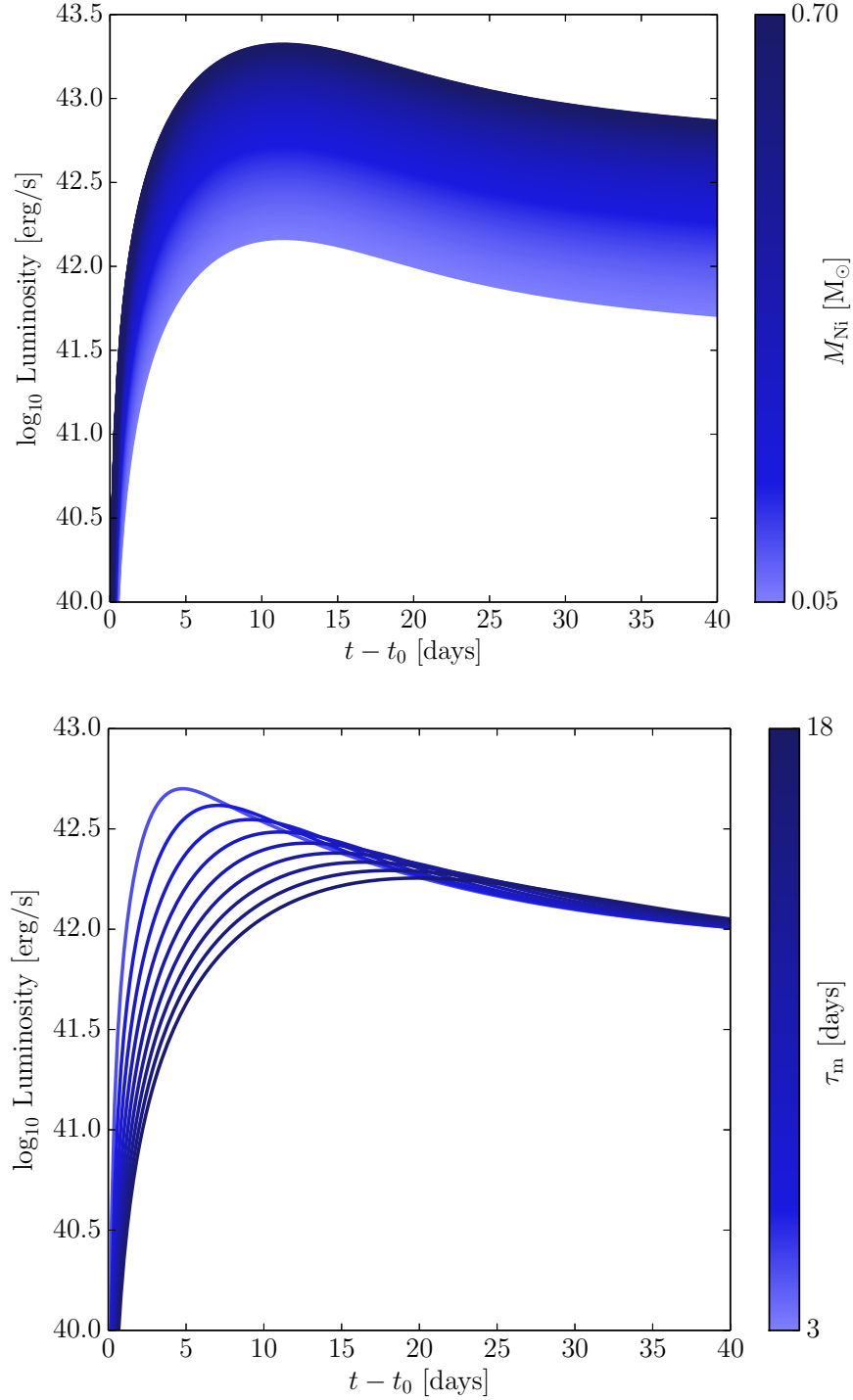


Figure 6.1: Photospheric phase model light curves of SE SNe. *Top*: the effect of changing  $M_{\text{Ni}}$  at constant  $\tau_m$  is shown. For a given rise time, the peak value is determined by  $M_{\text{Ni}}$ , the value of  $\tau_m$  used is 9 days (i.e. a SN with  $M_{\text{ej}} \sim 1 M_{\odot}$  and  $E_K \sim 1 \times 10^{51}$  ergs). *Bottom*: the effect of altering  $\tau_m$  at a constant  $M_{\text{Ni}}$ .  $\tau_m$  dictates the rise time to peak and also the decay, effectively determining the ‘width’ of the light curve and also the peak –  $M_{\text{Ni}}$  for this plot is  $0.1 M_{\odot}$  for each model.

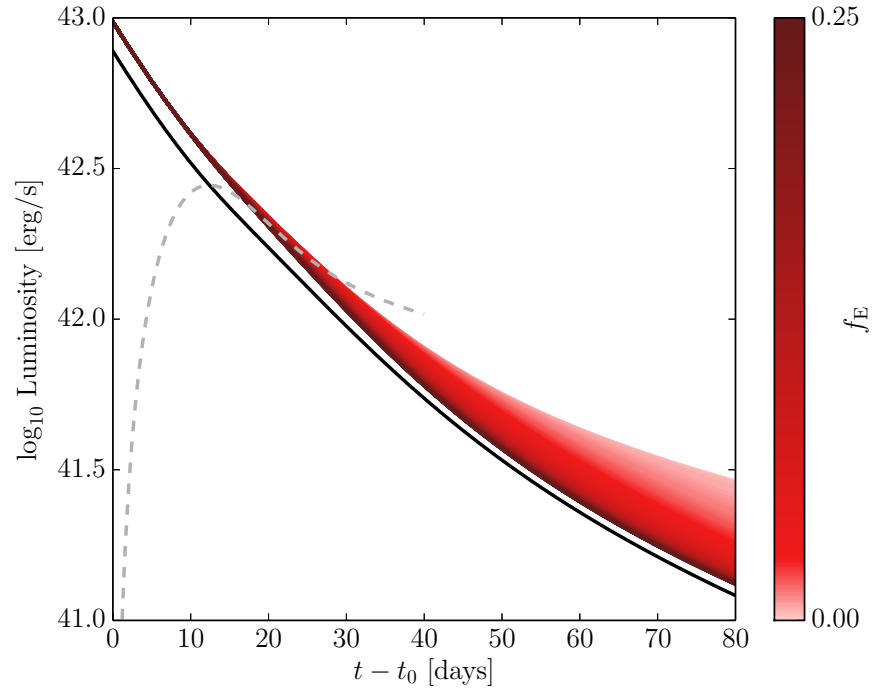


Figure 6.2: Nebular phase model light curves of SE SNe. The solid black line indicates the case of no mass and no energy being contained in the inner dense component. The colour bar indicates varying  $f_E$  when  $f_M = 0.2$ . The corresponding photospheric phase fit is shown (grey dashed) for comparison. The (outer layer) SN parameters used were  $M_{\text{Ni}} = 0.1 M_{\odot}$ ,  $M_{\text{ej}} = 1 M_{\odot}$  and  $E_K = 1 \times 10^{51}$  ergs. Varying  $f_M$  and  $f_E$  then allows an additional contribution from an inner dense component to reveal itself during the late phase modelling.

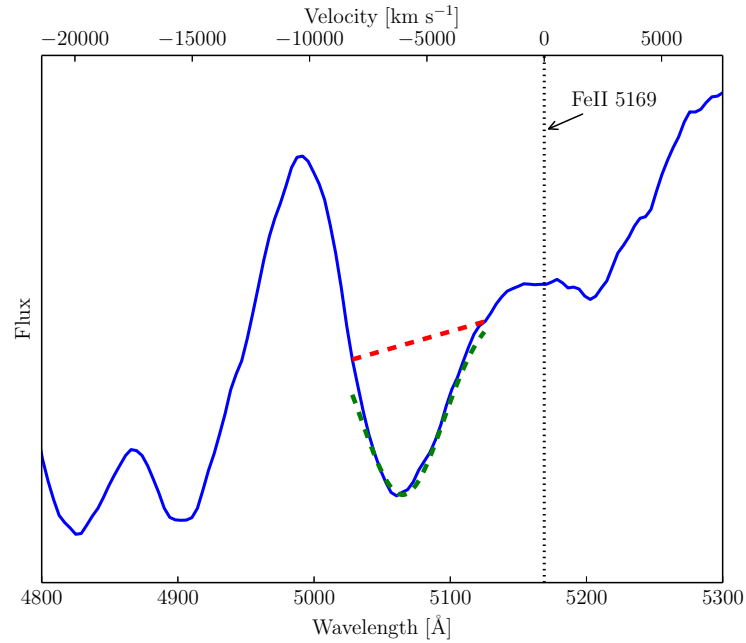


Figure 6.3: An example of extracting a photospheric velocity measurement from a SN spectrum. The emission from the Fe II  $\lambda 5169$  transition is evident at the rest-frame wavelength of the transition (black dotted line). A Gaussian (green dashed line) is fitted over the blue-shifted absorption. The minimum of this Gaussian gives the velocity of the ion responsible for the transition, approximately that of the photosphere in the case of Fe. The complications arising from neighbouring features, which may skew the minimum of the feature (thus affecting velocity measurements), are evident in this case as the large emission feature peaking at  $\sim 5000$  Å. (Spectrum is that of SN 2009jf, obtained from WISeREP.)

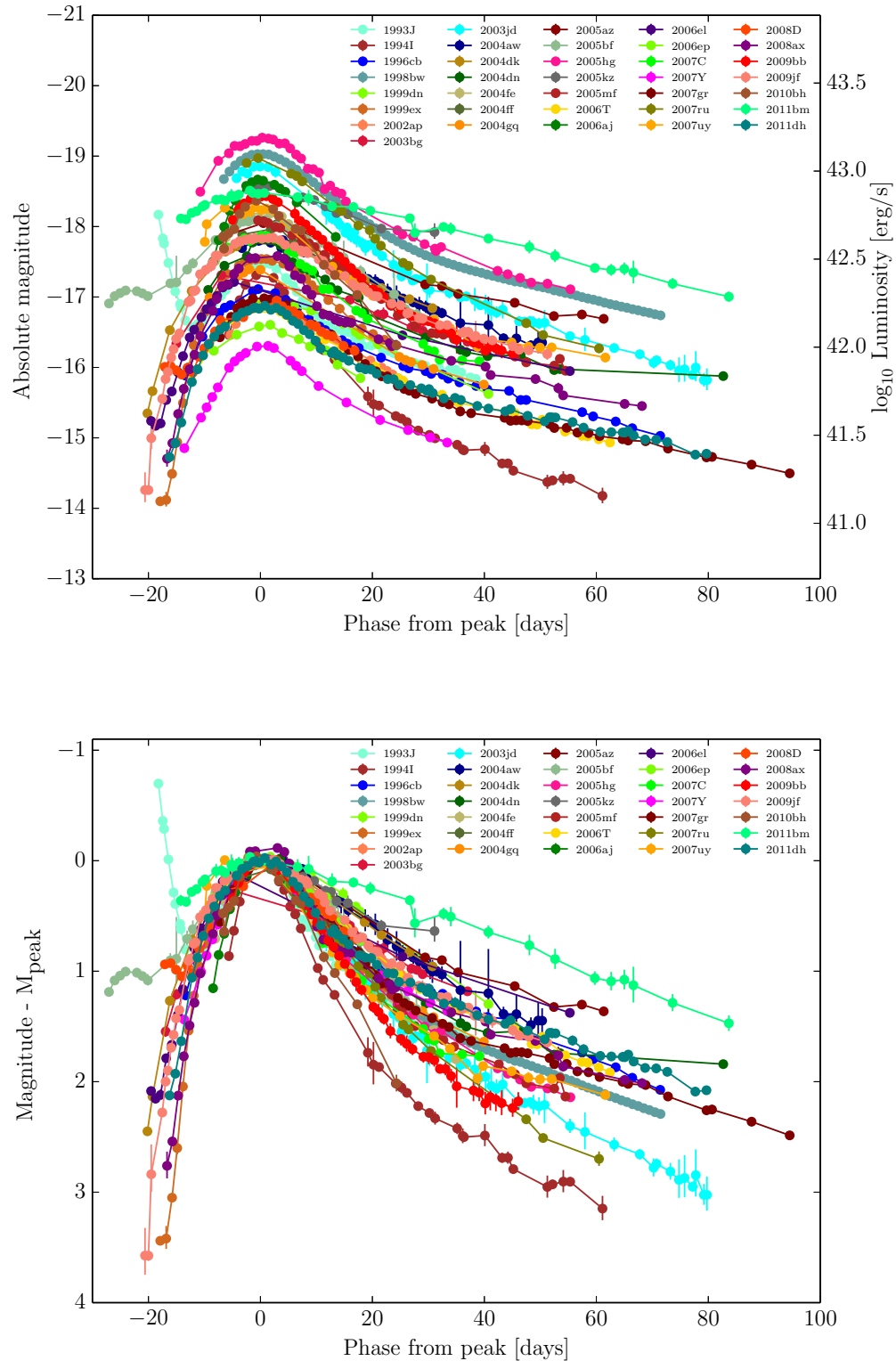


Figure 6.4: Bolometric light curves of SN in the sample using the BC fits of Chapter 5 (top). The peak-normalised light curves are also displayed (bottom). Error bars are indicative of the uncertainty of the BC only, which is found by taking the uncertainty in the colour and translating that as an error on the BC fits. Distances, for example, will be a significant source of uncertainty in the top plot.

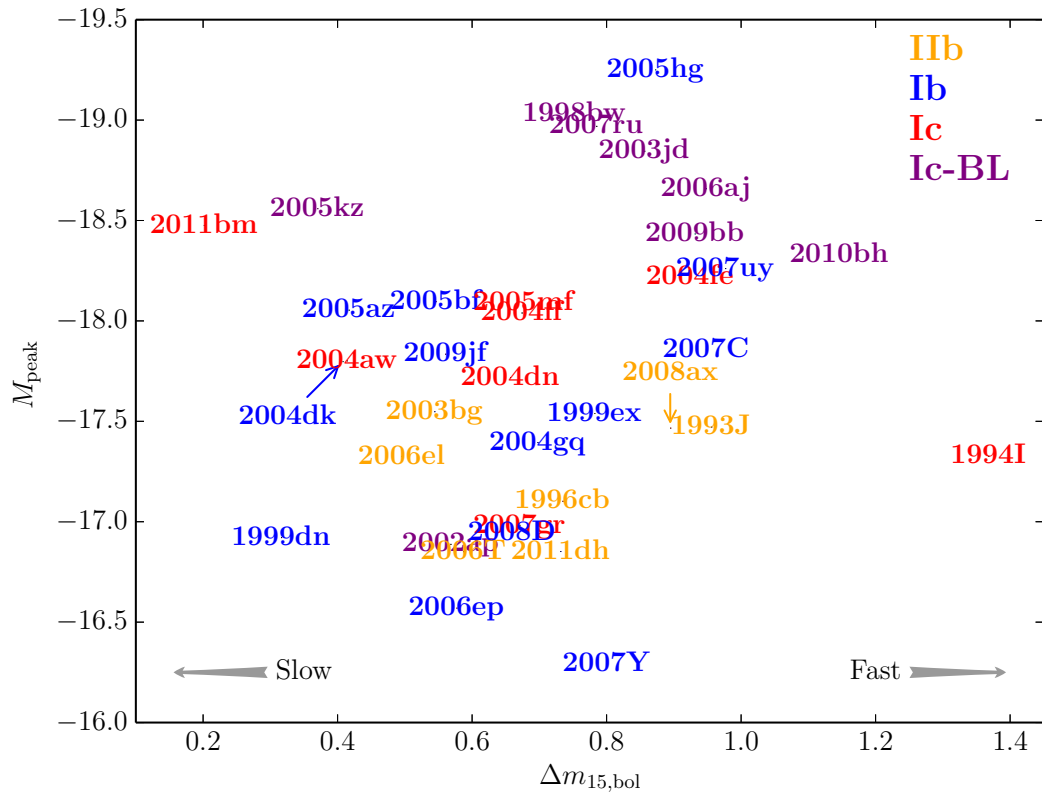


Figure 6.5: The peak magnitude of the evolution of the bolometric light curves against speed (parameterised as  $\Delta m_{15,\text{bol}}$ , see text); the direction of light curve evolution speed is denoted by the labelled grey arrows. The thin, coloured arrows indicate the positions of SNe 2004dk and 2008ax, which have been offset for clarity. SNe are colour-coded according to their type.

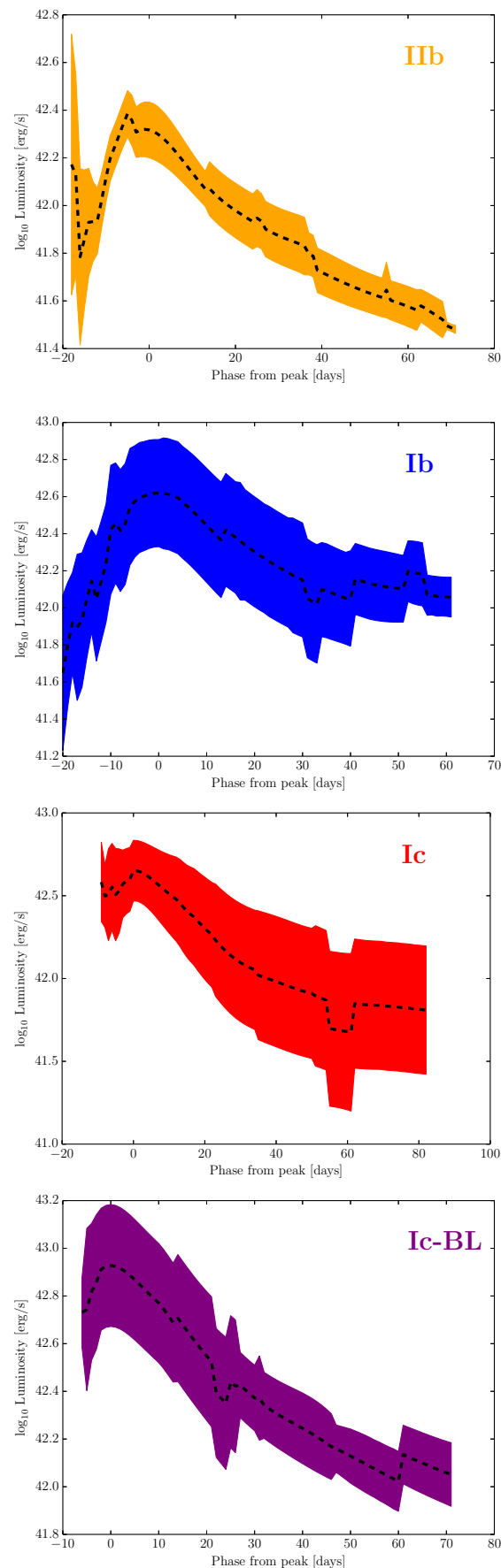


Figure 6.6: Template bolometric light curves for SE SNe, indicating the median value (black dashed line) and the standard deviation of the sample of light curves for that phase (coloured filled regions).

Table 6.6: Photospheric velocity measurements for SE SNe

SN name	Type	Line(s) used	$v_{\text{ph}}$ km s <sup>-1</sup>	Phase <sup>a</sup> (days)	Notes
1993J	I Ib	Fe II	8000	0	Agrees with Fe II velocities found by <a href="#">Ohta et al. (1994)</a> ; <a href="#">Barbon et al. (1995)</a> ; <a href="#">Pastorello et al. (2008)</a> .
1994I	Ic	Fe II	11500	-1	Agrees with spectral modelling value of $v_{\text{ph}}$ in <a href="#">Sauer et al. (2006)</a> .
1996cb	I Ib	Fe II	8500	1	<a href="#">Qiu et al. (1999)</a> , however, find a velocity of He I of 8870km s <sup>-1</sup> at epoch -15 days which would indicate extremely low $v_{\text{ph}}$ at peak. Inconsistency was found when measuring velocities on the same spectrum, and the Fe II measurement found here is preferred.
1998bw	Ic-BL	Si II	19500	1	Fe II lines are largely blended. $v_{\text{ph}}$ agrees with value found by <a href="#">Patat et al. (2001)</a> and is similar to Si II velocity found by <a href="#">Pignata et al. (2011)</a> .
1999dn	Ib	Fe II	10500	0	Taken from <a href="#">Benetti et al. (2011)</a>
1999ex	Ib	Fe II	8500	1	Agrees with velocities given in <a href="#">Hamuy et al. (2002)</a>
2002ap	Ic-BL	Fe II	13000	2	<a href="#">Gal-Yam et al. (2002)</a> find the velocity of Si II to be 15000km s <sup>-1</sup> at peak. Features blended somewhat.
2003bg	I Ib	He I	10000	0	Taken from <a href="#">Hamuy et al. (2009)</a> .
2003jd	Ic-BL	Si II	13500	0	Taken from <a href="#">Valenti et al. (2008)</a> .
2004aw	Ic	Fe II	11000	-2	<a href="#">Taubenberger et al. (2006)</a> show a contemporaneous Si II velocity of 12500km s <sup>-1</sup> .

2004dk	Ib	Si II	9200	1	Taken from <a href="#">Harutyunyan et al. (2008)</a> .
2004dn	Ic	Si II	12500	1	Taken from <a href="#">Harutyunyan et al. (2008)</a> .
2004fe	Ic	n/a <sup>b</sup>	8150	–	–
2004ff	Ic	n/a <sup>b</sup>	8150	–	–
2004gq	Ib	n/a <sup>b</sup>	7700	–	<a href="#">Modjaz (2007)</a> show a He I velocity of 14000km s <sup>-1</sup> at peak.
2005az	Ib	n/a <sup>b</sup>	7700	–	–
2005bf	Ib-pec	Fe II	7500	3	Matches value for Fe II lines found by <a href="#">Folatelli et al. (2006)</a> .
2005hg	Ib	n/a <sup>b</sup>	7700	–	<a href="#">Modjaz (2007)</a> show a He I velocity of 10000km s <sup>-1</sup> at peak.
2005kz	Ic-BL	n/a <sup>b</sup>	14000	–	–
2005mf	Ic	n/a <sup>b</sup>	8150	–	–
2006T	I Ib	n/a <sup>b</sup>	7700	–	–
2006aj	Ic-BL	(Si II)	18000	0	The value of $v_{ph}$ presented in <a href="#">Pian et al. (2006)</a> is used as the spectrum is noisy and heavily blended. This value agrees with that found by <a href="#">Pignata et al. (2011)</a> from measuring Si II.
2006el	I Ib	n/a <sup>b</sup>	7700	–	A velocity of H $\beta$ , somewhat past peak, is given as 11500km s <sup>-1</sup> in <a href="#">Blondin et al. (2006)</a> .
2006ep	Ib	n/a <sup>b</sup>	7700	–	–
2007C	Ib	n/a <sup>b</sup>	7700	–	–
2007Y	Ib	Fe II	9000	-2	Matches the values for Fe II velocities found by <a href="#">Stritzinger et al. (2009)</a> and <a href="#">Valenti et al. (2011)</a> .

2007gr	Ic	Fe II	10000	0	Agrees with values from spectral modelling presented in <a href="#">Hunter et al. (2009)</a> .
2007ru	Ic-BL	Si II	19000	0	Taken from <a href="#">Sahu et al. (2009)</a> .
2007uy	Ib	Fe II	14500	-3	<a href="#">Roy et al. (2013)</a> find the velocity of He I to be $15200\text{km s}^{-1}$ at the same epoch.
2008D	Ib	Fe II	9500	3	<a href="#">Modjaz et al. (2009)</a> show He I velocity as $11000\text{km s}^{-1}$ at this epoch; <a href="#">Soderberg et al. (2008)</a> show the Si II velocity to be $9000\text{--}10000\text{km s}^{-1}$ .
2008ax	Iib	Fe II	7500	4	Matches the values for Fe II velocities found by <a href="#">Pastorello et al. (2008)</a> and <a href="#">Taubenberger et al. (2011)</a> .
2009bb	Ic-BL	Fe II	17000	3	<a href="#">Pignata et al. (2011)</a> find Si II velocities at this epoch to be $18000\text{km s}^{-1}$ and find Fe II lines to be at $17000\text{km s}^{-1}$ using a spectral modelling code.
2009jf	Ib	Fe II	9500	3	Matches values found by <a href="#">Valenti et al. (2011)</a> .
2010bh	Ic-BL	Si II	30000	0	Taken from a linear interpolation of the Si II velocities presented in <a href="#">Chornock et al. (2010)</a> .
2011bm	Ic	Fe II	9000	0	Taken from <a href="#">Valenti et al. (2011)</a> .
2011dh	Iib	Fe II	7000	0	Taken from <a href="#">Bersten et al. (2012)</a> .

<sup>a</sup> Approximate phase measured relative to the bolometric light curve peak of spectrum used to measure  $v_{\text{ph}}$ .

<sup>b</sup> No value of  $v_{\text{ph}}$  could be measured or was available in the literature. The average  $v_{\text{ph}}$  for the appropriate SN type was used from [Cano \(2013\)](#) (see text).

The results of the fitting are given in Table 6.7 and some example fits are shown in Fig. 6.7. Behaviour shortly after the photospheric phase is not well described by the assumptions in either the photospheric or nebular model, which is shown particularly for SNe 2007gr and 2011dh in Fig. 6.7. As such data used to constrain the nebular model do not begin immediately after the photospheric data points.

As may be expected, explosion parameters found here agree broadly with those in the literature where the same analytical model was applied to the SN (e.g. Valenti et al., 2008; Benetti et al., 2011; Pignata et al., 2011; Taubenberger et al., 2011; Valenti et al., 2011; Olivares et al., 2012; Cano, 2013; Roy et al., 2013). This modelling could take the form of either a direct fitting of the entire model, as is done here, or scaling relations for the peak and width ( $\tau_m$ ) of the light curve and appropriately scaling the values of a better-studied SN by assuming similarity in the other properties of the explosion. Given the often differing choices of  $\Lambda$ ,  $\kappa_{\text{opt}}$  and  $v_{\text{ph}}$  employed by various authors, as well as variations arising from the time-scales over which the data were fit, the agreement between the results is reassuring, as it shows the method is not overly sensitive to such uncertainties. However, since here truly bolometric light curves are being modelled, some differences from previous modelling on pseudo-bolometric light curves is to be expected. Most notable was an increase in the derived  $M_{\text{Ni}}$  found for the SNe. Since this is intrinsically linked to the peak of the bolometric light curve, this is naturally explained by the light curves presented here accounting for flux that was not accounted for in previous modelling. The relatively large uncertainties in the determinations of  $M_{\text{ej}}$  and  $E_{\text{K}}$ , coupled with the less straightforward effect that these BCs have on the width of the light curve compared to a pseudo-bolometric light curve, makes any offset in these parameters less obvious. Indeed the parameter ranges found here had generally a large overlap with those previously published and as such there appears to be, at most, an effect from the BC on these parameters that is at a level beyond the precision of this modelling scheme.

Also presented in Table 6.7 are values for the explosion parameters determined for the SNe as found by more detailed spectral or hydrodynamical modelling. It should be noted that these values just encompass the ranges of preferred values or are the best-guess of the modelling, and generally do not include uncertainties arising from, for example, the distance

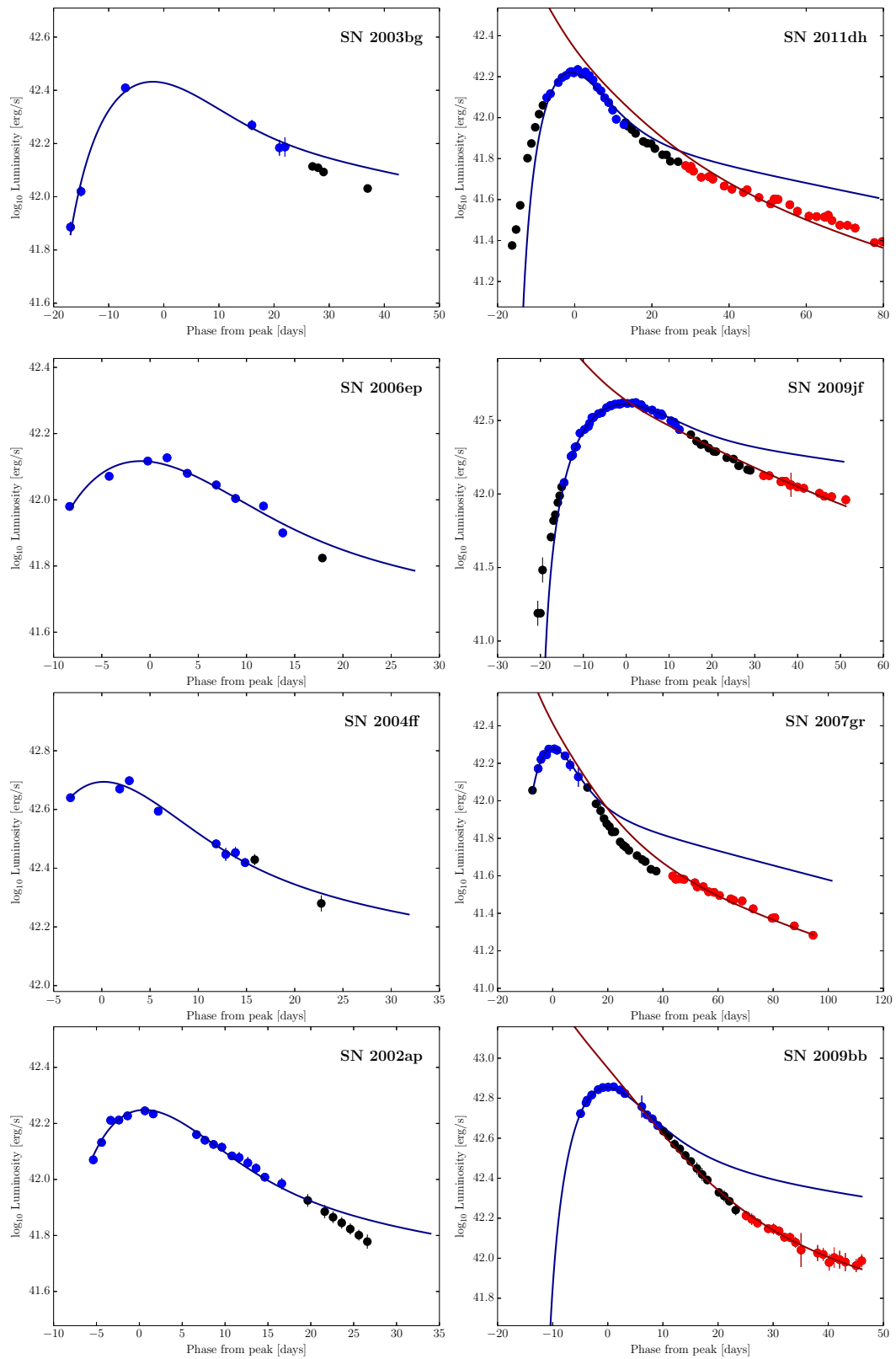


Figure 6.7: Some examples of the fits found when modelling the bolometric light curves with the analytical prescription. Data points in blue indicate those that were used in the fitting routine for the photospheric phase, red data points show the data that were used in the nebular phase. The photospheric and nebular fits are shown as the blue and red lines respectively. From top to bottom: Ib, Ib, Ic, Ic-BL, with an example of more poorly constrained fits on the left and exemplary fits on the right.

(see below). On the whole, given the simplifications inherent in the analytical model, the agreement is very good and thus the analytical prescription provides a good way to obtain population statistics for SNe. Although larger uncertainties are inherent in this analytical model compared to more involved studies, one must bear in mind these results are effectively arising from just two-filter optical observations of the SNe and a single spectrum (compared to multi-band UV/optical/NIR photometry and at least several epochs of spectral coverage, required for more detailed modelling), making this is a remarkable method to dramatically improve the current statistics of explosion parameters for various SN types.

As mentioned in Section 6.2.1, the findings of Maeda et al. (2003) indicate that modelling of the nebular light curve is required to determine accurately the contribution of the inner, denser region of the ejecta. This manifests itself as the parameters  $f_M$  and  $f_E$ . For the cases where direct modelling could not determine  $f_M$  and  $f_E$ , due to a lack of data in the nebular phase, the average values for the same SN type was used instead. Therefore, all further discussion of explosion parameters relates to the *total* values, where the SNe without nebular modelling (see Table 6.7) had their photospheric values corrected by the average  $f_M$  and  $f_E$  values of its type.

Although such a simple treatment of the explosions allows populations of explosion parameters to be derived relatively cheaply, the uncertainties are consequently large compared to more detailed studies. It is difficult to quantify the systematic uncertainties per object a priori. With more detailed modelling, aspects such as the asphericity,  $^{56}\text{Ni}$  mass distribution and  $\kappa_{\text{opt}}$  can be constrained, but these are unknown for the majority of the SNe presented here. Observational uncertainties come in the form of the distance determination, photometric errors and  $v_{\text{ph}}$  measurements.<sup>3</sup>

The error on  $M_{\text{Ni}}$  is primarily driven by the error in the distance to the SN, photometric errors were found to affect the light curve comparatively little. Where possible, the error on the distance modulus was based on the collection of distance determinations presented in NED for each host (with a 2-sigma clipping applied to the distribution if there were sufficient values). Otherwise literature uncertainties were used, or, finally, a reasonable error assumed

---

<sup>3</sup>Statistical uncertainties from the fit, along with those found from varying the epochs of data used in the fit (within sensible limits), were found to be much less than these errors and as such are not included.

based on the uncertainty of other hosts. As can be inferred from Fig. 6.1 (top panel), an over (under) estimated distance would result in an over (under) estimated peak luminosity and thus  $M_{\text{Ni}}$ , since  $\tau_m$  will be unaffected. Additionally, SNe 2006T and 2006ep have more uncertain upper limits on  $M_{\text{Ni}}$ , found by assuming that they suffer the median  $E(B - V)_{\text{host}}$  of the sample.

The errors on  $v_{\text{ph}}$  directly affects the  $M_{\text{ej}}/E_{\text{K}}$  ratio at a given  $\tau_m$ . The uncertainties were estimated by taking into account both intrinsic uncertainties in the fitting method ( $\sim 1000 \text{ km s}^{-1}$ ) as well as accounting for the fact that not all spectra were directly observed at peak. For example, a  $v_{\text{ph}}$  determination before peak could overestimate  $v_{\text{ph}}$  at peak and similarly underestimate it for a determination after peak. Therefore  $v_{\text{ph}}$  values derived from spectra before (after) peak had an additional component to the lower (upper) error budget. The power law of Branch et al. (2002) ( $v_{\text{ph}} \propto t^{-2/(n-1)}$ , where  $n = 3.6$ ) was used as a gauge of the size of this potential offset from the  $v_{\text{ph}}$  at peak. Fe II and Si II lines were assumed to trace  $v_{\text{ph}}$  although SN 2003bg, where the only velocity determination was found from He I lines, had an additional lower uncertainty in  $v_{\text{ph}}$  of  $2500 \text{ km s}^{-1}$ , found to be reasonable given the discrepancies between He I and Si II/Fe II line velocities around peak (e.g. Valenti et al., 2008; Pastorello et al., 2008; Taubenberger et al., 2011). Errors on the  $v_{\text{ph}}$  values of SNe that were assigned the average  $v_{\text{ph}}$  for their type were taken to be  $2500 \text{ km s}^{-1}$ . As an example, for a SN with a fixed  $\tau_m$  of 9 days and  $v_{\text{ph}} = 10000 \text{ km s}^{-1}$ , an uncertainty in  $v_{\text{ph}}$  of  $1000 \text{ km s}^{-1}$  represents an uncertainty in  $M_{\text{ej}}$  and  $E_{\text{K}}$  of  $\sim 10$  and  $\sim 30$  per cent respectively. Each SN was remodelled using the lower and upper limits to  $v_{\text{ph}}$  in order to obtain uncertainties on the fitted parameters arising from inaccurate velocity determination.

One additional parameter that has a large impact on the derived  $M_{\text{ej}}$  and  $E_{\text{K}}$  values is the choice of  $\kappa_{\text{opt}}$ . An assumption within to the model is that the opacity is constant over the optically thick, photospheric phase, however some gauge of the uncertainty this assumption introduces can be probed by varying  $\kappa_{\text{opt}}$ . Taking a 20 per cent uncertainty in  $\kappa_{\text{opt}}$  for fixed  $\tau_m$  and  $v_{\text{ph}}$  translates to an uncertainty of  $+25/-17$  per cent in  $M_{\text{ej}}$  and  $E_{\text{K}}$  (since both have the same dependence on  $\kappa_{\text{opt}}$ <sup>4</sup>).

<sup>4</sup>Using Eqs. (6.2) and (6.5):  $M_{\text{ej}}^3/E_{\text{K}} \propto \kappa_{\text{opt}}^{-2} \rightarrow M_{\text{ej}} \propto \kappa_{\text{opt}}^{-1} v_{\text{ph}}$ , given  $E_{\text{K}}/M_{\text{ej}} \propto v_{\text{ph}}^2$  – and therefore  $E_{\text{K}} \propto \kappa_{\text{opt}}^{-1} v_{\text{ph}}^3$ .

Uncertainties on the explosion parameters arising from the above described sources of error are included in the results, which are shown in Table 6.7.

With such population studies, the statistical distribution of explosion parameters as a function of SN type can be investigated. This was initially done by plotting the cumulative distributions of the parameters for each type, shown in Fig. 6.8. This figure highlights the extreme nature of the SNe Ic-BL in the  $M_{\text{Ni}}$  and  $E_{\text{K}}$  distributions. SN Ic-BL are hugely more energetic than any of the other subtypes (the least energetic SN Ic-BL has an  $E_{\text{K}}$  value similar to the most energetic of any of the other sub types), and also have much larger  $M_{\text{Ni}}$  values on average, although it should be noted that SNe Ib and Ic can reach such high  $M_{\text{Ni}}$  values, but the bulk of these SNe have much lower values. However,  $M_{\text{ej}}$  distributions do not distinguish SNe Ic-BL from other SE SNe clearly, indicating that the mass of the ejecta is not an important factor in the explanation for these events. SNe I Ib, Ib and Ic are indistinguishable in all three parameters. There appears to be a hint that SNe I Ib favour lower values of  $M_{\text{Ni}}$  and  $E_{\text{K}}$  cf. SNe Ib and Ic, but their  $M_{\text{ej}}$  do not show this to such an extent, which may be a result of their additional envelope retention (i.e. having more mass to be ejected on explosion).

The two-sample Kolmogorov-Smirnov test (K-S test) was applied to each pair of SN types to ascertain the probability ( $p$  value) that the two samples are drawn from the same parent population (i.e. the two cumulative distributions being tested are just differently sampled realisations of a single, continuous, underlying distribution). Note, however, that the K-S test does not give any indication on what this distribution is. The  $p$  value is determined by the sample sizes and the  $D$  parameter, where  $D$  is the maximal difference between the two normalised cumulative distributions. Succinctly put, a small  $p$  value indicates it is statistically unlikely the two samples are explained by a single population. The results of the K-S test are given in Table 6.8, which confirm the ‘by-eye’ judgements on the distributions made above. Significant ( $p \leq 0.01$ ) differences are found between the  $M_{\text{Ni}}$  values of SNe Ic-BL and SNe I Ib and Ic, with Ib being also close to this significance limit. The  $E_{\text{K}}$  distribution of SNe Ic-BL is statistically distinguished from those of SNe I Ib and Ib at very high confidence and SNe Ic to a lesser extent ( $\sim 2\sigma$ ). As expected,  $M_{\text{ej}}$  distributions cannot be distinguished and all 4 subtypes are consistent with being drawn from any of the other samples. There are

no significant values to distinguish between the samples of SNe I Ib, Ib and Ic.<sup>5</sup>

These conclusions do not include results based on modelling done on SN 2012bz (Chapter 4) since the SN is at a moderate redshift and as such requires  $K$ -corrections to be applied to the photometry. The construction of a bolometric light curve for SN 2012bz is not possible using the method describe here and it is therefore neglected. Despite this, based on pseudo-bolometric light curve modelling, SN 2012bz was a spectacular SN even by SNe Ic-BL standards with  $M_{\text{Ni}} \sim 0.6 M_{\odot}$ ,  $M_{\text{ej}} \sim 5.9 M_{\odot}$   $E_{\text{K}} \sim 41 \times 10^{51}$  ergs. Its inclusion in the cumulative distribution or K-S tests, would only serve to enhance the statistical distinction of SNe Ic-BL from other SE SNe types.

These results back up the findings of [Cano \(2013\)](#), where the use of SN 1998bw as a template is used to make pseudo-bolometric light curves. The improvements of this investigation include the use of truly bolometric light curves that are independent of the assumption that SN 1998bw is an appropriate template for all SE SNe, the inclusion of SNe I Ib as a sample, and a larger proportion of SNe that have had their  $v_{\text{ph}}$  value directly measured near peak.

Each of the parameters derived from the modelling are plotted against each other in Fig. 6.9. A zoom-in of the  $M_{\text{ej}}$  against  $E_{\text{K}}$  plot is also shown including only SNe I Ib, Ib and Ic. The bulk of these SNe appear to form a fairly tight correlation in this plot. This is a result of the fairly similar  $v_{\text{ph}}$  values they exhibit (which, in turn, dictates the  $M_{\text{ej}}/E_{\text{K}}$  ratio). Conversely, SNe Ic-BL, which can have very high velocities (Table 6.6), are found at smaller  $M_{\text{ej}}/E_{\text{K}}$  ratios, as dictated by Eq. 6.5.

---

<sup>5</sup>The discussion is largely unchanged when neglecting to correct the SNe without nebular modelling for  $f_{\text{M}}$  and  $f_{\text{E}}$ , however, the significance levels of any differences drop slightly.

Table 6.7: Results of explosion parameter modelling for SE SNe

SN name	Type	This chapter			Literature values			Reference
		$M_{\text{Ni}}$ ( $M_{\odot}$ )	$M_{\text{ej}}$ ( $M_{\odot}$ )	$E_{\text{K}}$ $10^{51}$ ergs	$M_{\text{Ni}}$ ( $M_{\odot}$ )	$M_{\text{ej}}$ ( $M_{\odot}$ )	$E_{\text{K}}$ $10^{51}$ ergs	
1993J	I <b>b</b>	$0.14 \pm 0.03$	$1.7_{-0.4}^{+0.5}$	$1.4_{-0.5}^{+0.7}$	0.06–0.14	1.9–3.5	1–1.6	Utrobin (1994); Woosley et al. (1994); Young et al. (1995)
1994I	I <b>c</b>	$0.08 \pm 0.02$	$0.6_{-0.1}^{+0.2}$	$1.0_{-0.4}^{+0.4}$	0.07	0.9–1.3	1	Iwamoto et al. (1994); Young et al. (1995); Sauer et al. (2006)
1996cb	I <b>b</b>	$0.12 \pm 0.03$	$2.3_{-0.5}^{+0.7}$	$1.9_{-0.7}^{+1.2}$	–	–	–	–
1998bw	I <b>c</b> -BL	$0.75 \pm 0.09$	$7.0_{-1.3}^{+1.9}$	$30.0_{-7.0}^{+12.3}$	0.4–0.7	$\sim 10$	20–50	Iwamoto et al. (1998); Nakamura et al. (2001)
1999dn <sup>a</sup>	I <b>b</b>	$0.11 \pm 0.03$	$4.7_{-1.1}^{+1.4}$	$7.1_{-2.0}^{+2.9}$	–	–	–	–
1999ex <sup>a</sup>	I <b>b</b>	$0.17 \pm 0.01$	$3.2_{-0.8}^{+1.1}$	$3.2_{-1.0}^{+1.9}$	0.16	–	2.7	Stritzinger et al. (2002)
2002ap <sup>a</sup>	I <b>c</b> -BL	$0.09 \pm 0.02$	$2.8_{-0.5}^{+0.9}$	$6.7_{-1.8}^{+4.1}$	0.07	2.5–5	4–10	Mazzali et al. (2002)
2003bg <sup>a</sup>	I <b>b</b>	$0.21 \pm 0.03$	$6.0_{-2.5}^{+1.7}$	$7.4_{-5.5}^{+3.1}$	0.2	4	5	Mazzali et al. (2009)
2003jd	I <b>c</b> -BL	$0.51 \pm 0.09$	$2.7_{-0.5}^{+0.7}$	$6.8_{-1.8}^{+2.4}$	–	–	–	–
2004aw	I <b>c</b>	$0.26 \pm 0.04$	$4.4_{-1.2}^{+1.2}$	$6.6_{-3.0}^{+2.6}$	–	–	–	–
2004dk <sup>a</sup>	I <b>b</b>	$0.25 \pm 0.04$	$3.6_{-0.9}^{+1.2}$	$4.2_{-1.3}^{+2.5}$	–	–	–	–

2004dn	Ic	$0.23 \pm 0.03$	$3.8_{-0.7}^{+1.1}$	$7.1_{-2.0}^{+3.4}$	–	–	–	–
2004fe <sup>a</sup>	Ic	$0.30 \pm 0.04$	$1.7_{-0.6}^{+0.7}$	$1.5_{-1.0}^{+1.8}$	–	–	–	–
2004ff <sup>a</sup>	Ic	$0.22 \pm 0.03$	$1.4_{-0.5}^{+0.6}$	$1.2_{-0.8}^{+1.5}$	–	–	–	–
2004gq	Ib	$0.13 \pm 0.05$	$1.4_{-0.6}^{+0.7}$	$1.1_{-0.8}^{+1.4}$	–	–	–	–
2005az	Ib	$0.37 \pm 0.07$	$3.2_{-1.3}^{+1.5}$	$2.1_{-1.5}^{+2.8}$	–	–	–	–
2005bf <sup>a</sup>	Ib-pec	$0.09 \pm 0.02$	$1.0_{-0.3}^{+0.4}$	$0.8_{-0.2}^{+0.8}$	0.08	–	–	Maeda et al. (2007)
2005hg	Ib	$0.66 \pm 0.09$	$2.7_{-1.1}^{+1.3}$	$2.4_{-1.5}^{+3.3}$	–	–	–	–
2005kz <sup>a</sup>	Ic-BL	$0.62 \pm 0.08$	$8.2_{-2.1}^{+2.6}$	$22.8_{-10.9}^{+15.5}$	–	–	–	–
2005mf	Ic	$0.24 \pm 0.03$	$1.5_{-0.6}^{+0.7}$	$1.4_{-1.0}^{+1.7}$	–	–	–	–
2006T <sup>b</sup>	IIb	$0.10_{-0.02}^{+0.05}$	$1.9_{-0.8}^{+0.9}$	$1.4_{-1.0}^{+1.9}$	–	–	–	–
2006aj <sup>a</sup>	Ic-BL	$0.36 \pm 0.07$	$1.4_{-0.9}^{+1.3}$	$6.4_{-3.3}^{+7.0}$	0.21	2	2	Mazzali et al. (2006)
2006el <sup>a</sup>	IIb	$0.27_{-0.04}^{+0.07}$	–	–	–	–	–	–
2006ep <sup>a,b</sup>	Ib	$0.08_{-0.02}^{+0.04}$	$2.6_{-1.1}^{+1.2}$	$2.1_{-1.5}^{+2.9}$	–	–	–	–
2007C	Ib	$0.19 \pm 0.03$	$1.5_{-0.6}^{+0.7}$	$1.3_{-0.9}^{+1.8}$	–	–	–	–
2007Y	Ib	$0.051 \pm 0.004$	$1.9_{-0.5}^{+0.5}$	$1.9_{-0.9}^{+0.8}$	0.06	1–2	0.5–2	Stritzinger et al. (2009); Maurer et al. (2010)
2007gr	Ic	$0.10 \pm 0.03$	$2.4_{-0.5}^{+0.7}$	$2.9_{-0.9}^{+1.2}$	–	–	–	–
2007ru	Ic-BL	$0.52 \pm 0.05$	$2.8_{-0.5}^{+0.7}$	$13.0_{-2.9}^{+3.9}$	–	–	–	–
2007uy	Ib	$0.33 \pm 0.07$	$3.7_{-1.0}^{+1.0}$	$9.9_{-4.8}^{+3.3}$	–	–	–	–

2008D <sup>a</sup>	Ib	$0.12 \pm 0.02$	$3.9^{+1.5}_{-0.9}$	$4.4^{+4.0}_{-1.4}$	0.05–0.1	3–7	2–8.5	Soderberg et al. (2008); Mazzali et al. (2008); Tanaka et al. (2009)
2008ax	IIb	$0.16 \pm 0.04$	$3.0^{+1.3}_{-0.7}$	$2.6^{+2.8}_{-1.0}$	–	–	–	–
2009bb	Ic-BL	$0.31 \pm 0.02$	$2.5^{+0.8}_{-0.5}$	$9.2^{+6.6}_{-2.2}$	–	–	–	–
2009jf	Ib	$0.24 \pm 0.04$	$4.2^{+1.7}_{-0.9}$	$5.8^{+5.2}_{-1.9}$	–	–	–	–
2010bh	Ic-BL	$0.37 \pm 0.05$	$1.2^{+0.3}_{-0.2}$	$33.0^{+8.5}_{-5.9}$	–	–	–	–
2011bm	Ic	$0.71 \pm 0.12$	$9.6^{+2.8}_{-2.1}$	$10.0^{+4.5}_{-3.4}$	–	–	–	–
2011dh	IIb	$0.09 \pm 0.02$	$1.8^{+0.6}_{-0.4}$	$1.1^{+0.6}_{-0.4}$	0.06–0.07	2	0.6–1	Bersten et al. (2012); Shivers et al. (2013)

<sup>a</sup> Inner component modelling based on the average  $f_M$  and  $f_E$  values for the SN type (see text).

<sup>b</sup> Only Galactic extinction is accounted for, thus the  $M_{Ni}$  value has a large upper uncertainty arising from the possibility of significant, unaccounted for, reddening.

<sup>c</sup> Uncertain peak  $L_{bol}$  value accounted for in  $M_{Ni}$  uncertainty.

Table 6.8: Results of two-sample Kolmogorov-Smirnov test on explosion parameters between SE SNe types

Sample 1	Sample 2	$M_{\text{Ni}}$		$M_{\text{ej}}$		$E_{\text{K}}$	
		$D$	$p$	$D$	$p$	$D$	$p$
I Ib	Ib	0.253	0.887	0.372	0.515	0.358	0.561
I Ib	Ic	0.607	0.075	0.375	0.608	0.333	0.749
I Ib	Ic-BL	0.875	<b>0.002</b>	0.417	0.471	0.833	<b>0.006</b>
I Ib	Ic	0.365	0.428	0.317	0.611	0.269	0.800
I Ib	Ic-BL	0.644	0.017	0.288	0.726	0.846	<b>0.001</b>
I Ic	Ic-BL	0.750	<b>0.010</b>	0.375	0.519	0.625	0.049

### Specific SN notes

**SN 2005bf** SN 2005bf was a very unusual burst that displayed a double-humped light curve (Fig. 6.10). There have been various models proposed for the SN with various energy sources powering the second, brighter hump. Among these,  $^{56}\text{Ni}$  decay has been proposed, and, given the high peak luminosity,  $\sim 5 \times 10^{42} \text{ erg s}^{-1}$ , this requires  $M_{\text{Ni}} \sim 0.32 M_{\odot}$  to power it (Tominaga et al., 2005). However, Maeda et al. (2007), from nebular modelling, find that  $\sim 0.08 M_{\odot}$  of  $^{56}\text{Ni}$  was synthesised, inconsistent with a  $^{56}\text{Ni}$ -powered explanation for the second peak. Conversely, it is found from modelling here that the first peak is well matched by a  $^{56}\text{Ni}$  mass similar to the value derived from nebular modelling ( $M_{\text{Ni}} \sim 0.087 M_{\odot}$ , see Table 6.7). This would suggest that the first hump is indeed powered by the  $^{56}\text{Ni}$  synthesised in the explosion, but also that the second hump has some other power source (e.g. magnetar Maeda et al., 2007).

**SN 2006el** The light curve of SN 2006el lacks data to properly tie the fit. Although the rise to peak is observed, no data exist beyond this on the decline before the end of the photospheric phase in order to tie the width of the light curve and thus constrain  $M_{\text{ej}}$  and  $E_{\text{K}}$ . As such, the  $M_{\text{Ni}}$  determination is trusted, although an additional uncertainty is included, arising from varying the true value of  $L_{\text{bol}}$  between reasonable limits and using equation 6 of Rest et al. (2011); the  $M_{\text{ej}}$  and  $E_{\text{K}}$  values are not used.

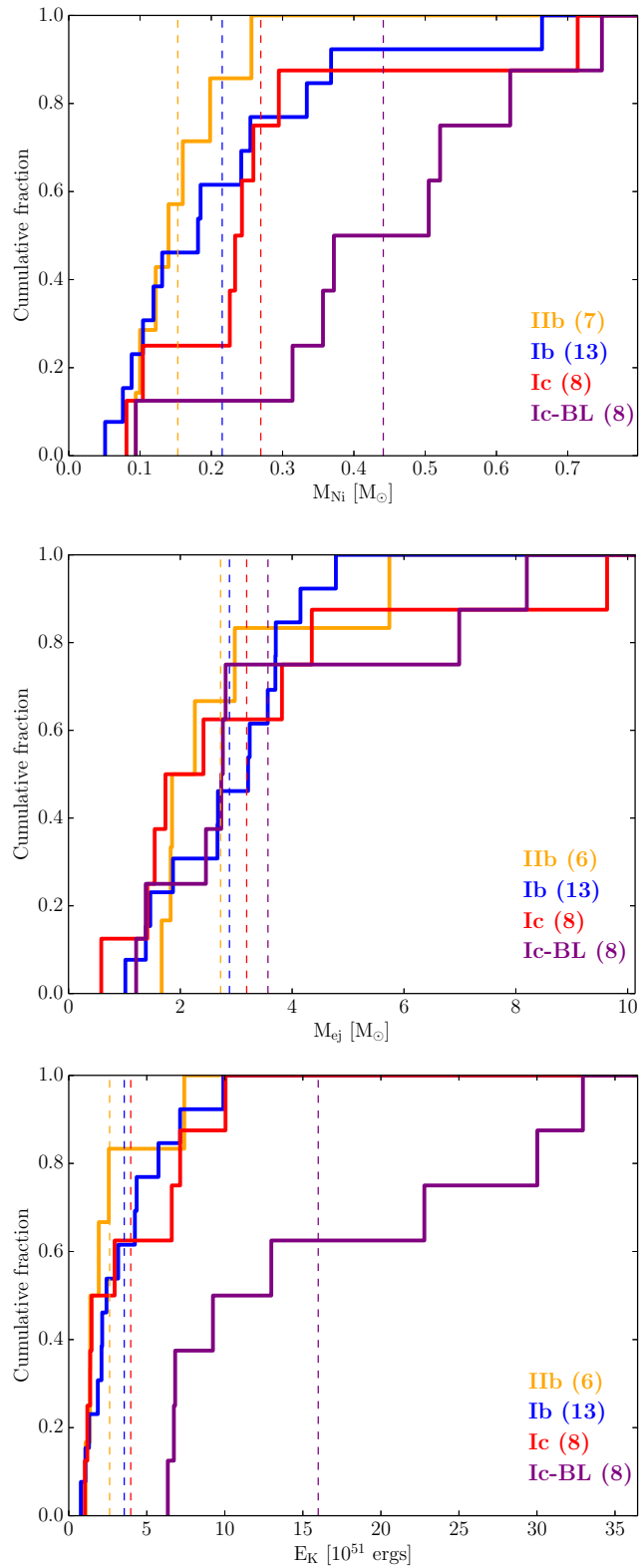


Figure 6.8: Cumulative distributions for explosion parameters of SE SNe (top:  $M_{\text{Ni}}$ , middle:  $M_{\text{ej}}$ , bottom:  $E_{\text{K}}$ ), divided by subtype. Where appropriate, values have been corrected for contributions from the inner component (see text). The average values for each SN type are indicated by the vertical dashed lines.

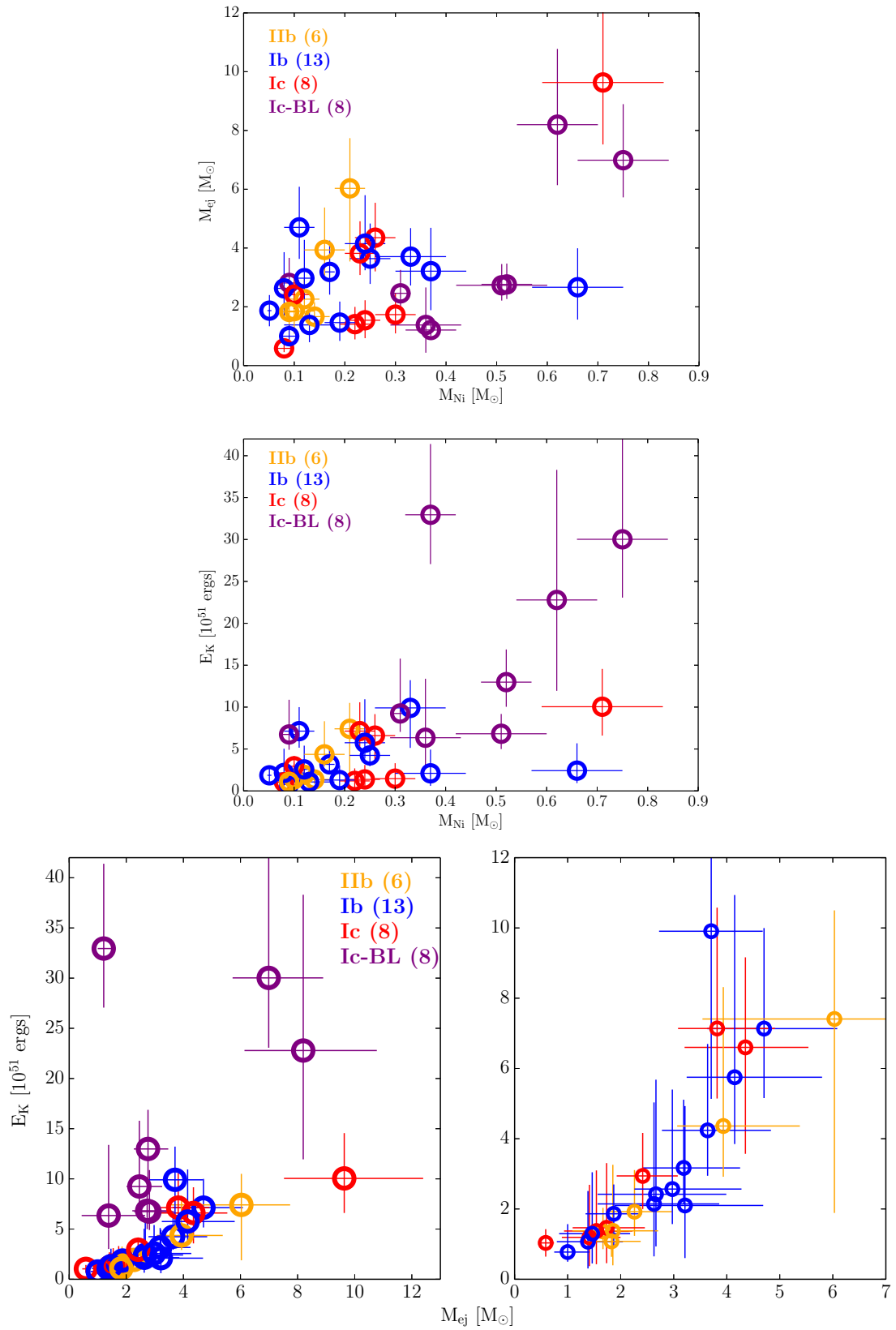


Figure 6.9: Correlations between explosion parameters of SE SNe, divided by subtype. Where appropriate, values have been corrected for contributions from the inner component (see text).

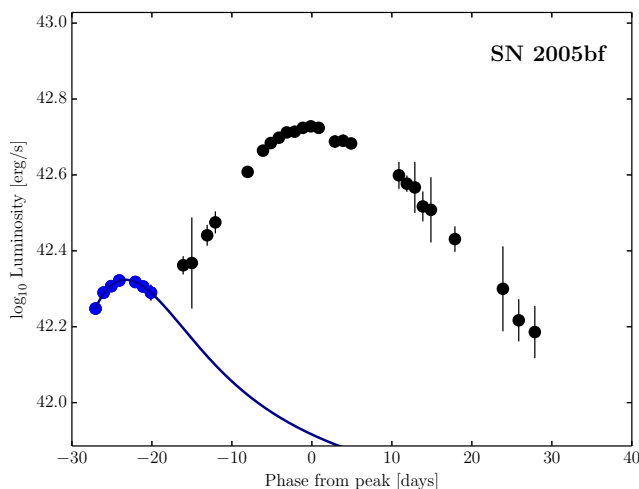


Figure 6.10: As for Fig. 6.7 but for SN 2005bf. Although the second hump can also be well fit by the analytical model, it requires a  $^{56}\text{Ni}$  mass far above that determined from nebular modelling. However, the first hump can be well modelled with a  $^{56}\text{Ni}$  mass consistent with nebular spectral modelling (blue line).

## 6.4 Summary

An analysis of a large sample of SE SN bolometric light curves has been made. Peak bolometric absolute magnitudes range from  $-16.3$  to  $-19.2$  mag, with both luminosity extremes occupied by a SN Ib.  $\Delta m_{15,\text{bol}}$  values range from 0.20 to 1.37 mag, with SNe Ic making up the extremes of this distribution. No correlation between peak luminosity and light curve width is found (cf. SNe Ia). The bolometric light curves were modelled using an analytical prescription utilising the velocity of the photosphere at peak light. These results agree well with those found from more computationally and observationally expensive models, which suggests a future, large-scale deployment of this method is feasible and will provide accurate results. The extreme nature of SNe Ic-BL was evident from the modelling, with their  $M_{\text{Ni}}$  and  $E_{\text{K}}$  values being statistically distinct from all other SE SNe type by at least  $2\sigma$ , with  $p \leq 0.01$  for two of the three other subtypes in each parameter. Conversely, the  $M_{\text{ej}}$  values for SNe Ic-BL are very similar to those of SNe Iib, Ib and Ic. This suggests the mass of the cores are of similar masses to those of other SNe upon explosion, although the initial zero-age main sequence masses may be different. As such, the mass of the core does not appear to play a major role in determining the presence of high velocity features, and this must be dictated by another property of the core (e.g. composition or angular momentum)

and/or the presence of a central engine that may initiate such high velocity features. Note that for several SNe Ic-BL the presence of a central engine is known, and this occurs when its jet axis is aligned with the line-of-sight and observed as a GRB or X-ray flash). The average  $M_{\text{Ni}}$ ,  $M_{\text{ej}}$  and  $E_{\text{K}}$  values *all* follow the same sequence of increasing value of IIb  $\rightarrow$  Ib  $\rightarrow$  Ic  $\rightarrow$  Ic-BL.

# Chapter 7

## Thesis summary and future research

### 7.1 Thesis summary

This thesis has continued the current effort that is being put into understanding the explosive deaths of stars.

The pipeline CLASP has been developed to make image alignment and subtraction painless for the purposes of transient follow-up and environmental studies. The pipeline is designed for ease of use, with the ability to align any arbitrarily shifted, rotated, scaled images with little or no parameter adjustment. The subtraction process also works well in the cases of reasonable seeing and has successfully subtracted data from a number of telescope and instrument configurations.

CLASP was employed to create  $H\alpha$  maps of the hosts of two peculiar types of transients whose nature is very poorly known. Through observing the association with  $H\alpha$  emission (recent SF), respective constraints were placed on the ages of the progenitor systems of these transients, which will inform future modelling of the explosions and provide an additional constraint for any proposed systems.

The GRB-SN 120422A/2012bz was investigated through construction of its pseudo-bolometric light curve. A simple modelling treatment of this light curve revealed its spectacular nature, being one of the brightest SN to have accompanied a GRB and also being one of the most

energetic SN known.

Given the usefulness of bolometric light curves in SN investigations, a method was sought to relieve the observational and time costs involved in their production. Well-observed literature SNe formed the basis of several polynomial fits that allows one to trivially create a bolometric light curve with a simple two-filter optical light curve. The rms scatter around these fits was found to be very small and, barring strongly interacting SNe (e.g. IIn, Ibn), an accurate determination of the bolometric light curve can be made for any CCSN.

These BCs were applied to literature SNe to create the largest sample of SE SN bolometric light curves, with each one modelled in the fashion of SN 2012bz. The simple modelling scheme revealed fitted explosion parameters that agreed well with more involved modelling of a sub-sample of the SNe. This modelling revealed the extreme nature of SNe Ic-BL in energetics and  $^{56}\text{Ni}$  mass, with the SN Iib, Ib and Ic explosion parameter distributions all appearing indistinguishable. Continuous distributions of light curve peaks and time scales were observed, with no clear correlation between the two. Template bolometric light curves for SNe Iib, Ib, Ic and IC-BL were also produced for the first time.

## 7.2 Future research

The research presented here has revealed a number of promising avenues for future research in the field. A few of the current and future studies to be performed are presented here:

- The rates of the peculiar SN 2002cx-like and Ca-rich transients are currently very uncertain. A calculation of these values is needed to further restrict potential progenitor models. Current wide-field untargeted surveys will allow a robust determination of these rates.
- A large number of PTF-discovered CCSN have been observed with the Liverpool Telescope, alongside follow-up done by PTF. These light curves provide an excellent resource from which to continue the creation and modelling of SE SN bolometric light curves. With a much less biased observational strategy, these will provide more com-

plete samples of the sub-types to further investigate the properties that have been investigated here for literature SNe. Once enough light curves have been accumulated, one can then begin to investigate *within* SN sub-types and investigate if the explosions themselves have any knowledge about, for example, the environment in which they are exploding. Given the methods presented, once the data exist, the creation of the bolometric light curves and modelling requires no significant computational or labour expense.

- Alongside this light curve investigation, the hosts of PTF CCSNe are being observed in  $H\alpha$ . Utilising the statistical method presented here for peculiar low-luminosity SNe I, the environments of these SNe can be investigated as a parallel line of study to the light curve analysis.
- The BCs presented will be improved upon as more well-observed SNe exist. These additions may increase the robustness of the fits or, more interestingly, produce SNe who appear to have unusual BCs. A particular area to improve upon is to include a sample of SNe observed in Sloan filters directly, to circumvent the need to transform Johnson-Cousins data.
- The GRB-SN connection is an area of research that has been well-established over the last 15 years, but still has a very low number of events. Many open questions exist about the link between the two (e.g. does the GRB know about the properties of the SN explosion and vice-versa), which will only be answered once a larger sample exists – current and future wide-field surveys (especially ones with deep imaging) will contribute heavily to this.
- The BCs presented are reliant upon a single colour and provide exceptionally tight correlations. Nevertheless, it may be that further information can be gleaned from optical observations. Since it is probable that SNe are followed in three (*gri*) or four (*BVRI*) filters, perhaps utilising two colours, or somehow including information for  $>2$  filters to produce a fit could further reduce the scatter.
- Given the low scatter observed on the BC for even the very heterogeneous CCSNe, it is expected that a similar investigation for SNe Ia would produce even tighter fits.

The pursuit of this investigation is contingent however on the author's desire to incur the wrath of the SN Ia community with his disregard for systematic uncertainties and ignorance of their value beyond very bright light bulbs, and as such may not come to fruition.

- Although the analytic prescription used to model the light curves here produces good agreement with other modelling, it may be that some of the simplifying assumptions can be removed in place of more data constraints, when observations allow, in order to reduce the systematic uncertainties in the model. This may include a description of the evolution of the velocity of the SN, rather than using a single velocity, or allowing for a treatment of the initial  $^{56}\text{Ni}$  mass distribution, for example.
- Observe a Galactic SN (hopefully!)

# Appendix A

## The Normalised Cumulative Rank method

The normalised cumulative rank (NCR) method is a pixel-based statistical analysis of locations (chosen pixels) within an astronomical image. Practically, it is a proxy for determining how associated a particular location in the image is to the detected flux in the image, and, given a large sample of such images and locations, can ascertain the statistical correlation between locations and the tracer chosen<sup>1</sup>. By normalising to the total sum of the pixel values, each pixel can be assigned an NCR value of between zero to one, where one is always the brightest pixel in the image and zero represents any pixel with no detected flux.

The calculations involved in determining an NCR for a chosen pixel location ( $p$ ) are:

- Sort all the pixels in the image by their value and note the index of  $p$  in this array
- Cumulatively sum these values and then normalise by the total sum of all pixel values
- The value of the normalised cumulative sum at the index of  $p$  is the NCR value of  $p$

In reality, however, we are not dealing with ideal data and several measures must be taken to ensure the NCR method is implemented consistently across different images. The NCR

---

<sup>1</sup>For the data analysis in this thesis, the chosen tracers were H $\alpha$  and far- and near-UV emission, as proxies for recent star formation, and the locations were those of various SN types; the method could plausibly be used on imaging of various tracers and various transients.

method has been packaged into a PYTHON script to handle the calculation and data manipulation required. Details of the steps included in this script now follow.

Since we are cumulatively summing the pixel values, in a typical image, where all pixels have a positive value, every location chosen would have a positive NCR. The NCR for a ‘background’ location (i.e. where there is no detected flux above that of the sky) would differ from image to image due to the varying ratio between background pixel brightness and detected flux pixel brightness, and each background location would have a differing NCR due to the Poisson noise in the image. For this reason the NCR method is reliant on the image having a sky-background mean of zero, i.e. the distribution of pixel values, caused by noise in the image, must be centred on zero. This naturally solves the above problem in that the equally negative and positive pixel values of the background will cancel out in the cumulative sum, leaving the sum at zero once we begin to encounter pixels with true detected flux above the noise of the image. Any location with an  $\text{NCR} < 0$  is set to zero since it is buried in the noise of the image and would have a pixel value of zero in idealised data. This technique is shown visually in Fig. A.1.

Practically, obtaining an image background with a mean of exactly zero is not possible. For the  $\text{H}\alpha$  data reduction in this thesis, CLASP (Section 2.2) was used to perform image subtraction prior to performing the NCR analysis on an image. The subtraction routine attempts to fit a varying background function to the images in order to make the difference image have a near-zero background over the entire image. This can struggle, particularly in the cases of large variations across the image background or different background variations for the image and subtracted template frame. To improve upon this, a median-mesh grid is constructed for the image after object masking via the IRAF task OBJMASKS, or iterative sigma-clipping of pixels. By taking the median values of background pixels, sampled across the entire image, the tie points for a low-order spline function are made. 2D-spline interpolation of the median mesh is performed and this function is subtracted from the image.<sup>2</sup> This results in a background that has a mean closer to zero at all areas of the image (with careful attention

---

<sup>2</sup>A smoothing factor can be applied to the spline instead of strictly interpolating the median mesh in the cases where object masking fails to completely mask all emission in the difference image. In these cases the median of a mesh-point containing, for example, the transient host, may be anomalously high compared to surrounding mesh-points, and a smoothed spline will be a better representation of the true background pixel values.

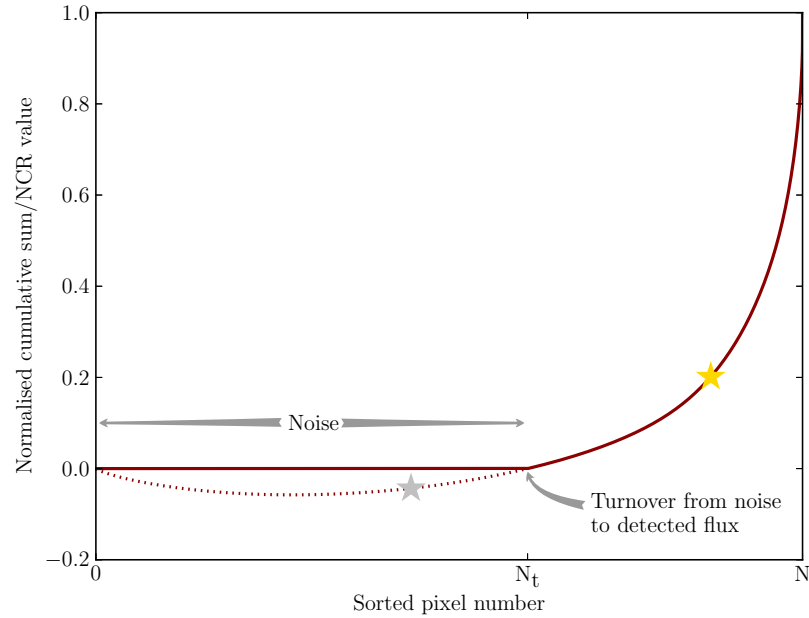


Figure A.1: The NCR values in a typical image are shown (solid line) along with the true value of the normalised cumulative sum (dotted line). At a certain turnover pixel,  $N_t$ , the cumulative sum becomes positive and the NCR of any location in the image with a pixel value greater than  $N_t$  is just equal to the cumulative sum at that pixel (e.g. the gold star has  $\text{NCR} = 0.2$ ). However, below this the cumulative sum only consists of noise, with negative values summing until the minimum of the cumulative sum and these being cancelled by positive values until  $N_t$ , where subsequent pixels have truly positive values, i.e. above that of the noise in the image – detected flux. For example, even though the pixel at the location given by the silver star has a positive value, it is considered an  $\text{NCR} = 0$  location since its value is within the noise of the image.

paid to the area of interest in the image – the location of the transient and its host). This technique is demonstrated in Fig. A.2.

The image is likely to contain artefacts that would erroneously affect the NCR value, for example foreground stars and residuals left by image subtraction. The pixel coordinates of these, along with a radius to mask in pixels, are used to paste over the pixel values within each mask. This is done using the standard manner of masking routines in other astronomical packages. For each mask region, the median and standard deviation of pixels (after sigma-clipping) in an annulus around the mask are determined and a random normal distribution with these characteristics is constructed. This distribution is used to replace pixel values within the mask, see Fig. A.3. A negative cut is also implemented, whereby pixels more than 5 standard deviations below the mean background value are set to zero value, since we do

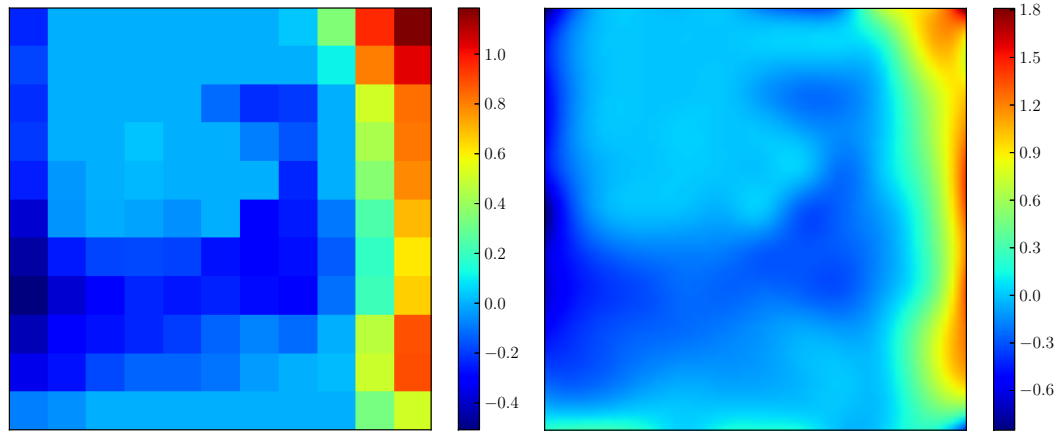


Figure A.2: An object-masked image is evenly sampled at 191-pixel intervals and a median of each interval box is made. These median points form a sparsely sampled mesh (left) which can be interpolated using a spline function to obtain the form of the background (right). This function is subtracted from the image to produce a more uniform, near-zero background in preparation for the NCR analysis. Colour bars indicate pixel values.

not expect such negative pixels in the subtracted image. Generally only a small portion of the image is of interest: the limits of the host and the transient's location. The images are therefore trimmed so that small variations in the background have less influence (since we will be summing fewer background pixels) and also to prevent the need to manually mask every object/residual in the image that is outside the area of interest.

The desired location to investigate in an image is often defined by the RA and DEC of a transient; as such, the NCR method is sensitive to incorrect WCS fits of images. Although WCS fits are generally robust (from visual and star centre comparisons to catalogue values), slight inaccuracies may still exist within the host galaxies where the WCS fit may be not constrained due to a lack of point sources. To combat this, a binning factor can be specified for the image (typically 3); the sectioning and binning of the image is performed such that the pixel at the desired RA and DEC forms the centre of a binned super-pixel.

For ease of use, the section, mask regions and mask radius can be defined interactively, via XPA messaging to DS9<sup>3</sup>. This makes the NCR trivial to perform in a few seconds for most cases, once the data are properly reduced and a WCS is fitted. As well as intuitively defining the section and the mask regions, a Digitized Sky Survey (DSS) image of the region can

<sup>3</sup><http://hea-www.harvard.edu/RD/ds9/site/Home.html>

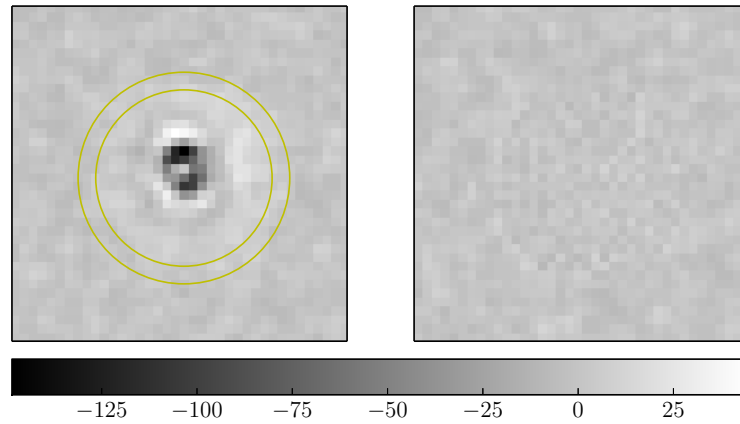


Figure A.3: A star residual (left) is masked (right) using the routine described in the text. Pixels within the annuli shown are used to determine the pixel distribution to use as replacement. Colour bar values indicate pixel values and show that the residual is cleanly masked, resulting in near-zero pixel values over the image section.

be displayed to aid in foreground star identification and determining host size. The DS9 interface is shown in Fig. A.4.

On the final, background-flattened, artefact-masked, sectioned and binned image, the NCR calculations shown above are performed to obtain an NCR value for the desired pixel location and maps of NCR values are provided for visual inspection. Some examples of what these NCR maps look like are shown in Fig. A.5.

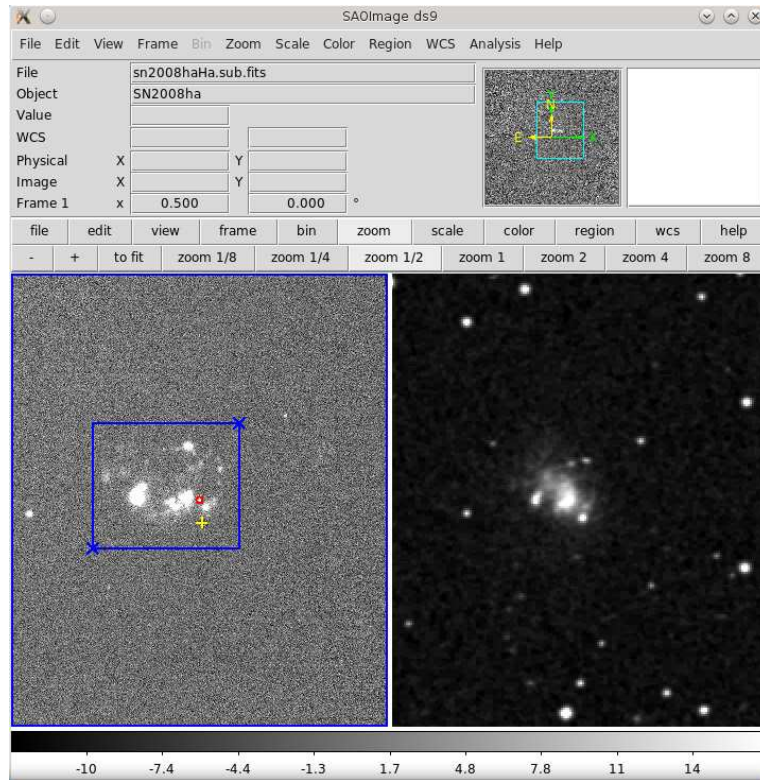


Figure A.4: The DS9 interface for interactive NCR analysis. The SN location (red circle) is shown to the user on the image. A DSS image of the region can be downloaded and displayed on another frame to aid with identifying foreground stars, whose coordinates can be marked for masking (yellow plus). The section is selected as two corners of a rectangle (blue crosses). These various commands are performed with key presses by the user and hovering the cursor over the desired pixel.

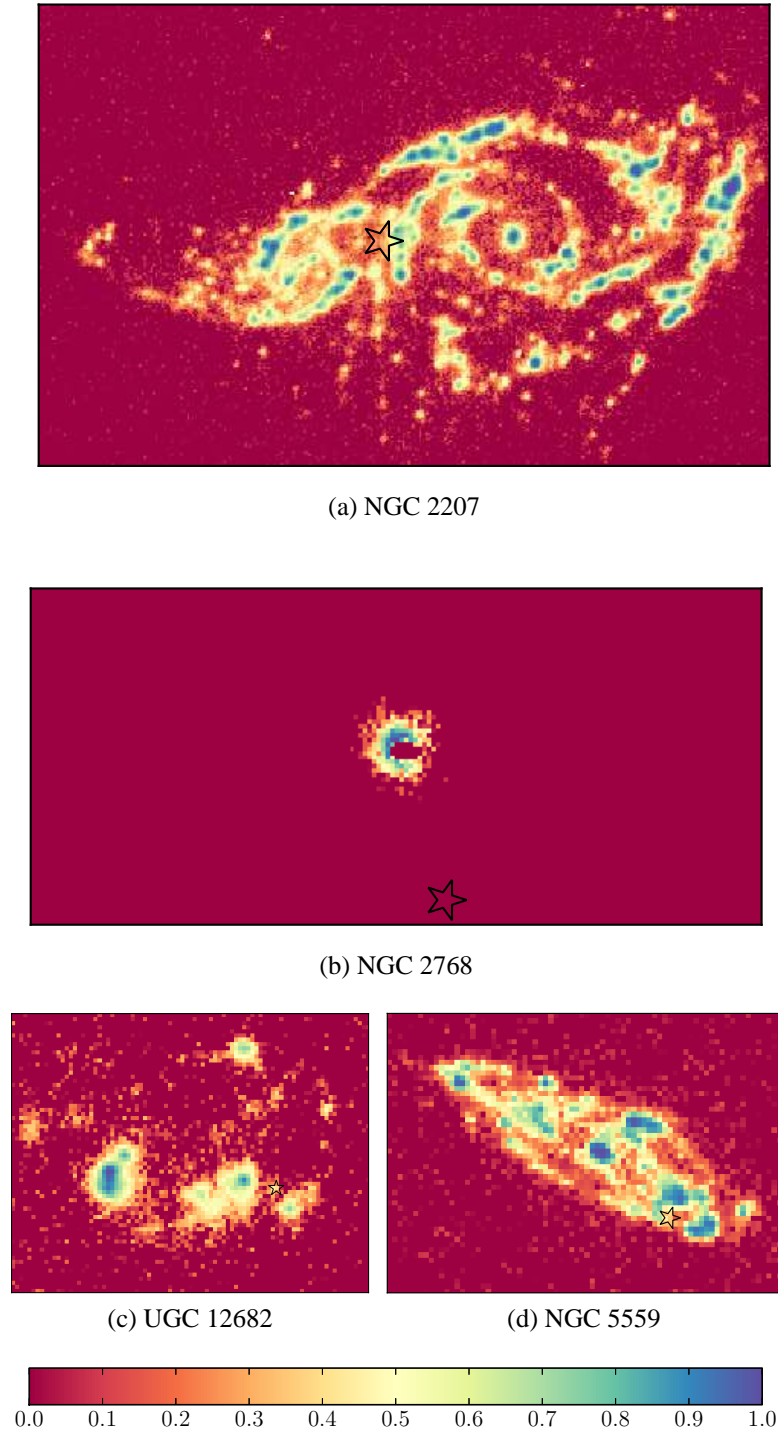
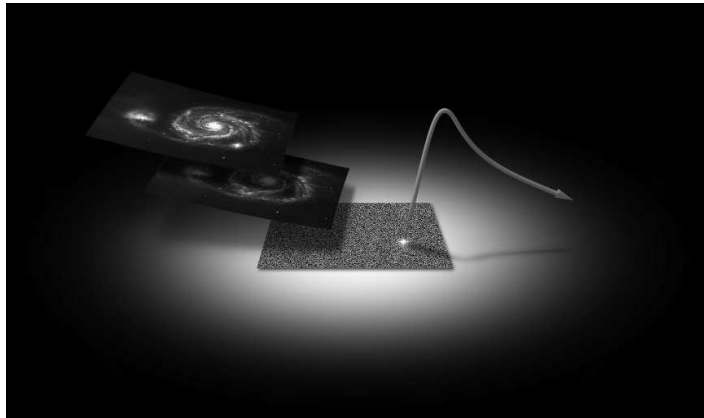


Figure A.5: Examples of NCR heat maps for transient hosts in  $H\alpha$  imaging. The regions of intense  $H\alpha$  emission have larger NCR values (see colour bar), with regions of no detected flux at  $NCR = 0$ . The imperfections of the background being exactly and truly centred on zero everywhere manifest themselves as pixels in background regions having very small, but positive NCR values, this typically does not substantially affect the value of the NCR for a given location. The location of the transient in each host investigated as part of Chapter 3 is marked by a star.

# Appendix B

## The CLASP pipeline



## B.1 CLASP usage manual

### B.1.1 Quick Use

SUBPIPE is run from the script `run-subpipe.py` (image alignment/subtraction) and PHOTPIPE from `run-photpipe.py` (photometry), or either via the GUI - `CLASP.py`, all found in the main CLASP directory.

Prior to running the pipelines, a check of `PIPEcfg.py` and `HOTPanTScfg.py` should be made to ensure the parameters in there to suit the data (see Appendix B.1.3).

Below are quick, arbitrary examples how to run them. See Appendices B.1.3 to B.1.5 for a more in-depth look at the configuration files, the command line arguments, and the GUI.

Running from command line (including required arguments):

```
$ python run-subpipe.py imagedir template workdir
```

```
$ python run-photpipe.py workdir
```

Help on command line arguments:

```
$ python run-subpipe.py -h
```

```
$ python run-photpipe.py -h
```

Example use of parameters (including all possible optional arguments):

```
$ python run-subpipe.py /path/to/imagedir /path/to/template.fits  
/path/to/workdir -s "*.fits" -u -f /path/to/fringeframe.fits  
-b /path/to/bpm.fits -ct -ti 1 -ii 1 -t 5 -c i  
-stamps /path/to/mystamps.txt -d
```

```
$ python run-photpipe.py /path/to/workdir -c -sa 3 -la 15 -o
```

```
345,678,234,567,567,678 -s /path/to/starcoords.txt -d
```

(Note the string quotes around the selection argument, `-s`, since it will often include a wildcard. `Imagedir` may also be a file path to perform subtraction for a single image.)

## B.1.2 Requirements

The following are required to run CLASP:

PYTHON (version 2.x,  $x \geq 7$ )

PYRAF

IRAF (the mosaic package MSCRED is also required for defringing)

PYFITS

NUMPY (version 1.5.1+)

SCIPY (version 0.9.0+)

SEXTRACTOR (version 2.5.0+)

HOTPANTS (version 5.1.0+)

## B.1.3 The configuration files

The CLASP pipelines can be run from either the command line or GUI. However, there are two configuration files that need to be set properly for your data before you begin running the pipelines.

The two configuration files are named `PIPECFG.py` and `HOTPanTScfg.py`, located in the main CLASP directory. These files hold parameters that may need to be modified depending on the data you are feeding the pipelines. Comments in these files should explain most of the parameters and the following can be used to guide you towards the parameters that should be checked for the best success rate.

`HOTPanTScfg.py` holds all the parameters for the HOTPANTS code and in most cases the parameter names are the same as when running HOTPANTS directly (these can be seen

by running your HOTPANTS executable with no arguments, which will give you more information on them). Particular attention should be paid to the pixel value limits and the number of stamps in each direction, `nsx,nsy` should be adjusted very roughly with the number of objects in your *image*. In images with few point sources, it may be prudent to reduce `kernelorder` to 1 as the kernel form can vary wildly if not sufficiently constrained (i.e. not enough stamps sampled across the entire image). The `hotpantsdir` should also point to your HOTPANTS executable directory

`PIPEcfg.py` holds data-dependent parameters. Some of these relate to the names of FITS headers which should be self-explanatory. Pay particular attention, however, to the parameters defining the min/max number of objects to find in *image* and *template*. The pipelines run `SEXTRACTOR` to detect objects at the given thresholds (initially `IMAGETHRESH` and `TEMPTHRESH`). This is adjusted (a limited number of times) by the pipeline to meet the min/max object requirements. A judgement by eye of the number of sources in *image* and *template* should allow these to be set sensibly and to broadly enclose these estimates. `XYXYMATCH` and `WREGISTER` relate to their namesakes in IRAF, and can be switched on and off as required. If both are true, `WREGISTER` will only be used in the event that `XYXYMATCH` fails to find a solution. The parameters for `XYXYMATCH` can also be set at the bottom of this configuration file; see the `XYXYMATCH` docs for more information on these.

## B.1.4 Command line

General command line argument help is obtained via:

```
$ python run-subpipe.py -h
```

```
$ python run-photpipe.py -h
```

### **run-subpipe.py**

Required arguments:

`imagedir` (string): the path to a directory containing science images to be subtracted. Alternatively can be set to the file path of a single file to subtract a single image. Selected files will not be altered as all images to be processed are copied to *workdir*.

`template` (string): the file path to *template*. Again, this file will not be affected and will be copied to the work directory in a subfolder, 'template/"/>.

`workdir` (string): the path to a directory to store all the output from SUBPIPE. If the path doesn't exist then it will be created. If the directory exists, SUBPIPE will ask whether you want to remove it, in which case *everything contained within the directory, including all sub-directories will be deleted*.

Optional arguments:

`-s SELECTION` (string): the pattern for sub-selecting files within `imagedir` (if it is indeed a directory). Note that SELECTION must be enclosed in string quotes since it will probably contain some kind of wildcard. Default = `'*.fits'`.

`-u`: including this flag will run SUBPIPE in 'update' mode. In this case an existing `workdir` must be specified containing output from a previous run of SUBPIPE. The log and report files will be appended to rather than overwritten. This is useful should a small subset of images have poor subtraction, for example. Parameters in `PIPECFG.py` and `HOTPanTSCfg.py` can be altered, and rerunning SUBPIPE, passing just the image(s) for which subtraction needs to be redone, will overwrite the previous output for the image(s). Similarly, extra subtractions can be added to an existing *workdir* using `u`, and these will be added alongside existing output without destroying previous work. Each time a *workdir* is updated, the configuration files are checked for similarity to the copies already in *workdir*, and if any changes are found the configuration files are copied with a `.[n].py` suffix – the `shelve` file will keep track of what images used what configuration file versions.

`-f FRINGEFRA`ME (string): the file path to the appropriate fringe frame for *image*. A single extension FITS file of the same dimensions as *image*.

`-b BADPIXELMASK` (string): the file path to the appropriate bad pixel mask for *image*. A single extension FITS file which must be of the same dimensions as *image* (if not, it will be

ignored). Zero at all good pixels and non-zero to indicate bad pixels.

`-ct`: including this flag will mark *template* for cleaning also, i.e. defringing, bad pixel removal (as supplied by `-f` and `-b`).

`-ti` TEMP\_ITER (integer): the number of cosmic ray cleaning iterations to perform on *template*. Additional passes may find more cosmic rays not found by the first pass but generally one or two will remove the bulk of them. Set to 0 to skip cosmic ray cleaning. Default = 2.

`-ii` IMAGE\_ITER (integer): as above but for *image*. Default = 2.

`-t` TRIM (integer): the border size in pixels to fix to a value of zero around the edge of the image. This can mask any instrumental effects at the edges of the image that may look like cosmic rays hits to the removal algorithm and will cause significant slowing. Default = 0.

`-c` CONVOLVE (char): the frame to be convolved prior to subtraction. By default the program will convolve the frame with the better-seeing (s), as measured by the median FWHM of point sources. Alternatively, one can let HOTPANTS determine the best frame for convolution (h) or to specify that *template* (t) or *image* (i) should always be convolved. Default = s.

`-s` STAMPS (string): the file path to a list of stamps to use for the subtraction (see HOTPANTS docs for more info on how these are used). x and y centres of stamps should be in columns 1 and 2 respectively.

`-d`: include this flag to run verbosely to stdout. The log file will always have full verbosity but this flag signifies to output to the terminal verbosely also.

### **run-photpipe.py**

Required arguments:

`workdir` (string): the path to the directory containing the output from SUBPIPE, upon which photometry is to be performed. Between calling `run-subpipe.py` and `run-photpipe.py`,

*workdir* should be unaltered (i.e. no renaming of files/directories or removal of files) or there is likely to be unanticipated behaviour or failures!

Optional arguments:

-c: including this flag will clobber the existing *lightcurve.txt* file in *workdir*. Use this to redo photometry, if a light curve file exists and this flag isn't present, then PHOTPIPE will let the user know and exit.

-sa SMALLAP (integer): an integer value denoting the radius of the aperture (in pixels) to use for small aperture photometry. This is the aperture used for initial photometry before applying an aperture correction to LARGEAP. `Default = 3`.

-la LARGEAP (integer): an integer value denoting the radius of the aperture (in pixels) to correct photometry to. Photometry will be performed on aperture correction stars in steps between SMALLAP and LARGEAP to compute the curve of growth. `Default = 15`.

-o OBJCOORDS (comma-separated floats): a string of the form "*x1,y1,x2,y2,...,xn,yn*" denoting the x and y pixel positions of the object(s) to perform photometry on (i.e. the transients/variables). Centering will be applied to these so high accuracy at this stage is not required. If omitted, a subtracted image will be displayed with instructions on how to provide the pipeline with the objects' coordinates.

-s STARCOOLIST (string): the file path to a list of star coordinates that are to be used for aperture correction and *image-template* offset determinations (i.e. these should be non-varying, foreground stars). Format is two column, white-space separated with x and y in columns 1 and 2 respectively.

-d: include this flag to run verbosely to stdout. The log file will always have full verbosity but this flag signifies to output to the terminal verbosely also.

### B.1.5 GUI

Optionally, either pipeline can be called from the GUI named *CLASP.py*. Running this file will open a window as below with input boxes for the various parameters and a box on the

right to display the pipeline output.

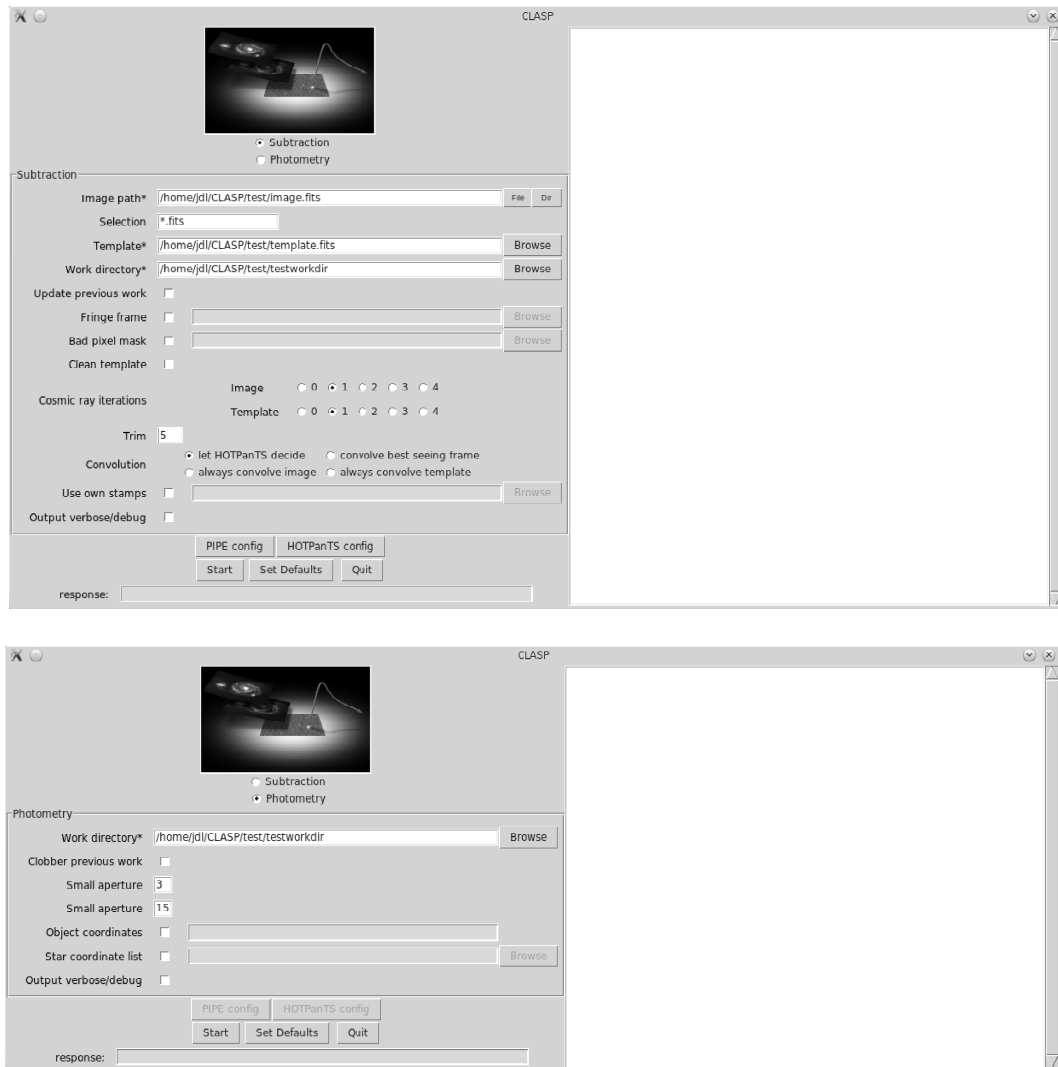


Figure B.1: Screenshots of CLASP GUI window for SUBPIPE (top) and PHOTPIPE (bottom). Output is redirected to the text widget on the right hand side.

SUBPIPE or PHOTPIPE are chosen using the radio buttons near the logo. The resultant boxes relate directly to the arguments explained above and should be self-explanatory.

When browsing for ‘Image Path’, choose ‘File’ to select a single image or ‘Dir’ to specify you want to use a directory that contains many images.

The ‘PIPE config’ and ‘HOTPanTS config’ buttons will open the configuration files for editing prior to running the pipeline.

Once the boxes have been filled as desired, pressing the ‘Start’ button will call the selected

pipe. Output will be shown on the right, which may include errors which cause the pipeline to cancel (e.g. *template* doesn't exist). A new call can be made after altering the parameters by clicking 'Start' again. Once the pipeline is running, 'Start' will be replaced by a 'STOP (term)' button, which, if pressed, will send the SIGTERM command to the pipeline. If this doesn't stop it a SIGKILL command can be sent by a subsequent click, effectively ending the pipeline if desired. Note this may not be immediate if the pipeline is waiting to receive a signal after an external call to SExtractor or HOTPANTS, for example. The pipeline will end once the call to the external package is complete.

Should the pipeline require input (e.g. asking whether to remove *workdir* or asking for the stars which to use for aperture correction/offset calculations), then it will ask for it in the right hand output box. You can interact with the pipeline via the 'response' entry bar at the bottom left. Type what you wish to send to the pipeline into this entry bar (e.g. 'y' for 'yes, remove the existing work directory' when asked) followed by the Return or Enter key to send the contents as input to the pipeline.

## B.1.6 Output

Ultimately the data products of interest will be the *image.sub.fits* files (the subtracted images) and *lightcurve.txt* (the photometry of the object(s) selected in the *template* system), after running SUBPIPE and PHOTPIPE respectively.

Here is an explanation of the other (many!) output files you will see appear in *workdir* and what they contain. (*template*) here indicates the template file name minus the file extension, (*image*) is the image file name minus the extension; there will be one of each of these files in *workdir* for every input science image.

After running SUBPIPE the following files will appear in *workdir*:

**template/** A directory containing:

**(*template*).stars** SExtractor output catalogue of objects found in *template*.

**(*template*).fits** cleaned *template* (defringed, bad pixels and cosmic rays removed, as

specified).

**(image).hotpants** Output from HOTPANTS detailing the subtraction process.

**(image).stars\_orig** SExtractor output catalogue of objects found in the original *image*.

**(image).stars** SExtractor output catalogue of objects found in the aligned *image*.

**(image).fits** cleaned (defringed, bad pixels and cosmic rays removed, as specified) and aligned *image*.

**(image).png** a quick look png of the aligned *image*.

**(image).sub.fits** subtracted image (*image* – *template*).

**(image).sub.png** a quick look png of the subtracted image.

**HOTPanTScfg.py** a copy of the `HOTPanTScfg.py` file as it existed when SUBPIPE was called; this makes it easy to see what parameters were used when returning to/repeating subtractions. Additional configuration files may appear with a `.[n].py` suffix if updates are made, see Appendix [B.1.4](#).

**pipe.shelve** a `shelve` file used by PHOTPIPE to read in all the information produced by SUBPIPE.

**PIPEcfg.py** as above for `HOTPanTScfg.py` but for `PIPEcfg.py`.

**subpipe.log.txt** output from SUBPIPE with verbosity turned on.

**subpipe\_report.txt** breakdown of interesting values found for the *template* and *image*, as well as the outcome of the subtraction for each image. Good to quickly see if anything went wrong and with what image(s).

Additionally, after calling PHOTPIPE the following will appear:

**template/** A directory containing:

**(template).apcor** aperture correction and error for *template* as calculated by MKAP-FILE.

**(*template*).apcorphot** PHOT output with apertures ranging from SMALLAP to LARGEAP.

**(*template*).mkap** MKAPFILE output with large aperture corrected photometry for *template* stars.

**(*template*).objcoo** x and y coordinates of object(s).

**(*template*).starcoo** x and y coordinates of stars used for aperture correction and offset calculations.

**(*image*).apcor** as above but for *image*.

***image*() .apcorphot** as above but for *image*.

**(*image*).mkap** as above but for *image*.

**(*image*).objcoo** PHOT output of initial object photometry using SMALLAP.

**lightcurve.txt** final photometry of object(s) in *template* system with name of image and time of observation.

**photpipe.log.txt** output from PHOTPIPE with verbosity turned on.

**photpipe.report.txt** breakdown of photometry values at various stages and the associated errors for every object within each *image*.

# Bibliography

- C. Alard. Image subtraction using a space-varying kernel. *A&AS*, 144:363–370, June 2000.
- C. Alard and R. H. Lupton. A Method for Optimal Image Subtraction. *ApJ*, 503:325–+, Aug. 1998.
- J. P. Anderson, S. M. Habergham, P. A. James, and M. Hamuy. Progenitor mass constraints for core-collapse supernovae from correlations with host galaxy star formation. *MNRAS*, 424:1372–1391, Aug. 2012.
- J. P. Anderson and P. A. James. Constraints on core-collapse supernova progenitors from correlations with H $\alpha$  emission. *MNRAS*, 390:1527–1538, Nov. 2008.
- I. Arcavi, A. Gal-Yam, M. M. Kasliwal, R. M. Quimby, E. O. Ofek, S. R. Kulkarni, P. E. Nugent, S. B. Cenko, J. S. Bloom, M. Sullivan, D. A. Howell, D. Poznanski, A. V. Filippenko, N. Law, I. Hook, J. Jönsson, S. Blake, J. Cooke, R. Dekany, G. Rahmer, D. Hale, R. Smith, J. Zolkower, V. Velur, R. Walters, J. Henning, K. Bui, D. McKenna, and J. Jacobsen. Core-collapse Supernovae from the Palomar Transient Factory: Indications for a Different Population in Dwarf Galaxies. *ApJ*, 721:777–784, Sept. 2010.
- I. Arcavi, A. Gal-Yam, O. Yaron, A. Sternberg, I. Rabinak, E. Waxman, M. M. Kasliwal, R. M. Quimby, E. O. Ofek, A. Horesh, S. R. Kulkarni, A. V. Filippenko, J. M. Silverman, S. B. Cenko, W. Li, J. S. Bloom, M. Sullivan, P. E. Nugent, D. Poznanski, E. Gorbikov, B. J. Fulton, D. A. Howell, D. Bersier, A. Riou, S. Lamotte-Bailey, T. Griga, J. G. Cohen, S. Hachinger, D. Polishook, D. Xu, S. Ben-Ami, I. Manulis, E. S. Walker, K. Maguire, Y.-C. Pan, T. Matheson, P. A. Mazzali, E. Pian, D. B. Fox, N. Gehrels, N. Law, P. James, J. M. Marchant, R. J. Smith, C. J. Mottram, R. M. Barnsley, M. T. Kandrashoff, and K. I.

- Clubb. SN 2011dh: Discovery of a Type IIb Supernova from a Compact Progenitor in the Nearby Galaxy M51. *ApJ Let.*, 742:L18, Dec. 2011.
- W. D. Arnett. Type I supernovae. I - Analytic solutions for the early part of the light curve. *ApJ*, 253:785–797, Feb. 1982.
- P. Astier, J. Guy, N. Regnault, R. Pain, E. Aubourg, D. Balam, S. Basa, R. G. Carlberg, S. Fabbro, D. Fouchez, I. M. Hook, D. A. Howell, H. Lafoux, J. D. Neill, N. Palanque-Delabrouille, K. Perrett, C. J. Pritchett, J. Rich, M. Sullivan, R. Taillet, G. Aldering, P. Antilogus, V. Arsenijevic, C. Balland, S. Baumont, J. Bronder, H. Courtois, R. S. Ellis, M. Filioi, A. C. Gonçalves, A. Goobar, D. Guide, D. Hardin, V. Lusser, C. Lidman, R. McMahon, M. Mouchet, A. Mourao, S. Perlmutter, P. Ripoche, C. Tao, and N. Walton. The Supernova Legacy Survey: measurement of  $\Omega_M$ ,  $\Omega$  and  $w$  from the first year data set. *A&A*, 447:31–48, Feb. 2006.
- W. Baade and F. Zwicky. On Super-novae. *Proceedings of the National Academy of Science*, 20:254–259, May 1934.
- R. Barbon, S. Benetti, E. Cappellaro, F. Patat, M. Turatto, and T. Iijima. SN 1993J in M 81: One year of observations at Asiago. *A&AS*, 110:513, May 1995.
- R. Barbon, F. Ciatti, and L. Rosino. Photometric properties of type II supernovae. *A&A*, 72: 287–292, Feb. 1979.
- A. C. Becker, D. Homrighausen, A. J. Connolly, C. R. Genovese, R. Owen, S. J. Bickerton, and R. H. Lupton. Regularization techniques for PSF-matching kernels - I. Choice of kernel basis. *MNRAS*, 425:1341–1349, Sept. 2012.
- S. Benetti, E. Cappellaro, M. Turatto, S. Taubenberger, A. Harutyunyan, and S. Valenti. Supernova 2002ic: The Collapse of a Stripped-Envelope, Massive Star in a Dense Medium? *ApJ Let.*, 653:L129–L132, Dec. 2006.
- S. Benetti, M. Turatto, S. Valenti, A. Pastorello, E. Cappellaro, M. T. Botticella, F. Bufano, F. Ghinassi, A. Harutyunyan, C. Inserra, A. Magazzù, F. Patat, M. L. Pumo, and S. Taubenberger. The Type Ib SN 1999dn: one year of photometric and spectroscopic monitoring. *MNRAS*, 411:2726–2738, Mar. 2011.

- S. Benitez-Herrera, S. Taubenberger, S. Valenti, S. Benetti, and A. Pastorello. ESO-NTT Large Program spectroscopic classification of SNhunt 121. *The Astronomer's Telegram*, 4047:1, Apr. 2012.
- M. C. Bersten, O. G. Benvenuto, K. Nomoto, M. Ergon, G. Folatelli, J. Sollerman, S. Benetti, M. T. Botticella, M. Fraser, R. Kotak, K. Maeda, P. Ochner, and L. Tomasella. The Type IIb Supernova 2011dh from a Supergiant Progenitor. *ApJ*, 757:31, Sept. 2012.
- M. C. Bersten and M. Hamuy. Bolometric Light Curves for 33 Type II Plateau Supernovae. *ApJ*, 701:200–208, Aug. 2009.
- M. Bessell and S. Murphy. Spectrophotometric Libraries, Revised Photonic Passbands, and Zero Points for UBVRI, Hipparcos, and Tycho Photometry. *PASP*, 124:140–157, Feb. 2012.
- M. S. Bessell, F. Castelli, and B. Plez. Model atmospheres broad-band colors, bolometric corrections and temperature calibrations for O - M stars. *A&A*, 333:231–250, May 1998.
- R. M. Bionta, G. Blewitt, C. B. Bratton, D. Casper, and A. Ciocio. Observation of a neutrino burst in coincidence with supernova 1987A in the Large Magellanic Cloud. *Physical Review Letters*, 58:1494–1496, Apr. 1987.
- S. Blondin, M. Modjaz, R. Kirshner, P. Challis, and M. Calkins. Supernova 2006el in UGC 12188. *Central Bureau Electronic Telegrams*, 626:1, Sept. 2006.
- J. S. Bloom, D. Kasen, K. J. Shen, P. E. Nugent, N. R. Butler, M. L. Graham, D. A. Howell, U. Kolb, S. Holmes, C. A. Haswell, V. Burwitz, J. Rodriguez, and M. Sullivan. A Compact Degenerate Primary-star Progenitor of SN 2011fe. *ApJ Let.*, 744:L17, Jan. 2012.
- M. T. Botticella, S. J. Smartt, R. C. Kennicutt, E. Cappellaro, M. Sereno, and J. C. Lee. A comparison between star formation rate diagnostics and rate of core collapse supernovae within 11 Mpc. *A&A*, 537:A132, Jan. 2012.
- D. M. Bramich. A new algorithm for difference image analysis. *MNRAS*, 386:L77–L81, May 2008.

- D. Branch, E. Baron, R. C. Thomas, D. Kasen, W. Li, and A. V. Filippenko. Reading the Spectra of the Most Peculiar Type Ia Supernova 2002cx. *PASP*, 116:903–908, Oct. 2004.
- D. Branch, S. Benetti, D. Kasen, E. Baron, D. J. Jeffery, K. Hatano, R. A. Stathakis, A. V. Filippenko, T. Matheson, A. Pastorello, G. Altavilla, E. Cappellaro, L. Rizzi, M. Turatto, W. Li, D. C. Leonard, and J. C. Shields. Direct Analysis of Spectra of Type Ib Supernovae. *ApJ*, 566:1005–1017, Feb. 2002.
- A. Bressan, M. Della Valle, and P. Marziani. On core-collapse supernovae in normal and in Seyfert galaxies. *MNRAS*, 331:L25–L29, Apr. 2002.
- P. J. Brown. *The ultraviolet properties of supernovae*. PhD thesis, The Pennsylvania State University, Sept. 2009.
- F. Bufano, E. Pian, J. Sollerman, S. Benetti, G. Pignata, S. Valenti, S. Covino, P. D’Avanzo, D. Malesani, E. Cappellaro, M. Della Valle, J. Fynbo, J. Hjorth, P. A. Mazzali, D. E. Reichart, R. L. C. Starling, M. Turatto, S. D. Vergani, K. Wiersema, L. Amati, D. Bersier, S. Campana, Z. Cano, A. J. Castro-Tirado, G. Chincarini, V. D’Elia, A. de Ugarte Postigo, J. Deng, P. Ferrero, A. V. Filippenko, P. Goldoni, J. Gorosabel, J. Greiner, F. Hammer, P. Jakobsson, L. Kaper, K. S. Kawabata, S. Klose, A. J. Levan, K. Maeda, N. Masetti, B. Milvang-Jensen, F. I. Mirabel, P. Møller, K. Nomoto, E. Palazzi, S. Piranomonte, R. Salvaterra, G. Stratta, G. Tagliaferri, M. Tanaka, N. R. Tanvir, and R. A. M. J. Wijers. The Highly Energetic Expansion of SN 2010bh Associated with GRB 100316D. *ApJ*, 753:67, July 2012.
- A. C. Calder, T. Plewa, N. Vladimirova, D. Q. Lamb, and J. W. Truran. Type Ia Supernovae: An Asymmetric Deflagration Model. *ArXiv Astrophysics e-prints*, May 2004.
- Z. Cano. A new method for estimating the bolometric properties of Ibc supernovae. *MNRAS*, 434:1098–1116, Sept. 2013.
- Z. Cano, D. Bersier, C. Guidorzi, S. Kobayashi, A. J. Levan, N. R. Tanvir, K. Wiersema, P. D’Avanzo, A. S. Fruchter, P. Garnavich, A. Gomboc, J. Gorosabel, D. Kasen, D. Kopač, R. Margutti, P. A. Mazzali, A. Melandri, C. G. Mundell, P. E. Nugent, E. Pian, R. J. Smith,

- I. Steele, R. A. M. J. Wijers, and S. E. Woosley. XRF 100316D/SN 2010bh and the Nature of Gamma-Ray Burst Supernovae. *ApJ*, 740:41, Oct. 2011.
- Y. Cao, M. M. Kasliwal, I. Arcavi, A. Horesh, P. Hancock, S. Valenti, S. B. Cenko, S. R. Kulkarni, A. Gal-Yam, E. Gorbikov, E. O. Ofek, D. Sand, O. Yaron, M. Graham, J. M. Silverman, J. C. Wheeler, G. H. Marion, E. S. Walker, P. Mazzali, D. A. Howell, K. L. Li, A. K. H. Kong, J. S. Bloom, P. E. Nugent, J. Surace, F. Masci, J. Carpenter, N. Degenaar, and C. R. Gelino. Discovery, Progenitor and Early Evolution of a Stripped Envelope Supernova iPTF13bvn. *ApJ Let.*, 775:L7, Sept. 2013.
- S. Cassisi, I. Iben, Jr., and A. Tornambe. Hydrogen-accreting Carbon-Oxygen White Dwarfs. *ApJ*, 496:376, Mar. 1998.
- R. M. Catchpole, J. W. Menzies, A. S. Monk, W. F. Wargau, D. Pollaco, B. S. Carter, P. A. Whitelock, F. Marang, C. D. Laney, L. A. Balona, M. W. Feast, T. H. H. Lloyd Evans, K. Sekiguchi, J. D. Laing, D. M. Kilkeny, J. Spencer Jones, G. Roberts, A. W. J. Cousins, G. van Vuuren, and H. Winkler. Spectroscopic and photometric observations of SN 1987a. II - Days 51 to 134. *MNRAS*, 229:15P–25P, Nov. 1987.
- E. Chatzopoulos, J. C. Wheeler, J. Vinko, Z. L. Horvath, and A. Nagy. Analytical Light Curve Models of Superluminous Supernovae:  $\chi^2$ -minimization of Parameter Fits. *ApJ*, 773:76, Aug. 2013.
- Y.-N. Chin and Y.-L. Huang. Identification of the guest star of AD 185 as a comet rather than a supernova. *Nature*, 371:398–399, Sept. 1994.
- L. Chomiuk, A. M. Soderberg, M. Moe, R. A. Chevalier, M. P. Rupen, C. Badenes, R. Margutti, C. Fransson, W.-f. Fong, and J. A. Dittmann. EVLA Observations Constrain the Environment and Progenitor System of Type Ia Supernova 2011fe. *ApJ*, 750:164, May 2012.
- R. Chornock, E. Berger, E. M. Levesque, A. M. Soderberg, R. J. Foley, D. B. Fox, A. Frebel, J. D. Simon, J. J. Bochanski, P. J. Challis, R. P. Kirshner, P. Podsiadlowski, K. Roth, R. E. Rutledge, B. P. Schmidt, S. S. Sheppard, and R. A. Simcoe. Spectroscopic Discovery

- of the Broad-Lined Type Ic Supernova 2010bh Associated with the Low-Redshift GRB 100316D. *ArXiv e-prints*, Apr. 2010.
- A. Clocchiatti, N. B. Suntzeff, R. Covarrubias, and P. Candia. The Ultimate Light Curve of SN 1998bw/GRB 980425. *AJ*, 141:163, May 2011.
- A. Clocchiatti and J. C. Wheeler. On the Light Curves of Stripped-Envelope Supernovae. *ApJ*, 491:375, Dec. 1997.
- S. A. Colgate and R. H. White. The Hydrodynamic Behavior of Supernovae Explosions. *ApJ*, 143:626, Mar. 1966.
- J. Cooke, M. Sullivan, A. Gal-Yam, E. J. Barton, R. G. Carlberg, E. V. Ryan-Weber, C. Horst, Y. Omori, and C. G. Díaz. Superluminous supernovae at redshifts of 2.05 and 3.90. *Nature*, 491:228–231, Nov. 2012.
- A. Corsi, E. O. Ofek, D. A. Frail, D. Poznanski, I. Arcavi, A. Gal-Yam, S. R. Kulkarni, K. Hurley, P. A. Mazzali, D. A. Howell, M. M. Kasliwal, Y. Green, D. Murray, M. Sullivan, D. Xu, S. Ben-ami, J. S. Bloom, S. B. Cenko, N. M. Law, P. Nugent, R. M. Quimby, V. Pal'shin, J. Cummings, V. Connaughton, K. Yamaoka, A. Rau, W. Boynton, I. Mitrofanov, and J. Goldsten. PTF 10bzf (SN 2010ah): A Broad-line Ic Supernova Discovered by the Palomar Transient Factory. *ApJ*, 741:76, Nov. 2011.
- P. A. Crowther. Physical Properties of Wolf-Rayet Stars. *ARA&A*, 45:177–219, Sept. 2007.
- P. A. Crowther. On the association between core-collapse supernovae and H ii regions. *MNRAS*, 428:1927–1943, Jan. 2013.
- I. J. Danziger, R. A. E. Fosbury, D. Alloin, S. Cristiani, J. Dachs, C. Gouiffes, B. Jarvis, and K. C. Sahu. Optical spectroscopy of SN 1987A. *A&A*, 177:L13–L16, May 1987.
- G. de Vaucouleurs. Recherches sur les Nebuleuses Extragalactiques. *Annales d'Astrophysique*, 11:247, Jan. 1948.
- G. de Vaucouleurs, A. de Vaucouleurs, H. G. Corwin, Jr., R. J. Buta, G. Paturel, and P. Fouqué. *Third Reference Catalogue of Bright Galaxies. Volume I: Explanations and*

- references. *Volume II: Data for galaxies between 0<sup>h</sup> and 12<sup>h</sup>. Volume III: Data for galaxies between 12<sup>h</sup> and 24<sup>h</sup>*. Springer, 1991.
- L. Dessart, D. J. Hillier, C. Li, and S. Woosley. On the nature of supernovae Ib and Ic. *MNRAS*, 424:2139–2159, Aug. 2012.
- B. Dilday, D. A. Howell, S. B. Cenko, J. M. Silverman, P. E. Nugent, M. Sullivan, S. Ben-Ami, L. Bildsten, M. Bolte, M. Endl, A. V. Filippenko, O. Gnat, A. Horesh, E. Hsiao, M. M. Kasliwal, D. Kirkman, K. Maguire, G. W. Marcy, K. Moore, Y. Pan, J. T. Parrent, P. Podsiadlowski, R. M. Quimby, A. Sternberg, N. Suzuki, D. R. Tytler, D. Xu, J. S. Bloom, A. Gal-Yam, I. M. Hook, S. R. Kulkarni, N. M. Law, E. O. Ofek, D. Polishook, and D. Poznanski. PTF 11kx: A Type Ia Supernova with a Symbiotic Nova Progenitor. *Science*, 337:942–, Aug. 2012.
- S. P. Driver, P. D. Allen, J. Liske, and A. W. Graham. The Millennium Galaxy Catalogue: The Luminosity Functions of Bulges and Disks and Their Implied Stellar Mass Densities. *ApJ Let.*, 657:L85–L88, Mar. 2007a.
- S. P. Driver, C. C. Popescu, R. J. Tuffs, J. Liske, A. W. Graham, P. D. Allen, and R. de Propris. The Millennium Galaxy Catalogue: the B-band attenuation of bulge and disc light and the implied cosmic dust and stellar mass densities. *MNRAS*, 379:1022–1036, Aug. 2007b.
- M. R. Drout, A. M. Soderberg, A. Gal-Yam, S. B. Cenko, D. B. Fox, D. C. Leonard, D. J. Sand, D.-S. Moon, I. Arcavi, and Y. Green. The First Systematic Study of Type Ibc Supernova Multi-band Light Curves. *ApJ*, 741:97, Nov. 2011.
- V. V. Dwarkadas. On luminous blue variables as the progenitors of core-collapse supernovae, especially Type II<sub>n</sub> supernovae. *MNRAS*, 412:1639–1649, Apr. 2011.
- J. J. Eldridge, M. Fraser, S. J. Smartt, J. R. Maund, and R. M. Crockett. The death of massive stars - II. Observational constraints on the progenitors of type Ibc supernovae. *ArXiv e-prints*, Jan. 2013.
- J. J. Eldridge, R. G. Izzard, and C. A. Tout. The effect of massive binaries on stellar populations and supernova progenitors. *MNRAS*, 384:1109–1118, Mar. 2008.

- J. J. Eldridge and C. A. Tout. The progenitors of core-collapse supernovae. *MNRAS*, 353: 87–97, Sept. 2004.
- A. Elmhamdi, I. J. Danziger, N. Chugai, A. Pastorello, M. Turatto, E. Cappellaro, G. Altavilla, S. Benetti, F. Patat, and M. Salvo. Photometry and spectroscopy of the Type IIP SN 1999em from outburst to dust formation. *MNRAS*, 338:939–956, Feb. 2003.
- A. Elmhamdi, D. Tsvetkov, I. J. Danziger, and A. Kordi. Photometric Evolution of SNe Ib/c 2004ao, 2004gk, and 2006gi. *ApJ*, 731:129, Apr. 2011.
- M. Ergon, J. Sollerman, M. Fraser, A. Pastorello, S. Taubenberger, N. Elias-Rosa, M. Bersten, A. Jerkstrand, S. Benetti, M. T. Botticella, C. Fransson, A. Harutyunyan, R. Kotak, S. Smartt, S. Valenti, F. Bufano, E. Cappellaro, M. Fiaschi, A. Howell, E. Kankare, L. Magill, S. Mattila, R. Naves, P. Ochner, J. Ruiz, K. Smith, L. Tomasella, and M. Turatto. Optical and near-infrared observations of SN 2011dh - The first 100 days. *ArXiv e-prints*, May 2013.
- R. Fernández and B. D. Metzger. Nuclear Dominated Accretion Flows in Two Dimensions. I. Torus Evolution with Parametric Microphysics. *ApJ*, 763:108, Feb. 2013.
- A. V. Filippenko. Optical Spectra of Supernovae. *ARA&A*, 35:309–355, 1997.
- E. L. Fitzpatrick. Correcting for the Effects of Interstellar Extinction. *PASP*, 111:63–75, Jan. 1999.
- G. Folatelli, C. Contreras, M. M. Phillips, S. E. Woosley, S. Blinnikov, N. Morrell, N. B. Suntzeff, B. L. Lee, M. Hamuy, S. González, W. Krzeminski, M. Roth, W. Li, A. V. Filippenko, R. J. Foley, W. L. Freedman, B. F. Madore, S. E. Persson, D. Murphy, S. Boissier, G. Galaz, L. González, P. J. McCarthy, A. McWilliam, and W. Pych. SN 2005bf: A Possible Transition Event between Type Ib/c Supernovae and Gamma-Ray Bursts. *ApJ*, 641: 1039–1050, Apr. 2006.
- R. J. Foley, P. J. Brown, A. Rest, P. J. Challis, R. P. Kirshner, and W. M. Wood-Vasey. Early- and Late-Time Observations of SN 2008ha: Additional Constraints for the Progenitor and Explosion. *ApJ Let.*, 708:L61–L65, Jan. 2010a.

- R. J. Foley, P. J. Challis, R. Chornock, M. Ganeshalingam, W. Li, G. H. Marion, N. I. Morrell, G. Pignata, M. D. Stritzinger, J. M. Silverman, X. Wang, J. P. Anderson, A. V. Filippenko, W. L. Freedman, M. Hamuy, S. W. Jha, R. P. Kirshner, C. McCully, S. E. Persson, M. M. Phillips, D. E. Reichart, and A. M. Soderberg. Type Iax Supernovae: A New Class of Stellar Explosion. *ApJ*, 767:57, Apr. 2013.
- R. J. Foley, R. Chornock, A. V. Filippenko, M. Ganeshalingam, R. P. Kirshner, W. Li, S. B. Cenko, P. J. Challis, A. S. Friedman, M. Modjaz, J. M. Silverman, and W. M. Wood-Vasey. SN 2008ha: An Extremely Low Luminosity and Exceptionally Low Energy Supernova. *AJ*, 138:376–391, Aug. 2009.
- R. J. Foley, M. S. Papenkova, B. J. Swift, A. V. Filippenko, W. Li, P. A. Mazzali, R. Chornock, D. C. Leonard, and S. D. Van Dyk. Optical Photometry and Spectroscopy of the SN 1998bw-like Type Ic Supernova 2002ap. *PASP*, 115:1220–1235, Oct. 2003.
- R. J. Foley, A. Rest, M. Stritzinger, G. Pignata, J. P. Anderson, M. Hamuy, N. I. Morrell, M. M. Phillips, and F. Salgado. On the Progenitor and Supernova of the SN 2002cx-like Supernova 2008ge. *AJ*, 140:1321–1328, Nov. 2010b.
- M. Fukugita, T. Ichikawa, J. E. Gunn, M. Doi, K. Shimasaku, and D. P. Schneider. The Sloan Digital Sky Survey Photometric System. *AJ*, 111:1748, Apr. 1996.
- A. Gal-Yam. Luminous Supernovae. *Science*, 337:927–, Aug. 2012.
- A. Gal-Yam and D. C. Leonard. A massive hypergiant star as the progenitor of the supernova SN 2005gl. *Nature*, 458:865–867, Apr. 2009.
- A. Gal-Yam, D. C. Leonard, D. B. Fox, S. B. Cenko, A. M. Soderberg, D.-S. Moon, D. J. Sand, W. Li, A. V. Filippenko, G. Aldering, and Y. Copin. On the Progenitor of SN 2005gl and the Nature of Type IIn Supernovae. *ApJ*, 656:372–381, Feb. 2007.
- A. Gal-Yam, P. Mazzali, E. O. Ofek, P. E. Nugent, S. R. Kulkarni, M. M. Kasliwal, R. M. Quimby, A. V. Filippenko, S. B. Cenko, R. Chornock, R. Waldman, D. Kasen, M. Sullivan, E. C. Beshore, A. J. Drake, R. C. Thomas, J. S. Bloom, D. Poznanski, A. A. Miller, R. J. Foley, J. M. Silverman, I. Arcavi, R. S. Ellis, and J. Deng. Supernova 2007bi as a pair-instability explosion. *Nature*, 462:624–627, Dec. 2009.

- A. Gal-Yam, E. O. Ofek, and O. Shemmer. Supernova 2002ap: the first month. *MNRAS*, 332:L73–L77, June 2002.
- T. J. Galama, P. M. Vreeswijk, J. van Paradijs, C. Kouveliotou, T. Augusteijn, H. Bönhardt, J. P. Brewer, V. Doublier, J.-F. Gonzalez, B. Leibundgut, C. Lidman, O. R. Hainaut, F. Patat, J. Heise, J. in't Zand, K. Hurley, P. J. Groot, R. G. Strom, P. A. Mazzali, K. Iwamoto, K. Nomoto, H. Umeda, T. Nakamura, T. R. Young, T. Suzuki, T. Shigeyama, T. Koshut, M. Kippen, C. Robinson, P. de Wildt, R. A. M. J. Wijers, N. Tanvir, J. Greiner, E. Pian, E. Palazzi, F. Frontera, N. Masetti, L. Nicastro, M. Feroci, E. Costa, L. Piro, B. A. Peterson, C. Tinney, B. Boyle, R. Cannon, R. Stathakis, E. Sadler, M. C. Begam, and P. Ianna. An unusual supernova in the error box of the  $\gamma$ -ray burst of 25 April 1998. *Nature*, 395:670–672, Oct. 1998.
- S. Gezari, A. Rest, M. E. Huber, G. Narayan, K. Forster, J. D. Neill, D. C. Martin, S. Valenti, S. J. Smartt, R. Chornock, E. Berger, A. M. Soderberg, S. Mattila, E. Kankare, W. S. Burgett, K. C. Chambers, T. Dombeck, T. Grav, J. N. Heasley, K. W. Hodapp, R. Jedicke, N. Kaiser, R. Kudritzki, G. Luppino, R. H. Lupton, E. A. Magnier, D. G. Monet, J. S. Morgan, P. M. Onaka, P. A. Price, P. H. Rhoads, W. A. Siegmund, C. W. Stubbs, J. L. Tonry, R. J. Wainscoat, M. F. Waterson, and C. G. Wynn-Williams. GALEX and Pan-STARRS1 Discovery of SN IIP 2010aq: The First Few Days After Shock Breakout in a Red Supergiant Star. *ApJ Let.*, 720:L77–L81, Sept. 2010.
- J. Goehermann, T. Schmidt-Kaler, and P. Goudfrooij. The Galactic foreground reddening of SN 1987 A. *A&A*, 213:333–338, Apr. 1989.
- S. M. Gogarten, J. J. Dalcanton, B. F. Williams, A. C. Seth, A. Dolphin, D. Weisz, E. Skillman, J. Holtzman, A. Cole, L. Girardi, R. S. de Jong, I. D. Karachentsev, K. Olsen, and K. Rosema. The ACS Nearby Galaxy Survey Treasury. II. Young Stars and their Relation to  $H\alpha$  and UV Emission Timescales in the M81 Outer Disk. *ApJ*, 691:115–130, Jan. 2009.
- J. H. Groh, C. Georgy, and S. Ekström. Progenitors of supernova Ibc: a single Wolf-Rayet star as the possible progenitor of the SN Ib iPTF13bvn. *A&A*, 558:L1, Oct. 2013a.

- J. H. Groh, G. Meynet, and S. Ekström. Massive star evolution: luminous blue variables as unexpected supernova progenitors. *A&A*, 550:L7, Feb. 2013b.
- D. Guetta and M. Della Valle. On the Rates of Gamma-Ray Bursts and Type Ib/c Supernovae. *ApJ Let.*, 657:L73–L76, Mar. 2007.
- A. A. Hakobyan, A. R. Petrosian, B. McLean, D. Kunth, R. J. Allen, M. Turatto, and R. Barbon. Early-type galaxies with core collapse supernovae. *A&A*, 488:523–531, Sept. 2008.
- N. J. Hammer, H.-T. Janka, and E. Müller. Three-dimensional Simulations of Mixing Instabilities in Supernova Explosions. *ApJ*, 714:1371–1385, May 2010.
- M. Hamuy. Observed and Physical Properties of Core-Collapse Supernovae. *ApJ*, 582:905–914, Jan. 2003.
- M. Hamuy, J. Deng, P. A. Mazzali, N. I. Morrell, M. M. Phillips, M. Roth, S. Gonzalez, J. Thomas-Osip, W. Krzeminski, C. Contreras, J. Maza, L. González, L. Huerta, G. Folatelli, R. Chornock, A. V. Filippenko, S. E. Persson, W. L. Freedman, K. Koviak, N. B. Suntzeff, and K. Krisciunas. Supernova 2003bg: The First Type IIb Hypernova. *ApJ*, 703:1612–1623, Oct. 2009.
- M. Hamuy, J. Maza, P. A. Pinto, M. M. Phillips, N. B. Suntzeff, R. D. Blum, K. A. G. Olsen, D. J. Pinfield, V. D. Ivanov, T. Augusteijn, S. Brilliant, M. Chadid, J.-G. Cuby, V. Doublier, O. R. Hainaut, E. Le Floc’h, C. Lidman, M. G. Petr-Gotzens, E. Pompei, and L. Vanzi. Optical and Infrared Spectroscopy of SN 1999ee and SN 1999ex. *AJ*, 124:417–429, July 2002.
- M. Hamuy, M. M. Phillips, N. B. Suntzeff, J. Maza, L. E. González, M. Roth, K. Krisciunas, N. Morrell, E. M. Green, S. E. Persson, and P. J. McCarthy. An asymptotic-giant-branch star in the progenitor system of a type Ia supernova. *Nature*, 424:651–654, Aug. 2003.
- A. H. Harutyunyan, P. Pfahler, A. Pastorello, S. Taubenberger, M. Turatto, E. Cappellaro, S. Benetti, N. Elias-Rosa, H. Navasardyan, S. Valenti, V. Stanishev, F. Patat, M. Riello, G. Pignata, and W. Hillebrandt. ESC supernova spectroscopy of non-ESC targets. *A&A*, 488:383–399, Sept. 2008.

- W. Hasubick and K. Hornoch. Supernova 2002ap in M74. *IAU Circular*, 7820:4, Feb. 2002.
- A. Heger, C. L. Fryer, S. E. Woosley, N. Langer, and D. H. Hartmann. How Massive Single Stars End Their Life. *ApJ*, 591:288–300, July 2003.
- G. Helou. The IRAS colors of normal galaxies. *ApJ Let.*, 311:L33–L36, Dec. 1986.
- P. C. Hewett, S. J. Warren, S. K. Leggett, and S. T. Hodgkin. The UKIRT Infrared Deep Sky Survey ZY JHK photometric system: passbands and synthetic colours. *MNRAS*, 367:454–468, Apr. 2006.
- K. Hirata, T. Kajita, M. Koshiba, M. Nakahata, and Y. Oyama. Observation of a neutrino burst from the supernova SN1987A. *Physical Review Letters*, 58:1490–1493, Apr. 1987.
- J. Hjorth. The supernova-gamma-ray burst-jet connection. *Royal Society of London Philosophical Transactions Series A*, 371:20275, Apr. 2013.
- J. Hjorth and J. S. Bloom. *The Gamma-Ray Burst - Supernova Connection*, pages 169–190. Nov. 2012.
- D. J. Hunter, S. Valenti, R. Kotak, W. P. S. Meikle, S. Taubenberger, A. Pastorello, S. Benetti, V. Stanishev, S. J. Smartt, C. Trundle, A. A. Arkharov, F. Bufano, E. Cappellaro, E. Di Carlo, M. Dolci, N. Elias-Rosa, S. Frandsen, J. U. Fynbo, U. Hopp, V. M. Larionov, P. Laursen, P. Mazzali, H. Navasardyan, C. Ries, A. Riffeser, L. Rizzi, D. Y. Tsvetkov, M. Turatto, and S. Wilke. Extensive optical and near-infrared observations of the nearby, narrow-lined type Ic  $\gamma$ ASTROBJ $\gamma$ SN 2007gr $\gamma$ /ASTROBJ $\gamma$ : days 5 to 415. *A&A*, 508:371–389, Dec. 2009.
- D. Ibeling and A. Heger. The Metallicity Dependence of the Minimum Mass for Core-collapse Supernovae. *ApJ Let.*, 765:L43, Mar. 2013.
- I. Iben, Jr. and A. Renzini. Asymptotic giant branch evolution and beyond. *ARA&A*, 21:271–342, 1983.
- I. Iben, Jr. and A. V. Tutukov. Supernovae of type I as end products of the evolution of binaries with components of moderate initial mass ( $M$  not greater than about 9 solar masses). *ApJS*, 54:335–372, Feb. 1984.

- C. Inserra, S. J. Smartt, A. Jerkstrand, S. Valenti, M. Fraser, D. Wright, K. Smith, T.-W. Chen, R. Kotak, A. Pastorello, M. Nicholl, F. Bresolin, R. P. Kudritzki, S. Benetti, M. T. Botticella, W. S. Burgett, K. C. Chambers, M. Ergon, H. Flewelling, J. P. U. Fynbo, S. Geier, K. W. Hodapp, D. A. Howell, M. Huber, N. Kaiser, G. Leloudas, L. Magill, E. A. Magnier, M. G. McCrum, N. Metcalfe, P. A. Price, A. Rest, J. Sollerman, W. Sweeney, F. Taddia, S. Taubenberger, J. L. Tonry, R. J. Wainscoat, C. Waters, and D. Young. Superluminous Type Ic Supernovae: Catching a Magnetar by the Tail. *ApJ*, 770:128, June 2013.
- C. Inserra, M. Turatto, A. Pastorello, M. L. Pumo, E. Baron, S. Benetti, E. Cappellaro, S. Taubenberger, F. Bufano, N. Elias-Rosa, L. Zampieri, A. Harutyunyan, A. S. Moskvitin, M. Nissinen, V. Stanishev, D. Y. Tsvetkov, V. P. Hentunen, V. N. Komarova, N. N. Pavlyuk, V. V. Sokolov, and T. N. Sokolova. The bright Type IIP SN 2009bw, showing signs of interaction. *MNRAS*, 422:1122–1139, May 2012.
- K. Iwamoto, P. A. Mazzali, K. Nomoto, H. Umeda, T. Nakamura, F. Patat, I. J. Danziger, T. R. Young, T. Suzuki, T. Shigeyama, T. Augusteijn, V. Doublier, J.-F. Gonzalez, H. Boehnhardt, J. Brewer, O. R. Hainaut, C. Lidman, B. Leibundgut, E. Cappellaro, M. Turatto, T. J. Galama, P. M. Vreeswijk, C. Kouveliotou, J. van Paradijs, E. Pian, E. Palazzi, and F. Frontera. A hypernova model for the supernova associated with the  $\gamma$ -ray burst of 25 April 1998. *Nature*, 395:672–674, Oct. 1998.
- K. Iwamoto, K. Nomoto, P. Hoflich, H. Yamaoka, S. Kumagai, and T. Shigeyama. Theoretical light curves for the type IC supernova SN 1994I. *ApJ Let.*, 437:L115–L118, Dec. 1994.
- P. A. James and J. P. Anderson. The  $H\alpha$  Galaxy Survey . III. Constraints on supernova progenitors from spatial correlations with  $H\alpha$  emission. *A&A*, 453:57–65, July 2006.
- P. A. James, J. H. Knapen, N. S. Shane, I. K. Baldry, and R. S. de Jong. The  $H\alpha$  Galaxy survey. IV. Star formation in the local Universe. *A&A*, 482:507–516, May 2008.
- A. Jerkstrand, C. Fransson, K. Maguire, S. Smartt, M. Ergon, and J. Spyromilio. The progenitor mass of the Type IIP supernova SN 2004et from late-time spectral modeling. *A&A*, 546:A28, Oct. 2012.

- A. Jerkstrand, S. J. Smartt, M. Fraser, C. Fransson, J. Sollerman, F. Taddia, and R. Kotak. The nebular spectra of SN 2012aw and constraints on stellar nucleosynthesis from oxygen emission lines. *ArXiv e-prints*, Nov. 2013.
- G. C. Jordan, IV, H. B. Perets, R. T. Fisher, and D. R. van Rossum. Failed-detonation Supernovae: Subluminous Low-velocity Ia Supernovae and their Kicked Remnant White Dwarfs with Iron-rich Cores. *ApJ Let.*, 761:L23, Dec. 2012.
- D. Kasen and L. Bildsten. Supernova Light Curves Powered by Young Magnetars. *ApJ*, 717: 245–249, July 2010.
- M. M. Kasliwal, S. R. Kulkarni, A. Gal-Yam, P. E. Nugent, M. Sullivan, L. Bildsten, O. Yaron, H. B. Perets, I. Arcavi, S. Ben-Ami, V. B. Bhalariao, J. S. Bloom, S. B. Cenko, A. V. Filippenko, D. A. Frail, M. Ganeshalingam, A. Horesh, D. A. Howell, N. M. Law, D. C. Leonard, W. Li, E. O. Ofek, D. Polishook, D. Poznanski, R. M. Quimby, J. M. Silverman, A. Sternberg, and D. Xu. Calcium-rich Gap Transients in the Remote Outskirts of Galaxies. *ApJ*, 755:161, Aug. 2012.
- K. S. Kawabata, K. Maeda, K. Nomoto, S. Taubenberger, M. Tanaka, J. Deng, E. Pian, T. Hattori, and K. Itagaki. A massive star origin for an unusual helium-rich supernova in an elliptical galaxy. *Nature*, 465:326–328, May 2010.
- P. L. Kelly and R. P. Kirshner. Core-collapse Supernovae and Host Galaxy Stellar Populations. *ApJ*, 759:107, Nov. 2012.
- P. L. Kelly, R. P. Kirshner, and M. Pahre. Long  $\gamma$ -Ray Bursts and Type Ic Core-Collapse Supernovae Have Similar Locations in Hosts. *ApJ*, 687:1201–1207, Nov. 2008.
- W. E. Kerzendorf, D. Yong, B. P. Schmidt, J. D. Simon, C. S. Jeffery, J. Anderson, P. Podsiadlowski, A. Gal-Yam, J. M. Silverman, A. V. Filippenko, K. Nomoto, S. J. Murphy, M. S. Bessell, K. A. Venn, and R. J. Foley. A High-resolution Spectroscopic Search for the Remaining Donor for Tycho’s Supernova. *ApJ*, 774:99, Sept. 2013.
- A. M. Khokhlov. Delayed detonation model for type IA supernovae. *A&A*, 245:114–128, May 1991.

- M. Kiewe, A. Gal-Yam, I. Arcavi, D. C. Leonard, J. Emilio Enriquez, S. B. Cenko, D. B. Fox, D.-S. Moon, D. J. Sand, A. M. Soderberg, and T. CCCP. Caltech Core-Collapse Project (CCCP) Observations of Type II<sub>n</sub> Supernovae: Typical Properties and Implications for Their Progenitor Stars. *ApJ*, 744:10, Jan. 2012.
- R. P. Kirshner and J. Kwan. Distances to extragalactic supernovae. *ApJ*, 193:27–36, Oct. 1974.
- M. D. Kistler, W. C. Haxton, and H. Yüksel. Tomography of Massive Stars from Core Collapse to Supernova Shock Breakout. *ApJ*, 778:81, Nov. 2013.
- D. Kocevski, M. Modjaz, J. S. Bloom, R. Foley, D. Starr, C. H. Blake, E. E. Falco, N. R. Butler, M. Skrutskie, and A. Szentgyorgyi. Multicolor Infrared Observations of SN 2006aj. I. The Supernova Associated with XRF 060218. *ApJ*, 663:1180–1186, July 2007.
- C. S. Kochanek. Failed Supernovae Explain the Compact Remnant Mass Function. *ArXiv e-prints*, July 2013.
- O. Krause, M. Tanaka, T. Usuda, T. Hattori, M. Goto, S. Birkmann, and K. Nomoto. Tycho Brahe’s 1572 supernova as a standard type Ia as revealed by its light-echo spectrum. *Nature*, 456:617–619, Dec. 2008.
- K. Krisciunas, M. Hamuy, N. B. Suntzeff, J. Espinoza, D. Gonzalez, L. Gonzalez, S. Gonzalez, K. Koviak, W. Krzeminski, N. Morrell, M. M. Phillips, M. Roth, and J. Thomas-Osip. Do the Photometric Colors of Type II-P Supernovae Allow Accurate Determination of Host Galaxy Extinction? *AJ*, 137:34–41, Jan. 2009.
- M. Kromer, M. Fink, V. Stanishev, S. Taubenberger, F. Ciaraldi-Schoolman, R. Pakmor, F. K. Röpkke, A. J. Rüter, I. R. Seitenzahl, S. A. Sim, G. Blanc, N. Elias-Rosa, and W. Hillebrandt. 3D deflagration simulations leaving bound remnants: a model for 2002cx-like Type Ia supernovae. *MNRAS*, 429:2287–2297, Mar. 2013.
- H. Kuncarayakti, M. Doi, G. Aldering, N. Arimoto, K. Maeda, T. Morokuma, R. Pereira, T. Usuda, and Y. Hashiba. Integral Field Spectroscopy of Supernova Explosion Sites: Constraining the Mass and Metallicity of the Progenitors. I. Type Ib and Ic Supernovae. *AJ*, 146:30, Aug. 2013.

- D. Larson, J. Dunkley, G. Hinshaw, E. Komatsu, M. R.olta, C. L. Bennett, B. Gold, M. Halpern, R. S. Hill, N. Jarosik, A. Kogut, M. Limon, S. S. Meyer, N. Odegard, L. Page, K. M. Smith, D. N. Spergel, G. S. Tucker, J. L. Weiland, E. Wollack, and E. L. Wright. Seven-year Wilkinson Microwave Anisotropy Probe (WMAP) Observations: Power Spectra and WMAP-derived Parameters. *ApJS*, 192:16, Feb. 2011.
- N. M. Law, S. R. Kulkarni, R. G. Dekany, E. O. Ofek, R. M. Quimby, P. E. Nugent, J. Surace, C. C. Grillmair, J. S. Bloom, M. M. Kasliwal, L. Bildsten, T. Brown, S. B. Cenko, D. Ciardi, E. Croner, S. G. Djorgovski, J. van Eyken, A. V. Filippenko, D. B. Fox, A. Gal-Yam, D. Hale, N. Hamam, G. Helou, J. Henning, D. A. Howell, J. Jacobsen, R. Laher, S. Mattingly, D. McKenna, A. Pickles, D. Poznanski, G. Rahmer, A. Rau, W. Rosing, M. Shara, R. Smith, D. Starr, M. Sullivan, V. Velur, R. Walters, and J. Zolkower. The Palomar Transient Factory: System Overview, Performance, and First Results. *PASP*, 121:1395–1408, Dec. 2009.
- J. C. Lee, A. Gil de Paz, C. Tremonti, R. C. Kennicutt, Jr., S. Salim, M. Bothwell, D. Calzetti, J. Dalcanton, D. Dale, C. Engelbracht, S. J. J. G. Funes, B. Johnson, S. Sakai, E. Skillman, L. van Zee, F. Walter, and D. Weisz. Comparison of H $\alpha$  and UV Star Formation Rates in the Local Volume: Systematic Discrepancies for Dwarf Galaxies. *ApJ*, 706:599–613, Nov. 2009.
- W. Li, J. S. Bloom, P. Podsiadlowski, A. A. Miller, S. B. Cenko, S. W. Jha, M. Sullivan, D. A. Howell, P. E. Nugent, N. R. Butler, E. O. Ofek, M. M. Kasliwal, J. W. Richards, A. Stockton, H.-Y. Shih, L. Bildsten, M. M. Shara, J. Bibby, A. V. Filippenko, M. Ganeshalingam, J. M. Silverman, S. R. Kulkarni, N. M. Law, D. Poznanski, R. M. Quimby, C. McCully, B. Patel, K. Maguire, and K. J. Shen. Exclusion of a luminous red giant as a companion star to the progenitor of supernova SN 2011fe. *Nature*, 480:348–350, Dec. 2011a.
- W. Li, R. Chornock, J. Leaman, A. V. Filippenko, D. Poznanski, X. Wang, M. Ganeshalingam, and F. Mannucci. Nearby supernova rates from the Lick Observatory Supernova Search - III. The rate-size relation, and the rates as a function of galaxy Hubble type and colour. *MNRAS*, 412:1473–1507, Apr. 2011b.

- W. Li, A. V. Filippenko, R. Chornock, E. Berger, P. Berlind, M. L. Calkins, P. Challis, C. Fassnacht, S. Jha, R. P. Kirshner, T. Matheson, W. L. W. Sargent, R. A. Simcoe, G. H. Smith, and G. Squires. SN 2002cx: The Most Peculiar Known Type Ia Supernova. *PASP*, 115:453–473, Apr. 2003.
- W. Li, X. Wang, S. D. Van Dyk, J.-C. Cuillandre, R. J. Foley, and A. V. Filippenko. On the Progenitors of Two Type II-P Supernovae in the Virgo Cluster. *ApJ*, 661:1013–1024, June 2007.
- E. Livne, S. M. Asida, and P. Höflich. On the Sensitivity of Deflagrations in a Chandrasekhar Mass White Dwarf to Initial Conditions. *ApJ*, 632:443–449, Oct. 2005.
- M. Long, G. C. Jordan, IV, D. R. van Rossum, B. Diemer, C. Graziani, R. Kessler, B. Meyer, P. Rich, and D. Q. Lamb. Three-dimensional Simulations of Pure Deflagration Models for Thermonuclear Supernovae. *ArXiv e-prints*, July 2013.
- J. D. Lyman, D. Bersier, and P. A. James. Bolometric corrections for optical light curves of core-collapse supernovae. *MNRAS*, 437:3848–3862, Feb. 2014.
- J. D. Lyman, P. A. James, H. B. Perets, J. P. Anderson, A. Gal-Yam, P. Mazzali, and S. M. Percival. Environment-derived constraints on the progenitors of low-luminosity Type I supernovae. *MNRAS*, 434:527–541, Sept. 2013.
- K. Maeda, K. Kawabata, P. A. Mazzali, M. Tanaka, S. Valenti, K. Nomoto, T. Hattori, J. Deng, E. Pian, S. Taubenberger, M. Iye, T. Matheson, A. V. Filippenko, K. Aoki, G. Kosugi, Y. Ohyama, T. Sasaki, and T. Takata. Asphericity in Supernova Explosions from Late-Time Spectroscopy. *Science*, 319:1220–, Feb. 2008.
- K. Maeda, P. A. Mazzali, J. Deng, K. Nomoto, Y. Yoshii, H. Tomita, and Y. Kobayashi. A Two-Component Model for the Light Curves of Hypernovae. *ApJ*, 593:931–940, Aug. 2003.
- K. Maeda, T. Nakamura, K. Nomoto, P. A. Mazzali, F. Patat, and I. Hachisu. Explosive Nucleosynthesis in Aspherical Hypernova Explosions and Late-Time Spectra of SN 1998bw. *ApJ*, 565:405–412, Jan. 2002.

- K. Maeda, M. Tanaka, K. Nomoto, N. Tominaga, K. Kawabata, P. A. Mazzali, H. Umeda, T. Suzuki, and T. Hattori. The Unique Type Ib Supernova 2005bf at Nebular Phases: A Possible Birth Event of a Strongly Magnetized Neutron Star. *ApJ*, 666:1069–1082, Sept. 2007.
- K. Maguire, E. Di Carlo, S. J. Smartt, A. Pastorello, D. Y. Tsvetkov, S. Benetti, S. Spiro, A. A. Arkharov, G. Beccari, M. T. Botticella, E. Cappellaro, S. Cristallo, M. Dolci, N. Elias-Rosa, M. Fiaschi, D. Gorshanov, A. Harutyunyan, V. M. Larionov, H. Navasardyan, A. Pietrinferni, G. Raimondo, G. di Rico, S. Valenti, G. Valentini, and L. Zampieri. Optical and near-infrared coverage of SN 2004et: physical parameters and comparison with other Type IIP supernovae. *MNRAS*, 404:981–1004, May 2010.
- K. Maguire, M. Sullivan, R. S. Ellis, P. E. Nugent, D. A. Howell, A. Gal-Yam, J. Cooke, P. Mazzali, Y.-C. Pan, B. Dilday, R. C. Thomas, I. Arcavi, S. Ben-Ami, D. Bersier, F. B. Bianco, B. J. Fulton, I. Hook, A. Horesh, E. Hsiao, P. A. James, P. Podsiadlowski, E. S. Walker, O. Yaron, M. M. Kasliwal, R. R. Laher, N. M. Law, E. O. Ofek, D. Poznanski, and J. Surace. Hubble Space Telescope studies of low-redshift Type Ia supernovae: evolution with redshift and ultraviolet spectral trends. *MNRAS*, 426:2359–2379, Nov. 2012.
- D. Maoz, F. Mannucci, and G. Nelemans. Observational clues to the progenitors of Type-Ia supernovae. *ArXiv e-prints*, Dec. 2013.
- T. Matheson, A. V. Filippenko, L. C. Ho, A. J. Barth, and D. C. Leonard. Detailed Analysis of Early to Late-Time Spectra of Supernova 1993J. *AJ*, 120:1499–1515, Sept. 2000.
- K. Matthews, G. Neugebauer, L. Armus, and B. T. Soifer. Early Near-Infrared Observations of SN 1993J. *AJ*, 123:753–759, Feb. 2002.
- S. Mattila, P. Meikle, and K. Chambers. Supernova 2002ap in M74. *IAU Circular*, 7820:1, Feb. 2002.
- J. R. Maund, M. Fraser, M. Ergon, A. Pastorello, S. J. Smartt, J. Sollerman, S. Benetti, M.-T. Botticella, F. Bufano, I. J. Danziger, R. Kotak, L. Magill, A. W. Stephens, and S. Valenti. The Yellow Supergiant Progenitor of the Type II Supernova 2011dh in M51. *ApJ Lett.*, 739:L37, Oct. 2011.

- I. Maurer, P. A. Mazzali, S. Taubenberger, and S. Hachinger. Hydrogen and helium in the late phase of supernovae of Type IIb. *MNRAS*, 409:1441–1454, Dec. 2010.
- P. A. Mazzali, J. Deng, M. Hamuy, and K. Nomoto. SN 2003bg: A Broad-Lined Type IIb Supernova with Hydrogen. *ApJ*, 703:1624–1634, Oct. 2009.
- P. A. Mazzali, J. Deng, K. Maeda, K. Nomoto, H. Umeda, K. Hatano, K. Iwamoto, Y. Yoshii, Y. Kobayashi, T. Minezaki, M. Doi, K. Enya, H. Tomita, S. J. Smartt, K. Kinugasa, H. Kawakita, K. Ayani, T. Kawabata, H. Yamaoka, Y. L. Qiu, K. Motohara, C. L. Gerardy, R. Fesen, K. S. Kawabata, M. Iye, N. Kashikawa, G. Kosugi, Y. Ohyama, M. Takada-Hidai, G. Zhao, R. Chornock, A. V. Filippenko, S. Benetti, and M. Turatto. The Type Ic Hypernova SN 2002ap. *ApJ Let.*, 572:L61–L65, June 2002.
- P. A. Mazzali, J. Deng, K. Nomoto, D. N. Sauer, E. Pian, N. Tominaga, M. Tanaka, K. Maeda, and A. V. Filippenko. A neutron-star-driven X-ray flash associated with supernova SN 2006aj. *Nature*, 442:1018–1020, Aug. 2006.
- P. A. Mazzali and L. B. Lucy. The application of Monte Carlo methods to the synthesis of early-time supernovae spectra. *A&A*, 279:447–456, Nov. 1993.
- P. A. Mazzali, S. Valenti, M. Della Valle, G. Chincarini, D. N. Sauer, S. Benetti, E. Pian, T. Piran, V. D’Elia, N. Elias-Rosa, R. Margutti, F. Pasotti, L. A. Antonelli, F. Bufano, S. Campana, E. Cappellaro, S. Covino, P. D’Avanzo, F. Fiore, D. Fugazza, R. Gilmozzi, D. Hunter, K. Maguire, E. Maiorano, P. Marziani, N. Masetti, F. Mirabel, H. Navasardyan, K. Nomoto, E. Palazzi, A. Pastorello, N. Panagia, L. J. Pellizza, R. Sari, S. Smartt, G. Tagliaferri, M. Tanaka, S. Taubenberger, N. Tominaga, C. Trundle, and M. Turatto. The Metamorphosis of Supernova SN 2008D/XRF 080109: A Link Between Supernovae and GRBs/Hypernovae. *Science*, 321:1185–, Aug. 2008.
- P. A. Mazzali, E. S. Walker, E. Pian, M. Tanaka, A. Corsi, T. Hattori, and A. Gal-Yam. The very energetic, broad-lined Type Ic supernova 2010ah (PTF10bzf) in the context of GRB/SNe. *MNRAS*, May 2013.
- A. Melandri, E. Pian, P. Ferrero, V. D’Elia, E. S. Walker, G. Ghirlanda, S. Covino, L. Amati, P. D’Avanzo, P. A. Mazzali, M. Della Valle, C. Guidorzi, L. A. Antonelli, M. G. Bernar-

- dini, D. Bersier, F. Bufano, S. Campana, A. J. Castro-Tirado, G. Chincarini, J. Deng, A. V. Filippenko, D. Fugazza, G. Ghisellini, C. Kouveliotou, K. Maeda, G. Marconi, N. Masetti, K. Nomoto, E. Palazzi, F. Patat, S. Piranomonte, R. Salvaterra, I. Saviane, R. L. C. Starling, G. Tagliaferri, M. Tanaka, and S. D. Vergani. The optical SN 2012bz associated with the long GRB 120422A. *A&A*, 547:A82, Nov. 2012.
- J. W. Menzies, R. M. Catchpole, G. van Vuuren, H. Winkler, C. D. Laney, P. A. Whitelock, A. W. J. Cousins, B. S. Carter, F. Marang, T. H. H. Lloyd Evans, G. Roberts, D. Kilkenny, J. Spencer Jones, K. Sekiguchi, A. P. Fairall, and R. D. Wolstencroft. Spectroscopic and photometric observations of SN 1987a - The first 50 days. *MNRAS*, 227:39P–49P, Aug. 1987.
- P. Mészáros. Gamma ray bursts. *Astroparticle Physics*, 43:134–141, Mar. 2013.
- R. Minkowski. Spectra of Supernovae. *PASP*, 53:224, Aug. 1941.
- N. Mirabal, J. P. Halpern, D. An, J. R. Thorstensen, and D. M. Terndrup. GRB 060218/SN 2006aj: A Gamma-Ray Burst and Prompt Supernova at  $z = 0.0335$ . *ApJ Let.*, 643:L99–L102, June 2006.
- S. Miyaji, K. Nomoto, K. Yokoi, and D. Sugimoto. Supernova Triggered by Electron Captures. *PASJ*, 32:303, 1980.
- M. Modjaz. *Varied deaths of massive stars: Properties of nearby type IIb, Ib and Ic supernovae*. PhD thesis, Harvard University, 2007.
- M. Modjaz, R. Kirshner, P. Challis, and T. Matheson. Supernovae 2005he and Sn 2005hg. *Central Bureau Electronic Telegrams*, 267:1, Oct. 2005a.
- M. Modjaz, R. Kirshner, P. Challis, T. Matheson, and P. Berlind. Supernova 2005hg in UGC 1394. *Central Bureau Electronic Telegrams*, 271:1, Nov. 2005b.
- M. Modjaz, W. Li, N. Butler, R. Chornock, D. Perley, S. Blondin, J. S. Bloom, A. V. Filippenko, R. P. Kirshner, D. Kocevski, D. Poznanski, M. Hicken, R. J. Foley, G. S. Stringfellow, P. Berlind, D. Barrado y Navascues, C. H. Blake, H. Bouy, W. R. Brown, P. Challis,

- H. Chen, W. H. de Vries, P. Dufour, E. Falco, A. Friedman, M. Ganeshalingam, P. Garnavich, B. Holden, G. Illingworth, N. Lee, J. Liebert, G. H. Marion, S. S. Olivier, J. X. Prochaska, J. M. Silverman, N. Smith, D. Starr, T. N. Steele, A. Stockton, G. G. Williams, and W. M. Wood-Vasey. From Shock Breakout to Peak and Beyond: Extensive Panchromatic Observations of the Type Ib Supernova 2008D Associated with Swift X-ray Transient 080109. *ApJ*, 702:226–248, Sept. 2009.
- C. Moellenhoff and R. Bender. The peculiar kinematics of the elliptical dust-lane galaxy NGC 4589. *A&A*, 214:61–67, Apr. 1989.
- T. J. Moriya, K. Maeda, F. Taddia, J. Sollerman, S. I. Blinnikov, and E. I. Sorokina. An Analytic Bolometric Light Curve Model of Interaction-Powered Supernovae and its Application to Type IIn Supernovae. *ArXiv e-prints*, July 2013.
- K. Motohara, K. Nomoto, C. Gerardy, R. Fesen, and P. Henry. Supernova 2002ap in M74. *IAU Circular*, 7834:2, Feb. 2002.
- J. S. Mulchaey, M. M. Kasliwal, and J. A. Kollmeier. Calcium-rich Gap Transients: Solving the Calcium Conundrum in the Intracluster Medium. *ApJ Let.*, 780:L34, Jan. 2014.
- T. Nakamura, P. A. Mazzali, K. Nomoto, and K. Iwamoto. Light Curve and Spectral Models for the Hypernova SN 1998BW Associated with GRB 980425. *ApJ*, 550:991–999, Apr. 2001.
- M. Nicholl, S. J. Smartt, A. Jerkstrand, C. Inserra, M. McCrum, R. Kotak, M. Fraser, D. Wright, T.-W. Chen, K. Smith, D. R. Young, S. A. Sim, S. Valenti, D. A. Howell, F. Bresolin, R. P. Kudritzki, J. L. Tonry, M. E. Huber, A. Rest, A. Pastorello, L. Tomasella, E. Cappellaro, S. Benetti, S. Mattila, E. Kankare, T. Kangas, G. Leloudas, J. Sollerman, F. Taddia, E. Berger, R. Chornock, G. Narayan, C. W. Stubbs, R. J. Foley, R. Lunnan, A. Soderberg, N. Sanders, D. Milisavljevic, R. Margutti, R. P. Kirshner, N. Elias-Rosa, A. Morales-Garoffolo, S. Taubenberger, M. T. Botticella, S. Gezari, Y. Urata, S. Rodney, A. G. Riess, D. Scolnic, W. M. Wood-Vasey, W. S. Burgett, K. Chambers, H. A. Flewelling, E. A. Magnier, N. Kaiser, N. Metcalfe, J. Morgan, P. A. Price, W. Sweeney,

- and C. Waters. Slowly fading super-luminous supernovae that are not pair-instability explosions. *Nature*, 502:346–349, Oct. 2013.
- K. Nomoto. Evolution of 8-10 solar mass stars toward electron capture supernovae. I - Formation of electron-degenerate O + NE + MG cores. *ApJ*, 277:791–805, Feb. 1984.
- K. Nomoto, F.-K. Thielemann, and K. Yokoi. Accreting white dwarf models of Type I supernovae. III - Carbon deflagration supernovae. *ApJ*, 286:644–658, Nov. 1984.
- K. I. Nomoto, K. Iwamoto, and T. Suzuki. The evolution and explosion of massive binary stars and Type Ib-Ic-IIb-III supernovae. *Phys. Rep.*, 256:173–191, May 1995.
- T. Nozawa, T. Kozasa, N. Tominaga, I. Sakon, M. Tanaka, T. Suzuki, K. Nomoto, K. Maeda, H. Umeda, M. Limongi, and T. Onaka. Early Formation of Dust in the Ejecta of Type Ib SN 2006jc and Temperature and Mass of the Dust. *ApJ*, 684:1343–1350, Sept. 2008.
- P. E. Nugent, M. Sullivan, S. B. Cenko, R. C. Thomas, D. Kasen, D. A. Howell, D. Bersier, J. S. Bloom, S. R. Kulkarni, M. T. Kandrashoff, A. V. Filippenko, J. M. Silverman, G. W. Marcy, A. W. Howard, H. T. Isaacson, K. Maguire, N. Suzuki, J. E. Tarlton, Y.-C. Pan, L. Bildsten, B. J. Fulton, J. T. Parrent, D. Sand, P. Podsiadlowski, F. B. Bianco, B. Dilday, M. L. Graham, J. Lyman, P. James, M. M. Kasliwal, N. M. Law, R. M. Quimby, I. M. Hook, E. S. Walker, P. Mazzali, E. Pian, E. O. Ofek, A. Gal-Yam, and D. Poznanski. Supernova SN 2011fe from an exploding carbon-oxygen white dwarf star. *Nature*, 480:344–347, Dec. 2011.
- E. O’Connor and C. D. Ott. Black Hole Formation in Failing Core-Collapse Supernovae. *ApJ*, 730:70, Apr. 2011.
- K. Ohta, H. Maemura, T. Ishigaki, K. Aoki, and H. Ohtani. Low-resolution spectra of the supernova 1993J in M81. *PASJ*, 46:117–122, Feb. 1994.
- J. B. Oke and L. Searle. The spectra of supernovae. *ARA&A*, 12:315–329, 1974.
- E. F. Olivares, J. Greiner, P. Schady, A. Rau, S. Klose, T. Krühler, P. M. J. Afonso, A. C. Updike, M. Nardini, R. Filgas, A. Nicuesa Guelbenzu, C. Clemens, J. Elliott, D. A. Kann,

- A. Rossi, and V. Sudilovsky. The fast evolution of SN 2010bh associated with XRF 100316D. *A&A*, 539:A76, Mar. 2012.
- A. Pastorello, M. M. Kasliwal, R. M. Crockett, S. Valenti, R. Arbour, K. Itagaki, S. Kaspi, A. Gal-Yam, S. J. Smartt, R. Griffith, K. Maguire, E. O. Ofek, N. Seymour, D. Stern, and W. Wiethoff. The Type IIb SN 2008ax: spectral and light curve evolution. *MNRAS*, 389: 955–966, Sept. 2008.
- A. Pastorello, S. Valenti, L. Zampieri, H. Navasardyan, S. Taubenberger, S. J. Smartt, A. A. Arkharov, O. Bärnbantner, H. Barwig, S. Benetti, P. Birtwhistle, M. T. Botticella, E. Cappellaro, M. Del Principe, F. di Mille, G. di Rico, M. Dolci, N. Elias-Rosa, N. V. Efimova, M. Fiedler, A. Harutyunyan, P. A. Höflich, W. Kloehr, V. M. Larionov, V. Lorenzi, J. R. Maund, N. Napoleone, M. Ragni, M. Richmond, C. Ries, S. Spiro, S. Temporin, M. Turatto, and J. C. Wheeler. SN 2005cs in M51 - II. Complete evolution in the optical and the near-infrared. *MNRAS*, 394:2266–2282, Apr. 2009.
- F. Patat, E. Cappellaro, J. Danziger, P. A. Mazzali, J. Sollerman, T. Augusteijn, J. Brewer, V. Doublier, J. F. Gonzalez, O. Hainaut, C. Lidman, B. Leibundgut, K. Nomoto, T. Nakamura, J. Spyromilio, L. Rizzi, M. Turatto, J. Walsh, T. J. Galama, J. van Paradijs, C. Kouveliotou, P. M. Vreeswijk, F. Frontera, N. Masetti, E. Palazzi, and E. Pian. The Metamorphosis of SN 1998bw. *ApJ*, 555:900–917, July 2001.
- H. B. Perets, A. Gal-yam, R. M. Crockett, J. P. Anderson, P. A. James, M. Sullivan, J. D. Neill, and D. C. Leonard. The Old Environment of the Faint Calcium-rich Supernova SN 2005cz. *ApJ Let.*, 728:L36, Feb. 2011.
- H. B. Perets, A. Gal-Yam, P. A. Mazzali, D. Arnett, D. Kagan, A. V. Filippenko, W. Li, I. Arcavi, S. B. Cenko, D. B. Fox, D. C. Leonard, D.-S. Moon, D. J. Sand, A. M. Soderberg, J. P. Anderson, P. A. James, R. J. Foley, M. Ganeshalingam, E. O. Ofek, L. Bildsten, G. Nelemans, K. J. Shen, N. N. Weinberg, B. D. Metzger, A. L. Piro, E. Quataert, M. Kiewe, and D. Poznanski. A faint type of supernova from a white dwarf with a helium-rich companion. *Nature*, 465:322–325, May 2010.
- S. Perlmutter, G. Aldering, M. della Valle, S. Deustua, R. S. Ellis, S. Fabbro, A. Fruchter,

- G. Goldhaber, D. E. Groom, I. M. Hook, A. G. Kim, M. Y. Kim, R. A. Knop, C. Lidman, R. G. McMahon, P. Nugent, R. Pain, N. Panagia, C. R. Pennypacker, P. Ruiz-Lapuente, B. Schaefer, and N. Walton. Discovery of a supernova explosion at half the age of the universe. *Nature*, 391:51, Jan. 1998.
- S. Perlmutter, G. Aldering, G. Goldhaber, R. A. Knop, P. Nugent, P. G. Castro, S. Deustua, S. Fabbro, A. Goobar, D. E. Groom, I. M. Hook, A. G. Kim, M. Y. Kim, J. C. Lee, N. J. Nunes, R. Pain, C. R. Pennypacker, R. Quimby, C. Lidman, R. S. Ellis, M. Irwin, R. G. McMahon, P. Ruiz-Lapuente, N. Walton, B. Schaefer, B. J. Boyle, A. V. Filippenko, T. Matheson, A. S. Fruchter, N. Panagia, H. J. M. Newberg, W. J. Couch, and Supernova Cosmology Project. Measurements of Omega and Lambda from 42 High-Redshift Supernovae. *ApJ*, 517:565–586, June 1999.
- M. M. Phillips. The absolute magnitudes of Type IA supernovae. *ApJ Let.*, 413:L105–L108, Aug. 1993.
- M. M. Phillips, W. Li, J. A. Frieman, S. I. Blinnikov, D. DePoy, J. L. Prieto, P. Milne, C. Contreras, G. Folatelli, N. Morrell, M. Hamuy, N. B. Suntzeff, M. Roth, S. González, W. Krzeminski, A. V. Filippenko, W. L. Freedman, R. Chornock, S. Jha, B. F. Madore, S. E. Persson, C. R. Burns, P. Wyatt, D. Murphy, R. J. Foley, M. Ganeshalingam, F. J. D. Serduke, K. Krisciunas, B. Bassett, A. Becker, B. Dilday, J. Eastman, P. M. Garnavich, J. Holtzman, R. Kessler, H. Lampeitl, J. Marriner, S. Frank, J. L. Marshall, G. Miknaitis, M. Sako, D. P. Schneider, K. van der Heyden, and N. Yasuda. The Peculiar SN 2005hk: Do Some Type Ia Supernovae Explode as Deflagrations?1,. *PASP*, 119:360–387, Apr. 2007.
- E. Pian, P. A. Mazzali, N. Masetti, P. Ferrero, S. Klose, E. Palazzi, E. Ramirez-Ruiz, S. E. Woosley, C. Kouveliotou, J. Deng, A. V. Filippenko, R. J. Foley, J. P. U. Fynbo, D. A. Kann, W. Li, J. Hjorth, K. Nomoto, F. Patat, D. N. Sauer, J. Sollerman, P. M. Vreeswijk, E. W. Guenther, A. Levan, P. O’Brien, N. R. Tanvir, R. A. M. J. Wijers, C. Dumas, O. Hainaut, D. S. Wong, D. Baade, L. Wang, L. Amati, E. Cappellaro, A. J. Castro-Tirado, S. Ellison, F. Frontera, A. S. Fruchter, J. Greiner, K. Kawabata, C. Ledoux, K. Maeda, P. Møller,

- L. Nicastro, E. Rol, and R. Starling. An optical supernova associated with the X-ray flash XRF 060218. *Nature*, 442:1011–1013, Aug. 2006.
- G. Pignata, M. Stritzinger, A. Soderberg, P. Mazzali, M. M. Phillips, N. Morrell, J. P. Anderson, L. Boldt, A. Campillay, C. Contreras, G. Folatelli, F. Förster, S. González, M. Hamuy, W. Krzeminski, J. Maza, M. Roth, F. Salgado, E. M. Levesque, A. Rest, J. A. Crain, A. C. Foster, J. B. Haislip, K. M. Ivarsen, A. P. LaCluyze, M. C. Nysewander, and D. E. Reichart. SN 2009bb: A Peculiar Broad-lined Type Ic Supernova. *ApJ*, 728:14, Feb. 2011.
- A. L. Piro and E. Nakar. What can we Learn from the Rising Light Curves of Radioactively Powered Supernovae? *ApJ*, 769:67, May 2013.
- M. Potashov, S. Blinnikov, P. Baklanov, and A. Dolgov. Direct distance measurements to SN 2009ip. *MNRAS*, 431:L98–L101, Apr. 2013.
- T. A. Pritchard, P. W. A. Roming, P. J. Brown, A. J. Bayless, and L. H. Frey. Bolometric and UV Light Curves of Core-Collapse Supernovae. *ArXiv e-prints*, Mar. 2013.
- T. Puckett, C. Moore, J. Newton, and T. Orff. Supernova 2008ha in UGC 12682. *Central Bureau Electronic Telegrams*, 1567:1, Nov. 2008.
- Y. Qiu, W. Li, Q. Qiao, and J. Hu. The Study of a Type IIB Supernova: SN 1996CB. *AJ*, 117:736–743, Feb. 1999.
- R. M. Quimby, J. C. Wheeler, P. Höflich, C. W. Akerlof, P. J. Brown, and E. S. Rykoff. SN 2006bp: Probing the Shock Breakout of a Type II-P Supernova. *ApJ*, 666:1093–1107, Sept. 2007.
- A. Rau, S. R. Kulkarni, N. M. Law, J. S. Bloom, D. Ciardi, G. S. Djorgovski, D. B. Fox, A. Gal-Yam, C. C. Grillmair, M. M. Kasliwal, P. E. Nugent, E. O. Ofek, R. M. Quimby, W. T. Reach, M. Shara, L. Bildsten, S. B. Cenko, A. J. Drake, A. V. Filippenko, D. J. Helfand, G. Helou, D. A. Howell, D. Poznanski, and M. Sullivan. Exploring the Optical Transient Sky with the Palomar Transient Factory. *PASP*, 121:1334–1351, Dec. 2009.
- A. Rest, R. J. Foley, S. Gezari, G. Narayan, B. Draine, K. Olsen, M. E. Huber, T. Matheson, A. Garg, D. L. Welch, A. C. Becker, P. Challis, A. Clocchiatti, K. H. Cook, G. Damke,

- M. Meixner, G. Miknaitis, D. Minniti, L. Morelli, S. Nikolaev, G. Pignata, J. L. Prieto, R. C. Smith, C. Stubbs, N. B. Suntzeff, A. R. Walker, W. M. Wood-Vasey, A. Zenteno, L. Wyrzykowski, A. Udalski, M. K. Szymański, M. Kubiak, G. Pietrzyński, I. Soszyński, O. Szewczyk, K. Ulaczyk, and R. Poleski. Pushing the Boundaries of Conventional Core-collapse Supernovae: The Extremely Energetic Supernova SN 2003ma. *ApJ*, 729:88, Mar. 2011.
- M. W. Richmond, R. R. Treffers, A. V. Filippenko, Y. Paik, B. Leibundgut, E. Schulman, and C. V. Cox. UBVRI photometry of SN 1993J in M81: The first 120 days. *AJ*, 107:1022–1040, Mar. 1994.
- M. W. Richmond, S. D. van Dyk, W. Ho, C. Y. Peng, Y. Paik, R. R. Treffers, A. V. Filippenko, J. Bustamante-Donas, M. Moeller, C. Pawellek, H. Tartara, and M. Spence. UBVRI Photometry of the Type IC SN 1994I in M51. *AJ*, 111:327, Jan. 1996.
- A. G. Riess, A. V. Filippenko, P. Challis, A. Clocchiatti, A. Diercks, P. M. Garnavich, R. L. Gilliland, C. J. Hogan, S. Jha, R. P. Kirshner, B. Leibundgut, M. M. Phillips, D. Reiss, B. P. Schmidt, R. A. Schommer, R. C. Smith, J. Spyromilio, C. Stubbs, N. B. Suntzeff, and J. Tonry. Observational Evidence from Supernovae for an Accelerating Universe and a Cosmological Constant. *AJ*, 116:1009–1038, Sept. 1998.
- A. Riffeser, C. A. Goessl, and C. Ries. Supernovae 2002ao, 2002ap, 2002ar, 2002au, 2002av. *IAU Circular*, 7825:2, Feb. 2002.
- F. K. Röpkke, M. Kromer, I. R. Seitenzahl, R. Pakmor, S. A. Sim, S. Taubenberger, F. Ciardi-Schoolmann, W. Hillebrandt, G. Aldering, P. Antilogus, C. Baltay, S. Benitez-Herrera, S. Bongard, C. Buton, A. Canto, F. Cellier-Holzem, M. Childress, N. Chotard, Y. Copin, H. K. Fakhouri, M. Fink, D. Fouchez, E. Gangler, J. Guy, S. Hachinger, E. Y. Hsiao, J. Chen, M. Kerschhaggl, M. Kowalski, P. Nugent, K. Paech, R. Pain, E. Pecontal, R. Pereira, S. Perlmutter, D. Rabinowitz, M. Rigault, K. Runge, C. Saunders, G. Smadja, N. Suzuki, C. Tao, R. C. Thomas, A. Tilquin, and C. Wu. Constraining Type Ia Supernova Models: SN 2011fe as a Test Case. *ApJ Let.*, 750:L19, May 2012.
- R. Roy, B. Kumar, J. R. Maund, P. Schady, O. E. F., D. Malesani, G. Leloudas, S. Nandi,

- N. Tanvir, D. Milisavljevic, J. Hjorth, K. Misra, B. Kumar, S. B. Pandey, R. Sagar, and H. C. Chandola. SN 2007uy - metamorphosis of an aspheric Type Ib explosion. *ArXiv e-prints*, June 2013.
- D. K. Sahu, U. K. Gurugubelli, G. C. Anupama, and K. Nomoto. Optical studies of SN 2009jf: a Type Ib supernova with an extremely slow decline and aspherical signature. *MNRAS*, 413:2583–2594, June 2011.
- D. K. Sahu, M. Tanaka, G. C. Anupama, U. K. Gurugubelli, and K. Nomoto. The Broad-Line Type Ic Supernova SN 2007ru: Adding to the Diversity of Type Ic Supernovae. *ApJ*, 697:676–683, May 2009.
- H. Sana, S. E. de Mink, A. de Koter, N. Langer, C. J. Evans, M. Gieles, E. Gosset, R. G. Izzard, J.-B. Le Bouquin, and F. R. N. Schneider. Binary Interaction Dominates the Evolution of Massive Stars. *Science*, 337:444–, July 2012.
- A. Sandage and J. Bedke. *The Carnegie Atlas of Galaxies. Volumes I, II*. 1994.
- D. N. Sauer, P. A. Mazzali, J. Deng, S. Valenti, K. Nomoto, and A. V. Filippenko. The properties of the ‘standard’ Type Ic supernova 1994I from spectral models. *MNRAS*, 369:1939–1948, July 2006.
- B. E. Schaefer. ‘Supernova’ 185 is Really a Nova Plus Comet P/Swift-Tuttle. *AJ*, 110:1793, Oct. 1995.
- E. M. Schlegel. A new subclass of Type II supernovae? *MNRAS*, 244:269–271, May 1990.
- B. P. Schmidt, N. B. Suntzeff, M. M. Phillips, R. A. Schommer, A. Clocchiatti, R. P. Kirshner, P. Garnavich, P. Challis, B. Leibundgut, J. Spyromilio, A. G. Riess, A. V. Filippenko, M. Hamuy, R. C. Smith, C. Hogan, C. Stubbs, A. Diercks, D. Reiss, R. Gilliland, J. Tonry, J. Maza, A. Dressler, J. Walsh, and R. Ciardullo. The High-Z Supernova Search: Measuring Cosmic Deceleration and Global Curvature of the Universe Using Type IA Supernovae. *ApJ*, 507:46–63, Nov. 1998.
- S. Schulze, A. J. Levan, D. Malesani, J. P. U. Fynbo, N. R. Tanvir, B. Milvang-Jensen, A. de

- Ugarte Postigo, V. D'Elia, J. Sollerman, and J. Hjorth. GRB 120422A: VLT/X-shooter spectroscopy of the GRB counterpart. *GRB Coordinates Network*, 13257:1, 2012.
- S. Schulze, D. Malesani, A. Cucchiara, N. R. Tanvir, T. Krühler, A. de Ugarte Postigo, G. Leloudas, J. Lyman, D. Bersier, K. Wiersema, D. A. Perley, P. Schady, J. Gorosabel, J. P. Anderson, A. J. Castro-Tirado, S. B. Cenko, A. De Cia, L. E. Ellerbroek, J. P. U. Fynbo, J. Greiner, J. Hjorth, D. A. Kann, L. Kaper, S. Klose, A. J. Levan, S. Martín, P. T. O'Brien, K. L. Page, G. Pignata, S. Rapaport, R. Sánchez-Ramírez, J. Sollerman, I. A. Smith, M. Sparre, C. C. Thöne, D. J. Watson, D. Xu, F. E. Bauer, M. Bayliss, G. Björnsson, M. Bremer, Z. Cano, S. Covino, V. D'Elia, D. A. Frail, S. Geier, P. Goldoni, O. E. Hartoog, P. Jakobsson, H. Korhonen, K. Y. Lee, B. Milvang-Jensen, M. Nardini, A. Nicuesa Guelbenzu, M. Oguri, S. B. Pandey, G. Petitpas, A. Rossi, A. Sandberg, S. Schmidl, G. Tagliaferri, R. P. J. Tilanus, J. M. Winters, D. Wright, and E. Wuyts. GRB 120422A/SN 2012bz: Bridging the Gap between Low- And High-Luminosity GRBs. *ArXiv e-prints*, Jan. 2014.
- I. R. Seitenzahl, F. Ciaraldi-Schoolmann, F. K. Röpkke, M. Fink, W. Hillebrandt, M. Kromer, R. Pakmor, A. J. Ruiter, S. A. Sim, and S. Taubenberger. Three-dimensional delayed-detonation models with nucleosynthesis for Type Ia supernovae. *MNRAS*, 429:1156–1172, Feb. 2013.
- K. J. Shen and L. Bildsten. Unstable Helium Shell Burning on Accreting White Dwarfs. *ApJ*, 699:1365–1373, July 2009.
- I. Shivvers, P. Mazzali, J. M. Silverman, J. Botyánszki, S. B. Cenko, A. V. Filippenko, D. Kasen, S. D. Van Dyk, and K. I. Clubb. Nebular spectroscopy of the nearby Type IIb supernova 2011dh. *MNRAS*, Oct. 2013.
- J. M. Silverman, P. E. Nugent, A. Gal-Yam, M. Sullivan, D. A. Howell, A. V. Filippenko, I. Arcavi, S. Ben-Ami, J. S. Bloom, S. B. Cenko, Y. Cao, R. Chornock, K. I. Clubb, A. L. Coil, R. J. Foley, M. L. Graham, C. V. Griffith, A. Horesh, M. M. Kasliwal, S. R. Kulkarni, D. C. Leonard, W. Li, T. Matheson, A. A. Miller, M. Modjaz, E. O. Ofek, Y.-C. Pan, D. A. Perley, D. Poznanski, R. M. Quimby, T. N. Steele, A. Sternberg, D. Xu, and O. Yaron. Type Ia Supernovae Strongly Interacting with Their Circumstellar Medium. *ApJS*, 207:3, July 2013.

- S. A. Sim, I. R. Seitenzahl, M. Kromer, F. Ciaraldi-Schoolmann, F. K. Röpke, M. Fink, W. Hillebrandt, R. Pakmor, A. J. Ruiter, and S. Taubenberger. Synthetic light curves and spectra for three-dimensional delayed-detonation models of Type Ia supernovae. *MNRAS*, Sept. 2013.
- S. J. Smartt. Progenitors of Core-Collapse Supernovae. *ARA&A*, 47:63–106, Sept. 2009.
- S. J. Smartt, J. R. Maund, M. A. Hendry, C. A. Tout, G. F. Gilmore, S. Mattila, and C. R. Benn. Detection of a Red Supergiant Progenitor Star of a Type II-Plateau Supernova. *Science*, 303:499–503, Jan. 2004.
- N. Smith, R. J. Foley, and A. V. Filippenko. Dust Formation and He II  $\lambda 4686$  Emission in the Dense Shell of the Peculiar Type Ib Supernova 2006jc. *ApJ*, 680:568–579, June 2008.
- N. Smith, W. Li, A. A. Miller, J. M. Silverman, A. V. Filippenko, J.-C. Cuillandre, M. C. Cooper, T. Matheson, and S. D. Van Dyk. A Massive Progenitor of the Luminous Type II In Supernova 2010jl. *ApJ*, 732:63–+, May 2011.
- A. M. Soderberg, E. Berger, K. L. Page, P. Schady, J. Parrent, D. Pooley, X.-Y. Wang, E. O. Ofek, A. Cucchiara, A. Rau, E. Waxman, J. D. Simon, D. C.-J. Bock, P. A. Milne, M. J. Page, J. C. Barentine, S. D. Barthelmy, A. P. Beardmore, M. F. Bietenholz, P. Brown, A. Burrows, D. N. Burrows, G. Byrngelson, S. B. Cenko, P. Chandra, J. R. Cummings, D. B. Fox, A. Gal-Yam, N. Gehrels, S. Immler, M. Kasliwal, A. K. H. Kong, H. A. Krimm, S. R. Kulkarni, T. J. Maccarone, P. Mészáros, E. Nakar, P. T. O’Brien, R. A. Overzier, M. de Pasquale, J. Racusin, N. Rea, and D. G. York. An extremely luminous X-ray outburst at the birth of a supernova. *Nature*, 453:469–474, May 2008.
- A. M. Soderberg, S. Chakraborti, G. Pignata, R. A. Chevalier, P. Chandra, A. Ray, M. H. Wieringa, A. Copete, V. Chaplin, V. Connaughton, S. D. Barthelmy, M. F. Bietenholz, N. Chugai, M. D. Stritzinger, M. Hamuy, C. Fransson, O. Fox, E. M. Levesque, J. E. Grindlay, P. Challis, R. J. Foley, R. P. Kirshner, P. A. Milne, and M. A. P. Torres. A relativistic type Ibc supernova without a detected  $\gamma$ -ray burst. *Nature*, 463:513–515, Jan. 2010.

- A. M. Soderberg, R. Margutti, B. A. Zauderer, M. Krauss, B. Katz, L. Chomiuk, J. A. Dittmann, E. Nakar, T. Sakamoto, N. Kawai, K. Hurley, S. Barthelmy, T. Toizumi, M. Morii, R. A. Chevalier, M. Gurwell, G. Petitpas, M. Rupen, K. D. Alexander, E. M. Levesque, C. Fransson, A. Brunthaler, M. F. Bietenholz, N. Chugai, J. Grindlay, A. Copete, V. Connaughton, M. Briggs, C. Meegan, A. von Kienlin, X. Zhang, A. Rau, S. Golenetskii, E. Mazets, and T. Cline. Panchromatic Observations of SN 2011dh Point to a Compact Progenitor Star. *ApJ*, 752:78, June 2012.
- K. Z. Stanek, T. Matheson, P. M. Garnavich, P. Martini, P. Berlind, N. Caldwell, P. Challis, W. R. Brown, R. Schild, K. Krisciunas, M. L. Calkins, J. C. Lee, N. Hathi, R. A. Jansen, R. Windhorst, L. Echevarria, D. J. Eisenstein, B. Pindor, E. W. Olszewski, P. Harding, S. T. Holland, and D. Bersier. Spectroscopic Discovery of the Supernova 2003dh Associated with GRB 030329. *ApJ Let.*, 591:L17–L20, July 2003.
- S. G. Stewart, M. N. Fanelli, G. G. Byrd, J. K. Hill, D. J. Westpfahl, K.-P. Cheng, R. W. O’Connell, M. S. Roberts, S. G. Neff, A. M. Smith, and T. P. Stecher. Star Formation Triggering Mechanisms in Dwarf Galaxies: The Far-Ultraviolet,  $H\alpha$ , and H I Morphology of Holmberg II. *ApJ*, 529:201–218, Jan. 2000.
- M. Stritzinger, M. Hamuy, N. B. Suntzeff, R. C. Smith, M. M. Phillips, J. Maza, L.-G. Strolger, R. Antezana, L. González, M. Wischnjewsky, P. Candia, J. Espinoza, D. González, C. Stubbs, A. C. Becker, E. P. Rubenstein, and G. Galaz. Optical Photometry of the Type Ia Supernova 1999ee and the Type Ib/c Supernova 1999ex in IC 5179. *AJ*, 124:2100–2117, Oct. 2002.
- M. Stritzinger, P. Mazzali, M. M. Phillips, S. Immler, A. Soderberg, J. Sollerman, L. Boldt, J. Braithwaite, P. Brown, C. R. Burns, C. Contreras, R. Covarrubias, G. Folatelli, W. L. Freedman, S. González, M. Hamuy, W. Krzeminski, B. F. Madore, P. Milne, N. Morrell, S. E. Persson, M. Roth, M. Smith, and N. B. Suntzeff. The He-Rich Core-Collapse Supernova 2007Y: Observations from X-Ray to Radio Wavelengths. *ApJ*, 696:713–728, May 2009.
- M. Sullivan, M. M. Kasliwal, P. E. Nugent, D. A. Howell, R. C. Thomas, E. O. Ofek, I. Arcavi, S. Blake, J. Cooke, A. Gal-Yam, I. M. Hook, P. Mazzali, P. Podsiadlowski,

- R. Quimby, L. Bildsten, J. S. Bloom, S. B. Cenko, S. R. Kulkarni, N. Law, and D. Poznanski. The Subluminous and Peculiar Type Ia Supernova PTF 09dav. *ApJ*, 732:118, May 2011.
- N. B. Suntzeff and P. Bouchet. The bolometric light curve of SN 1987A. I - Results from ESO and CTIO U to Q0 photometry. *AJ*, 99:650–663, Feb. 1990.
- M. Takada-Hidai, W. Aoki, and G. Zhao. Na I D Lines in the SN 2002ap Spectrum. *PASJ*, 54:899–903, Dec. 2002.
- M. Tanaka, N. Tominaga, K. Nomoto, S. Valenti, D. K. Sahu, T. Minezaki, Y. Yoshii, M. Yoshida, G. C. Anupama, S. Benetti, G. Chincarini, M. Della Valle, P. A. Mazzali, and E. Pian. Type Ib Supernova 2008D Associated With the Luminous X-Ray Transient 080109: An Energetic Explosion of a Massive Helium Star. *ApJ*, 692:1131–1142, Feb. 2009.
- S. Taubenberger, H. Navasardyan, J. I. Maurer, L. Zampieri, N. N. Chugai, S. Benetti, I. Agnoletto, F. Bufano, N. Elias-Rosa, M. Turatto, F. Patat, E. Cappellaro, P. A. Mazzali, T. Iijima, S. Valenti, A. Harutyunyan, R. Claudi, and M. Dolci. The He-rich stripped-envelope core-collapse supernova 2008ax. *MNRAS*, 413:2140–2156, May 2011.
- S. Taubenberger, A. Pastorello, P. A. Mazzali, S. Valenti, G. Pignata, D. N. Sauer, A. Arbey, O. Bärnbantner, S. Benetti, A. Della Valle, J. Deng, N. Elias-Rosa, A. V. Filippenko, R. J. Foley, A. Goobar, R. Kotak, W. Li, P. Meikle, J. Mendez, F. Patat, E. Pian, C. Ries, P. Ruiz-Lapuente, M. Salvo, V. Stanishev, M. Turatto, and W. Hillebrandt. SN 2004aw: confirming diversity of Type Ic supernovae. *MNRAS*, 371:1459–1477, Sept. 2006.
- L. Tomasella, E. Cappellaro, M. Fraser, M. L. Pumo, A. Pastorello, G. Pignata, S. Benetti, F. Bufano, M. Dennefeld, A. Harutyunyan, T. Iijima, A. Jerkstrand, E. Kankare, R. Kotak, L. Magill, V. Nascimbeni, P. Ochner, A. Siviero, S. Smartt, J. Sollerman, V. Stanishev, F. Taddia, S. Taubenberger, M. Turatto, S. Valenti, D. E. Wright, and L. Zampieri. Comparison of progenitor mass estimates for the type IIP SN 2012A. *ArXiv e-prints*, May 2013.

- N. Tominaga, S. I. Blinnikov, and K. Nomoto. Supernova Explosions of Super-asymptotic Giant Branch Stars: Multicolor Light Curves of Electron-capture Supernovae. *ApJ Let.*, 771:L12, July 2013.
- N. Tominaga, T. Morokuma, S. I. Blinnikov, P. Baklanov, E. I. Sorokina, and K. Nomoto. Shock Breakout in Type II Plateau Supernovae: Prospects for High-Redshift Supernova Surveys. *ApJS*, 193:20, Mar. 2011.
- N. Tominaga, M. Tanaka, K. Nomoto, P. A. Mazzali, J. Deng, K. Maeda, H. Umeda, M. Modjaz, M. Hicken, P. Challis, R. P. Kirshner, W. M. Wood-Vasey, C. H. Blake, J. S. Bloom, M. F. Skrutskie, A. Szentgyorgyi, E. E. Falco, N. Inada, T. Minezaki, Y. Yoshii, K. Kawabata, M. Iye, G. C. Anupama, D. K. Sahu, and T. P. Prabhu. The Unique Type Ib Supernova 2005bf: A WN Star Explosion Model for Peculiar Light Curves and Spectra. *ApJ Let.*, 633:L97–L100, Nov. 2005.
- D. Y. Tsvetkov, I. M. Volkov, P. Baklanov, S. Blinnikov, and O. Tuchin. Photometric Observations and Modeling of Type IIb Supernova 2008ax. *Peremennye Zvezdy*, 29:2, Nov. 2009.
- M. Turatto. Classification of Supernovae. In K. Weiler, editor, *Supernovae and Gamma-Ray Bursters*, volume 598 of *Lecture Notes in Physics*, Berlin Springer Verlag, pages 21–36, 2003.
- V. Utrobin. Type IIb supernova 1993J in M81: The explosion of a approximately 4 solar mass star in a close binary system. *A&A*, 281:L89–L92, Jan. 1994.
- V. P. Utrobin. An optimal hydrodynamic model for the normal type IIP supernova 1999em. *A&A*, 461:233–251, Jan. 2007.
- W. D. Vacca and B. Leibundgut. The Rise Times and Bolometric Light Curve of SN 1994D: Constraints on Models of Type IA Supernovae. *ApJ Let.*, 471:L37, Nov. 1996.
- S. Valenti, S. Benetti, E. Cappellaro, F. Patat, P. Mazzali, M. Turatto, K. Hurley, K. Maeda, A. Gal-Yam, R. J. Foley, A. V. Filippenko, A. Pastorello, P. Challis, F. Frontera, A. Harutyunyan, M. Iye, K. Kawabata, R. P. Kirshner, W. Li, Y. M. Lipkin, T. Matheson,

- K. Nomoto, E. O. Ofek, Y. Ohyama, E. Pian, D. Poznanski, M. Salvo, D. N. Sauer, B. P. Schmidt, A. Soderberg, and L. Zampieri. The broad-lined Type Ic supernova 2003jd. *MNRAS*, 383:1485–1500, Feb. 2008.
- S. Valenti, M. Fraser, S. Benetti, G. Pignata, J. Sollerman, C. Inserra, E. Cappellaro, A. Pastorello, S. J. Smartt, M. Ergon, M. T. Botticella, J. Brimacombe, F. Bufano, M. Crockett, I. Eder, D. Fugazza, J. B. Haislip, M. Hamuy, A. Harutyunyan, K. M. Ivarsen, E. Kankare, R. Kotak, A. P. Lacluyze, L. Magill, S. Mattila, J. Maza, P. A. Mazzali, D. E. Reichart, S. Taubenberger, M. Turatto, and L. Zampieri. SN 2009jf: a slow-evolving stripped-envelope core-collapse supernova. *MNRAS*, 416:3138–3159, Oct. 2011.
- S. Valenti, A. Pastorello, E. Cappellaro, S. Benetti, P. A. Mazzali, J. Manteca, S. Taubenberger, N. Elias-Rosa, R. Ferrando, A. Harutyunyan, V. P. Hentunen, M. Nissinen, E. Pian, M. Turatto, L. Zampieri, and S. J. Smartt. A low-energy core-collapse supernova without a hydrogen envelope. *Nature*, 459:674–677, June 2009.
- S. Valenti, S. Taubenberger, A. Pastorello, L. Aramyan, M. T. Botticella, M. Fraser, S. Benetti, S. J. Smartt, E. Cappellaro, N. Elias-Rosa, M. Ergon, L. Magill, E. Magnier, R. Kotak, P. A. Price, J. Sollerman, L. Tomasella, M. Turatto, and D. E. Wright. A Spectroscopically Normal Type Ic Supernova from a Very Massive Progenitor. *ApJ Let.*, 749:L28, Apr. 2012.
- S. Valenti, F. Yuan, S. Taubenberger, K. Maguire, A. Pastorello, S. Benetti, S. J. Smartt, E. Cappellaro, D. A. Howell, L. Bildsten, K. Moore, M. Stritzinger, J. P. Anderson, S. Benitez-Herrera, F. Bufano, S. Gonzalez-Gaitan, M. G. McCrum, G. Pignata, M. Fraser, A. Gal-Yam, L. Le Guillou, C. Inserra, D. E. Reichart, R. Scalzo, M. Sullivan, O. Yaron, and D. R. Young. PESSTO monitoring of SN 2012hn: further heterogeneity among faint Type I supernovae. *MNRAS*, 437:1519–1533, Jan. 2014.
- P. G. van Dokkum. Cosmic-Ray Rejection by Laplacian Edge Detection. *PASP*, 113:1420–1427, Nov. 2001.
- S. D. Van Dyk, T. J. Davidge, N. Elias-Rosa, S. Taubenberger, W. Li, E. M. Levesque,

- S. Howerton, G. Pignata, N. Morrell, M. Hamuy, and A. V. Filippenko. Supernova 2008bk and Its Red Supergiant Progenitor. *AJ*, 143:19, Jan. 2012.
- S. D. Van Dyk, W. Li, S. B. Cenko, M. M. Kasliwal, A. Horesh, E. O. Ofek, A. L. Kraus, J. M. Silverman, I. Arcavi, A. V. Filippenko, A. Gal-Yam, R. M. Quimby, S. R. Kulkarni, O. Yaron, and D. Polishook. The Progenitor of Supernova 2011dh/PTF11eon in Messier 51. *ApJ Let.*, 741:L28, Nov. 2011.
- S. D. Van Dyk, W. Li, and A. V. Filippenko. On the Progenitor of the Type II-Plateau Supernova 2003gd in M74. *PASP*, 115:1289–1295, Nov. 2003.
- S. D. Van Dyk, W. Zheng, K. I. Clubb, A. V. Filippenko, S. B. Cenko, N. Smith, O. D. Fox, P. L. Kelly, I. Shivvers, and M. Ganeshalingam. The Progenitor of Supernova 2011dh Has Vanished. *ArXiv e-prints*, May 2013.
- J. S. Vink and A. de Koter. On the metallicity dependence of Wolf-Rayet winds. *A&A*, 442: 587–596, Nov. 2005.
- J. S. Vink, A. de Koter, and H. J. G. L. M. Lamers. Mass-loss predictions for O and B stars as a function of metallicity. *A&A*, 369:574–588, Apr. 2001.
- R. Waldman, D. Sauer, E. Livne, H. Perets, A. Glasner, P. Mazzali, J. W. Truran, and A. Gal-Yam. Helium Shell Detonations on Low-mass White Dwarfs as a Possible Explanation for SN 2005E. *ApJ*, 738:21, Sept. 2011.
- A. R. Walker and N. B. Suntzeff. UBVRI CCD photometry of stars near SN 1987A. *PASP*, 102:131–138, Feb. 1990.
- R. F. Webbink. Double white dwarfs as progenitors of R Coronae Borealis stars and Type I supernovae. *ApJ*, 277:355–360, Feb. 1984.
- S. E. Woosley. Gamma-ray bursts from stellar mass accretion disks around black holes. *ApJ*, 405:273–277, Mar. 1993.
- S. E. Woosley, S. Blinnikov, and A. Heger. Pulsational pair instability as an explanation for the most luminous supernovae. *Nature*, 450:390–392, Nov. 2007.

- S. E. Woosley, R. G. Eastman, T. A. Weaver, and P. A. Pinto. SN 1993J: A Type IIb supernova. *ApJ*, 429:300–318, July 1994.
- S. E. Woosley, A. Heger, and T. A. Weaver. The evolution and explosion of massive stars. *Reviews of Modern Physics*, 74:1015–1071, Nov. 2002.
- D. Xu, A. de Ugarte Postigo, G. Leloudas, T. Krühler, Z. Cano, J. Hjorth, D. Malesani, J. P. U. Fynbo, C. C. Thöne, R. Sánchez-Ramírez, S. Schulze, P. Jakobsson, L. Kaper, J. Sollerman, D. J. Watson, A. Cabrera-Lavers, C. Cao, S. Covino, H. Flores, S. Geier, J. Gorosabel, S. M. Hu, B. Milvang-Jensen, M. Sparre, L. P. Xin, T. M. Zhang, W. K. Zheng, and Y. C. Zou. Discovery of the Broad-lined Type Ic SN 2013cq Associated with the Very Energetic GRB 130427A. *ApJ*, 776:98, Oct. 2013.
- O. Yaron and A. Gal-Yam. WISEREP - An Interactive Supernova Data Repository. *PASP*, 124:668–681, July 2012.
- Y. Yoshii, H. Tomita, Y. Kobayashi, J. Deng, K. Maeda, K. Nomoto, P. A. Mazzali, H. Umeda, T. Aoki, M. Doi, K. Enya, T. Minezaki, M. Suganuma, and B. A. Peterson. The Optical/Near-Infrared Light Curves of SN 2002ap for the First 140 Days after Discovery. *ApJ*, 592:467–474, July 2003.
- D. R. Young, S. J. Smartt, S. Valenti, A. Pastorello, S. Benetti, C. R. Benn, D. Bersier, M. T. Botticella, R. L. M. Corradi, A. H. Harutyunyan, M. Hrudkova, I. Hunter, S. Mattila, E. J. W. de Mooij, H. Navasardyan, I. A. G. Snellen, N. R. Tanvir, and L. Zampieri. Two type Ic supernovae in low-metallicity, dwarf galaxies: diversity of explosions. *A&A*, 512:A70, Mar. 2010.
- T. R. Young, E. Baron, and D. Branch. Light Curve Studies of SN 1993J and SN 1994I. *ApJ Let.*, 449:L51, Aug. 1995.
- F. Yuan, C. Kobayashi, B. P. Schmidt, P. Podsiadlowski, S. A. Sim, and R. A. Scalzo. Locations of peculiar supernovae as a diagnostic of their origins. *MNRAS*, 432:1680–1686, June 2013.
- B.-B. Zhang, B. Zhang, K. Murase, V. Connaughton, and M. S. Briggs. How Long does a Burst Burst? *ArXiv e-prints*, Oct. 2013.

- F.-Y. Zhao, R. G. Strom, and S.-Y. Jiang. The Guest Star of AD185 must have been a Supernova. *Chinese J. Astron. Astrophys.*, 6:635–640, Oct. 2006.
- W. Zheng, J. M. Silverman, A. V. Filippenko, D. Kasen, P. E. Nugent, M. Graham, X. Wang, S. Valenti, F. Ciabattari, P. L. Kelly, O. D. Fox, I. Shivvers, K. I. Clubb, S. B. Cenko, D. Balam, D. A. Howell, E. Hsiao, W. Li, G. H. Marion, D. Sand, J. Vinko, J. C. Wheeler, and J. Zhang. The Very Young Type Ia Supernova 2013dy: Discovery, and Strong Carbon Absorption in Early-Time Spectra. *ArXiv e-prints*, Oct. 2013.
- F. Zwicky. On the Frequency of Supernovae. II. *ApJ*, 96:28, July 1942.
- T. Zwitter, U. Munari, and S. Moretti. Supernova 2004et in NGC 6946. *IAU Circular*, 8413: 1, Sept. 2004.